

NUMERICAL AND EXPERIMENTAL ANALYSIS OF MAGNETIC GEARS

A Dissertation

by

MATTHEW C. GARDNER

Submitted to the Office of Graduate and Professional Studies of  
Texas A&M University  
in partial fulfillment of the requirements for the degree of

DOCTOR OF PHILOSOPHY

|                     |                       |
|---------------------|-----------------------|
| Chair of Committee, | Hamid A. Toliyat      |
| Committee Members,  | Mehrdad Ehsani        |
|                     | Shankar Bhattacharyya |
|                     | Won-Jong Kim          |
| Head of Department, | Miroslav Begovic      |

August 2019

Major Subject: Electrical Engineering

Copyright 2019 Matthew C. Gardner

## ABSTRACT

Like mechanical gears, magnetic gears convert power between low-speed, high-torque rotation and high-speed, low-torque rotation. This work compares various magnetic gear designs and topologies, introduces an approach for evaluating their dynamic behavior, and describes a prototype's design, fabrication, and test results. Significant differences are illustrated between the designs minimizing cost and those minimizing volume, especially regarding the usage of permanent magnet material. Axial flux coaxial magnetic gears can outperform their radial flux counterparts at form factors with outer radii much larger than the axial length, but axial flux gears suffer from large forces on the rotors. Cycloidal magnetic gears achieve higher torque densities at high gear ratios than coaxial magnetic gears, but cycloidal magnetic gears perform worse at low gear ratios and suffer from increased mechanical complexity and large forces on the bearings. For coaxial magnetic gears, the torque density and efficiency of a single-stage reduce significantly as the gear ratio increases; however, a high gear ratio can be achieved with less reduction in torque density if magnetic gears are connected in series to form a multistage magnetic gearbox. Alternatively, a compound differential coaxial magnetic gear can be formed from two single-stage coaxial magnetic gears and can achieve a very high gear ratio, but it suffers from circulating power, which results in poor efficiencies. The gear ratio significantly impacts the dynamic behavior of magnetically geared systems. This dynamic behavior can be evaluated by separating the system's motion into rigid body motion and fixed center motion and by applying the

conservation of energy principle to the torque angle reference frame. Halbach arrays and air cores can significantly increase a magnetic gear's torque density with respect to mass, when used together. To further explore this concept, a prototype magnetic gear with Halbach arrays and air cores was designed, fabricated, and tested. The prototype showed good agreement with simulation regarding slip torque and gear ratio. The prototype achieved a mass competitive with some similarly rated commercially available mechanical gears and also achieved a favorable projected efficiency compared to these mechanical gears.

## DEDICATION

To everyone who reads this and learns something from it.

## ACKNOWLEDGEMENTS

I would like to thank my advisor, Dr. Toliyat, for all of the support and guidance that made this research possible. Additionally, I would like to thank my other committee members, Dr. Ehsani, Dr. Bhattacharyya, and Dr. Kim, for contributing their time to support my studies and for what I learned from their classes. Also, I would like to thank Dr. Kalafatis for being able to be a substitute to attend my defense.

Furthermore, I would like to thank my labmates for their advice, aid, and amicability. Specifically, I would like to thank Dr. Siavash Pakdelian, Dr. Yateendra Deshpande, Dr. Jae-Bum Park, Dr. Vivek Sundaram, Mr. Yongqi Li, Dr. Khaled Jaafari, Dr. Abdulkadir Bostanci, Dr. Hussain Hussain, Dr. Morteza Moosavi, Dr. Niloofar Torabi, Dr. Bahar Anvari, Dr. Ajay Morya, Dr. Amir Negahdari, Mr. Derek Janak, Mr. Yichi Zhang, Mr. Benjamin Jack, Mr. Farid Naghavi, Ms. Shima Hasanpour, Ms. Dorsa Talebi, Mr. Mesaad AlBader, and Mr. Bryton Praslicka. A special thanks is due to Dr. Matthew Johnson, who in many ways served as an extra advisor for me. Much of my research builds on his discoveries and accomplishments. Without his help, I would not have been able to accomplish anywhere near what I have been able to do during my time at Texas A&M. I have thoroughly enjoyed working with him and am extremely grateful for his generous assistance, excellent character, and friendship.

Also, I would like to thank all of the ECEN department staff who facilitated my study and research at Texas A&M. I would especially like to thank Mrs. Lisa Cauvel and Mrs. Tiphany Bode, both of whom I visited almost daily over the weeks when I was

fabricating my prototype. Additionally, I would like to thank Mrs. Ping Luo from High Performance Research Computing for helping to get simulations set up on the high performance research computing clusters.

## CONTRIBUTORS AND FUNDING SOURCES

### **Contributors**

This work was supervised by a dissertation committee consisting of Professor Hamid Toliyat, the advisor, Professor Mehrdad Ehsani, and Professor Shankar Bhattacharyya of the Department of Electrical and Computer Engineering and Professor Won-Jong Kim of the Department of Mechanical Engineering.

Much of this work was done in collaboration with Dr. Matthew Johnson, who provided significant assistance in generating and analyzing the data in Sections 2, 3, 4, 5, and 7. Dr. Johnson, Mr. Yichi Zhang, and Ms. Shima Hasanpour also provided additional hands and advice during the assembly and testing of the prototype described in Section 8. Additionally, the genetic algorithm employed in Sections 2 and 5 was developed in collaboration with Mr. Benjamin Jack. All other work was completed independently.

### **Funding Sources**

Graduate study was supported by fellowships from Texas A&M University, the Department of Electrical and Computer Engineering, the Electrical Power and Power Electronics Institute at Texas A&M University, and the Texas A&M Energy Institute.

This work was also made possible in part by the US Army Research Laboratory through the Industry & University Cooperative Research Center for Next Generation Photovoltaics and under Contract No. W911NF1820289. Its contents are solely the

responsibility of the author and do not necessarily represent the official views of the US Army Research Laboratory.



## TABLE OF CONTENTS

|   | Page |
|---|------|
| ABSTRACT .....  | ii   |
| DEDICATION .....  | iv   |
| ACKNOWLEDGEMENTS .....  | v    |
| CONTRIBUTORS AND FUNDING SOURCES.....   | vii  |
| TABLE OF CONTENTS .....   | ix   |
| LIST OF FIGURES.....  | xii  |
| LIST OF TABLES .....  | xxiv |
| 1. INTRODUCTION.....  | 1    |
| 1.1. The Motivation for Magnetic Gears.....   | 1    |
| 1.2. Early Magnetic Gears.....  | 3    |
| 1.3. Modern Magnetic Gears.....   | 5    |
| 1.4. Magnetically Geared Machines.....  | 11   |
| 1.5. A Comparison of Magnetic Gears and Conventional Alternatives.....                              | 16   |
| 2. OPTIMIZATION FOR DIFFERENT METRICS.....  | 20   |
| 2.1. Design Study Methodology.....  | 21   |
| 2.2. Results .....  | 25   |
| 2.3. Conclusion.....  | 48   |
| 3. COMPARISON OF AXIAL FLUX AND RADIAL FLUX COAXIAL<br>MAGNETIC GEARS.....                          | 51   |
| 3.1. Design Study Methodology.....  | 53   |
| 3.2. Results .....  | 58   |
| 3.2.1. 2D Cross-Sectional Design Parameters.....  | 58   |
| 3.2.2. 3D Design Scaling Parameters .....   | 71   |
| 3.3. Conclusion.....  | 88   |
| 4. COMPARISON OF SURFACE PERMANENT MAGNET COAXIAL AND<br>CYCLOIDAL RADIAL FLUX MAGNETIC GEARS ..... | 91   |

|   |            |
|---|------------|
| 4.1. Design Study Methodology.....  | 93         |
| 4.2. Results .....  | 96         |
| 4.3. The Spatial Distribution of Torque Production.....   | 108        |
| 4.4. Rotor Forces and Torque Ripples.....   | 112        |
| 4.5. Conclusion.....  | 117        |
| <b>5. ANALYSIS OF HIGH GEAR RATIO CAPABILITIES FOR SINGLE-STAGE, SERIES MULTISTAGE, AND COMPOUND DIFFERENTIAL COAXIAL MAGNETIC GEARS.....</b> | <b>120</b> |
| 5.1. Single-Stage Coaxial Magnetic Gears.....   | 121        |
| 5.2. Series Multistage Coaxial Magnetic Gears .....   | 130        |
| 5.3. Compound Differential Coaxial Magnetic Gears.....  | 135        |
| 5.4. Conclusion.....  | 143        |
| <b>6. NONLINEAR ANALYSIS OF MAGNETIC GEAR DYNAMICS USING SUPERPOSITION AND CONSERVATION OF ENERGY .....</b>                                   | <b>145</b> |
| 6.1. Magnetic Gear Dynamic Model.....   | 146        |
| 6.1.1. Superposition of Rigid Body and Fixed Center Motion.....   | 148        |
| 6.1.2. Conservation of Energy.....  | 152        |
| 6.2. Design Implications.....   | 153        |
| 6.2.1. Effective Inertia Ratio .....  | 153        |
| 6.2.2. Responses to Step Changes in Torque .....  | 155        |
| 6.3. Model Validation.....  | 157        |
| 6.4. Conclusion.....  | 176        |
| <b>7. ANALYSIS OF RADIAL FLUX COAXIAL MAGNETIC GEARS WITH HALBACH ARRAYS .....</b>  | <b>179</b> |
| 7.1. Design Study Methodology.....  | 182        |
| 7.2. Results .....  | 184        |
| 7.3. Conclusion.....  | 207        |
| <b>8. PROTOTYPE RADIAL FLUX COAXIAL MAGNETIC GEAR WITH HALBACH ARRAYS AND AIR CORES .....</b>   | <b>209</b> |
| 8.1. Magnetic and Mechanical Tradeoff Analysis .....  | 209        |
| 8.1.1. Modulators Support.....  | 211        |
| 8.1.2. Magnet Retention .....   | 215        |
| 8.1.3. Impact of Back Irons .....   | 220        |
| 8.2. Prototype Fabrication .....  | 222        |
| 8.2.1. Structural Material Selection.....   | 222        |
| 8.2.2. Assembly .....   | 225        |
| 8.3. Experimental Results.....  | 232        |

|   |     |
|---|-----|
| 8.4. Comparison with Mechanical Gears ..... | 236 |
| 9. CONCLUSIONS.....                         | 237 |
| REFERENCES .....                            | 242 |

## LIST OF FIGURES

|  | Page |
|--|------|
| Figure 1.1 Early magnetic gear patent drawings by (a) Armstrong in 1901 and (b) Faus in 1941. Reprinted from [12] and [13].          | 4    |
| Figure 1.2 Early flux modulated magnetic gear proposed by Neuland in 1916. Reprinted from [14].                                      | 5    |
| Figure 1.3 Radial flux coaxial magnetic gear.  | 6    |
| Figure 1.4 Axial flux coaxial magnetic gear.   | 7    |
| Figure 1.5 Cross-sections of radial flux (a) cycloidal and (b) harmonic magnetic gears.  | 9    |
| Figure 1.6 Magnetically decoupled inner stator radial flux magnetically geared machine cross-section.                                | 13   |
| Figure 1.7 Exploded view of an outer stator radial flux magnetically geared machine.   | 14   |
| Figure 1.8 Exploded view of a series connected axial flux magnetically geared machine.   | 15   |
| Figure 1.9 Exploded view of a compact axial flux magnetically geared machine.  | 16   |
| Figure 1.10 Volumetric torque density trends for high safety factor mechanical planetary gears. Reprinted with permission from [29]. | 17   |
| Figure 1.11 Volumetric torque density trends for low safety factor mechanical planetary gears. Reprinted with permission from [29].  | 18   |
| Figure 1.12 Volumetric torque density trends for radial flux coaxial magnetic gears. Reprinted with permission from [29].            | 18   |
| Figure 2.1 Performances of designs based on 2D FEA simulations.  | 26   |
| Figure 2.2 Performances of designs based on 3D FEA simulations.  | 27   |
| Figure 2.3 Performances of designs based on 3D FEA simulations with an axial buffer.   | 27   |
| Figure 2.4 The Pareto optimal fronts maximizing VTD (or LA VTD), TPD, and GTD.   | 28   |

|   |    |
|---|----|
| Figure 2.5 GA driven evolution of the VTD of the three optimal designs based on 2D simulations..... | 31 |
| Figure 2.6 GA driven evolution of the TPD of the three optimal designs based on 2D simulations..... | 31 |
| Figure 2.7 GA driven evolution of the GTD of the three optimal designs based on 2D simulations..... | 32 |
| Figure 2.8 Variation of maximum VTD and LA VTD with outer radius. ....                              | 33 |
| Figure 2.9 Variation of maximum TPD with outer radius. ....   | 33 |
| Figure 2.10 Variation of maximum GTD with outer radius. ....  | 34 |
| Figure 2.11 Variation of maximum VTD and LA VTD with Rotor 1 PM thickness. ....                     | 35 |
| Figure 2.12 Variation of maximum TPD with Rotor 1 PM thickness. ....                                | 36 |
| Figure 2.13 Variation of maximum GTD with Rotor 1 PM thickness.....                                 | 36 |
| Figure 2.14 Variation of maximum VTD and LA VTD with Rotor 1 pole pair count. ....                  | 37 |
| Figure 2.15 Variation of maximum TPD with Rotor 1 pole pair count. ....                             | 38 |
| Figure 2.16 Variation of maximum GTD with Rotor 1 pole pair count. ....                             | 38 |
| Figure 2.17 Variation of maximum VTD and LA VTD with back iron thicknesses.....                     | 39 |
| Figure 2.18 Variation of maximum TPD with back iron thicknesses. ....                               | 40 |
| Figure 2.19 Variation of maximum GTD with back iron thicknesses. ....                               | 40 |
| Figure 2.20 Variation of maximum VTD and LA VTD with modulator fill factor.....                     | 41 |
| Figure 2.21 Variation of maximum TPD with modulator fill factor.....                                | 42 |
| Figure 2.22 Variation of maximum GTD with modulator fill factor. ....                               | 42 |
| Figure 2.23 Variation of maximum VTD and LA VTD with PM fill factors. ....                          | 43 |
| Figure 2.24 Variation of maximum TPD with PM fill factors.....                                      | 44 |
| Figure 2.25 Variation of maximum GTD with PM fill factors. ....                                     | 44 |
| Figure 2.26 Variation of maximum VTD and LA VTD with modulator thickness.....                       | 45 |

|  |    |
|--|----|
| Figure 2.27 Variation of maximum TPD with modulator thickness. ....  | 46 |
| Figure 2.28 Variation of maximum GTD with modulator thickness. ....  | 46 |
| Figure 2.29 Variation of maximum VTD and LA VTD with magnet thickness ratio. ....  | 47 |
| Figure 2.30 Variation of maximum TPD with magnet thickness ratio. ....   | 48 |
| Figure 2.31 Variation of maximum GTD with magnet thickness ratio. ....   | 48 |
| Figure 3.1 Variation of maximum VTD with Rotor 1 PM thickness for radial flux designs with a stack length of 50 mm and axial designs, both based on 3D FEA and having $G_{Int} = 4$ . ....   | 58 |
| Figure 3.2 Variation of maximum GTD with Rotor 1 PM thickness for radial flux designs with a stack length of 50 mm and axial designs, both based on 3D FEA and having $G_{Int} = 4$ . ....   | 59 |
| Figure 3.3 Variation of maximum PM GTD with Rotor 1 PM thickness for radial flux designs with a stack length of 50 mm and axial designs, both based on 3D FEA and having $G_{Int} = 4$ . ....  | 60 |
| Figure 3.4 Variation of maximum VTD with Rotor 1 pole pair count for radial flux designs with a stack length of 50 mm and axial designs, both based on 3D FEA and having $G_{Int} = 4$ . ....  | 63 |
| Figure 3.5 Variation of maximum GTD with Rotor 1 pole pair count for radial flux designs with a stack length of 50 mm and axial designs, both based on 3D FEA and having $G_{Int} = 4$ . ....  | 64 |
| Figure 3.6 Variation of maximum PM GTD with Rotor 1 pole pair count for radial flux designs with a stack length of 50 mm and axial designs, both based on 3D FEA and having $G_{Int} = 4$ . ....   | 65 |
| Figure 3.7 Variation of maximum average low speed air gap shear stress with Rotor 1 PM thickness and pole pair count for axial flux gears with 200 mm outer radii and $G_{Int} = 4$ . The dashed line indicates the optimal Rotor 1 pole pair count for each Rotor 1 PM thickness. ....                        | 66 |
| Figure 3.8 Variation of maximum average low speed air gap shear stress with Rotor 1 PM thickness and pole pair count for radial flux gears with 50 mm stack lengths, 200 mm outer radii, and $G_{Int} = 4$ . The dashed line indicates the optimal Rotor 1 pole pair count for each Rotor 1 PM thickness. .... | 67 |

|  |    |
|--|----|
| Figure 3.9 Variation of (a) maximum VTD and (b) the corresponding optimum Rotor 1 pole pair count for maximizing VTD with $G_{Int}$ at different outer radius values for both axial flux gears and 50 mm stack length radial flux gears. ....        | 68 |
| Figure 3.10 Variation of (a) maximum GTD and (b) the corresponding optimum Rotor 1 pole pair count for maximizing GTD with $G_{Int}$ at different outer radius values for both axial flux gears and 50 mm stack length radial flux gears. ....       | 69 |
| Figure 3.11 Variation of (a) maximum PM GTD and (b) the corresponding optimum Rotor 1 pole pair count for maximizing PM GTD with $G_{Int}$ at different outer radius values for both axial flux gears and 50 mm stack length radial flux gears. .... | 70 |
| Figure 3.12 Variation of maximum VTD with outer radius for both axial flux gears and 50 mm stack length radial flux gears at different $G_{Int}$ values. ....  | 72 |
| Figure 3.13 Variation of maximum GTD with outer radius for both axial flux gears and 50 mm stack length radial flux gears at different $G_{Int}$ values. ....  | 73 |
| Figure 3.14 Variation of maximum PM GTD with outer radius for both axial flux gears and 50 mm stack length radial flux gears at different $G_{Int}$ values. ....   | 74 |
| Figure 3.15 Variation of maximum VTD (a) at a 50 mm outer radius and (b) at a 200 mm outer radius with stack length for radial flux gears at different $G_{Int}$ values (based on 2D and 3D FEA). ....   | 75 |
| Figure 3.16 Variation of maximum GTD (a) at a 50 mm outer radius and (b) at a 200 mm outer radius with stack length for radial flux gears at different $G_{Int}$ values (based on 2D and 3D FEA). ....   | 76 |
| Figure 3.17 Variation of maximum PM GTD (a) at a 50 mm outer radius and (b) at a 200 mm outer radius with stack length for radial flux gears at different $G_{Int}$ values (based on 2D and 3D FEA). ....  | 77 |
| Figure 3.18 Variation of maximum VTD (a) at a 50 mm outer radius and (b) at a 200 mm outer radius with radii ratio for axial flux gears at different $G_{Int}$ values. ..  | 78 |
| Figure 3.19 Variation of maximum GTD (a) at a 50 mm outer radius and (b) at a 200 mm outer radius with radii ratio for axial flux gears at different $G_{Int}$ values. ..  | 79 |
| Figure 3.20 Variation of maximum PM GTD (a) at a 50 mm outer radius and (b) at a 200 mm outer radius with radii ratio for axial flux gears at different $G_{Int}$ values. ....   | 80 |

|   |     |
|---|-----|
| Figure 3.21 Variation of maximum VTD with radii ratio and Rotor 1 pole pair count for axial flux gears (with a 200 mm outer radius and $G_{Int} = 4$ ). The dashed line indicates the optimal Rotor 1 pole pair count for each radii ratio. ....    | 82  |
| Figure 3.22 Variation of maximum GTD with radii ratio and Rotor 1 pole pair count for axial flux gears (with a 200 mm outer radius and $G_{Int} = 4$ ). The dashed line indicates the optimal Rotor 1 pole pair count for each radii ratio. ....    | 82  |
| Figure 3.23 Variation of maximum PM GTD with radii ratio and Rotor 1 pole pair count for axial flux gears (with a 200 mm outer radius and $G_{Int} = 4$ ). The dashed line indicates the optimal Rotor 1 pole pair count for each radii ratio. .... | 83  |
| Figure 3.24 Variation of maximum average low speed air gap shear stress for radial flux gears with $G_{Int} = 4$ . ....   | 84  |
| Figure 3.25 Variation of maximum average low speed air gap shear stress for axial flux gears with $G_{Int} = 4$ . ....  | 84  |
| Figure 3.26 Rotor 2 slip torques corresponding to the radial flux gear design points in Figure 3.24. ....   | 85  |
| Figure 3.27 Rotor 2 slip torques corresponding to the axial flux gear design points in Figure 3.25. ....  | 86  |
| Figure 3.28 Rotor 1 axial magnetic forces corresponding to the slip torque alignments of the axial flux gear design points in Figure 3.25. ....   | 87  |
| Figure 3.29 Rotor 3 axial magnetic forces corresponding to the slip torque alignments of the axial flux gear design points in Figure 3.25. ....   | 88  |
| Figure 4.1 Variation of the maximum VTD with outer radius for designs with (a) $T_{AG} = 1$ mm and (b) $T_{AG} = R_{Out}/50$ . ....   | 97  |
| Figure 4.2 Variation of the maximum PM GTD with outer radius for designs with (a) $T_{AG} = 1$ mm and (b) $T_{AG} = R_{Out}/50$ . ....  | 98  |
| Figure 4.3 Variation of the maximum (a) VTD and (b) PM GTD with the inner rotor PM thickness for designs with $R_{Out} = 150$ mm and $T_{AG} = 1$ mm. ....  | 99  |
| Figure 4.4 Variation of the maximum VTD with outer radius and gear ratio for cycloidal designs with (a) $T_{AG} = 1$ mm and (b) $T_{AG} = R_{Out}/50$ . The dotted line indicates the gear ratio that maximizes VTD for each outer radius. ....     | 101 |



|   |     |
|---|-----|
| Figure 4.5 Variation of the maximum PM GTD with outer radius and gear ratio for cycloidal designs with (a) $T_{AG} = 1$ mm and (b) $T_{AG} = R_{Out} / 50$ . The dotted line indicates the gear ratio that maximizes PM GTD for each outer radius.....                              | 101 |
| Figure 4.6 Variation of the maximum (a) VTD and (b) PM GTD with axis offset and gear ratio for cycloidal designs with $R_{Out} = 150$ mm and $T_{AG} = 1$ mm. The dotted line indicates the gear ratio that maximizes VTD or PM GTD for each axis offset. ....                      | 102 |
| Figure 4.7 Variation of the maximum VTD with the stack length for (a) coaxial designs with $T_{AG} = 1$ mm and (b) coaxial designs with $T_{AG} = R_{Out} / 50$ based on both 2D and 3D FEA. ....   | 103 |
| Figure 4.8 Variation of the maximum VTD with the stack length for (a) cycloidal designs with $T_{AG} = 1$ mm and (b) cycloidal designs with $T_{AG} = R_{Out} / 50$ based on both 2D and 3D FEA. ....   | 104 |
| Figure 4.9 Variation of the maximum PM GTD with the stack length for (a) coaxial designs with $T_{AG} = 1$ mm and (b) coaxial designs with $T_{AG} = R_{Out} / 50$ based on both 2D and 3D FEA. ....  | 105 |
| Figure 4.10 Variation of the maximum PM GTD with the stack length for (a) cycloidal designs with $T_{AG} = 1$ mm and (b) cycloidal designs with $T_{AG} = R_{Out} / 50$ based on both 2D and 3D FEA. ....   | 106 |
| Figure 4.11 Variation of 3D end-effects on the maximum VTD designs of Figure 4.4, but at a stack length of 20 mm, with outer radius and gear ratio for cycloidal designs with (a) $T_{AG} = 1$ mm and (b) $T_{AG} = R_{Out} / 50$ . ....  | 107 |
| Figure 4.12 Variation of 3D end-effects on the maximum PM GTD designs of Figure 4.5, but at a stack length of 20 mm, with outer radius and gear ratio for cycloidal designs with (a) $T_{AG} = 1$ mm and (b) $T_{AG} = R_{Out} / 50$ .....  | 107 |
| Figure 4.13 Variation of $k_{\tau}$ and the inverse effective air gap function (both in per unit values) with spatial position in an example cycloidal magnetic gear.....   | 109 |
| Figure 4.14 $k_{\tau}$ plotted as the color in the air gap of the same cycloidal magnetic gear from Figure 4.13. ....   | 109 |
| Figure 4.15 Variation of the maximum (a) VTD and (b) PM GTD with the inner PM thickness and axis offset for cycloidal designs with $R_{Out} = 150$ mm and $T_{AG} = 1$ mm. The dotted line indicates the axis offset that maximizes VTD or PM GTD for each inner PM thickness. .... | 111 |

|   |     |
|---|-----|
| Figure 4.16 The net forces on the inner rotor at the maximum torque points of (a) the maximum VTD designs corresponding to the points in Figure 4.1(a) and of (b) the maximum PM GTD designs corresponding to the points in Figure 4.2(a) based on 3D FEA for designs with 50 mm stack lengths..... | 113 |
| Figure 4.17 The 2D FEA variation of (a) low speed shaft torque and (b) net magnetic forces on the inner rotor as the torque angle is varied for the maximum VTD and PM GTD cycloidal designs from the entire simulation study. ....   | 114 |
| Figure 4.18 The variation of the forces in the direction of the axis offset and in the direction perpendicular to the axis offset based on 2D FEA as the torque angle is varied for the maximum VTD and PM GTD cycloidal designs from the entire simulation study.....                              | 115 |
| Figure 4.19 The variation of the (a) low speed shaft torque and (b) net magnetic forces on the inner rotor based on 2D FEA during steady-state operation at the maximum torque angle for the maximum VTD and PM GTD cycloidal designs from the entire simulation study. ....                        | 117 |
| Figure 5.1 Pareto optimal fronts maximizing the gear's GTD over a range of gear ratios and outer radii for a single-stage magnetic gear with a low speed rotor slip torque of 1000 N·m. ....  | 124 |
| Figure 5.2 Variation of the maximum achievable system GTD with gear ratio and machine GTD for systems with a low speed slip torque of 1000 N·m. The dashed line traces the maximum achievable system GTD and the corresponding gear ratio for each machine GTD. ....                                | 126 |
| Figure 5.3 Variation of the maximum achievable gear GTD at various $G_{Int}$ values with the Rotor 1 pole pair count for designs with an outer radius of 150 mm based on 2D FEA.....  | 127 |
| Figure 5.4 Variation of the maximum achievable gear GTD at various $G_{Int}$ values with the Rotor 1 magnet thickness for designs with an outer radius of 150 mm based on 2D FEA.....   | 128 |
| Figure 5.5 Full load electromagnetic efficiencies of the optimal 150 mm outer radius points shown in Figure 5.1 over a wide range of speeds. ....   | 129 |
| Figure 5.6 Pareto optimal fronts maximizing gearbox GTD over a range of gear ratios for single-stage magnetic gearboxes and multistage magnetic gearboxes with 2, 3, or 4 series-connected stages and their last stage outer radii. ....  | 132 |

|   |     |
|---|-----|
| Figure 5.7 Pareto optimal fronts maximizing gearbox GTD over a range of gear ratios for single-stage magnetic gearboxes and multistage magnetic gearboxes with 2, 3, or 4 series-connected stages and their first stage gear ratios. ....   | 132 |
| Figure 5.8 Full load electromagnetic efficiencies of the optimal 2-stage coaxial magnetic gearboxes shown in Figure 5.6 and Figure 5.7. ....  | 134 |
| Figure 5.9 Full load electromagnetic efficiencies of the optimal 3-stage coaxial magnetic gearboxes shown in Figure 5.6 and Figure 5.7. ....  | 135 |
| Figure 5.10 $\theta$ -z transverse-sections of a radial flux CDCMG connected in the (a) Free Spinning Rotor 3 (FSR3) and (b) Free Spinning Rotor 2 (FSR2) configurations. ....  | 136 |
| Figure 5.11 Full load electromagnetic efficiencies for CDCMG Designs 1 and 2 in Table 5.3. ....   | 141 |
| Figure 6.1 Magnetic gear dynamic model. ....  | 147 |
| Figure 6.2 Magnetic gear dynamic model transformed to 1:1 gear ratio. ....  | 148 |
| Figure 6.3 Rigid body motion component of the magnetic gear dynamic model. ....   | 149 |
| Figure 6.4 Fixed center motion component of the magnetic gear dynamic model. ....   | 149 |
| Figure 6.5 Both the HSR and the LSR represented as moving relative to a fixed center of inertia. ....   | 151 |
| Figure 6.6 Both the HSR and the LSR transformed to the torque angle reference frame. ....   | 152 |
| Figure 6.7 The energy input into the Figure 6.6 system is the area under the step torque curve, and the energy stored in the nonlinear spring is the area under the nonlinear torque curve. The kinetic energy of the inertia is the difference between these two energies (assuming negligible losses). .... | 153 |
| Figure 6.8 The impact of $k_I$ on how much the per unit (relative to the slip torques of their respective rotors) machine torque and load torque contribute to $T^{FC}$ . ...   | 155 |
| Figure 6.9 The Simulink model used for comparison in this study. ....   | 159 |
| Figure 6.10 Cross-sections of the (a) FEA 1, (b) FEA 2, and (c) FEA 3 coaxial magnetic gear designs. ....   | 159 |
| Figure 6.11 Torque angle curves of the FEA 1 design. ....   | 160 |

|  |     |
|--|-----|
| Figure 6.12 Torque angle curves of the FEA 2 design.....   | 160 |
| Figure 6.13 Torque angle curves of the FEA 3 design.....   | 161 |
| Figure 7.1 Conventional surface permanent magnet magnetization arrangement,<br>which is equivalent to a discrete Halbach array with one segment per<br>pole. ....  | 180 |
| Figure 7.2 Discrete Halbach array with two segments per pole.....  | 180 |
| Figure 7.3 Discrete Halbach array with four segments per pole.....   | 180 |
| Figure 7.4 Magnetically active cross-sections of radial flux coaxial magnetic gears<br>with (a) permanent magnets mounted on back irons and (b) Halbach arrays<br>mounted on air cores.....  | 182 |
| Figure 7.5 Variation of the maximum achievable GTD with the numbers of segments<br>per pole on Rotor 1 and Rotor 3 for designs with $G_{Int} = 4$ and 50 mm stack<br>lengths, based on 3D FEA, depicted as a (a) contour plot and (b) line plot. ...   | 185 |
| Figure 7.6 Variation of the maximum achievable GTD with the numbers of segments<br>per pole on Rotor 1 and Rotor 3 for designs with $G_{Int} = 9$ and 50 mm stack<br>lengths, based on 3D FEA, depicted as a (a) contour plot and (b) line plot. ...   | 186 |
| Figure 7.7 Variation of the maximum achievable GTD with the numbers of segments<br>per pole on Rotor 1 and Rotor 3 for designs with $G_{Int} = 16$ and 50 mm stack<br>lengths, based on 3D FEA, depicted as a (a) contour plot and (b) line plot. ...  | 187 |
| Figure 7.8 Variation of the maximum achievable GTD with (a) the number of<br>segments per pole on Rotor 1 with and without Rotor 1 back irons and (b)<br>the number of segments per pole on Rotor 3 with and without Rotor 3 back<br>irons for designs with $G_{Int} = 4$ and 50 mm stack lengths, based on 3D<br>FEA.....   | 189 |
| Figure 7.9 Variation of the maximum achievable GTD with (a) the number of<br>segments per pole on Rotor 1 with and without Rotor 1 back irons and (b)<br>the number of segments per pole on Rotor 3 with and without Rotor 3 back<br>irons for designs with $G_{Int} = 9$ and 50 mm stack lengths, based on 3D<br>FEA.....   | 190 |
| Figure 7.10 Variation of the maximum achievable GTD with (a) the number of<br>segments per pole on Rotor 1 with and without Rotor 1 back irons and (b)<br>the number of segments per pole on Rotor 3 with and without Rotor 3 back<br>irons for designs with $G_{Int} = 16$ and 50 mm stack lengths, based on 3D<br>FEA..... | 191 |

|  |     |
|--|-----|
| Figure 7.11 Pareto optimal front indicating the tradeoff between maximizing GTD and maximizing PM GTD with and without Halbach arrays on Rotor 1 and with and without Rotor 1 back irons for designs with $G_{Int} = 4$ , based on 3D FEA.....                     | 192 |
| Figure 7.12 Pareto optimal front indicating the tradeoff between maximizing GTD and maximizing PM GTD with and without Halbach arrays on Rotor 3 and with and without Rotor 3 back irons for designs with $G_{Int} = 4$ , based on 3D FEA.....                     | 193 |
| Figure 7.13 Pareto optimal front indicating the tradeoff between maximizing GTD and maximizing PM GTD with and without Halbach arrays on Rotor 1 and with and without Rotor 1 back irons for designs with $G_{Int} = 9$ , based on 3D FEA.....                     | 194 |
| Figure 7.14 Pareto optimal front indicating the tradeoff between maximizing GTD and maximizing PM GTD with and without Halbach arrays on Rotor 3 and with and without Rotor 3 back irons for designs with $G_{Int} = 9$ , based on 3D FEA.....                     | 195 |
| Figure 7.15 Pareto optimal front indicating the tradeoff between maximizing GTD and maximizing PM GTD with and without Halbach arrays on Rotor 1 and with and without Rotor 1 back irons for designs with $G_{Int} = 16$ , based on 3D FEA.....                    | 196 |
| Figure 7.16 Pareto optimal front indicating the tradeoff between maximizing GTD and maximizing PM GTD with and without Halbach arrays on Rotor 3 and with and without Rotor 3 back irons for designs with $G_{Int} = 16$ , based on 3D FEA.....                    | 197 |
| Figure 7.17 Variation of the maximum achievable GTD with the number of segments per pole on Rotor 1 and the Rotor 1 PM thickness for designs (a) with Rotor 1 back irons and (b) without Rotor 1 back irons for designs with $G_{Int} = 4$ , based on 2D FEA.....  | 199 |
| Figure 7.18 Variation of the maximum achievable GTD with the number of segments per pole on Rotor 1 and the Rotor 1 PM thickness for designs (a) with Rotor 1 back irons and (b) without Rotor 1 back irons for designs with $G_{Int} = 9$ , based on 2D FEA.....  | 200 |
| Figure 7.19 Variation of the maximum achievable GTD with the number of segments per pole on Rotor 1 and the Rotor 1 PM thickness for designs (a) with Rotor 1 back irons and (b) without Rotor 1 back irons for designs with $G_{Int} = 16$ , based on 2D FEA..... | 201 |

|   |     |
|---|-----|
| Figure 7.20 Impact of stack length on the maximum achievable GTD for designs with and without Halbach arrays on Rotor 1 and with and without Rotor 1 back irons for designs with $G_{Int} = 4$ , based on 2D and 3D FEA. ....   | 202 |
| Figure 7.21 Impact of stack length on the maximum achievable GTD for designs with and without Halbach arrays on Rotor 1 and with and without Rotor 1 back irons for designs with $G_{Int} = 9$ , based on 2D and 3D FEA. ....   | 203 |
| Figure 7.22 Impact of stack length on the maximum achievable GTD for designs with and without Halbach arrays on Rotor 1 and with and without Rotor 1 back irons for designs with $G_{Int} = 16$ , based on 2D and 3D FEA. ....  | 204 |
| Figure 7.23 Impact of stack length on the maximum achievable GTD for designs with and without Halbach arrays on Rotor 3 and with and without Rotor 3 back irons for designs with $G_{Int} = 4$ , based on 2D and 3D FEA. ....   | 205 |
| Figure 7.24 Impact of stack length on the maximum achievable GTD for designs with and without Halbach arrays on Rotor 3 and with and without Rotor 3 back irons for designs with $G_{Int} = 9$ , based on 2D and 3D FEA. ....   | 206 |
| Figure 7.25 Impact of stack length on the maximum achievable GTD for designs with and without Halbach arrays on Rotor 3 and with and without Rotor 3 back irons for designs with $G_{Int} = 16$ , based on 2D and 3D FEA. ....  | 207 |
| Figure 8.1 Cross-section of the magnetically active portions of the prototype.....  | 210 |
| Figure 8.2 Impact of the modulator holes radii (varied together) on (a) Rotor 2 slip torque, based on 3D FEA simulations, and (b) electromagnetic efficiency at rated speed and maximum torque, based on 2D FEA simulations. ....   | 213 |
| Figure 8.3 Impact of the bridge position (BP) and thickness on (a) Rotor 2 slip torque, based on 3D FEA simulations, and (b) electromagnetic efficiency at rated speed and maximum torque and (c) impact of bridge thickness with BP = 0 on the loss distribution at rated speed, as in (b), both based on 2D FEA simulations. .... | 214 |
| Figure 8.4 Impact of the effective air gap thicknesses on (a) Rotor 2 slip torque, based on 3D FEA simulations, (b) electromagnetic efficiency at rated speed and maximum torque, based on 2D FEA simulations, and (c) Rotor 1 peak-to-peak torque ripple as a percentage of Rotor 1 slip torque, based on 2D FEA simulations. .... | 216 |
| Figure 8.5 Impact of the effective air gap thicknesses on loss distribution at rated speed and maximum torque as the inner air gap is varied with the outer air gap fixed at 1 mm, based on 2D FEA simulations. ....  | 217 |

|  |     |
|--|-----|
| Figure 8.6 Impact of the thickness of the nonmagnetic walls between adjacent Rotor 3 PMs on the Rotor 2 slip torque, based on 3D FEA simulations. ....                                 | 218 |
| Figure 8.7 Impact of the thickness of the nonmagnetic walls between adjacent Rotor 1 PMs on the Rotor 2 slip torque, based on 2D FEA simulations. ....                                 | 219 |
| Figure 8.8 Impact of the difference between the PM axial lengths and the modulators axial length with the modulator’s stack length fixed at 37.8 mm, based on 3D FEA simulations. .... | 220 |
| Figure 8.9 Flux density at different radial distances (a) beyond the 5 mm back iron or Rotor 3 plastic core and (b) inside the 5 mm back iron or Rotor 1 plastic core. ....            | 221 |
| Figure 8.10 Rotor 1 PMs placed in the original Rotor 1 plastic core, which was attached to the high speed shaft. ....  | 226 |
| Figure 8.11 Rotor 1 PMs placed in the revised Rotor 1 plastic core with the revised Rotor 1 end cap attached. ....   | 226 |
| Figure 8.12 Modulator stack with all of the spacers and rods inserted and with one of the end caps attached with a penny shown to provide a reference for size. ...                    | 227 |
| Figure 8.13 Rotor 2 placed around Rotor 1 with a penny provided for a size reference. ....   | 228 |
| Figure 8.14 Rotor 3 plastic core with a bearing inserted with a penny provided for a size reference. ....  | 229 |
| Figure 8.15 Rotor 3 PM with a penny provided for a size reference. ....  | 229 |
| Figure 8.16 The Rotor 3 plastic core with its PMs and bearings being slid along the low speed shaft into position. ....  | 230 |
| Figure 8.17 Prototype with all three rotors assembled. ....  | 231 |
| Figure 8.18 Fully assembled prototype with end supports. ....  | 232 |
| Figure 8.19 Measured speeds on both rotors compared with the ideal gear ratio. ....  | 234 |
| Figure 8.20 (a) Simulated electromagnetic losses for the prototype and (b) measured no load losses in the prototype. ....  | 235 |
| Figure 8.21 Projected prototype efficiency. ....   | 235 |

## LIST OF TABLES

|  | Page |
|--|------|
| Table 2.1 Magnetic Gear Active Material Properties. ....   | 22   |
| Table 2.2 Magnetic Gear Design Parameter Ranges.....   | 24   |
| Table 2.3 Optimal Design Parameters.....   | 30   |
| Table 2.4 Optimal Design Performances. ....  | 30   |
| Table 3.1 Comparison of Ideal Geometrical Scaling Trends for Radial Flux and Axial<br>Flux Magnetic Gears..... | 52   |
| Table 3.2 Common Cross-Sectional Parameter Sweep Values.....   | 54   |
| Table 3.3 Topology Specific Parameter Sweep Values. ....   | 54   |
| Table 3.4 Rotor 1 Pole Pair Count Sweep Values.....  | 55   |
| Table 4.1 Coaxial and Cycloidal Gear Parameter Sweep Values. ....  | 94   |
| Table 4.2 Inner Pole Pair Count ( $P_1$ ) Values with $T_{AG} = 1$ mm.....                                     | 95   |
| Table 4.3 Inner Pole Pair Count ( $P_1$ ) Values with $T_{AG} = R_{Out}/50$ . ....                             | 95   |
| Table 5.1 Magnetic Gear Single-State Design Parameter Ranges. ....   | 122  |
| Table 5.2 Magnetic Gear Single-Stage Design Discrete Parameter Values.....                                     | 122  |
| Table 5.3 CDCMG Design Examples. ....  | 139  |
| Table 6.1 Analysis Methods Oscillation Comparison with $k_J = 0.25$ and $B_T = 0$ . ....                       | 162  |
| Table 6.2 Analysis Methods Frequency and Velocity Comparison with $k_J = 0.25$ and<br>$B_T = 0$ .....          | 163  |
| Table 6.3 Analysis Methods Oscillation Comparison with $k_J = 1$ and $B_T = 0$ . ....                          | 164  |
| Table 6.4 Analysis Methods Frequency and Velocity Comparison with $k_J = 1$ and $B_T$<br>$= 0$ . ....          | 165  |
| Table 6.5 Analysis Methods Oscillation Comparison with $k_J = 4$ and $B_T = 0$ . ....                          | 166  |



|  |     |
|--|-----|
| Table 6.6 Analysis Methods Frequency and Velocity Comparison with $k_J = 4$ and $B_T = 0$ .          | 167 |
| Table 6.7 Analysis Methods Oscillation Comparison with $k_J = 0.25$ and $B_T = 0.1$ pu.              | 170 |
| Table 6.8 Analysis Methods Frequency and Velocity Comparison with $k_J = 0.25$ and $B_T = 0.1$ pu.   | 171 |
| Table 6.9 Analysis Methods Oscillation Comparison with $k_J = 1$ and $B_T = 0.1$ pu.                 | 172 |
| Table 6.10 Analysis Methods Frequency and Velocity Comparison with $k_J = 1$ and $B_T = 0.1$ pu.     | 173 |
| Table 6.11 Analysis Methods Oscillation Comparison with $k_J = 4$ and $B_T = 0.1$ pu.                | 174 |
| Table 6.12 Analysis Methods Frequency and Velocity Comparison with $k_J = 4$ and $B_T = 0.1$ pu.     | 175 |
| Table 7.1 Parameter Sweep Values.  | 183 |
| Table 7.2 Rotor 1 Pole Pair Counts for Each Outer Radius and Nearest Integer Gear Ratio Combination. | 184 |
| Table 8.1 Prototype Design Parameter Values.   | 211 |
| Table 8.2 Additive Manufacturing Material Properties Comparison.                                     | 222 |
| Table 8.3 Prototype Mass Breakdown.  | 232 |
| Table 8.4 Mechanical Gear Comparison.  | 236 |

## 1. INTRODUCTION

### 1.1. The Motivation for Magnetic Gears

The size, weight, and cost of an electric machine, whether a motor or a generator, are often more strongly correlated to its rated torque than to its rated power. Thus, a high-speed, low-torque machine will generally be smaller, lighter, and less expensive than a low-speed, high-torque machine with the same power rating. However, the electric machine must often interact with a physical system operating at a certain speed. For example, in a wind turbine, the power that is fed into the generator comes from the wind turning the blades at a relatively low speed, often in the range of 10 to 20 rpm. There are two conventional approaches to connecting an electric machine to a physical system. First, a direct drive electric machine can operate at the same speed as the physical system. Second, a mechanical gearbox can be used to couple the physical system to the electric machine, which allows the electric machine to operate at a higher speed and lower torque than the physical system.

Because the mechanically geared approach uses a higher speed machine, it often yields a smaller, lighter, and less expensive drivetrain than the direct drive approach. However, the use of a mechanical gearbox introduces additional issues. Mechanical gears require regular maintenance, especially lubrication. Additionally, mechanical gears experience wear during operation, especially if contaminants, such as sand or dirt, get into the gear. On the other hand, lubricant may leak from the gear, which can be an

issue in clean environments, such as food processing. Furthermore, mechanical gears produce acoustic noise. These issues result from the mechanical contact between interlocking teeth, which is used to transform mechanical power between high-speed, low-torque rotation and low-speed, high-torque rotation.

One solution that has been proposed for mitigating or eliminating these issues with mechanical gears is to use magnetic gears, which transform power using magnetic fields instead of mechanical contact. This also provides some additional benefits over mechanical gears. Magnetic gears have inherent overload protection; if too much torque is applied to one of the shafts, the magnets can slip past each other without causing any permanent damage. Also, mechanical power can be transferred through a physical barrier; this potentially allows mechanical power to be provided to a sealed environment.

Therefore, magnetic gears have been proposed for use in many applications. Wind turbine blades spin at relatively low speeds with very large torques. Thus, direct drive generators for wind turbines are quite large, heavy, and expensive. However, mechanical gearboxes are a significant source of downtime and maintenance and operations expenses in wind turbines [1]. Due to magnetic gears' potential benefits regarding reliability and maintenance, they have been proposed as a hybrid solution for wind turbines, which offers some of the size, weight, and cost advantages of mechanically geared systems without the problems associated with using physical contact to transform mechanical power [2], [3]. Wave energy converters face similar challenges to wind turbines regarding the size of direct drive solutions. However, maintenance and replacement costs can be even higher for wave energy converters due

to their location. Additionally, wave energy converters must be able to withstand the extreme conditions presented by storms. Thus, magnetically geared solutions have been proposed for wave energy converters for the same reasons as for wind turbines and because the inherent overload protection of magnetic gears can help withstand storms [4], [5]. Magnetic gears have also been proposed for ship propulsion, as a hybrid solution combining some of the benefits of direct drive systems, reduced maintenance and improved reliability, with benefits associated with mechanically geared systems, reduced size, cost, and weight [6], [7], [8]. Similarly, magnetic gears have been proposed for electric vehicle [9], downhole [10], and aerospace [11] applications. Each of these different applications places different priorities on reducing size, reducing weight, reducing cost, increasing efficiency, and minimizing torque ripple.

## **1.2. Early Magnetic Gears**

Due to the benefits of noncontact power transfer, magnetic gears began to receive attention in the early 1900's in the form of several patents. These patents proposed various magnetic gear topologies, two of which are illustrated in Figure 1.1 [12], [13]. However, a few challenges prevented these early magnetic gears from achieving widespread commercial success. First, many of these early topologies, including the ones shown in Figure 1.1, were created by simply replacing the teeth in mechanical gears with permanent magnets (PMs), electromagnets, or reluctance poles. This resulted in poor magnet utilization, because only a small percentage of the magnetic fields were contributing to producing torque at any given instant. Second, the PM materials available at that time were relatively weak. While electromagnets could be used, they

were limited by copper losses and thermal constraints. Third, these early innovators lacked the computational power to optimize their designs to achieve the best performance possible.

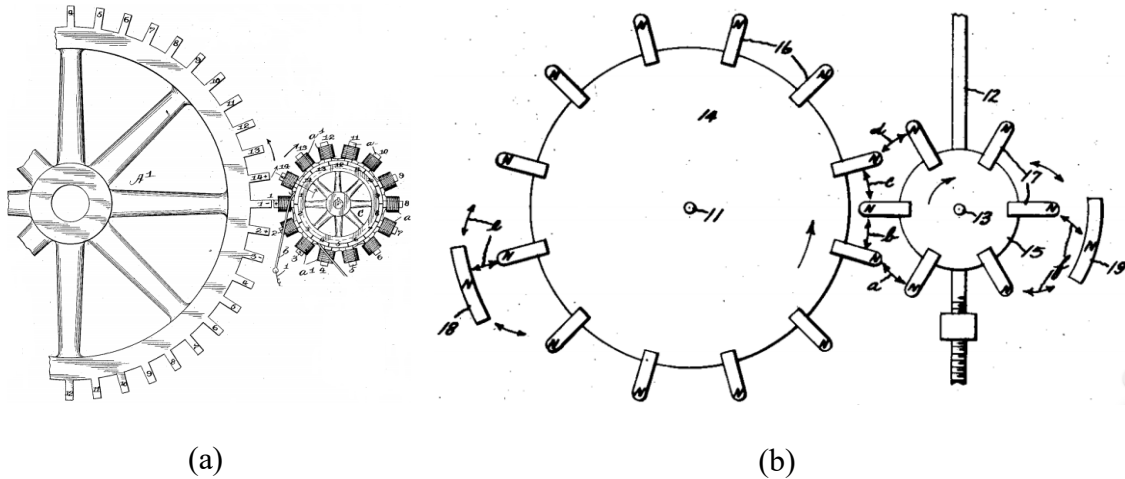


**Figure 1.1 Early magnetic gear patent drawings by (a) Armstrong in 1901 and (b) Faus in 1941. Reprinted from [12] and [13].**

Each of these issues was addressed over the course of the 20th century. First, new topologies were proposed, which could achieve better magnet utilization. As early as 1916, Neuland patented a topology where the flux from electromagnets was modulated by steel poles to produce different harmonics in concentric air gaps [14], as shown in Figure 1.2. This flux modulation principle enables more of the magnetic field to contribute to producing torque at any given instant. More patents were filed on similar flux modulating topologies over the course of the 20th century as the concept of flux modulation continued to be refined [15], [16]. Second, the development of rare earth magnets, such as SmCo and NdFeB magnets, significantly improved the strength

of magnetic fields that could be generated using PMs. This resulted in the potential for a significant reduction in magnetic gear size and weight. Third, the development of computers and finite element analysis (FEA) significantly improved designers' ability to improve and optimize designs. FEA was especially important for flux modulated designs, which contain numerous spatial flux harmonics and significant leakage flux. This makes evaluation with traditional analytical models less accurate.

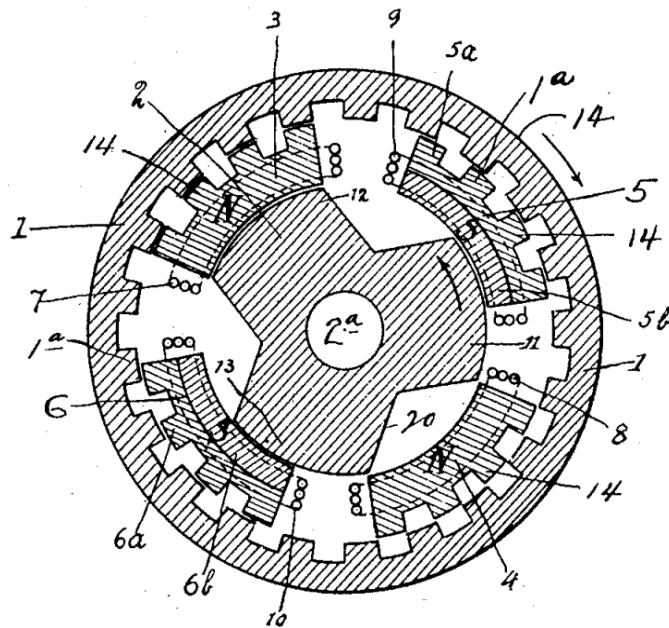


**Figure 1.2 Early flux modulated magnetic gear proposed by Neuland in 1916. Reprinted from [14].**

### 1.3. Modern Magnetic Gears

In 2001, Atallah published an influential paper using FEA to show that a radial flux coaxial magnetic gear, such as the one illustrated in Figure 1.3, could achieve volumetric torque densities (VTDs) in excess of  $100 \text{ kN}\cdot\text{m}/\text{m}^3$  using rare earth magnets

[17]. VTD is defined as the low speed rotor slip torque divided by the active volume, as shown in (1), where the active volume is the volume of the magnetically active materials (not including the space occupied by the structural materials). The axial flux coaxial magnetic gear, which is illustrated in Figure 1.4, has also been proposed [18]. Both of these coaxial topologies are based on the flux modulation principles that had been proposed and refined in the 20th century.

$$\text{Volumetric Torque Density} = \frac{\text{Low Speed Rotor Slip Torque}}{\text{Active Volume}} \quad (1)$$

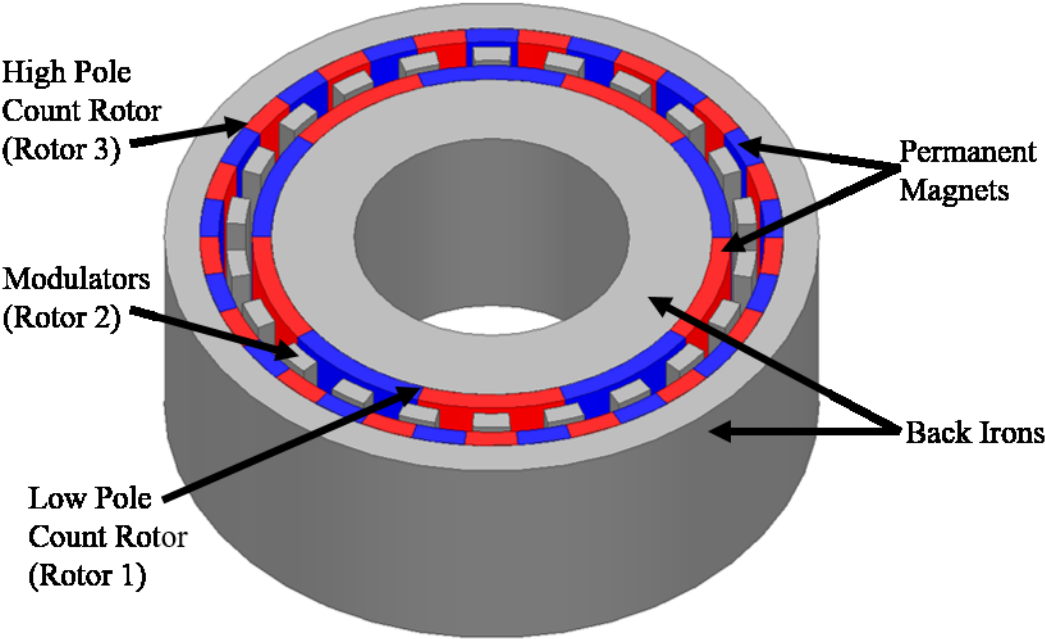
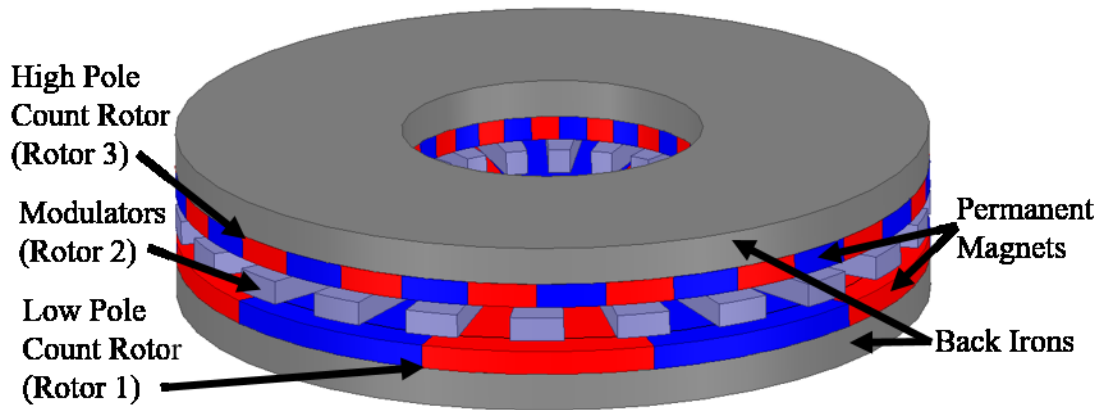


Figure 1.3 Radial flux coaxial magnetic gear.



**Figure 1.4 Axial flux coaxial magnetic gear.**

Both coaxial magnetic gear topologies have two rotors with PMs and a set of ferromagnetic modulators in between the two PM rotors. The ferromagnetic modulators create a varying air gap permeance, which modulates the spatial flux harmonics produced by the PMs on Rotor 1 and Rotor 3. If the number of modulators,  $Q_2$ , is related to the number of pole pairs on the two PM rotors,  $P_1$  and  $P_3$ , according to (2), where  $k$ ,  $m$ , and  $n$  are integers, the two PM rotors will produce some of the same spatial flux harmonics and can create a non-zero average torque, as described in [17]. However, the best performance is generally achieved if the number of modulators is the sum of the number of pole pairs on the two rotors, as in (3) [17]. If (3) holds, then the steady-state speeds of the three rotors,  $\omega_1$ ,  $\omega_2$ , and  $\omega_3$ , respectively, will be related by (4). While (4) indicates that a continuously variable transmission can be achieved if one of the rotors is used as a control rotor, often one rotor, either Rotor 2 or Rotor 3, is held stationary to create a fixed gear ratio between the other two rotors, as shown in (5) and (6). A comparison of (5) and (6) shows that, if Rotor 3 is fixed, the gear ratio will be larger in



magnitude by 1 than with Rotor 2 fixed. This increase in gear ratio will be accompanied by a proportional increase in the low speed rotor slip torque.

$$k \cdot Q_2 = m \cdot P_1 \pm n \cdot P_3 \quad (2)$$

$$Q_2 = P_1 + P_3 \quad (3)$$

$$P_1 \cdot \omega_1 - Q_2 \cdot \omega_2 + P_3 \cdot \omega_3 = 0 \quad (4)$$

$$\text{Gear Ratio} \Big|_{\omega_2=0} = \frac{\omega_1}{\omega_3} = \frac{-P_3}{P_1} \quad (5)$$

$$\text{Gear Ratio} \Big|_{\omega_3=0} = \frac{\omega_1}{\omega_2} = \frac{Q_2}{P_1} \quad (6)$$

While coaxial magnetic gears have attracted most of the recent magnetic gear research, several other topologies have been proposed and have demonstrated potential benefits. Cycloidal [19] and harmonic [20] magnetic gears have been proposed for applications requiring high torque densities at high gear ratios. Cross-sections of the radial flux versions of these two topologies are illustrated in Figure 1.5.

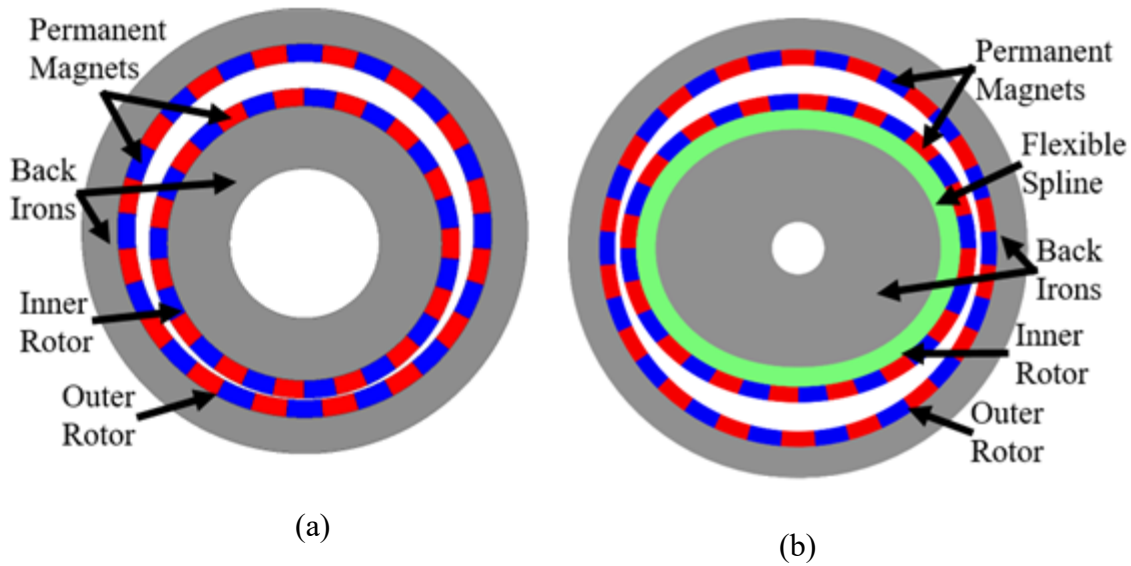


**Figure 1.5 Cross-sections of radial flux (a) cycloidal and (b) harmonic magnetic gears.**

As with the coaxial magnetic gear, in the cycloidal and harmonic magnetic gears, the gearing effect is created by the interaction of PMs with different pole counts across a nonuniform air gap. In the case of the cycloidal magnetic gear, this nonuniform air gap is created by having an offset between the axes of the inner and outer rotors. During operation, the inner rotor's axis orbits around the outer rotor's axis, which rotates the air gap permeance function. Because the fundamental spatial frequency of the air gap permeance function is unity, the number of pole pairs on the outer rotor,  $P_{\text{Out}}$ , should be one more than the number of pole pairs on the inner rotor,  $P_{\text{In}}$ , as given in (7). For example, the cycloidal magnetic gear illustrated in Figure 1.5(a) has 15 pole pairs on the inner rotor and 16 pole pairs on the outer rotor. As shown in [19], if the outer rotor is fixed, this produces the gear ratio in (8), which relates the angular velocity of the inner rotor's rotation about its own axis,  $\omega_{\text{In}}$ , to the angular velocity of the orbital motion of

the inner rotors axis about the axis of the outer rotor,  $\omega_{Orb}$ ; alternatively, if the inner rotor does not rotate about its own axis, the gear ratio in (9) relates  $\omega_{Orb}$  to the angular velocity of the outer rotor's rotation about its own axis,  $\omega_{Out}$ .

$$P_{Out} = P_{In} + 1 \quad (7)$$

$$\text{Gear Ratio} \Big|_{\omega_{Out}=0} = \frac{\omega_{Orb}}{\omega_{In}} = -P_{In} \quad (8)$$

$$\text{Gear Ratio} \Big|_{\omega_{In}=0} = \frac{\omega_{Orb}}{\omega_{Out}} = P_{Out} \quad (9)$$

In the case of the harmonic magnetic gear, the inner rotor is not cylindrical, which produces an air gap permeance function with a fundamental spatial frequency of  $Q_{AG}$ . Therefore, the inner and outer pole pair counts,  $P_{In}$  and  $P_{Out}$ , respectively, are related by (10). For example, the air gap permeance function of the harmonic magnetic gear illustrated in Figure 1.5(b) has a fundamental spatial frequency of two, and the gear has 16 pole pairs on the inner rotor and 18 pole pairs on the outer rotor. As shown in [20], if the outer rotor is fixed, this produces the gear ratio in (11), which relates the angular velocity of the air gap deformation,  $\omega_{AG}$ , to the angular velocity of the magnets on the inner rotor,  $\omega_{In}$ . Alternatively, if the magnets on the inner rotor do not rotate about the inner rotor's axis, the gear ratio is given by (12), which relates  $\omega_{AG}$  to the angular velocity of the outer rotor. Thus, the cycloidal magnetic gear's operating principle is the same as that of a harmonic magnetic gear with  $Q_{AG}$  equal to unity.

$$P_{Out} = P_{In} + Q_{AG} \quad (10)$$

$$\text{Gear Ratio} \Big|_{\omega_{Out}=0} = \frac{\omega_{AG}}{\omega_{In}} = \frac{-P_{In}}{Q_{AG}} \quad (11)$$

$$\text{Gear Ratio} \Big|_{\omega_{\text{in}}=0} = \frac{\omega_{\text{AG}}}{\omega_{\text{Out}}} = \frac{P_{\text{Out}}}{Q_{\text{AG}}} \quad (12)$$

These gear ratios enable the cycloidal and harmonic magnetic gears to achieve high gear ratios without having to use very different PM pole pair counts on the rotors. However, both of these topologies suffer from mechanical challenges, which mitigate some of the benefits from noncontact power transfer. In the case of the cycloidal magnetic gear, the orbital motion of the inner rotor about the axis of the outer rotor must be decoupled from its rotation about its own axis. Additionally, the orbital motion causes the gear's center of mass to move, which can cause significant vibrations if measures are not taken to counteract this effect. For the harmonic magnetic gear, the magnets must be attached to a flexible spline. While prototype results have been published for cycloidal magnetic gears [19], [21], [22], no experimental results have been published for harmonic magnetic gear prototypes.

In addition to rotary magnetic gears, a linear-to-linear version of the coaxial magnetic gear has been proposed [23], and two linear-to-rotary magnetic gear topologies have been proposed [24], [25].

#### **1.4. Magnetically Geared Machines**

Either the radial flux or axial flux coaxial magnetic gear can be integrated directly with an electric machine to form a magnetically geared machine (MGM). This MGM provides a relatively compact device capable of interfacing directly with a high-torque, low-speed physical system. An MGM can function as either a motor or a

generator. There are a few different types of MGMs based on how the machine is integrated with the magnetic gear.

The inner stator radial flux MGM (IS-RFMGM) places an electric machine in the bore of a radial flux coaxial magnetic gear, as illustrated in Figure 1.6. The low speed shaft is connected to either Rotor 2 or Rotor 3, which is geared down to a lower speed than Rotor 1. Rotor 1 also serves as the rotor for the electric machine. The machine and the gear in an IS-RFMGM can be either magnetically coupled or decoupled. If they are magnetically coupled, both the magnetic gear and the electric machine are constrained to use the same pole counts on Rotor 1. However, if they are decoupled, as in Figure 1.6, then Rotor 1 must have an adequately thick back iron to accommodate the fluxes from both the magnetic gear and the electric machine. The IS-RFMGM has been experimentally shown to achieve a VTD of almost  $100 \text{ kN}\cdot\text{m}/\text{m}^3$  [9]. However, the IS-RFMGM has significant mechanical design complexity because three concentric air gaps must be maintained.

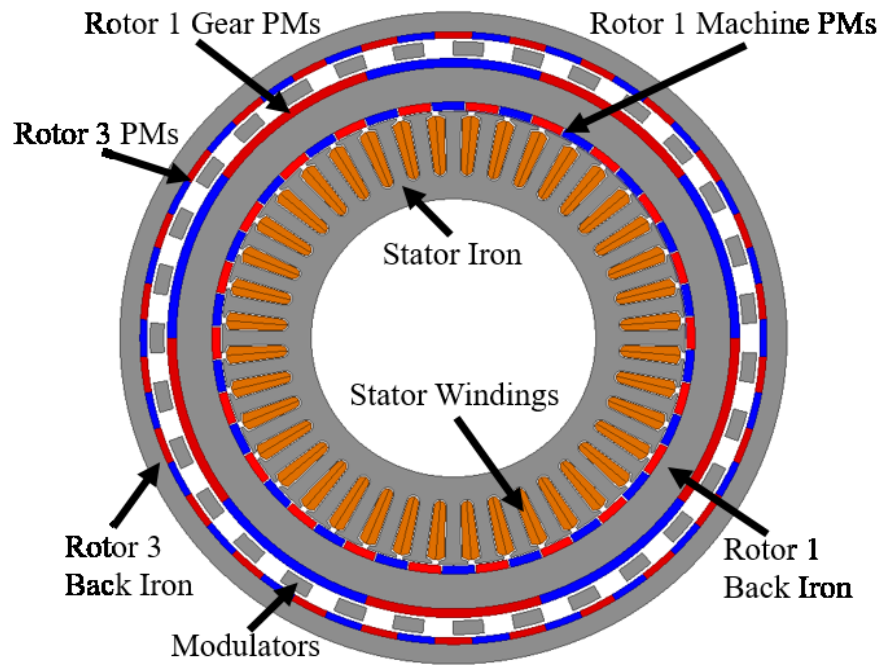


**Figure 1.6** Magnetically decoupled inner stator radial flux magnetically geared machine cross-section.

In the outer stator radial flux MGM (OS-RFMGM), the electric machine’s stator is integrated with a radial flux magnetic gear’s Rotor 3, as illustrated in Figure 1.7. This means that the Rotor 3 PMs are physically mounted on the stator teeth. The low speed shaft is connected to Rotor 2, while the stator windings interact with Rotor 1. The OS-RFMGM results in an inherently magnetically coupled design as both the magnetic gear and the electric machine employ the same Rotor 1 PMs. However, since the stator is placed on the outside, it contributes to the overall size of the MGM, which reduces the torque density. Nonetheless, OS-RFMGMs have been shown to achieve VTDs in excess of  $60 \text{ kN}\cdot\text{m}/\text{m}^3$  [26]. Since the OS-RFMGM only has two concentric air gaps, it is mechanically simpler than the IS-RFMGM.

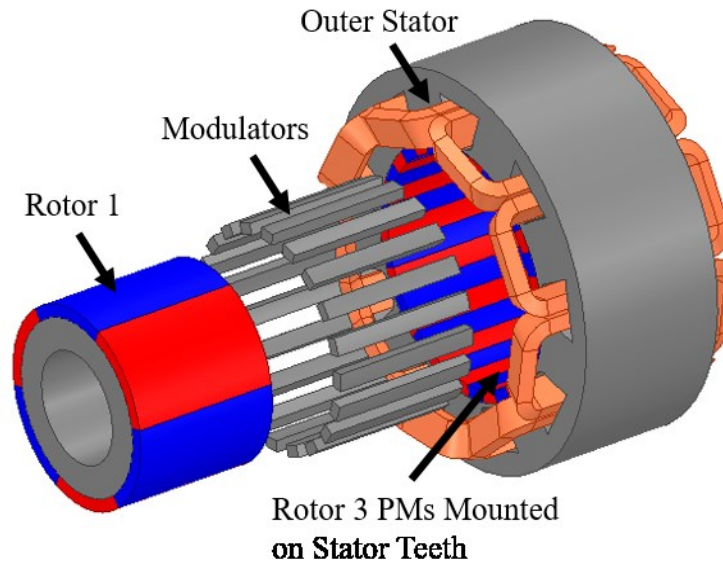


**Figure 1.7 Exploded view of an outer stator radial flux magnetically geared machine.**

A series connected axial flux MGM (SC-AFMGM) can be formed by placing an electric machine directly beyond an axial flux magnetic gear and using it to drive Rotor 1, as illustrated in Figure 1.8. This effectively eliminates the shaft between the MGM and the electric machine and allows them to share the same package; however, the electric machine still contributes to the overall volume of the SC-AFMGM. A SC-AFMGM can be either magnetically coupled or magnetically decoupled, as with the IS-RFMGM. A prototype SC-AFMGM demonstrated a VTD over  $100 \text{ kN}\cdot\text{m}/\text{m}^3$  in the gear portion; however, this VTD was approximately halved when the additional volume of the machine was considered [27]. The SC-AFMGM does present some significant

mechanical design challenges because three air gaps must be maintained despite the presence of strong axial forces on each body.

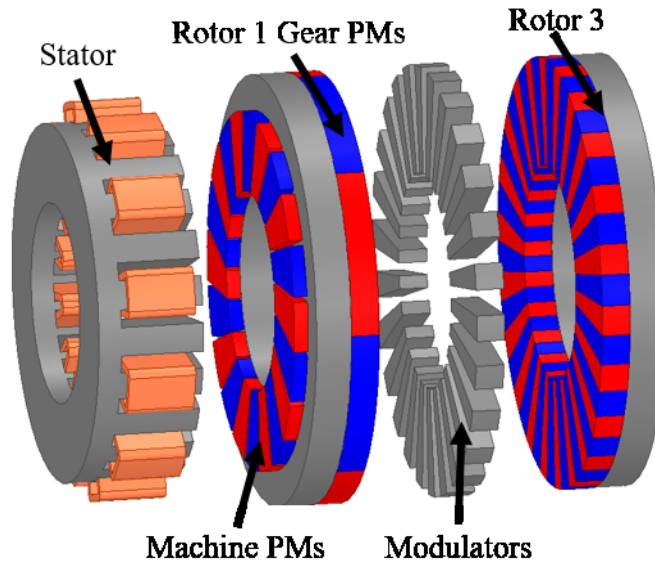


**Figure 1.8 Exploded view of a series connected axial flux magnetically geared machine.**

Alternatively, a compact axial flux MGM (C-AFMGM) can be formed by placing an electric machine in the bore of an axial flux magnetic gear, as illustrated in Figure 1.9. Thus, the electric machine does not add to the overall package volume. Additionally, this can result in a more appropriate sizing ratio between the gear and the machine because the gear's low speed rotor slip torque is several times larger than the rated torque of the machine. A quite conservative prototype C-AFMGM demonstrated a VTD of about  $8 \text{ kN}\cdot\text{m}/\text{m}^3$ , but simulations illustrated that a less conservative design could achieve a VTD of  $60 \text{ kN}\cdot\text{m}/\text{m}^3$  [28].



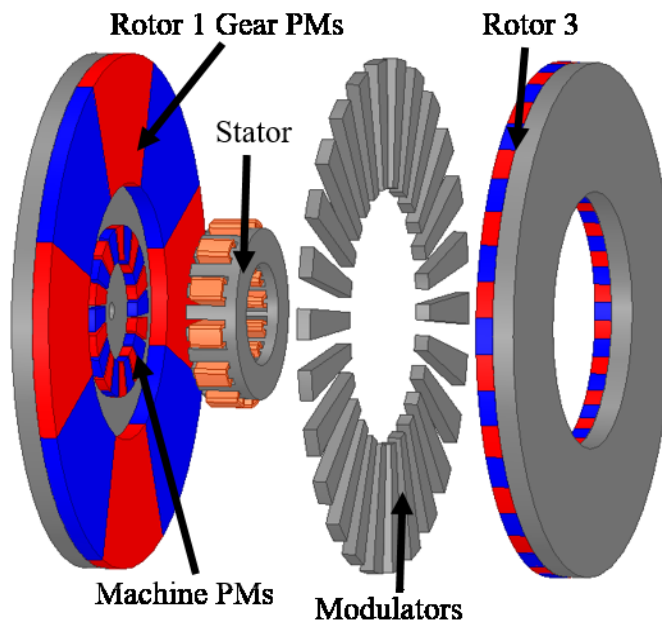


**Figure 1.9 Exploded view of a compact axial flux magnetically geared machine.**

### **1.5. A Comparison of Magnetic Gears and Conventional Alternatives**

Magnetically geared systems must compete against two conventional alternatives. For magnetic gears to gain widespread commercial adoption, they must demonstrate advantages over both mechanical gears and direct-drive solutions. Relative to mechanical gears, magnetic gears have the potential benefits inherent to non-contact power transfer, including reduced acoustic noise, higher reliability, reduced maintenance, and inherent overload protection; however, in many applications, these benefits will be inadequate to replace mechanical gears if magnetic gears are significantly larger than the mechanical gears they are replacing. One paper providing a preliminary comparison between magnetic gears and mechanical gears produced the

graphs in Figure 1.10, Figure 1.11, and Figure 1.12 for mechanical planetary gears with a high safety factor, mechanical planetary gears with a low safety factor, and radial flux coaxial magnetic gears, respectively [29]. These graphs show that magnetic gears may achieve a size competitive with mechanical gears. However, it is important to note that the performances of both mechanical and magnetic gears depend on numerous factors, such as the torque ratings, the safety factor, the gear ratio, the materials employed, and the aggressiveness of the design.

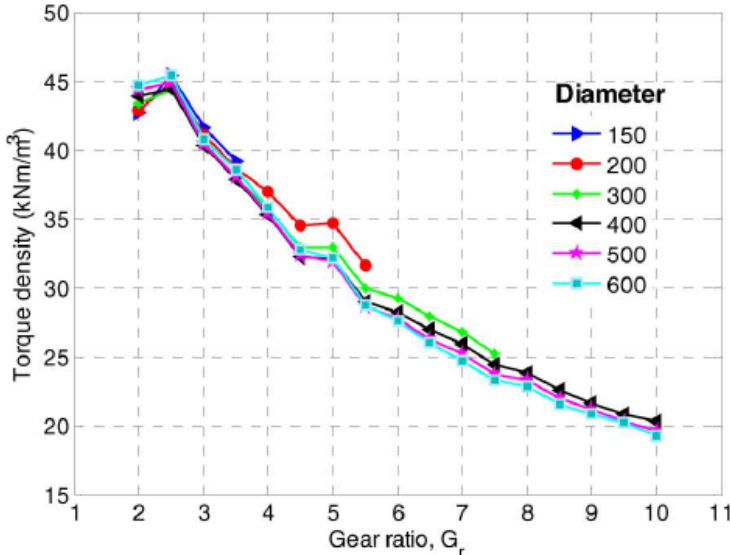


**Figure 1.10 Volumetric torque density trends for high safety factor mechanical planetary gears. Reprinted with permission from [29] © 2011 IEEE.**

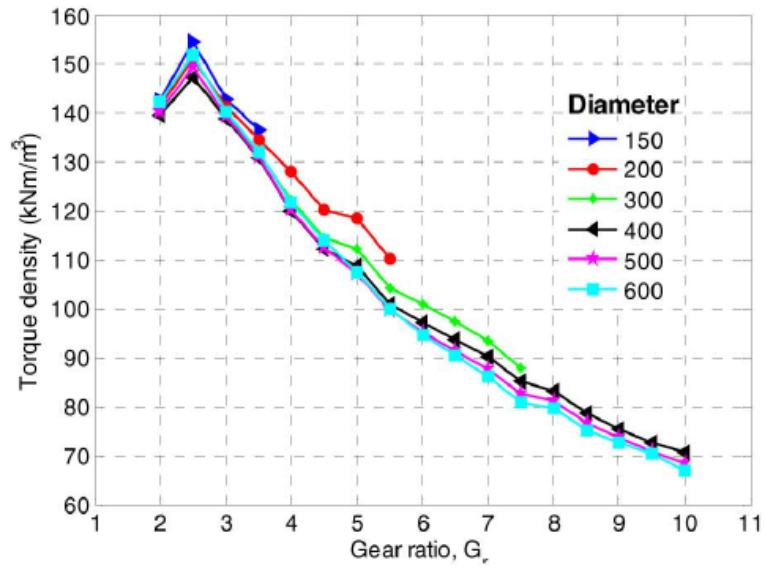


Figure 1.11 Volumetric torque density trends for low safety factor mechanical planetary gears. Reprinted with permission from [29] © 2011 IEEE.

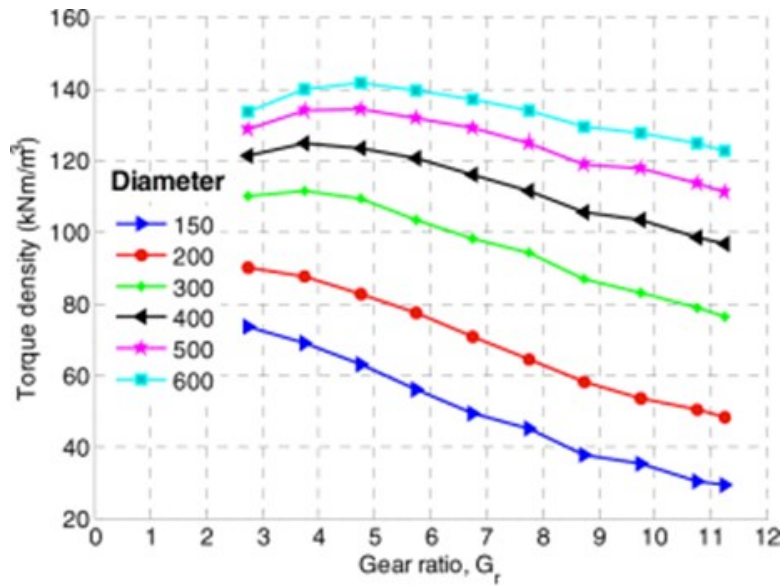


Figure 1.12 Volumetric torque density trends for radial flux coaxial magnetic gears. Reprinted with permission from [29] © 2011 IEEE.

Additionally, magnetic gears must be able to outperform direct-drive machines. The use of a magnetic gear adds more complexity and moving parts to the system relative to a direct-drive solution. Therefore, magnetic gears must significantly reduce the system size in order to be beneficial. Radial flux PM machines often achieve VTDs of 10-20 kN·m/m<sup>3</sup> with natural air cooling, 20-30 kN·m/m<sup>3</sup> with forced air cooling, and 30-60 kN·m/m<sup>3</sup> when liquid cooled [17]. While transverse flux machines can achieve even higher VTDs than radial flux PM machines, they suffer from poor power factors, which results in a large power converter, reducing the overall system benefits. As with gears, the VTDs of electric machines depend on numerous factors, including ratings, topology, cooling, and materials. Nonetheless, Figure 1.12 illustrates that magnetic gears can achieve significantly higher VTDs than those typically achieved by electric machines. Thus, magnetic gears have significant potential to reduce the system size.

## 2. OPTIMIZATION FOR DIFFERENT METRICS\*

While most magnetic gear literature focuses on maximizing magnetic gears' volumetric torque densities (VTDs) to make their sizes competitive with those of mechanical gears [30], [31], improvements in other areas, such as material cost, mass, and efficiency, are also critical for this technology to achieve commercial success. However, the importance of each objective varies significantly between applications, and the optimal design parameters depend on the relative weight of each objective [32]. This section compares the designs of magnetic gears independently optimized to maximize VTD, torque per dollar (TPD), or gravimetric torque density (GTD). This section also illustrates the impacts of different design parameters on the achievable performance of a magnetic gear. Furthermore, it investigates the impact of end-effects on the optimal design parameters and performance metrics. The optimal designs were determined using a genetic algorithm (GA) to independently optimize VTD, TPD, or GTD based on 2D and 3D FEA simulations. Furthermore, a multi-objective GA optimization was used to find the Pareto optimal front for the three metrics. The results of all simulations performed in this analysis are examined to discern the performance tradeoffs, the design trends, the interactions between the optimal values of different parameters, and the impacts of end-effects. This work also introduces a metric to account for an axial buffer for the leakage flux, leakage adjusted VTD (LA VTD).

---

© 2018 IEEE. Part of this section is reprinted with permission from M. C. Gardner, B. E. Jack, M. Johnson, and H. A. Toliyat, "Comparison of Coaxial Radial Flux Magnetic Gears Independently Optimized for Volume, Cost, and Mass," *IEEE Trans. Ind. Appl.*, vol. 54, no. 3, pp. 2237-2245, May-Jun. 2018.

## 2.1. Design Study Methodology

This section focuses on the coaxial radial flux magnetic gear topology with surface mounted permanent magnets, which is shown in Figure 1.3. In this section, Rotor 1 serves as the high speed rotor (HSR), Rotor 2 is the low speed rotor (LSR), and Rotor 3 is fixed, yielding the gear ratio in (6). While fixing Rotor 2 and using Rotor 3 as the LSR would reduce the magnitude of the gear ratio and reduce the slip torque of the LSR proportionally to the reduction in gear ratio magnitude, this would not have a significant impact on the optimization trends.

A GA was used to independently optimize three different coaxial radial flux magnetic gear designs, one for each of the three aforementioned metrics, VTD, TPD, and GTD. Although each of the different designs was optimized to separately maximize its corresponding performance metric, every gear analyzed in the section is rated for a consistent LSR slip torque of 500 N·m with a nearest integer gear ratio of 5 and uses the same two active materials specified in Table 2.1. The magnets are made of NdFeB N42, and the back irons and modulators are made from M47 steel. Furthermore, the analysis was first conducted using 2D finite element analysis simulations, and then it was repeated to find the designs optimizing each of the three metrics based on 3D FEA simulations in order to characterize the impact of end effects. Also, a fourth metric, leakage adjusted VTD (LA VTD) was considered and independently optimized based on 3D simulations. Additionally, a multi-objective GA was used to characterize the Pareto optimal fronts for VTD, TPD, and GTD based on both 2D FEA results and 3D FEA results.

**Table 2.1 Magnetic Gear Active Material Properties.**

| <b>Material</b>      | <b>Density</b>         | <b>B<sub>r</sub></b> | <b>Cost Rate</b> |
|----------------------|------------------------|----------------------|------------------|
| NdFeB N42            | 7400 kg/m <sup>3</sup> | 1.3 T                | \$50/kg          |
| M47 Steel (26 Gauge) | 7870 kg/m <sup>3</sup> | N/A                  | \$3/kg           |

For these gears, VTD is defined as the LSR slip torque divided by the volume of the smallest cylinder that encloses all of the active material, as shown in (13). GTD is defined as the LSR slip torque divided by the total mass of the PMs and steel, as shown in (14). TPD is defined as the LSR slip torque divided by the active material cost of the design, assuming the cost of each material is proportional to the mass of that material used in the design, as shown in (15). While the TPD value is heavily dependent on the assumed cost rates listed in Table 2.1, the optimal design parameters and trends are relatively independent of these settings, as long as the magnet cost rate is significantly greater than that of the steel, which comprises the back irons and modulators [32]. To calculate LA VTD, the cylinder is extended axially to the distance at which the rms magnetic flux density axially beyond the modulators is 50 mT. This is the same as adding a buffer to the stack length in (13) to accommodate this flux density on both ends of the gear. It is critical to consider the extent of the axial leakage flux because this flux can cause eddy current losses in nearby structural material, as has been the case with previous magnetic gear prototypes [33], [34]. While these losses depend on numerous factors, such as the magnetic gear pole counts, rotational speeds, and conductivity of the structural material, this analysis uses the 50 mT limit as a simple way to quantify the extent of this leakage flux. The axial leakage flux is evaluated on a circular path axially

beyond the modulators, which is where it is generally the strongest [35]. These calculations neglect all structural materials and only consider the permanent magnets, modulators, and back irons. Also, they ignore any manufacturing or material cost penalties associated with the quantities or dimensions of individual pieces.

$$VTD = \frac{\text{Low Speed Rotor Slip Torque}}{\pi \cdot (\text{Outer Radius})^2 \cdot (\text{Stack Length})} \quad (13)$$

$$GTD = \frac{\text{Low Speed Rotor Slip Torque}}{(\text{PM Mass}) + (\text{Back Irons Mass}) + (\text{Modulators Mass})} \quad (14)$$

$$TPD = \frac{\text{Low Speed Rotor Slip Torque}}{(\text{PM Mass}) \cdot (\text{PM Cost Rate}) + (\text{Steel Mass}) \cdot (\text{Steel Cost Rate})} \quad (15)$$

GAa are frequently employed for the design and optimization of electric machines [36], [37], [38], and this section employs the GOSET GA described in [39] to optimize the gear designs. GAs use the survival of the fittest concept to optimize design functions. The algorithm produces a generation of design cases, retains the “fittest” (highest performing) cases, produces a new generation similar to the previous generation’s best cases, and then repeats the process. Each case consists of a set of specific gene values representing the parameter values of the design. Each case’s VTD, TPD, GTD, or LA VTD determines its fitness, depending on the optimization objective. Aside from selecting values similar to the previous generation’s most fit individuals (cases), the GOSET algorithm incorporates more advanced optimization techniques to introduce diversity into the population, thus ensuring that no single solution dominates the final solution too early in the optimization process. For example, it evaluates the proximity of each design case to similar cases and penalizes less diverse cases.



Table 2.2 provides the range of values considered for each design parameter. Each case is evaluated by magnetostatic 2D FEA to determine the stack length necessary to achieve the 500 N·m LSR slip torque. For the optimizations based on 3D simulations, a magnetostatic 3D FEA simulation is performed at the stack length predicted by the 2D simulation of the same cross-sectional design and, based on the result, the stack length is linearly rescaled to achieve the 500 N·m slip torque. However, one exception to this procedure is that designs requiring stack lengths greater than 150 mm are assumed to be suboptimal and to experience only a minimal impact on torque from end-effects; therefore, these designs were not simulated using 3D FEA models. For each case, the values of the cross-sectional design parameters summarized in Table 2.2 and the required stack length, in conjunction with the material properties in Table 2.1, determine the associated VTD, TPD, and GTD.

**Table 2.2 Magnetic Gear Design Parameter Ranges.**

| <b>Name</b>     | <b>Description</b>                              | <b>Range</b> | <b>Units</b> |
|-----------------|---|--------------|--------------|
| $G_{Int}$       | Integer portion of the gear ratio               | 5            |              |
| $P_1$           | Rotor 1 pole pair count                         | 3 – 30       |              |
| $R_{Out}$       | Outer back iron outer radius                    | 75 – 150     | mm           |
| $T_{B11}$       | Rotor 1 back iron thickness                     | 5 – 25       | mm           |
| $T_{PM1}$       | Rotor 1 permanent magnet thickness              | 2.5 – 12.5   | mm           |
| $T_{AG}$        | Air gap thicknesses                             | 1            | mm           |
| $T_{Mods}$      | Modulator thickness                             | 5 – 20       | mm           |
| $k_{PM}$        | Magnet thickness ratio                          | 0.5 – 1      |              |
| $T_{B13}$       | Rotor 3 back iron thickness                     | 5 – 25       | mm           |
| $\alpha_{PM1}$  | Rotor 1 permanent magnet tangential fill factor | 0.01 – 1     |              |
| $\alpha_{Mods}$ | Modulators tangential fill factor               | 0.01 – 0.99  |              |
| $\alpha_{PM3}$  | Rotor 3 permanent magnet tangential fill factor | 0.01 – 1     |              |

Due to strong interdependencies between the effects of different dimensions, the values of certain variables are coupled through derived parameters, which are included in Table 2.2. First,  $G_{Int}$ , which represents the integer portion of the gear ratio, was used with  $P_1$  to determine the number of pole pairs on Rotor 3 ( $P_3$ ), as shown in (16). This equation ensures that the number of modulators is even, which causes a symmetrical cancellation of the net forces on each rotor. Additionally, this approach maintains a relatively high least common multiple (LCM) between  $P_1$  and  $P_3$ , which reduces the gear's torque ripple [3]. Second,  $k_{PM}$  controls the relationship between the radial thicknesses of the outer magnets ( $T_{PM3}$ ) and the inner magnets ( $T_{PM1}$ ) according to (17). This is advantageous because there is significantly greater flux leakage between adjacent poles on Rotor 3 than there is on Rotor 1, due to the higher number of poles on Rotor 3. Therefore, it is generally most effective to concentrate more of the permanent magnet material on Rotor 1, especially with high gear ratios. However, if  $k_{PM}$  is too low, the Rotor 1 magnets may demagnetize the Rotor 3 magnets. The use of both  $G_{Int}$  and  $k_{PM}$  was derived from [32].

$$P_3 = \begin{cases} (G_{Int}-1) \cdot P_1 + 1 & \text{for } G_{Int} \cdot P_1 \text{ odd} \\ (G_{Int}-1) \cdot P_1 + 2 & \text{for } G_{Int} \cdot P_1 \text{ even} \end{cases} \quad (16)$$

$$T_{PM3} = T_{PM1} \cdot k_{PM} \quad (17)$$

## 2.2. Results

During the course of the analysis, over 61,000 unique 2D simulations and 24,000 unique 3D simulations were run. Figure 2.1 and Figure 2.2 show the performances achieved by all of the evaluated designs based on 2D and 3D simulations, respectively, while Figure 2.3 illustrates the leakage adjusted VTD results for the same 3D

simulations. Figure 2.4 illustrates the Pareto optimal fronts for maximizing all three metrics for each of the data sets shown in Figure 2.1, Figure 2.2, and Figure 2.3.

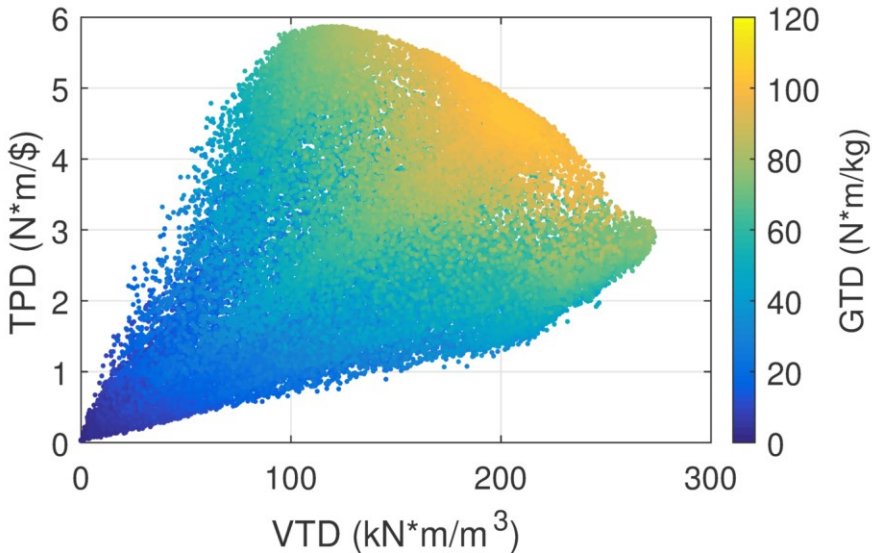


**Figure 2.1 Performances of designs based on 2D FEA simulations.**

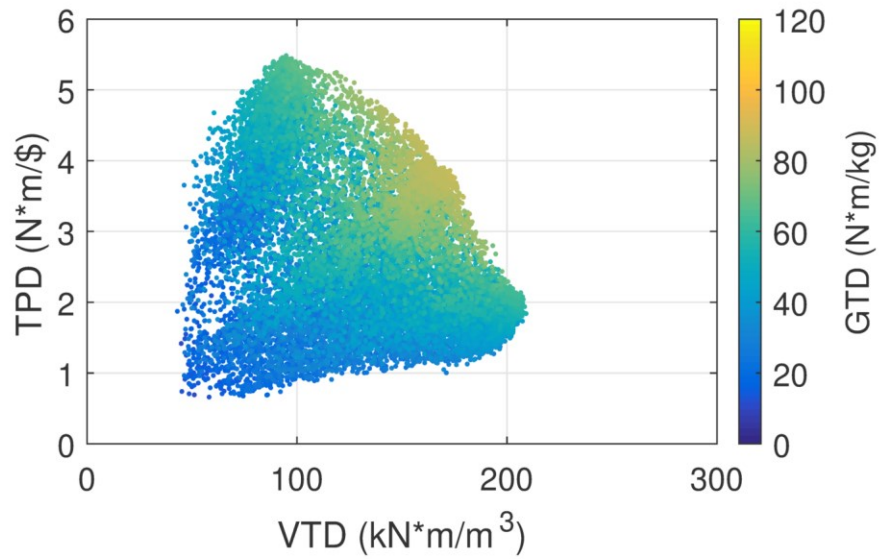


**Figure 2.2 Performances of designs based on 3D FEA simulations.**

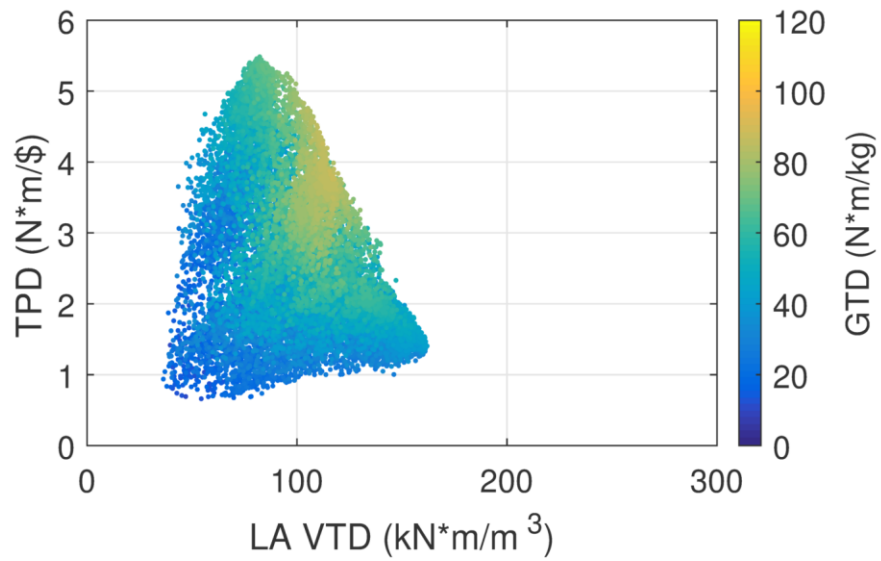


**Figure 2.3 Performances of designs based on 3D FEA simulations with an axial buffer.**

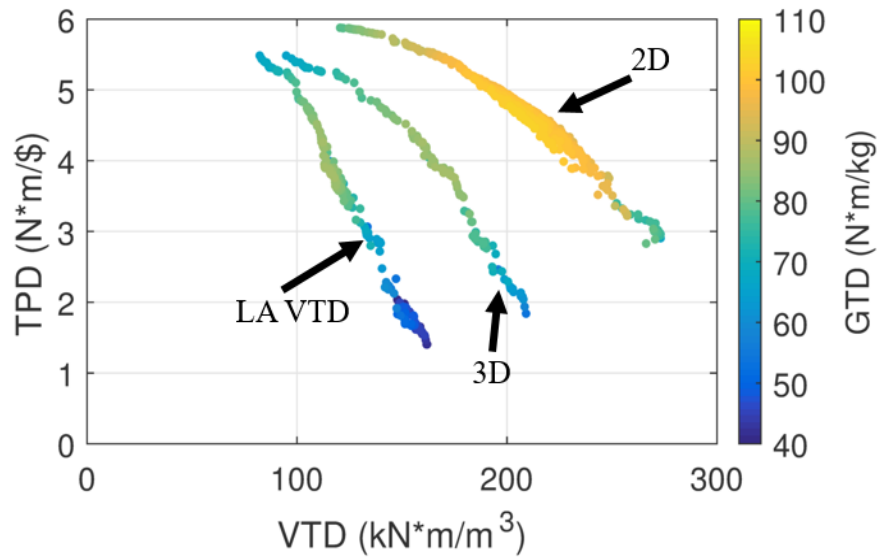


**Figure 2.4 The Pareto optimal fronts maximizing VTD (or LA VTD), TPD, and GTD.**

These figures show a significant tradeoff between VTD and TPD. In the evaluated design space, the highest VTD designs cost approximately twice as much as the highest TPD designs, while the highest TPD designs require about twice as much volume as the highest VTD designs. If the cost and weight of structural materials were considered, it would likely reduce the magnitude of this tradeoff because the larger size of the highest TPD designs would result in larger structural material costs than those of the highest VTD designs. The maximum GTD designs represent a compromise, as they achieve higher VTD values than the maximum TPD designs and higher TPD values than the maximum VTD designs. Additionally, these figures show that the end-effects quantified by the 3D simulations have the most significant impact on the maximum VTD designs and much less impact on the maximum TPD designs. Similarly, the axial buffer

for leakage flux has a greater impact on the volumes required by the maximum VTD designs than on those required by the maximum TPD designs. Both of these phenomena are strongly related to the stack lengths of the designs, as designs with larger stack lengths often experience less significant end-effects [32], [35]. Thus, the extent to which end-effects will impact the results is determined by the range of the design space relative to the target slip torque. For example, if the design space includes relatively larger outer radii, those designs will generally require shorter stack lengths to achieve the target torque and suffer a more significant reduction in torque from end-effects. Also, for a given parametric design space, lowering the target slip torque will reduce the required stack lengths, which will make the impact of end-effects more significant.

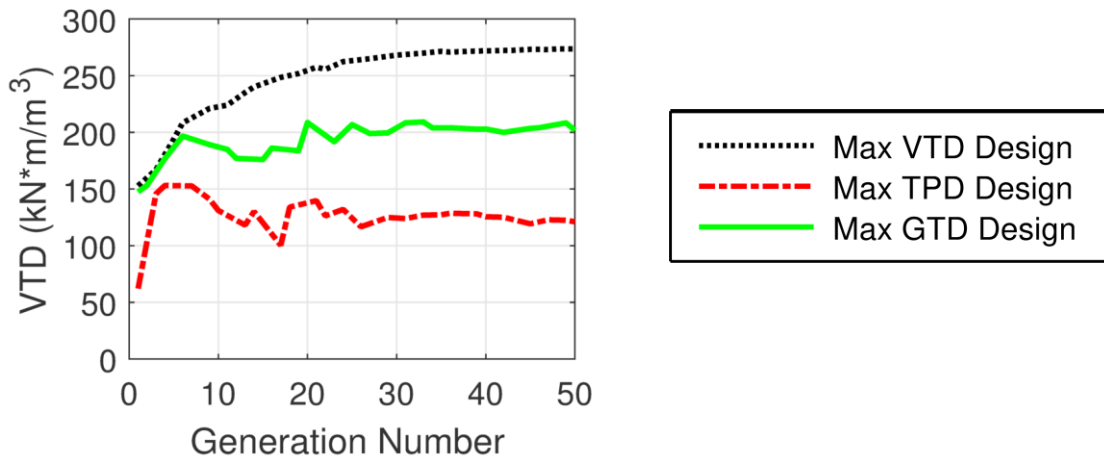
Table 2.3 and Table 2.4 summarize the design parameters and performances of the seven different optimal designs generated by the GA to independently maximize VTD or LA VTD, TPD, and GTD, based on either 2D or 3D simulations. Figure 2.5, Figure 2.6, and Figure 2.7 illustrate the diverging evolutions of the VTDs, TPDs, and GTDs achieved by the three different optimum designs, throughout the 2D simulation GA generations. These results neglect the additional size, mass, and cost of structural material. The maximum TPD designs would likely require the most structural material due to their large stack lengths and diameters. However, due to the maximum VTD designs' small volumes, any structural material would likely reduce the maximum VTDs significantly, especially when including a buffer for the axial leakage flux.

**Table 2.3 Optimal Design Parameters.**

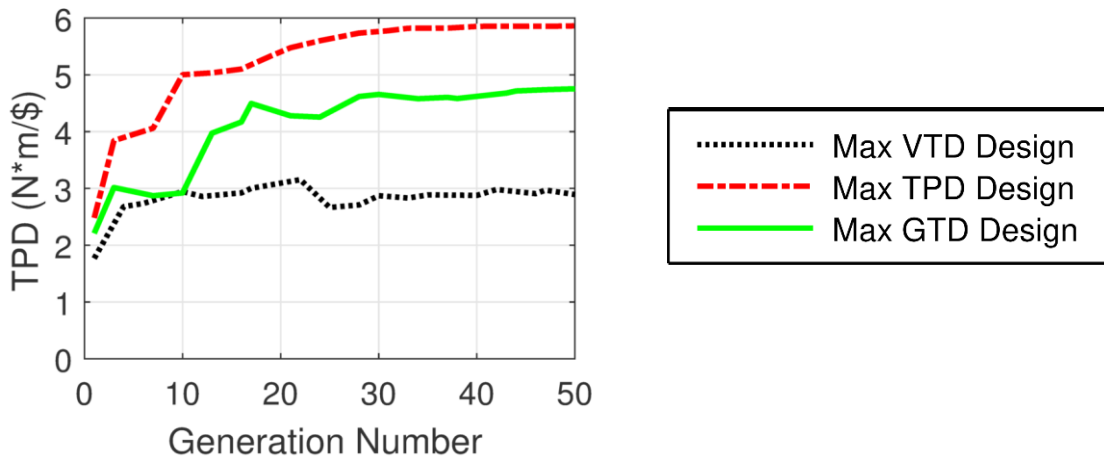
| Parameter         | Maximum VTD |      |       | Maximum TPD |      | Maximum GTD |      |
|-------------------|-------------|------|-------|-------------|------|-------------|------|
|                   | 2D          | 3D   | LA    | 2D          | 3D   | 2D          | 3D   |
| $G_{Int}$         | 5           | 5    | 5     | 5           | 5    | 5           | 5    |
| $P_1$             | 9           | 7    | 5     | 17          | 20   | 13          | 15   |
| $R_{Out}$ (mm)    | 150         | 106  | 75    | 150         | 150  | 150         | 150  |
| $T_{BI1}$ (mm)    | 20.9        | 6.0  | 5.0   | 5.0         | 5.0  | 5.0         | 5.0  |
| $T_{PM1}$ (mm)    | 12.5        | 12.5 | 12.0  | 3.1         | 2.5  | 7.2         | 6.9  |
| $T_{AG}$ (mm)     | 1           | 1    | 1     | 1           | 1    | 1           | 1    |
| $T_{Mods}$ (mm)   | 5.6         | 5.3  | 5.0   | 5.0         | 5.1  | 5.0         | 5.0  |
| $k_{PM}$          | 0.65        | 0.57 | 0.51  | 0.55        | 0.53 | 0.57        | 0.51 |
| $T_{BI3}$ (mm)    | 5.0         | 5.0  | 5.0   | 5.0         | 5.0  | 5.0         | 5.0  |
| $\alpha_{PM1}$    | 0.99        | 0.99 | 0.98  | 0.75        | 0.75 | 0.80        | 0.88 |
| $\alpha_{Mods}$   | 0.55        | 0.53 | 0.55  | 0.47        | 0.41 | 0.49        | 0.41 |
| $\alpha_{PM3}$    | 0.98        | 0.97 | 0.99  | 0.84        | 0.85 | 0.90        | 1.0  |
| Stack Length (mm) | 25.9        | 67.6 | 146.9 | 58.5        | 74.2 | 33.9        | 40.6 |
| Axial Buffer (mm) | N/A         | 14.4 | 13.6  | N/A         | 5.7  | N/A         | 9.7  |

**Table 2.4 Optimal Design Performances.**

| Parameter                   | Maximum VTD |      |      | Maximum TPD |      | Maximum GTD |      |
|-----------------------------|-------------|------|------|-------------|------|-------------|------|
|                             | 2D          | 3D   | LA   | 2D          | 3D   | 2D          | 3D   |
| VTD ( $kN \cdot m/m^3$ )    | 274         | 210  | 193  | 121         | 95   | 209         | 174  |
| LA VTD ( $kN \cdot m/m^3$ ) | N/A         | 147  | 162  | N/A         | 83   | N/A         | 118  |
| TPD ( $N \cdot m/\$$ )      | 2.89        | 1.83 | 1.39 | 5.86        | 5.47 | 4.57        | 3.76 |
| GTD ( $N \cdot m/kg$ )      | 66.5        | 54.2 | 40.8 | 78.3        | 65.5 | 102.8       | 86.8 |

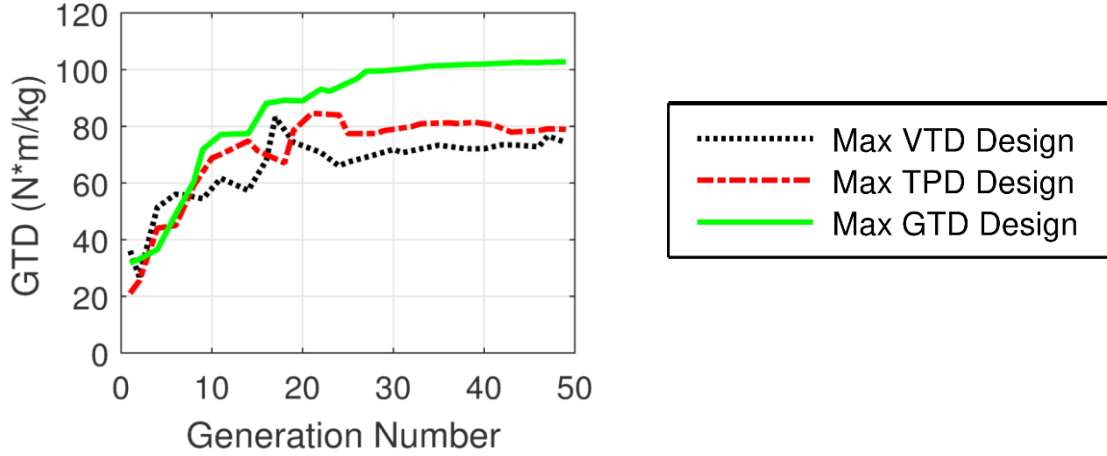


**Figure 2.5 GA driven evolution of the VTD of the three optimal designs based on 2D simulations.**



**Figure 2.6 GA driven evolution of the TPD of the three optimal designs based on 2D simulations.**

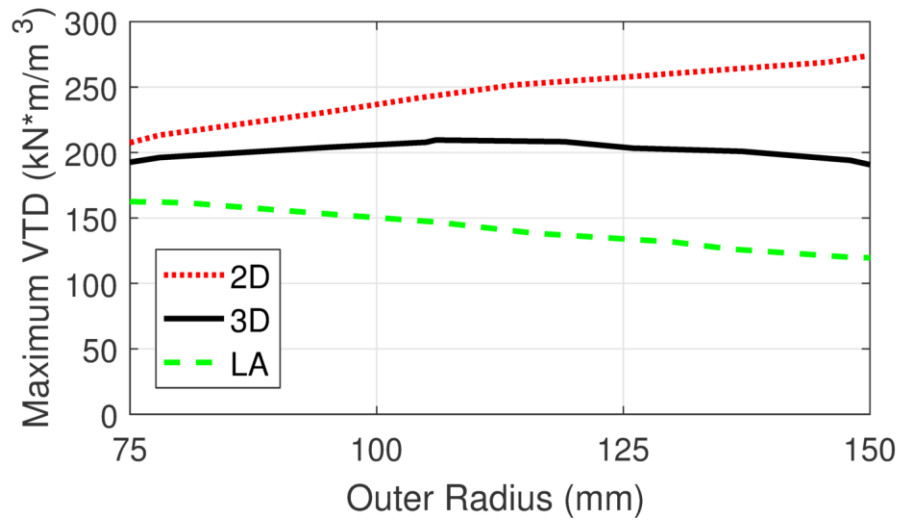




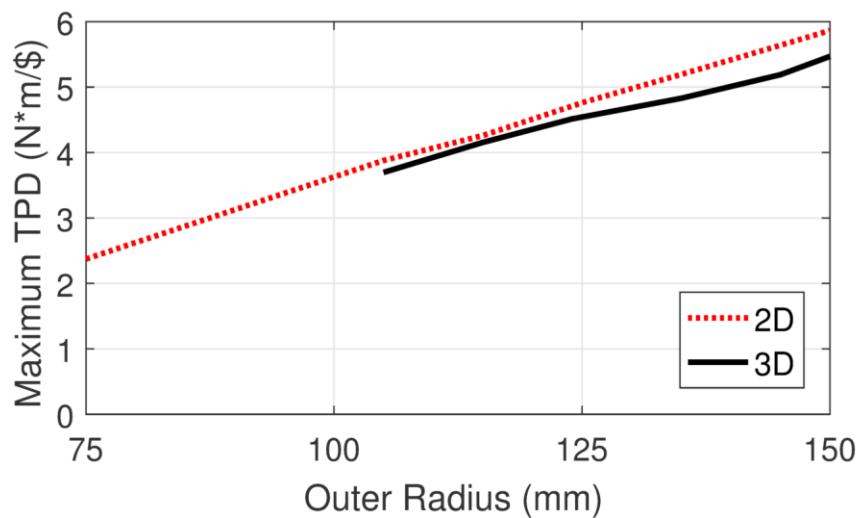
**Figure 2.7 GA driven evolution of the GTD of the three optimal designs based on 2D simulations.**

Figure 2.8, Figure 2.9, and Figure 2.10 show the variations in the optimal design performances as the outer radius varies. Based on 2D FEA, increasing the outer radius improves all three metrics, but the percentage improvement of the VTD is less than that of the TPD and GTD. Increasing the outer radius linearly raises the air gap area and the torque arm, which quadratically improves a design's 2D slip torque. However, it also quadratically increases the cross-sectional area, so the VTD increases sub-linearly with outer radius [28]. Alternatively, the magnet and steel cross-sectional areas only increase linearly with the radius, so the TPD and GTD increase linearly with the outer radius. End-effects further complicate these trends because increasing the radius decreases the stack length (for a fixed torque), which increases the impact of axial leakage flux and reduces the advantages gained by increasing the radius. This decreases the optimal outer radius for VTD and LA VTD, but not for TPD and GTD (within the ranges considered in this section). Additionally, for a given outer radius, the maximum TPD and GTD

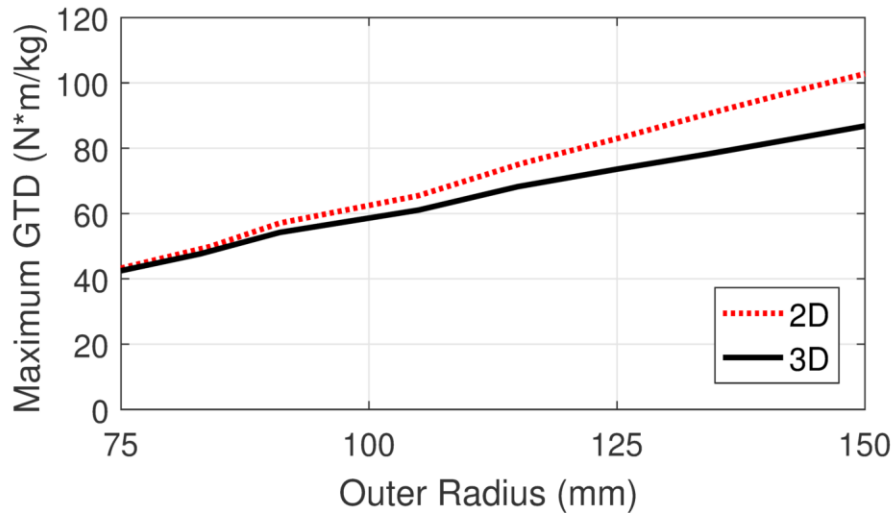
designs have longer stack lengths than the maximum VTD design, so they suffer less from end-effects at that radius. This also resulted in the optimal TPD designs for small outer radii not being simulated in 3D, due to the 150 mm stack length constraint.



**Figure 2.8** Variation of maximum VTD and LA VTD with outer radius.



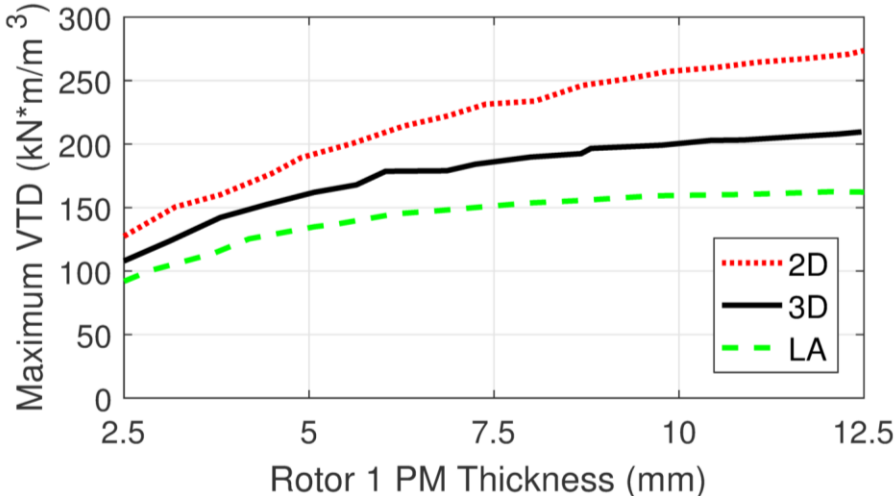
**Figure 2.9** Variation of maximum TPD with outer radius.



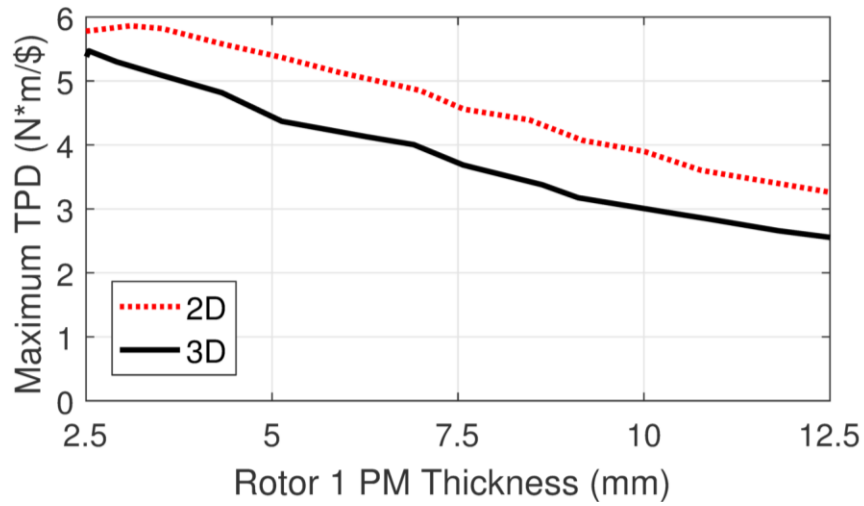
**Figure 2.10 Variation of maximum GTD with outer radius.**

Figure 2.11, Figure 2.12, and Figure 2.13 show the envelopes illustrating the optimal performances achieved as the Rotor 1 PM thickness varies. Magnet volume is a major aspect of the tradeoff between VTD and TPD, and magnet thickness is one of the dominant factors in determining the magnet volume. Accordingly, these figures illustrate significantly different trends for optimizing VTD, TPD, and GTD. Because increasing the magnet thickness increases the effective air gap, the torque returns diminish as magnet thickness continues to increase. Therefore, while high VTD designs generally have very thick magnets, high TPD designs often have much thinner magnets to use the expensive magnet material more cost-effectively. Optimal GTD designs usually have intermediate magnet thicknesses. At some optimal thickness, the additional torque produced by increasing the magnet thickness does not outweigh the added mass of the magnets. Additionally, Figure 2.11, Figure 2.12, and Figure 2.13 indicate that

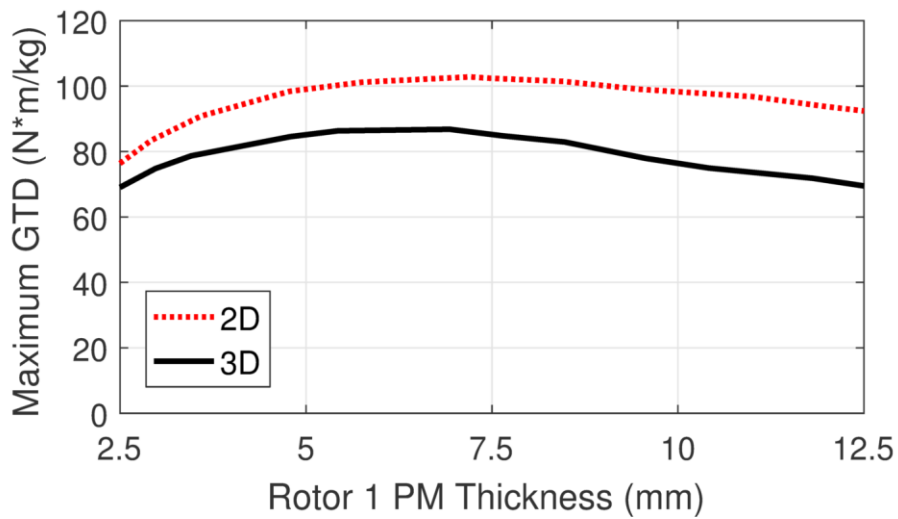
increasing the magnet thickness tends to increase the impact of end-effects. This occurs because increasing the magnet thickness generally reduces the stack length required to achieve the target torque. Thus, when end-effects are considered, the torque returns gained by increasing the magnet thickness diminish even faster.



**Figure 2.11 Variation of maximum VTD and LA VTD with Rotor 1 PM thickness.**



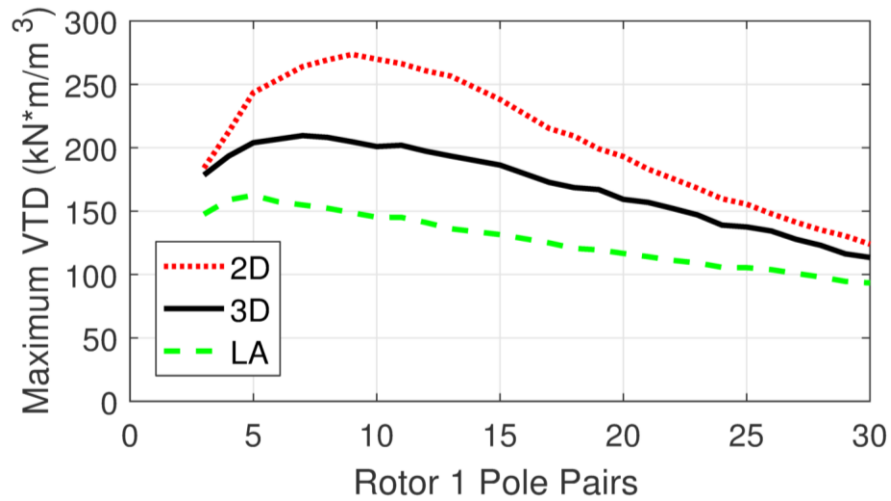
**Figure 2.12 Variation of maximum TPD with Rotor 1 PM thickness.**



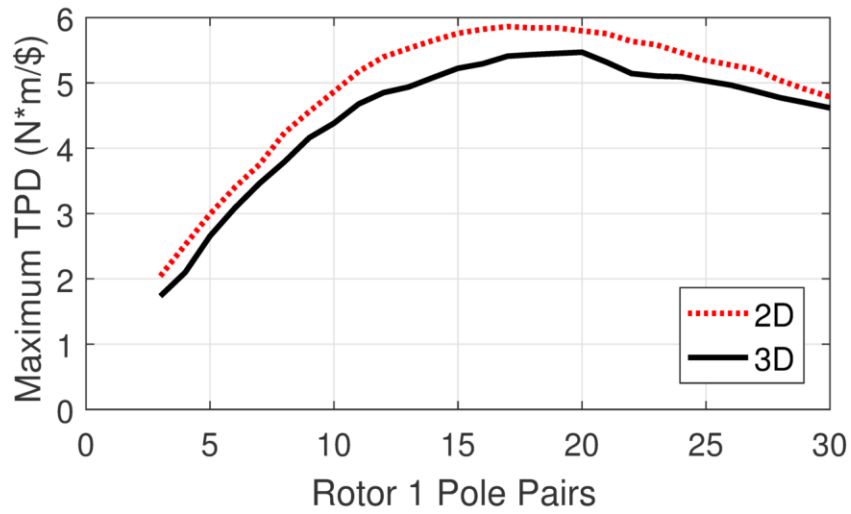
**Figure 2.13 Variation of maximum GTD with Rotor 1 PM thickness.**

Figure 2.14, Figure 2.15, and Figure 2.16 show the envelopes illustrating the optimal performances achieved as the Rotor 1 pole pair count varies. There are a few different factors that affect the optimal pole count. First, the magnet thicknesses impact

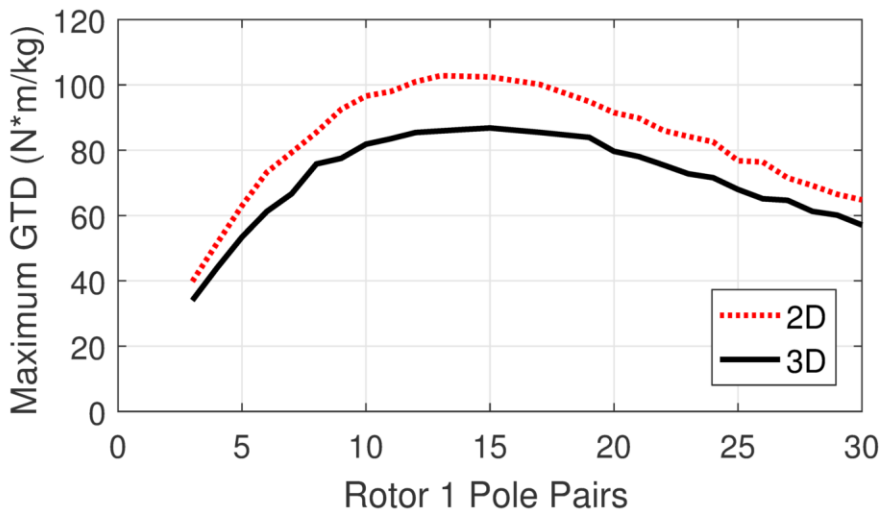
the effective air gap, which significantly influences the optimal pole arc. Larger effective air gaps result in increased leakage flux between adjacent poles, which tends to favor larger optimal pole arcs. Larger pole arcs are achieved by reducing the pole pair count. Thus, the thicker magnets in the optimal VTD designs usually favor lower pole pair counts than the thinner magnets in the optimal TPD designs. Because the magnets in the optimal GTD designs have intermediate thicknesses, the optimal GTD designs have optimal pole pair counts between those of the optimal VTD and optimal TPD designs. Conversely, selecting a fixed pole pair count affects the performance trends as magnet thickness is varied. The pole arcs are also affected by the air gap radii, which are determined by the different radial thickness parameters and the outer radius. Therefore, because the outer radii of the optimal 3D VTD design and the optimal LA VTD design are lower than that of the optimal 2D VTD design, the optimal 3D VTD and LA VTD designs favor lower pole pair counts.



**Figure 2.14 Variation of maximum VTD and LA VTD with Rotor 1 pole pair count.**



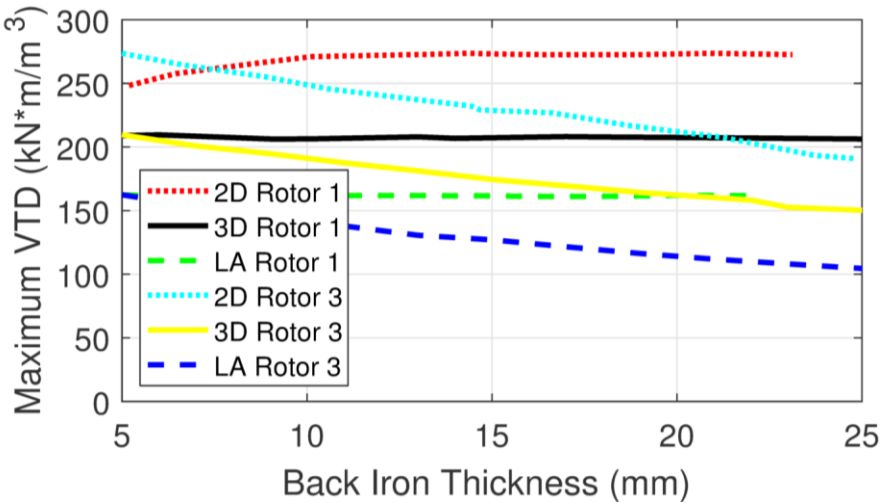
**Figure 2.15** Variation of maximum TPD with Rotor 1 pole pair count.



**Figure 2.16** Variation of maximum GTD with Rotor 1 pole pair count.

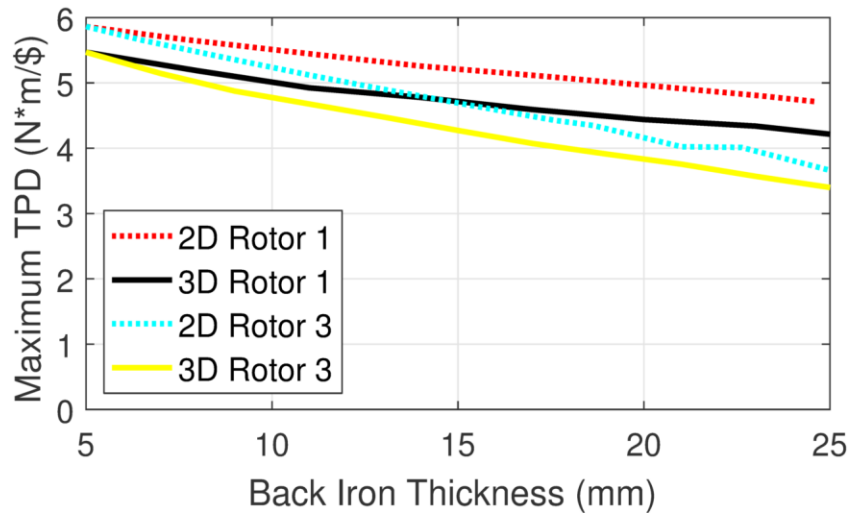
Figure 2.17, Figure 2.18, and Figure 2.19 show the envelopes of the optimal performances achieved as the back iron thicknesses vary. Increasing the thickness of the Rotor 3 back iron significantly decreases the torque because it reduces the air gap radii,

which are where the torque is produced. Thus, all three metrics favor designs with very thin Rotor 3 back irons. While saturation of the Rotor 3 back iron can reduce the torque, the impact of iron saturation is relatively small compared to the large linear reluctances of the two air gaps and two sets of permanent magnets. Generally, mechanical considerations, rather than excessive iron saturation, will determine the minimum Rotor 3 back iron thickness. On the other hand, the thickness of the Rotor 1 back iron has a very small impact on torque because it does not affect the air gap radii (based on the independent design parameters used in this section). However, the Rotor 1 back iron thickness impacts the material cost and mass of the gear, so the optimal TPD and GTD designs favor very thin Rotor 1 back irons. Another major consideration for sizing the back irons is magnetic flux containment. If the back irons are too thin, magnetic flux will leak beyond them, which could cause eddy current losses in structural material or create a hazard. However, this analysis neglects the issue of flux containment.

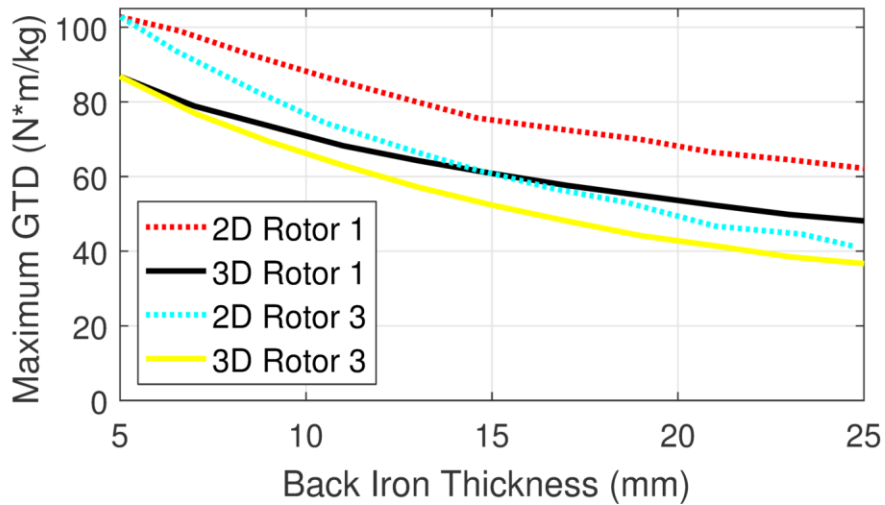


**Figure 2.17 Variation of maximum VTD and LA VTD with back iron thicknesses.**





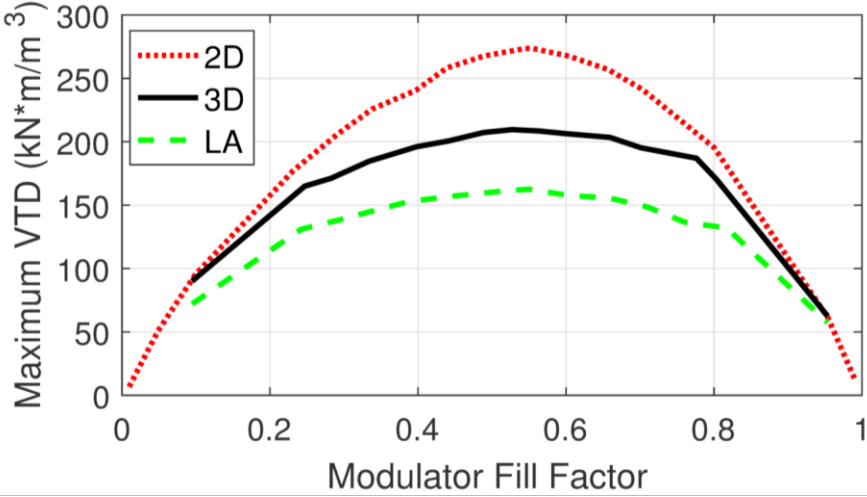
**Figure 2.18 Variation of maximum TPD with back iron thicknesses.**



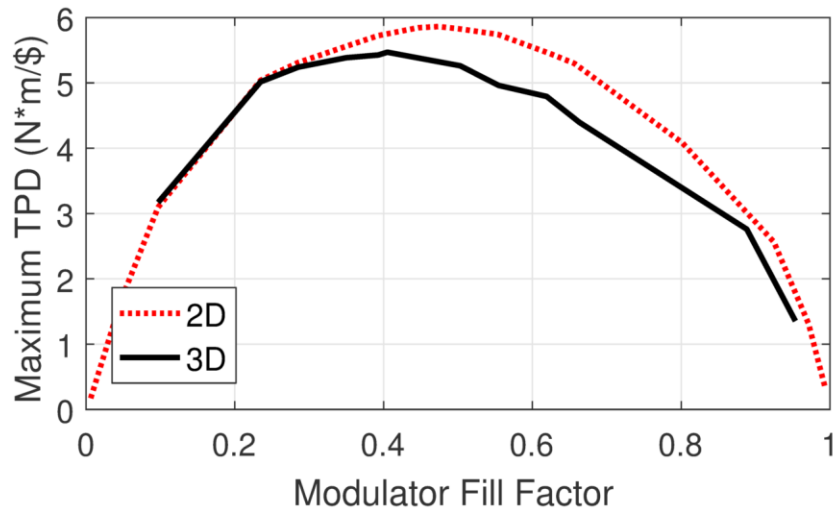
**Figure 2.19 Variation of maximum GTD with back iron thicknesses.**

Figure 2.20, Figure 2.21, and Figure 2.22 show the envelopes of the optimal performances as the modulator fill factor varies. While a modulator fill factor slightly greater than 0.5 can provide the most torque for the optimal VTD designs, increasing the

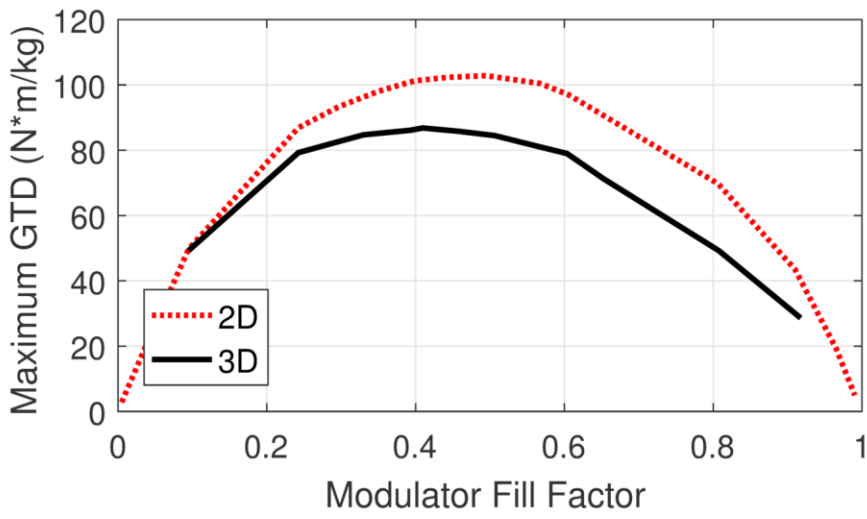
fill factor adds material cost and mass to the design. Additionally, the optimal pole pair count affects the optimal modulator fill factor. With a higher pole pair count, the modulators and the slots between adjacent modulators become tangentially narrower, which results in increased flux leakage between adjacent modulators. However, this increased flux leakage can be counteracted by slightly lowering the modulator fill factor. Accordingly, the optimal TPD and optimal GTD designs favor fill factors slightly below 0.5. Another interesting finding is that the 3D simulations tend to favor slightly lower modulator fill factors than the 2D simulations. This occurs in part because a significant portion of the axial flux at the ends of the magnetic gear passes through the modulators [35]. Therefore, reducing the fill factor of the modulators increases the reluctance “seen” by axially escaping leakage flux and generally reduces the impact of end-effects on the magnetic gear torque rating. Ultimately, in most cases, a modulator fill factor of 0.5 is fairly close to optimal for all three metrics.



**Figure 2.20 Variation of maximum VTD and LA VTD with modulator fill factor.**



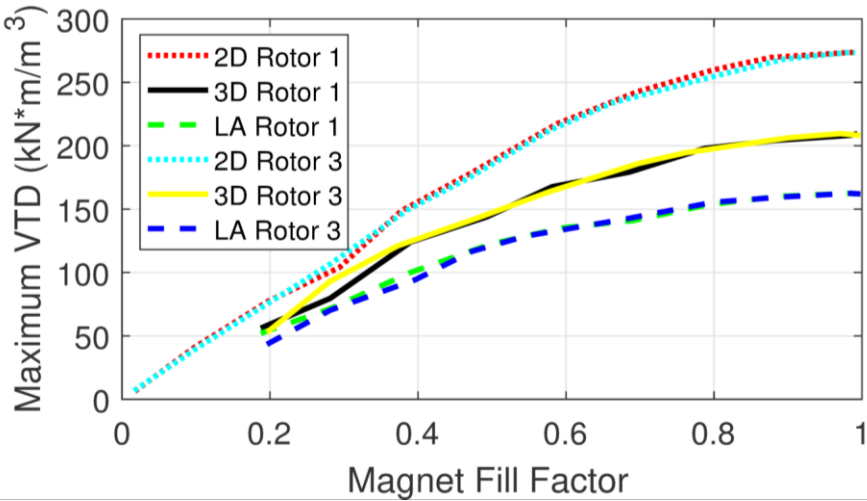
**Figure 2.21 Variation of maximum TPD with modulator fill factor.**



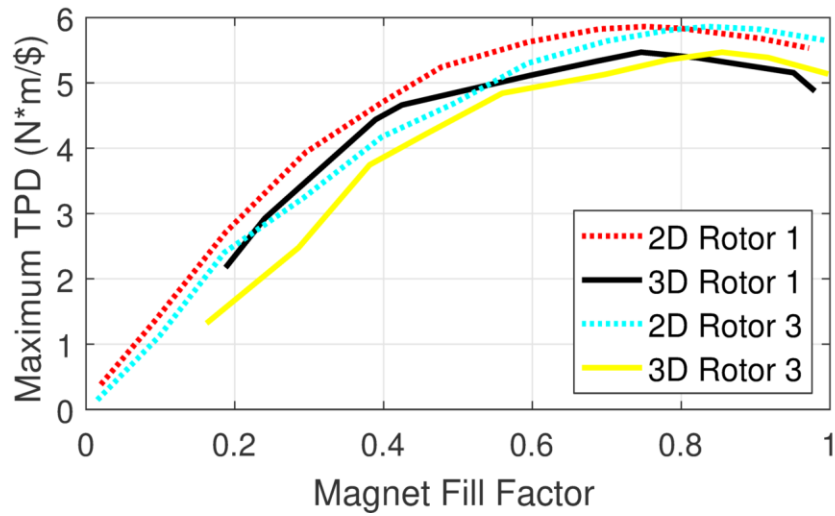
**Figure 2.22 Variation of maximum GTD with modulator fill factor.**

Figure 2.23, Figure 2.24, and Figure 2.25 show the envelopes of the optimal performances as the magnet fill factors vary. Generally, increasing either of the magnet fill factors results in increased torque due to an increase in the magnitude of the

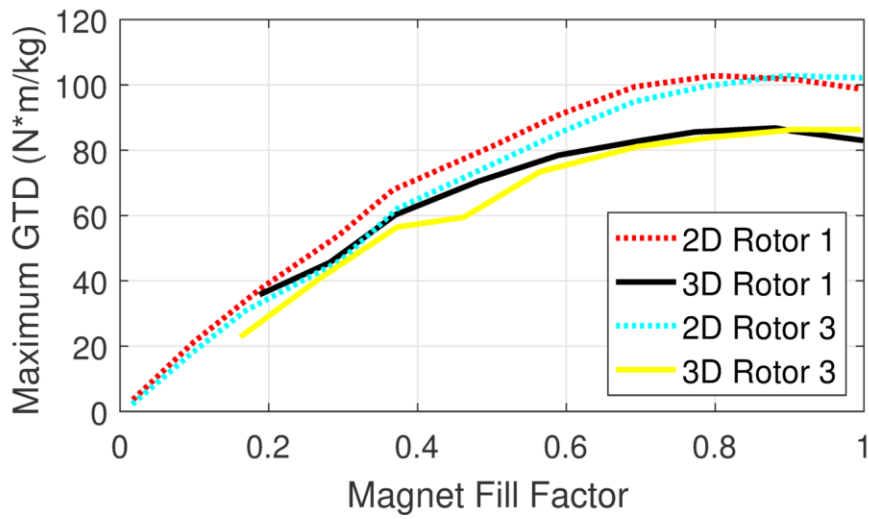
fundamental spatial harmonic of the magnetomotive force (MMF) from that set of magnets. However, the torque returns diminish as the magnet fill factors continue to increase towards 1. Additionally, increasing the magnet fill factors increases the magnet volume, which significantly increases the material cost of the magnetic gear; therefore, the optimal TPD designs favor lower magnet fill factors than those required for the optimal VTD designs. Furthermore, because increasing the magnet fill factors tends to reduce the stack length required to achieve the target slip torque, the designs with higher magnet fill factors also generally experience more significant end-effects. Nonetheless, all three metrics converge to optimal designs with relatively high magnet fill factors of at least 0.75 on both Rotor 1 and Rotor 3. This analysis considered ideal arc shaped magnets; however, in addition to creating a non-uniform air gap, using rectangular magnets would also place practical limits on the maximum achievable magnet fill factors.



**Figure 2.23 Variation of maximum VTD and LA VTD with PM fill factors.**



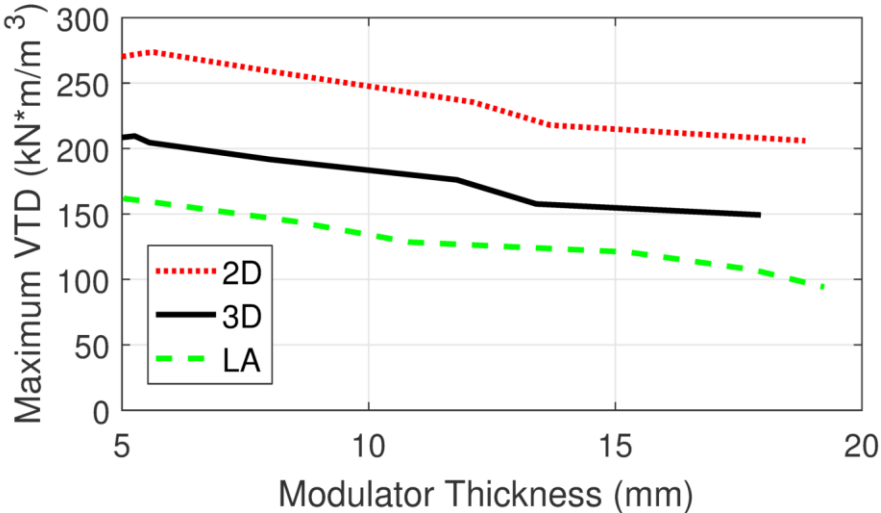
**Figure 2.24 Variation of maximum TPD with PM fill factors.**



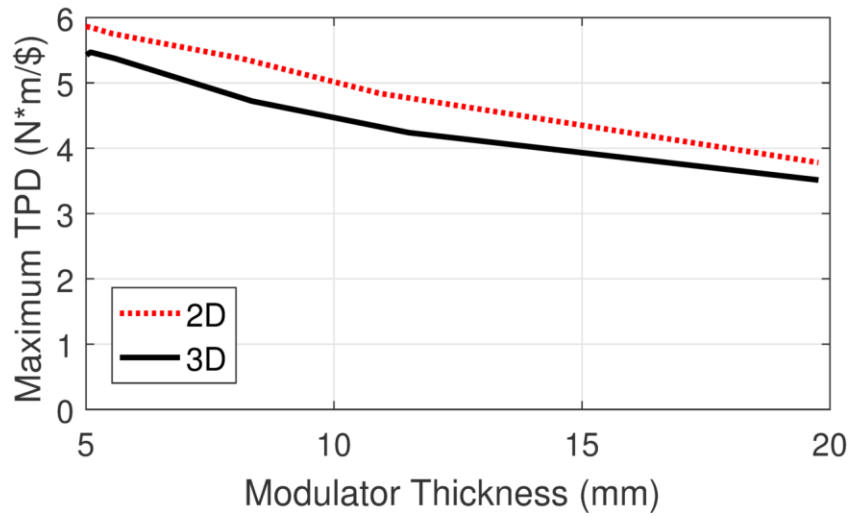
**Figure 2.25 Variation of maximum GTD with PM fill factors.**

Figure 2.26, Figure 2.27, and Figure 2.28 show the envelopes of the optimal performances as the modulator thickness varies. Increasing the modulator thickness reduces the inner air gap radius for a given outer radius, so it generally reduces a gear's

slip torque. Additionally, increasing the modulator thickness increases the leakage flux both in the modulators and in the slots between adjacent modulators, which can further decrease the torque. Therefore, the optimal designs for each of the three metrics have relatively thin modulators. Nonetheless, the modulator layer must be thick enough that the reluctance of the slots between adjacent modulators is large enough that the flux is modulated by the alternating reluctances of the modulators and the slots. However, in most cases, mechanical concerns will dictate that the modulators must be appreciably thicker than the magnetically optimal value [40]. In particular, the modulators must be thick enough to mechanically withstand the significant attractive forces from the inner and outer magnets and to transfer the torque to the LSR shaft. Additionally, the forces on individual modulators change as the gear operates, and the modulators should be stiff enough to minimize vibrations from these varying forces.



**Figure 2.26 Variation of maximum VTD and LA VTD with modulator thickness.**



**Figure 2.27 Variation of maximum TPD with modulator thickness.**

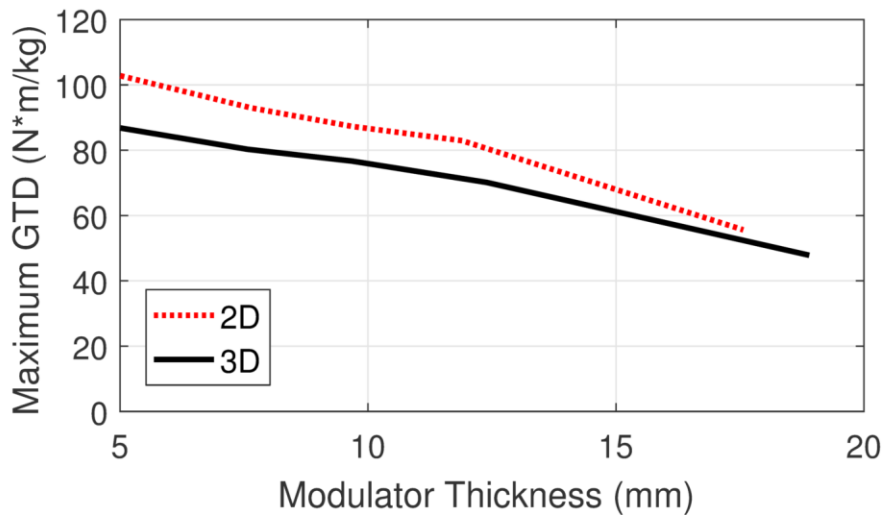


**Figure 2.28 Variation of maximum GTD with modulator thickness.**

Figure 2.29, Figure 2.30, and Figure 2.31 show the envelopes of the optimal performances as the magnet thickness ratio varies. While increasing the magnet thickness ratio increases the amount of magnet present in the gear, it also reduces the air

gap radii (for a fixed outer radius). Additionally, because the Rotor 3 magnets have a much higher pole count, there is significantly more leakage flux between adjacent poles when the Rotor 3 magnet thickness is increased. Accordingly, increasing the magnet thickness ratio does not have a large overall impact on the VTD of the design. However, because adding magnet material on the outer cylinder increases the cost and mass of the magnetic gear, the optimal TPD and GTD designs converge to lower optimal magnet thickness ratios. The minimum Rotor 3 magnet thickness may often be limited by manufacturing considerations, such as the minimum practical magnet thickness. Additionally, if the magnet thickness ratio is too low, the flux from the inner magnets may demagnetize the outer magnets, especially if the gear is operated at high temperatures. While this analysis only considers a single gear ratio, a past study [32] shows that the gear ratio affects the extent of these magnet thickness ratio design trends.

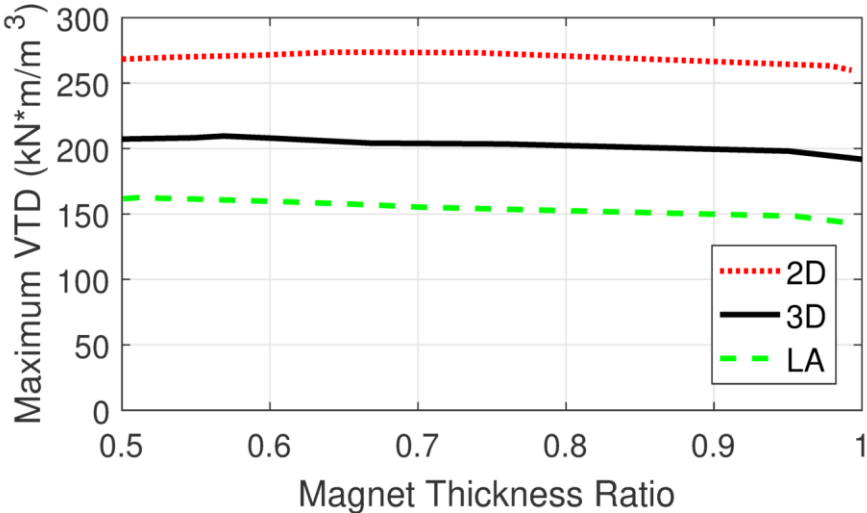


**Figure 2.29 Variation of maximum VTD and LA VTD with magnet thickness ratio.**



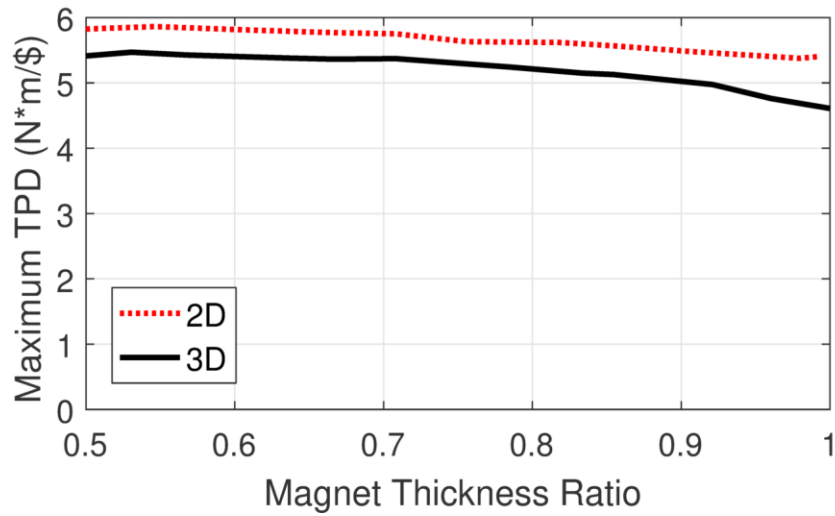


**Figure 2.30 Variation of maximum TPD with magnet thickness ratio.**

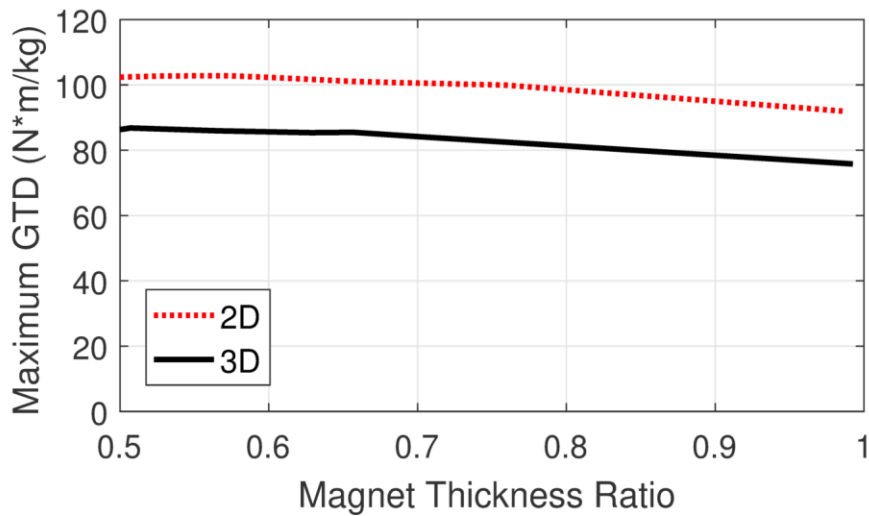


**Figure 2.31 Variation of maximum GTD with magnet thickness ratio.**

### 2.3. Conclusion

A genetic algorithm was used to independently optimize different coaxial radial flux magnetic gear designs for maximum volumetric torque density (VTD), maximum

torque per dollar (TPD), and maximum gravimetric torque density (GTD) based on both 2D simulations and 3D simulations within a parametric design space. The maximum VTD obtained was  $274 \text{ kN}\cdot\text{m}/\text{m}^3$  based on 2D simulations and  $210 \text{ kN}\cdot\text{m}/\text{m}^3$  based on 3D simulations; the maximum leakage adjusted VTD obtained was  $162 \text{ kN}\cdot\text{m}/\text{m}^3$ . The maximum TPD obtained was  $5.86 \text{ N}\cdot\text{m}/\$$  based on 2D simulations and  $5.47 \text{ N}\cdot\text{m}/\$$  based on 3D simulations. The maximum GTD obtained was  $102.8 \text{ N}\cdot\text{m}/\text{kg}$  based on 2D simulations and  $86.8 \text{ N}\cdot\text{m}/\text{kg}$  based on 3D simulations. The difference between 2D and 3D results is dependent on the magnetic gear's form factor, which is determined by the design space (especially the maximum permissible outer radius) and the target torque. Larger torques require longer stack lengths, which reduce the relative impact of end-effects. In this analysis, the design space and required torque favored form factors characterized by relatively short stack lengths and relatively wide diameters. This led to significant end-effects, especially for the optimal VTD designs. Thus, when 3D effects were considered, the optimal VTD designs had a smaller outer radius and a larger stack length than most of the other optimal designs.

There are stark differences between the optimal VTD, TPD, and GTD designs. The optimal VTD designs favor significantly thicker magnets and higher magnet volumes than the optimal TPD designs. The difference in optimal magnet thicknesses also results in a difference in the optimal pole pair counts required for the optimal VTD and optimal TPD designs, with the optimal VTD designs having much lower pole counts than the optimal TPD designs. The optimal GTD designs tend to have optimal parameter values between those of the maximum VTD and maximum TPD designs.

These differences resulted in the VTDs of the maximum TPD designs being much lower than those of the maximum VTD designs and the TPDs of the maximum VTD designs being much lower than those of the maximum TPD designs. However, the maximum GTD designs achieved a good compromise in performance between VTD and TPD. Nonetheless, all of the optimal designs have very thin Rotor 3 back irons, modulators that are very thin radially, and modulator fill factors near 0.5.

Considering end-effects significantly impacted both optimal design performance predictions and optimal parameter value selections. Many designs experienced a significant reduction in torque transmission capabilities, which necessitated a corresponding increase in stack length to maintain the target torque rating. Furthermore, because several design parameters influence the significance of end-effects, the optimal design parameters also changed once this important phenomenon was considered in the analysis. Notably, considering 3D effects significantly reduced the optimal outer radius for the maximum VTD designs. This resulted in a reduction in the optimal pole pair counts. If the VTD is adjusted to provide an axial buffer for the leakage flux so that it does not cause losses in nearby conductive materials, the optimal radius and optimal pole pair count are reduced even further. Additionally, consideration of end-effects slightly decreased the optimal modulator fill factor required to maximize each metric. These results clearly demonstrate that 3D end-effects can dramatically reduce the torque ratings of certain magnetic gear designs, and they should be considered in studies of magnetic gears with relatively short stack lengths and wide diameters in order to ensure the correct selection of proper optimal design parameters.

### 3. COMPARISON OF AXIAL FLUX AND RADIAL FLUX COAXIAL MAGNETIC GEARS\*

The previous section illustrates the impact of various design parameters on the performance of a radial flux coaxial magnetic gear with surface mounted PMs. Selecting the appropriate magnetic gear topology is another major decision that affects a magnetic gear's performance. Most of the existing magnetic gear literature focuses on the radial flux coaxial magnetic gear, which is shown with surface-mounted PMs in Figure 1.3. However, the axial dual of this topology, which is shown in Figure 1.4 has also received some attention [18], [31], [41], [42]. Although magnetic gears of either topology can be used as standalone gears, several magnetically geared machine (MGM) topologies integrate a radial or axial flux coaxial magnetic gear with an electric machine to form a single compact device [2], [26], [28], [43]. Information about prototype designs and experimental results can be found in [2], [5], [9], [33], [44], [45], [46] for radial flux magnetic gears and MGMs and in [28], [43], [47] for axial flux magnetic gears and MGMs. Throughout this section, Rotor 3 is held stationary and Rotor 2 is used as the LSR, yielding the gear ratio in (6).

Although the fundamental operating principles of both topologies are similar, there are some important design, performance, and scaling differences. First, for radial flux gears, the radial magnetic forces on each rotor can be canceled out with symmetry

---

© 2018 IEEE. Part of this section is reprinted with permission from M. C. Gardner, M. Johnson and H. A. Toliyat, "Comparison of Surface Permanent Magnet Axial and Radial Flux Coaxial Magnetic Gears," *IEEE Trans. Energy Convers.*, vol. 33, no. 4, pp. 2250-2259, Dec. 2018.

[5], [48], [49]. On the other hand, in axial flux gears, symmetry cancels out the off-axis torques, but there are still unbalanced net axial magnetic forces on the rotors [28].

Second, the two topologies' performances scale differently, as summarized by [28] and in Table 3.1, which is a simplistic but useful idealistic analysis based on the assumption of a fixed air gap shear stress,  $\sigma$ . Whereas the lever arm (the perpendicular distance between the axis of rotation and the location where the force is produced) is proportional to the radius for both topologies, the air gap area of the radial flux gear is approximately proportional to the product of its outer radius ( $R_{Out}$ ) and axial height ( $H$ ), but the air gap area of the axial flux gear is proportional to the outer radius squared. Thus, the volumetric torque density (VTD), which is the Rotor 2 slip torque ( $\tau_2$ ) divided by the active volume, as given by (18), scales differently for the two topologies. The axial flux gear's VTD ideally grows linearly with the outer radius, but the radial flux gear's VTD is ideally invariant with outer radius. Therefore, the axial flux gear favors a form factor with a large outer radius and short axial height, but the radial flux gear's VTD is ideally much less dependent on form factor.

$$VTD = \frac{\tau_2}{\pi \cdot R_{Out}^2 \cdot H} \quad (18)$$

**Table 3.1 Comparison of Ideal Geometrical Scaling Trends for Radial Flux and Axial Flux Magnetic Gears.**

| <b>Parameter</b> | <b>Radial Flux Gear</b>                  | <b>Axial Flux Gear</b>             |
|------------------|--|------------------------------------|
| Air Gap Area     | $\propto R_{Out} \cdot H$                | $\propto R_{Out}^2$                |
| Lever Arm        | $\propto R_{Out}$                        | $\propto R_{Out}$                  |
| Torque           | $\propto \sigma \cdot R_{Out}^2 \cdot H$ | $\propto \sigma \cdot R_{Out}^3$   |
| Volume           | $\propto R_{Out}^2 \cdot H$              | $\propto R_{Out}^2 \cdot H$        |
| VTD              | $\propto \sigma$                         | $\propto \sigma \cdot R_{Out} / H$ |

Although this qualitative finding is unsurprising given that it is a generally accepted pattern for other more conventional axial and radial flux electric machines, it is also of limited value without a more detailed numeric characterization of these trends. However, to this point, only a single limited direct comparison has been made between axial flux and radial flux magnetic gears. Furthermore, because that study only compares designs at a single outer radius and axial length, it draws conclusions that contradict the aforementioned theoretically predicted and conventionally accepted form factor trends [50]. This section provides a thorough quantitative comparison of radial flux and axial flux coaxial magnetic gears with surface PMs by comparing optimal designs for different operating points and performance metrics. Additionally, this section evaluates and characterizes the scaling behaviors of both radial flux and axial flux coaxial magnetic gears. As with any design study, the exact numerical results presented in this section depend on its assumptions, such as the use of a fixed air gap regardless of the design's radius or topology, but, due to the breadth of the parametric designs considered, the results still provide useful general indications of the two topologies' relative merits and design trend differences, which can be used to draw general conclusions and provide guidance at the outset of design specific studies.

### **3.1. Design Study Methodology**

To compare the two topologies, a broad parametric simulation sweep was performed for both topologies using nonlinear finite element analysis (FEA). Table 3.2, Table 3.3, and Table 3.4 specify the parametric design combinations considered in this section, which were selected based on the results of past studies reported in [28], [32],

[51], in order to include a reasonable range and resolution for the values of the most significant and interesting parameters. Table 3.2 provides the common ranges of values considered for each parameter used in both gear topologies, while Table 3.3 provides the ranges considered for each parameter unique to either of the two topologies. In addition to the parameters shown in Table 3.2 and Table 3.3, Table 3.4 summarizes the various  $P_1$  values evaluated for each  $G_{Int}$ ,  $R_{Out}$ , and topology combination to ensure that the optimal  $P_1$  value for each performance metric is within the range considered for each scenario, without including unnecessary sub-optimal cases.

**Table 3.2 Common Cross-Sectional Parameter Sweep Values.**

| <b>Parameter</b>                          | <b>Values</b>         | <b>Units</b> |
|---|-----------------------|--------------|
| Integer part of gear ratio ( $G_{Int}$ )  | 4, 9, 16              |              |
| Outer radius ( $R_{Out}$ )                | 50, 75, 100, 150, 200 | mm           |
| Rotor 1 back iron thickness ( $T_{BI1}$ ) | 5, 10, 20             | mm           |
| Rotor 3 back iron thickness ( $T_{BI3}$ ) |                       |              |
| For $T_{BI1} = 5$ mm                      | 5                     | mm           |
| For $T_{BI1} = 10$ mm                     | 5, 10                 | mm           |
| For $T_{BI1} = 20$ mm                     | 5, 10, 20             | mm           |
| Rotor 1 PM thickness ( $T_{PM1}$ )        | 3, 6, 9, 12, 15       | mm           |
| PM thickness ratio ( $k_{PM}$ )           | 0.5, 0.625, 0.75      |              |
| Air gap thicknesses ( $T_{AG}$ )          | 1                     | mm           |
| Modulator thickness ( $T_{Mods}$ )        | 10                    | mm           |

**Table 3.3 Topology Specific Parameter Sweep Values.**

| <b>Parameter</b>      | <b>Radial Flux Gears</b>                      | <b>Axial Flux Gears</b>                 | <b>Units</b> |
|-----------------------|---|---|--------------|
| Radii ratio ( $k_R$ ) | N/A   | 0.25, 0.375, 0.5,<br>0.625, 0.75, 0.875 |              |
| Stack length (H)      | 5, 10, 15, 20, 25, 30,<br>40, 50, 60, 80, 100 | N/A                                     | mm           |

**Table 3.4 Rotor 1 Pole Pair Count Sweep Values.**

| <b>R<sub>Out</sub><br/>(mm)</b> | <b>G<sub>Int</sub> = 4<br/>Radial</b> | <b>G<sub>Int</sub> = 4<br/>Axial</b> | <b>G<sub>Int</sub> = 9<br/>Radial</b> | <b>G<sub>Int</sub> = 9<br/>Axial</b> | <b>G<sub>Int</sub> = 16<br/>Radial</b> | <b>G<sub>Int</sub> = 16<br/>Axial</b> |
|---------------------------------|---------------------------------------|--------------------------------------|---------------------------------------|--------------------------------------|--|---------------------------------------|
| 50                              | 3, 5, 7                               | 3, 5, 7                              | 3, 5, 7                               | 3, 5, 7                              | 3, 5                                   | 3, 5                                  |
| 75                              | 3, 5, 7, 9                            | 3, 5, 7, 9                           | 3, 5, 7, 9                            | 3, 5, 7                              | 3, 5                                   | 3, 5                                  |
| 100                             | 3, 5, ... 11                          | 3, 5, ... 11                         | 3, 5, ... 11                          | 3, 5, 7, 9                           | 3, 5                                   | 3, 5                                  |
| 150                             | 3, 5, ... 19                          | 3, 5, ... 17                         | 3, 5, ... 13                          | 3, 5, ... 11                         | 3, 5, 7                                | 3, 5, 7                               |
| 200                             | 3, 5, ... 23                          | 3, 5, ... 21                         | 3, 5, ... 15                          | 3, 5, ... 13                         | 3, 5, 7, 9                             | 3, 5, 7, 9                            |

As in [28], [32], [51], a few derived parameters were used to facilitate the parametric sweep. As in the previous section,  $G_{Int}$  represents the integer part of the gear ratio and determines the Rotor 3 pole pair count,  $P_3$ , in terms of the Rotor 1 pole pair count,  $P_1$ , according to (16). Likewise,  $k_{PM}$  gives the ratio between the PM thicknesses on Rotor 1 and Rotor 3 according to (17). The third derived parameter,  $k_R$ , determines the radii ratio of the axial flux gears according to (19), where  $R_{In}$  is the inner radius of the gear and  $R_{Out}$  is the outer radius of the gear. As indicated in Table 3.3, this relationship is only used for the axial flux gears because the radii ratio for each radial flux gear is determined by  $R_{Out}$  and the radial thicknesses of the radial layers. Similarly, the axial height of each axial flux gear is determined by the various axial layer axial thicknesses, instead of an additional stack length parameter.

$$R_{In} = k_{PM} \cdot R_{Out} \quad (19)$$

As  $G_{Int}$  is increased, the ratio of  $P_3$  to  $P_1$  increases according to (4). Thus, for higher values of  $G_{Int}$ , the optimal  $P_1$  values are lower to prevent excessively short Rotor 3 pole arcs, which result in high leakage flux between adjacent poles. Similarly, larger



$R_{Out}$  values increase the pole arcs for a given pole count and lead to higher optimal  $P_1$  values. Even values of  $P_1$  were excluded solely to reduce the case count.

Magnetic performance is generally optimized by simply minimizing the air gap, so only a single air gap value was used in this study. In practice, the minimum viable air gap (from a mechanical design and manufacturing cost standpoint) should generally be used; however, this value may change depending on the outer radius and topology. Similarly, the results of past studies consistently indicate that the magnetically optimal modulator thicknesses tend to be smaller than the minimum mechanically practical thicknesses [40], [51], so only a single modulator thickness was considered in this study. In practice, the minimum mechanically acceptable modulator thickness should generally be used in most designs. Furthermore, as in the gear illustrated in Figure 1.3, all PM tangential fill factors were set to 1, and the modulator tangential fill factors were set to 0.5. More information about the generally less complex effects of these parameters can be found in [51]. Finally, some parameter value combinations from Table 3.2 would result in radial flux gears with negative inner radii, so these combinations were discarded from the radial flux gear design set.

Each design case was simulated using nonlinear FEA. For both the radial flux and axial flux designs, the PMs are made of NdFeB N42 with a remanent flux density of 1.3 T, the back irons are made of isotropic M47 magnetic steel, and the modulators are made of a soft magnetic composite, Somaloy 700 3P. All 5928 of the radial flux designs were simulated using 2D FEA, then 2481 of the best designs were simulated at each of the 11 different stack lengths specified in Table 3.3 using 3D FEA. All of the radial flux

gear results presented in this section are based on 3D FEA unless specifically indicated otherwise. All 34,560 of the axial flux designs were simulated using 3D FEA exclusively.

The designs are evaluated primarily based on four metrics: volumetric torque density (VTD), gravimetric torque density (GTD), PM gravimetric torque density (PM GTD), and average air gap shear stress in the low speed air gap between Rotor 2 and Rotor 3 ( $\sigma_{\text{LSAG}}$ ). VTD normalizes the torque of the magnetic gear based on its size as shown in (1), and GTD normalizes the torque of the magnetic gear based on its mass, as shown in (14). PM GTD is the Rotor 2 slip torque divided by the total mass of the PMs in the gear, as given by (20), where  $m_{\text{PM}}$  is the total mass of the PMs in the gear. PM GTD provides a normalized measure of how effectively each design uses the magnet material, which is the dominant source of active material cost in gears using NdFeB magnets [32]. Shear stress is a useful, but slightly more abstract, metric that characterizes the average tangential (torque producing) force per unit of air gap area yielded by a given design, without considering the lever arm (radius) at which that force is generated [52], [53]. This is useful for comparing the effects of design parameters besides outer radius on the performances of designs at different outer radius values. For radial flux designs,  $\sigma_{\text{LSAG,Rad}}$  is given by (21), where  $R_{\text{LSAG}}$  is the radius of the low speed air gap and  $\tau_3$  is the Rotor 3 slip torque. Similarly, for axial flux designs,  $\sigma_{\text{LSAG,Ax}}$  is given by (22).

$$\text{PM GTD} = \frac{\tau_2}{m_{\text{PM}}} \quad (20)$$

$$\sigma_{\text{LSAG,Rad}} = \frac{\tau_3}{2\pi \cdot R_{\text{LSAG}}^2 \cdot H} \quad (21)$$

$$\sigma_{\text{LSAG,Ax}} = \frac{\tau_3}{\frac{2\pi}{3} \cdot (R_{\text{Out}}^3 - R_{\text{In}}^3)} \quad (22)$$

### 3.2. Results

#### 3.2.1. 2D Cross-Sectional Design Parameters

The following figures illustrate several important design trends based on the parametric FEA results. Figure 3.1, Figure 3.2, and Figure 3.3 depict the variation of the maximum achievable VTD, GTD and PM GTD with the Rotor 1 PM thickness for the various  $R_{\text{Out}}$  value and topology combinations.

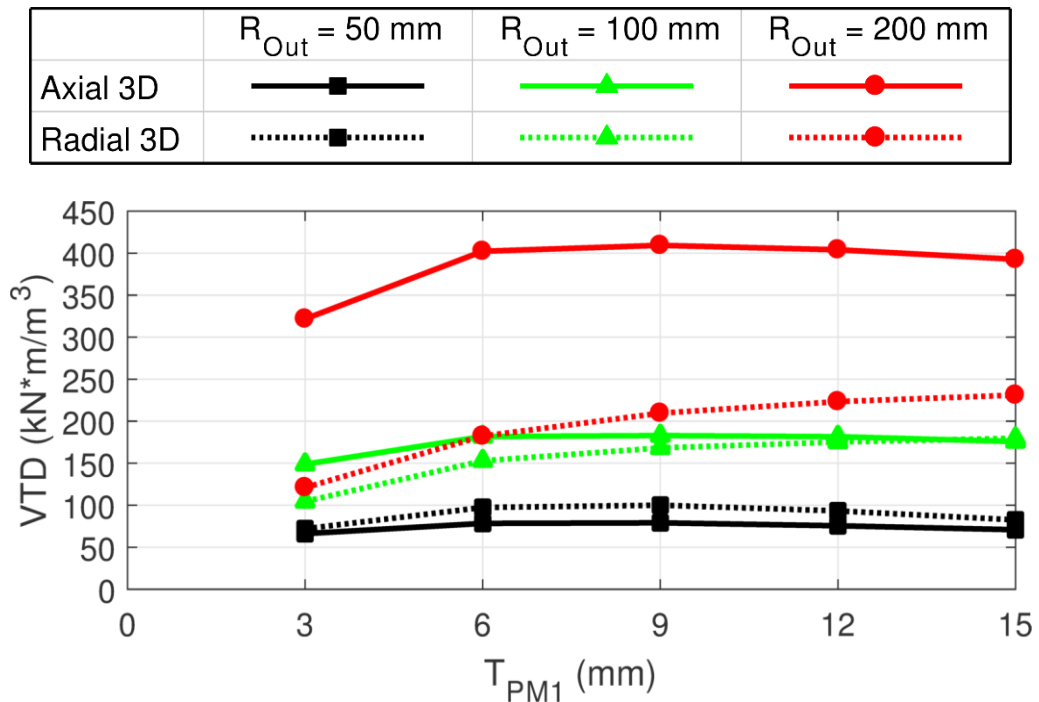


**Figure 3.1** Variation of maximum VTD with Rotor 1 PM thickness for radial flux designs with a stack length of 50 mm and axial designs, both based on 3D FEA and having  $G_{\text{int}} = 4$ .

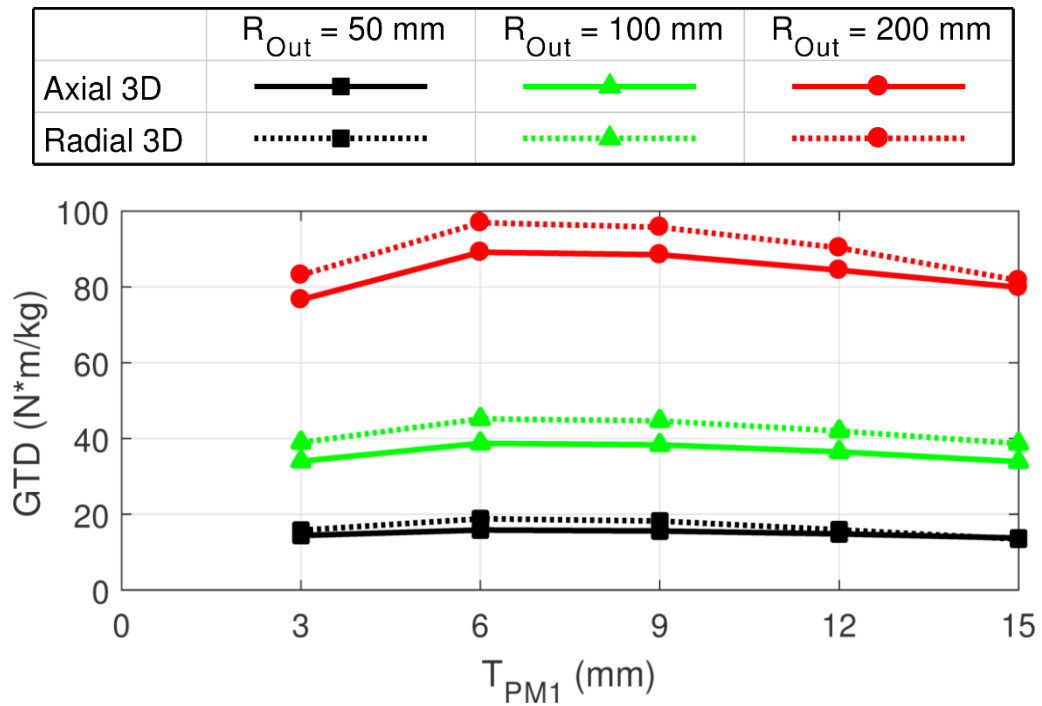


**Figure 3.2** Variation of maximum GTD with Rotor 1 PM thickness for radial flux designs with a stack length of 50 mm and axial designs, both based on 3D FEA and having  $G_{Int} = 4$ .

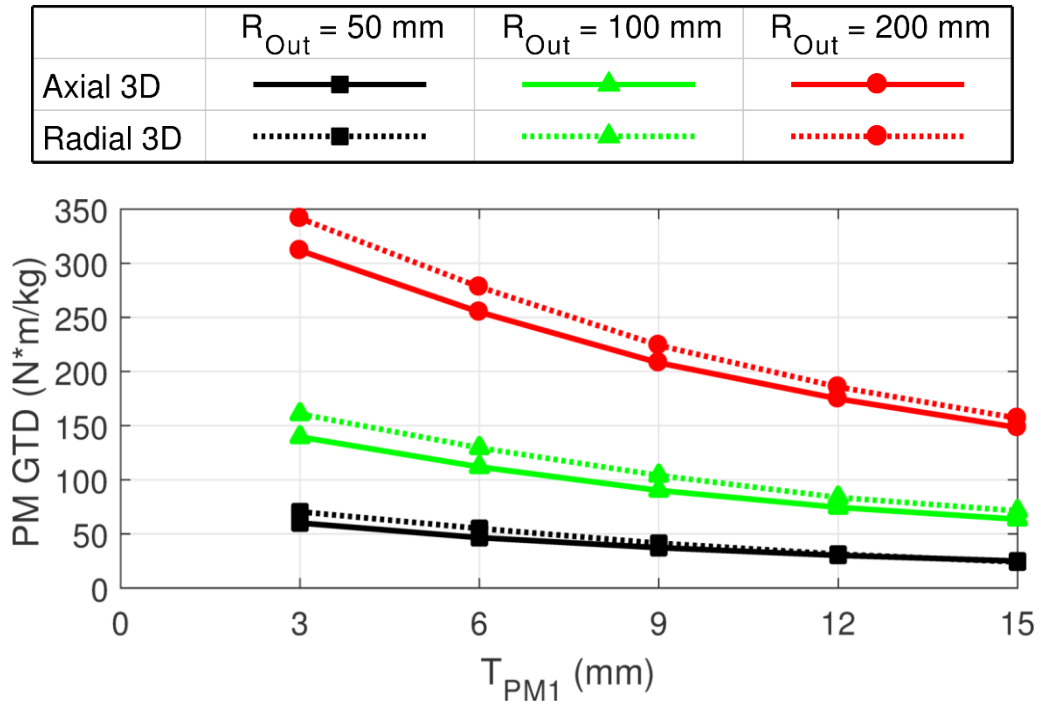


**Figure 3.3** Variation of maximum PM GTD with Rotor 1 PM thickness for radial flux designs with a stack length of 50 mm and axial designs, both based on 3D FEA and having  $G_{Int} = 4$ .

The results in Figure 3.1 demonstrate that, for most radial flux gears, the VTD is maximized by simply using the thickest magnets considered in the study, which is consistent with findings from previous studies [32], [51]. The lone exception to this trend in Figure 3.1 is the 50 mm outer radius design set, where the decreased radial space limits the amount of magnet material that can be used effectively. If even thicker magnets were considered in this study, the finite radial space would eventually limit the optimal magnet thicknesses for radial flux gears with larger outer radii. When the available radial space is not an issue, the trend of increased PM thicknesses increasing the VTD occurs because increasing the radial thickness of the magnets does not increase

the volume of the radial flux gears (for a fixed outer radius). However, because increasing the magnet thickness increases the effective air gap, the torque density returns diminish as magnet thickness continues to increase. As a result, the axial flux gear's behavior is more complicated. Increasing the axial thickness of the magnets in an axial flux gear is not a very effective means of increasing a design's torque rating, because it also increases the effective air gap. Furthermore, increasing the axial thickness of the magnets in the axial flux gear also increases the gear's axial height and overall volume; therefore, the VTD of the axial flux gears is maximized by choosing the appropriate intermediate PM thickness instead of simply using the largest permissible value.

Similarly, Figure 3.3 reveals that the PM GTD is maximized for each topology and outer radius combination by choosing the minimum magnet thickness considered in the study to minimize the effective air gap and use the magnet material as effectively as possible. The theoretically optimal magnet thicknesses for maximizing PM GTD would likely be impractically thin for manufacturing and handling. As in [51], the magnet thicknesses that maximize GTD tend to be between the thicknesses that are optimal for VTD and PM GTD.

It is important to note that because magnetic gears have large linear reluctances from the two air gaps and two sets of PMs, their design often favors a higher degree of saturation than typical electric machines, which typically have much smaller linear reluctances. For some of the highest VTD designs, flux densities reached peak levels of almost 2.5 T in the Rotor 1 back iron, approximately 1.75 T in the modulators, and nearly 2.5 T in the Rotor 3 back iron. For some of the highest PM GTD designs, flux

densities reached peak levels of almost 1.75 T in the Rotor 1 back iron, approximately 1.15 T in the modulators, and nearly 2.25 T in the Rotor 3 back iron. Despite these high flux densities, magnetic gears can achieve high efficiencies, especially under high torque, low speed operating conditions [32]. While these high iron flux densities do cause some core losses, the eddy current losses in the PMs often account for the majority of the total losses in a magnetic gear, especially as the operating speed increases [5], [32], and laminated PMs can be used to improve the efficiency if necessary.

Figure 3.4, Figure 3.5, and Figure 3.6 demonstrate that the Rotor 1 pole pair sweep ranges summarized in Table 3.4 contain the optimum values for VTD, GTD, and PM GTD at each of the design outer radius and gear ratio combinations, except for the 50 mm outer radius maximum VTD and maximum GTD design sets. The VTD and GTD for this design space could be maximized by using a Rotor 1 pole pair count of less than 3; however, as indicated in Table 3.4, Rotor 1 pole pair counts below 3 were not considered in the study because they generally lead to high torque ripple unless additional measures, such as magnet skewing, are employed [3]. In general, the results in Figure 3.4, Figure 3.5, and Figure 3.6 suggest the fairly obvious conclusion that the larger outer radius designs favor higher pole pair counts than the lower outer radius designs.

|           | $R_{Out} = 50 \text{ mm}$ | $R_{Out} = 100 \text{ mm}$ | $R_{Out} = 200 \text{ mm}$ |
|-----------|---------------------------|----------------------------|----------------------------|
| Axial 3D  |                           |                            |                            |
| Radial 3D |                           |                            |                            |

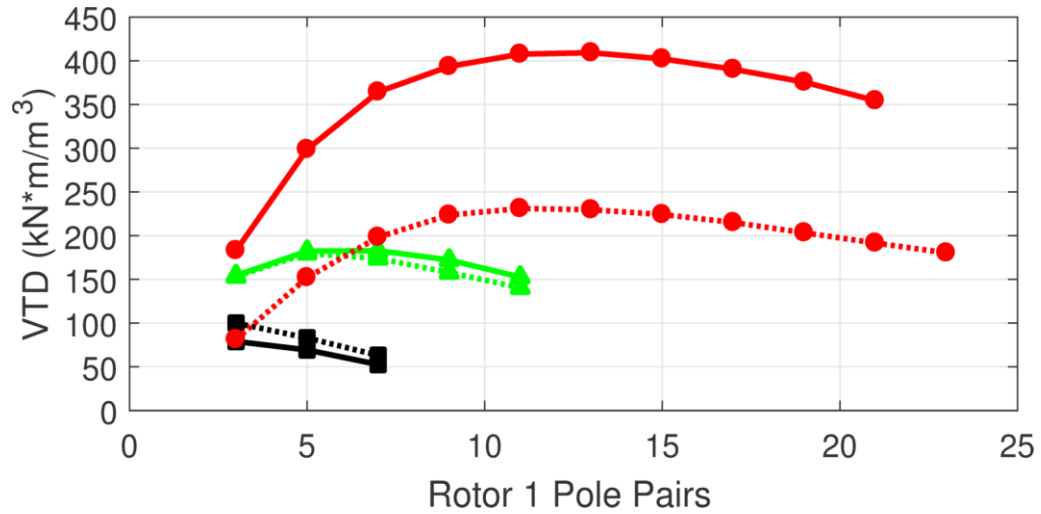


**Figure 3.4** Variation of maximum VTD with Rotor 1 pole pair count for radial flux designs with a stack length of 50 mm and axial designs, both based on 3D FEA and having  $G_{Int} = 4$ .



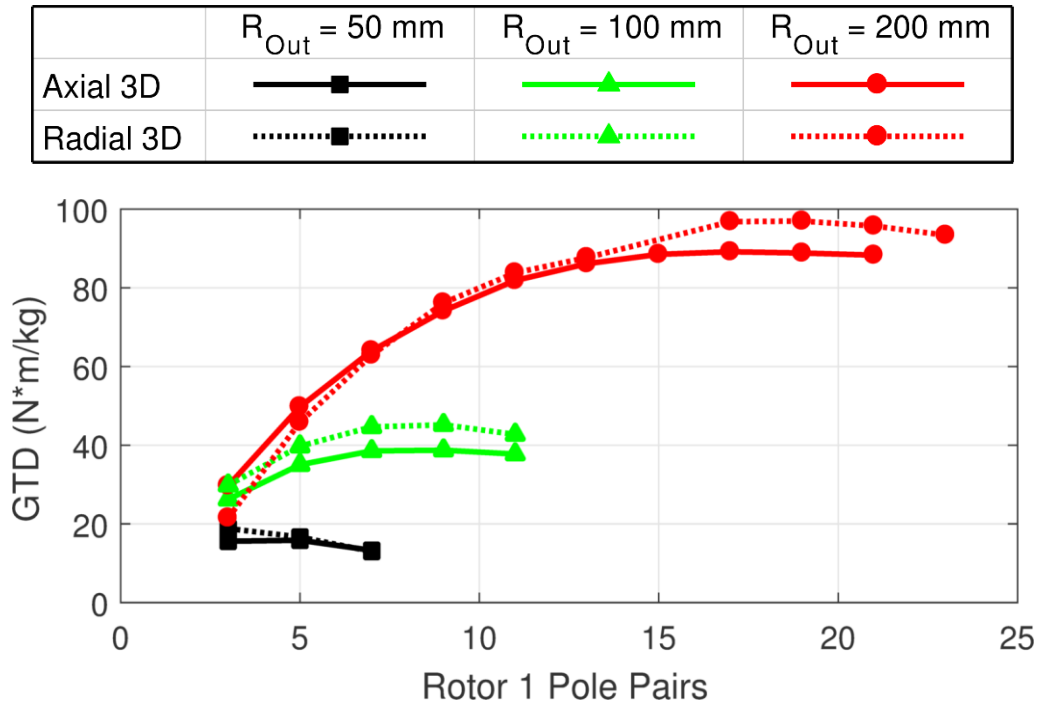


**Figure 3.5** Variation of maximum GTD with Rotor 1 pole pair count for radial flux designs with a stack length of 50 mm and axial designs, both based on 3D FEA and having  $G_{Int} = 4$ .

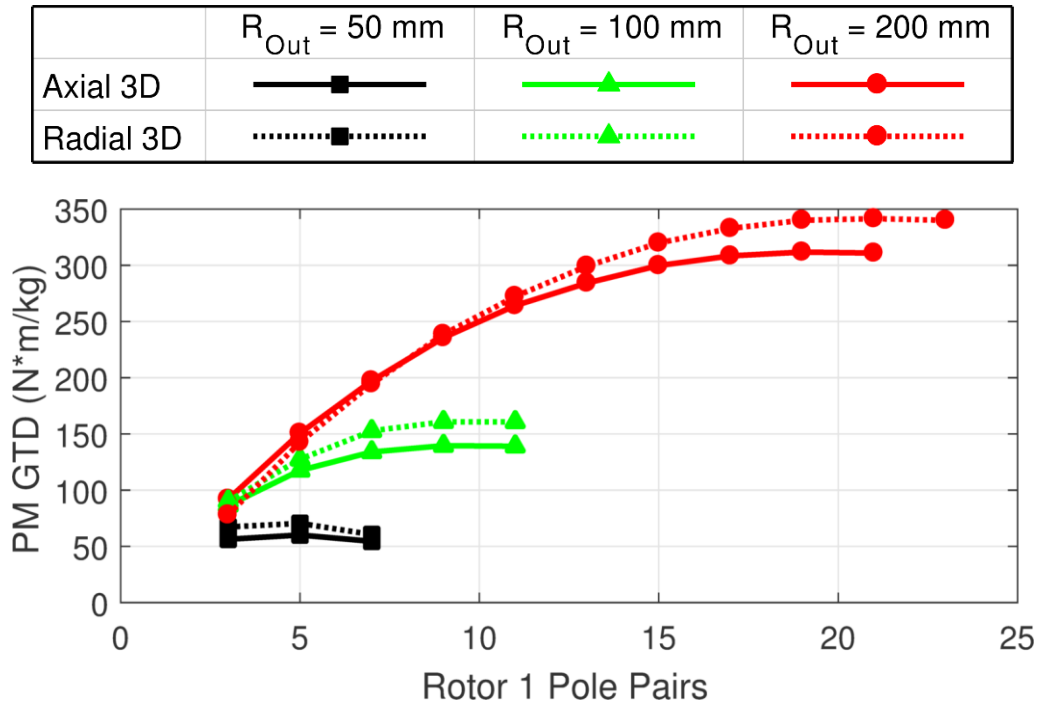


**Figure 3.6 Variation of maximum PM GTD with Rotor 1 pole pair count for radial flux designs with a stack length of 50 mm and axial designs, both based on 3D FEA and having  $G_{Int} = 4$ .**

A comparison of the graphs in Figure 3.4, Figure 3.5, and Figure 3.6 also indicates that the maximum PM GTD designs use higher Rotor 1 pole pair counts than the maximum VTD designs, while the maximum GTD designs favor intermediate pole counts. This is because the thicker magnets used in the maximum VTD designs increase the effective air gaps, which results in increased leakage flux between adjacent poles. This must be counteracted by using lower pole pair counts to achieve larger pole arcs [51]. Figure 3.7 and Figure 3.8 illustrate this principle by depicting the impact of the Rotor 1 magnet thickness on the optimal Rotor 1 pole pair count that maximizes the

average low speed air gap shear stress (indicated by the dashed line) in axial flux gears and 50 mm stack length radial flux gears, both with 200 mm outer radii and  $G_{Int} = 4$ .

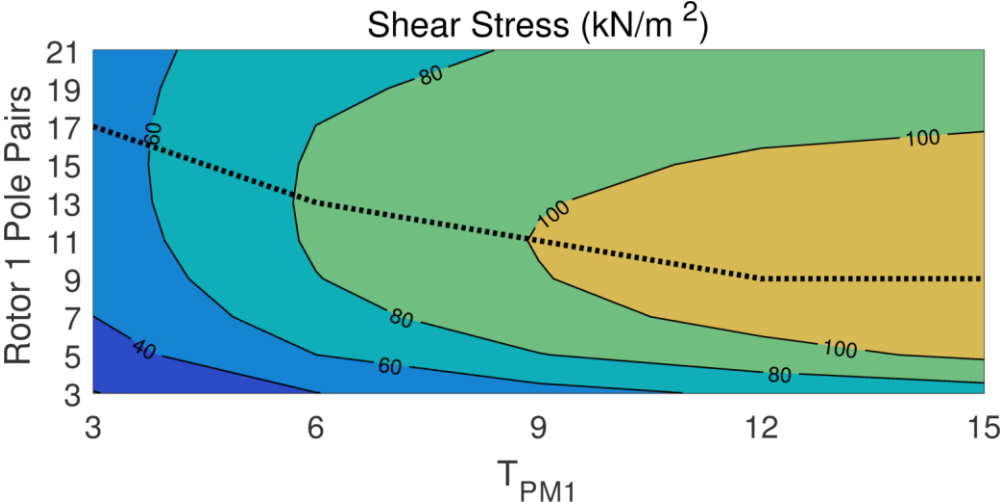


**Figure 3.7** Variation of maximum average low speed air gap shear stress with Rotor 1 PM thickness and pole pair count for axial flux gears with 200 mm outer radii and  $G_{Int} = 4$ . The dashed line indicates the optimal Rotor 1 pole pair count for each Rotor 1 PM thickness.

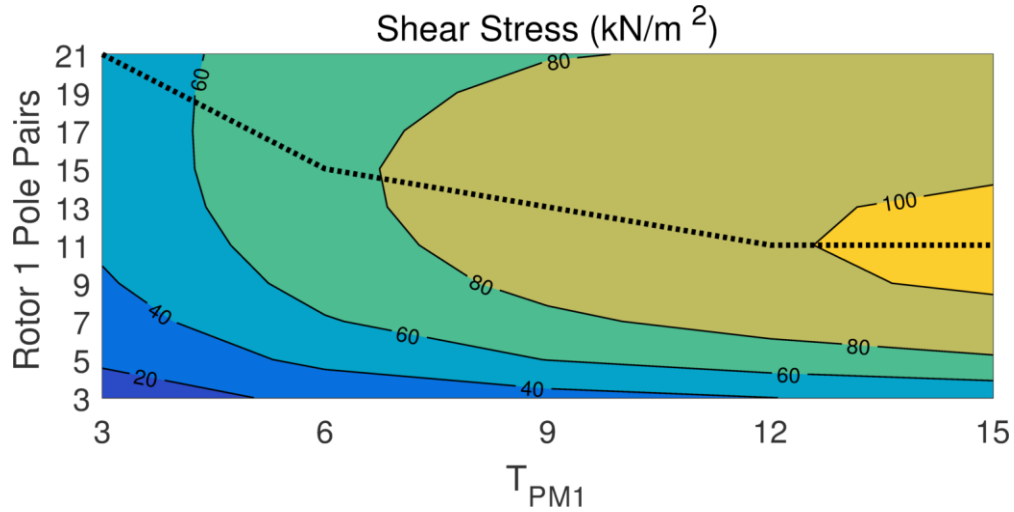


**Figure 3.8** Variation of maximum average low speed air gap shear stress with Rotor 1 PM thickness and pole pair count for radial flux gears with 50 mm stack lengths, 200 mm outer radii, and  $G_{Int} = 4$ . The dashed line indicates the optimal Rotor 1 pole pair count for each Rotor 1 PM thickness.

The results in Figure 3.9, Figure 3.10, and Figure 3.11 reveal that increasing the gear ratio yields lower maximum VTDs, GTDs, and PM GTDs for both the axial and radial flux topologies. This is primarily because the larger gear ratio increases the disparity between the pole pair counts on the different rotors, which makes it more difficult to simultaneously optimize the pole pair counts on each rotor. As illustrated by the curves in Figure 3.9(b), Figure 3.10(b), and Figure 3.11(b), higher gear ratio designs favor lower Rotor 1 pole pair counts in order to decrease the Rotor 3 pole pair and modulator counts and decrease leakage flux in those regions; however, that leads to decreased coenergy derivatives with respect to rotor positions. Consequently, VTD, GTD, and PM GTD tend to decrease as the gear ratio increases (within the evaluated range), and the resulting optimums (maximum torque densities) depicted in Figure 3.9,

Figure 3.10, and Figure 3.11 represent compromises between these competing influences at each design point.

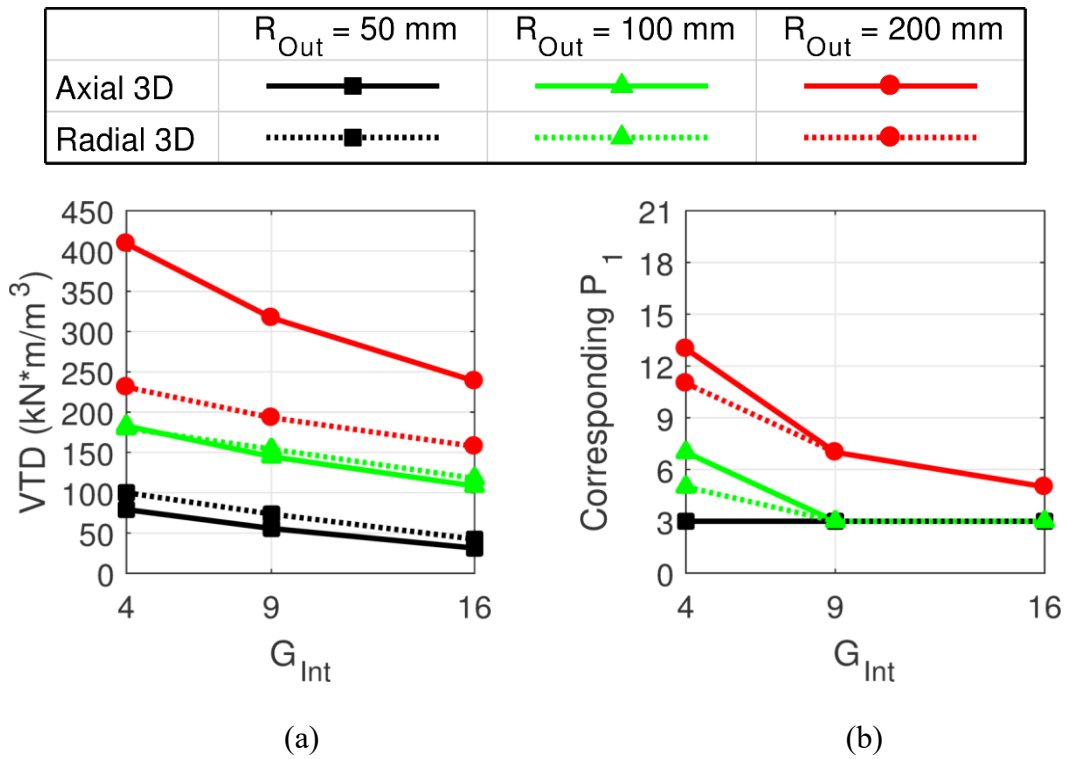


**Figure 3.9** Variation of (a) maximum VTD and (b) the corresponding optimum Rotor 1 pole pair count for maximizing VTD with  $G_{Int}$  at different outer radius values for both axial flux gears and 50 mm stack length radial flux gears.

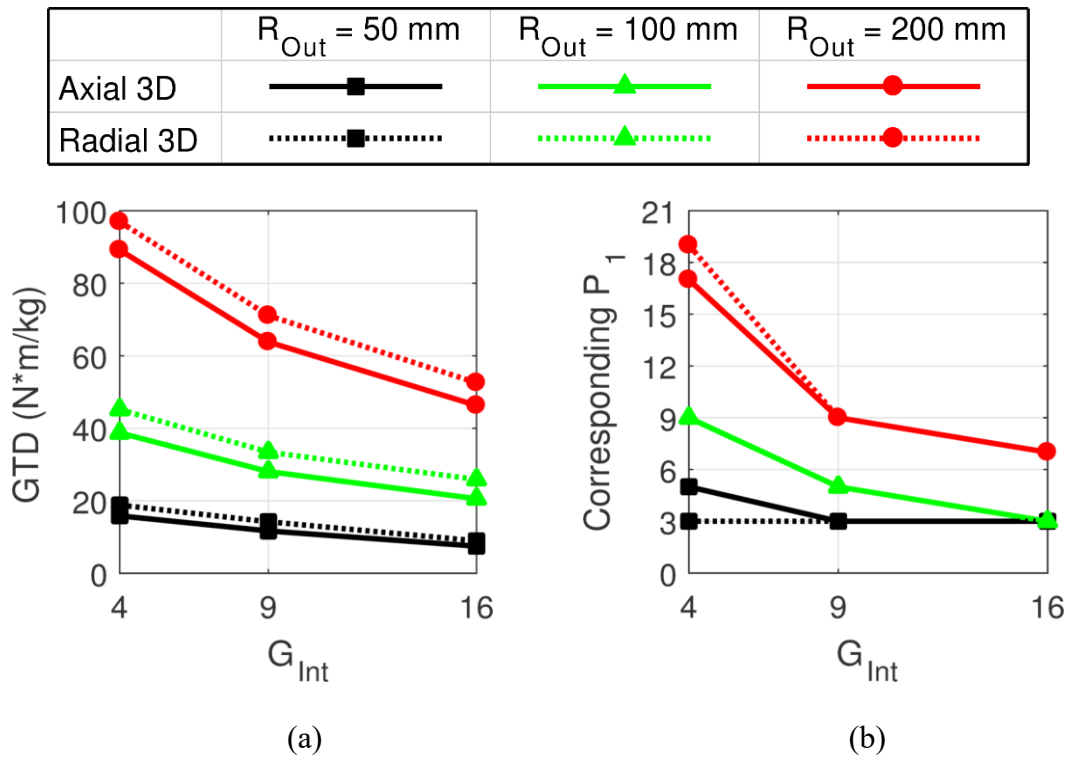


**Figure 3.10** Variation of (a) maximum GTD and (b) the corresponding optimum Rotor 1 pole pair count for maximizing GTD with  $G_{Int}$  at different outer radius values for both axial flux gears and 50 mm stack length radial flux gears.

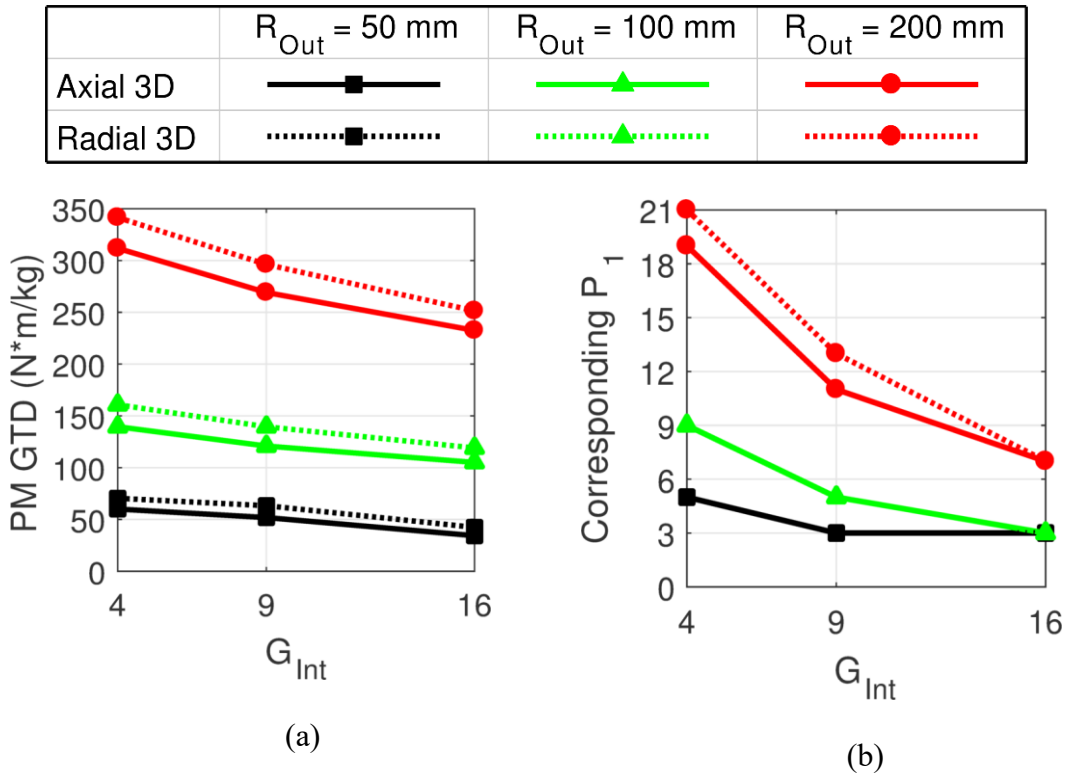


**Figure 3.11 Variation of (a) maximum PM GTD and (b) the corresponding optimum Rotor 1 pole pair count for maximizing PM GTD with  $G_{Int}$  at different outer radius values for both axial flux gears and 50 mm stack length radial flux gears.**

Additionally, Figure 3.11 illustrates that for the maximum PM GTD designs, the optimal radial flux designs tend to have higher pole counts than the optimal axial flux designs. This likely occurs because torque is produced across a much wider range of radii in an axial flux design than a radial flux design with the same outer radius. Thus, the pole counts of the axial flux design must optimize torque production across a wider range of radii. However, as illustrated in Figure 3.9, for the maximum VTD designs, the optimal radial flux designs tend to have similar or slightly lower pole counts than the optimal axial flux designs. This likely occurs because the optimal axial flux designs

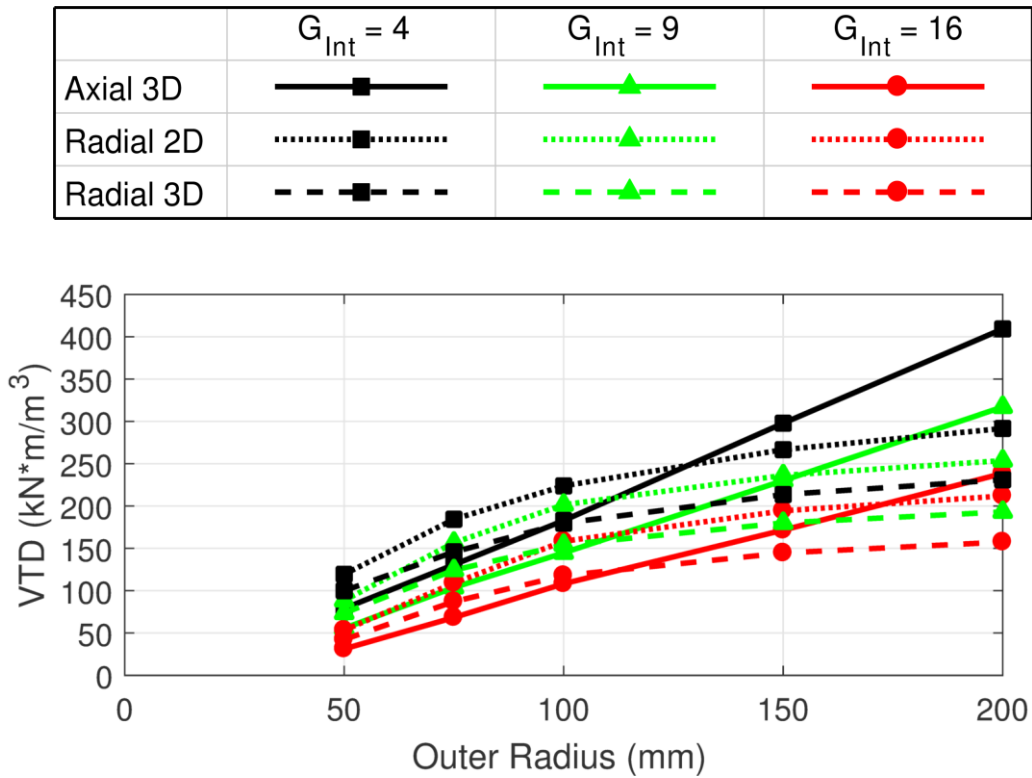
have thinner PMs than the optimal radial flux designs, which tends to increase the optimal pole count, as previously discussed.

### **3.2.2. 3D Design Scaling Parameters**

Figure 3.12, Figure 3.13, and Figure 3.14 show how the maximum torque density values scale with the gear's outer radius, which is one of the most noteworthy differences between the axial flux and radial flux topologies. As predicted by the analysis summarized in Table 3.1, the VTD of the axial flux gears grows almost linearly with the outer radius. On the other hand, while Table 3.1 suggests that the VTD of radial flux gears is ideally invariant with the outer radius, the results in Figure 3.12 demonstrate that it actually increases at a diminishingly sublinear rate with the outer radius (due to several considerations not accounted for in Table 3.1). One basic major factor causing this growth is that the ratio of the air gap radius to the outer radius increases as the outer radius increases. Another important consideration for both radial flux and axial flux gears is that higher outer radius designs favor larger pole counts, as previously indicated in Figure 3.4, Figure 3.5, and Figure 3.6, which means that there is finer resolution (on a percent change basis) for better optimization between consecutive discrete pole pair count values. Furthermore, as previously noted, the lowest pole pair count considered, 3, is sub-optimal for maximizing VTD at an outer radius of 50 mm. Regardless, axial flux magnetic gears are able to achieve significantly higher VTDs than radial flux gears at relatively larger outer radii but achieve lower VTDs than radial flux gears at lower outer radii. However, the GTDs and PM GTDs tend to scale approximately linearly with outer radius for each topology. Since the PM mass, back

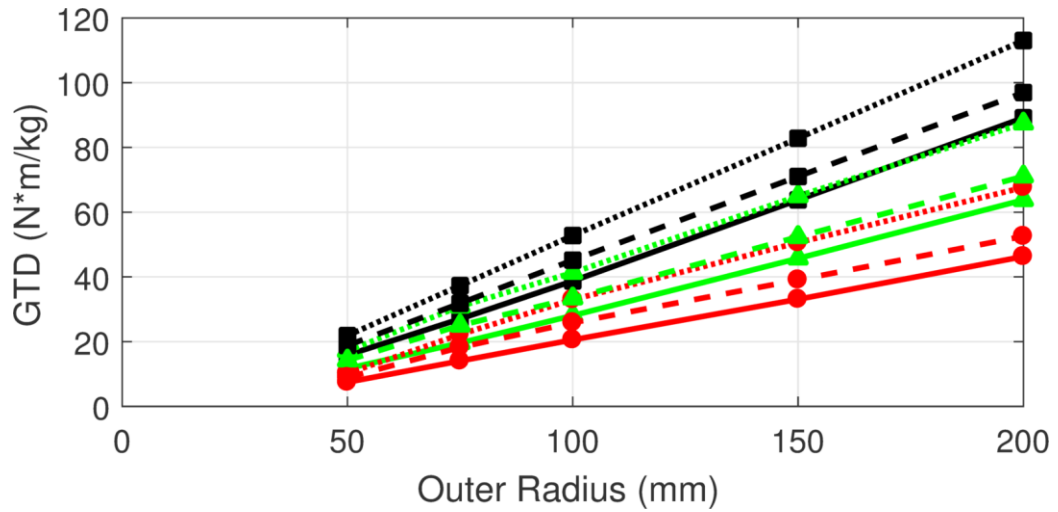


iron mass, and modulator mass are approximately proportional to the air gap area, this is consistent with behavior predicted by the analysis in Table 3.1. Additionally, Figure 3.12, Figure 3.13, and Figure 3.14 reinforce the observation that the designs with larger gear ratios tend to perform worse (within the evaluated range of gear ratios).

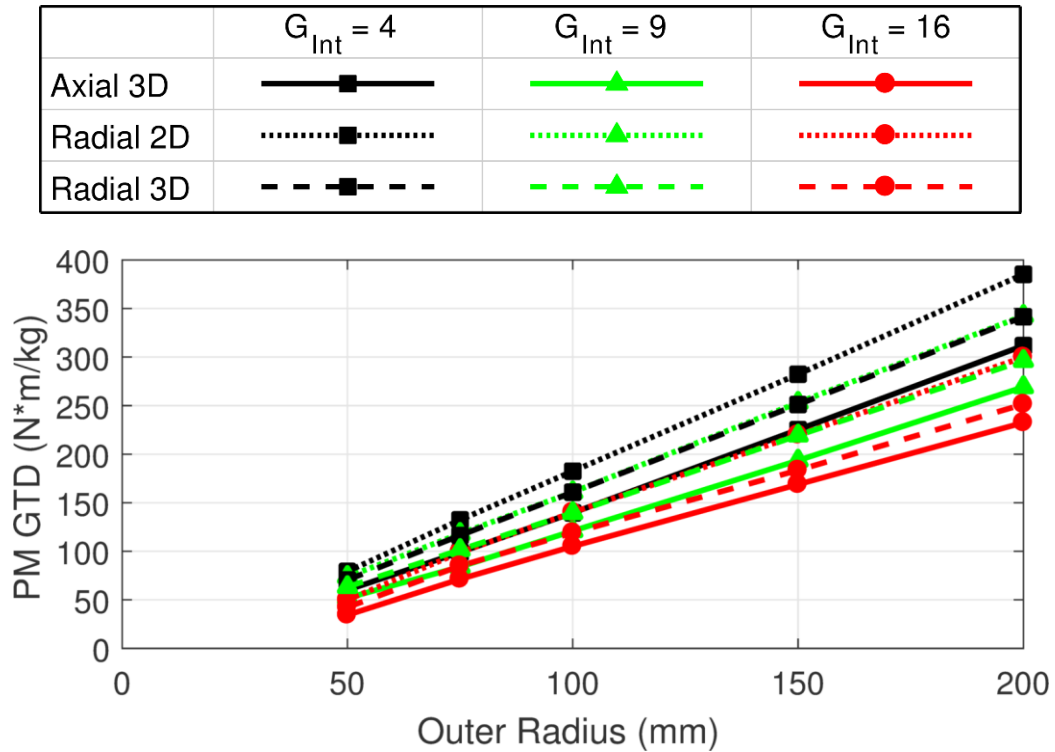


**Figure 3.12** Variation of maximum VTD with outer radius for both axial flux gears and 50 mm stack length radial flux gears at different  $G_{Int}$  values.

|           | $G_{Int} = 4$ | $G_{Int} = 9$ | $G_{Int} = 16$ |
|-----------|---------------|---------------|----------------|
| Axial 3D  |               |               |                |
| Radial 2D |               |               |                |
| Radial 3D |               |               |                |



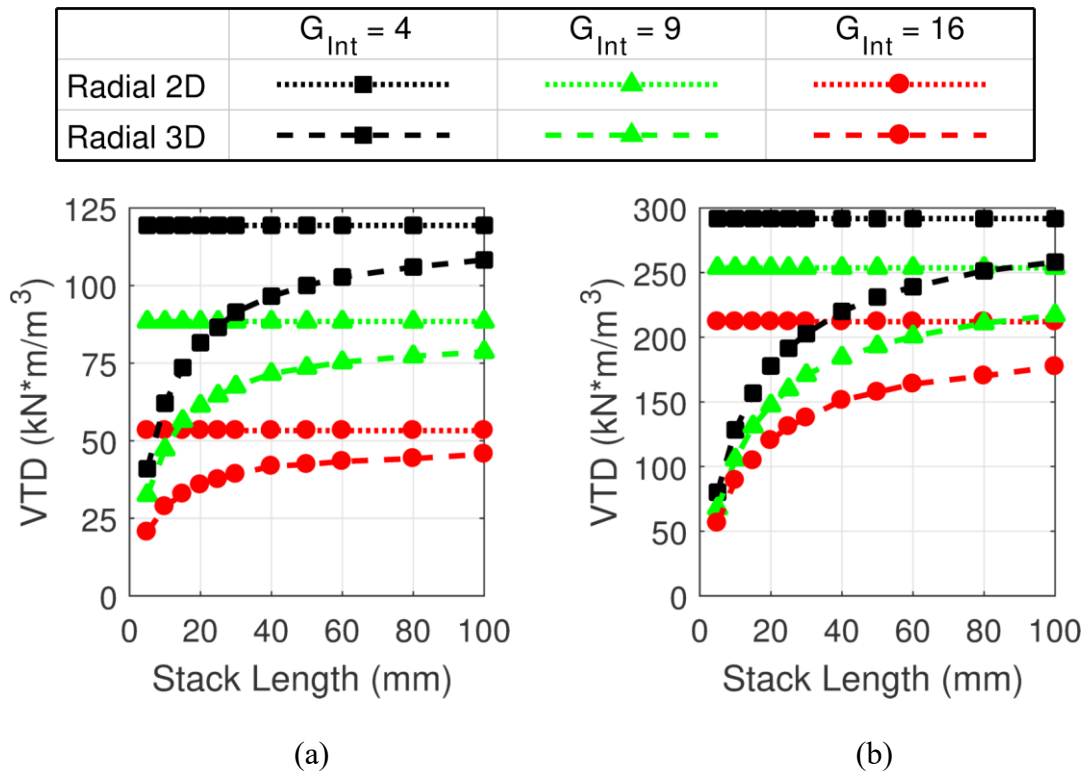
**Figure 3.13** Variation of maximum GTD with outer radius for both axial flux gears and 50 mm stack length radial flux gears at different  $G_{Int}$  values.



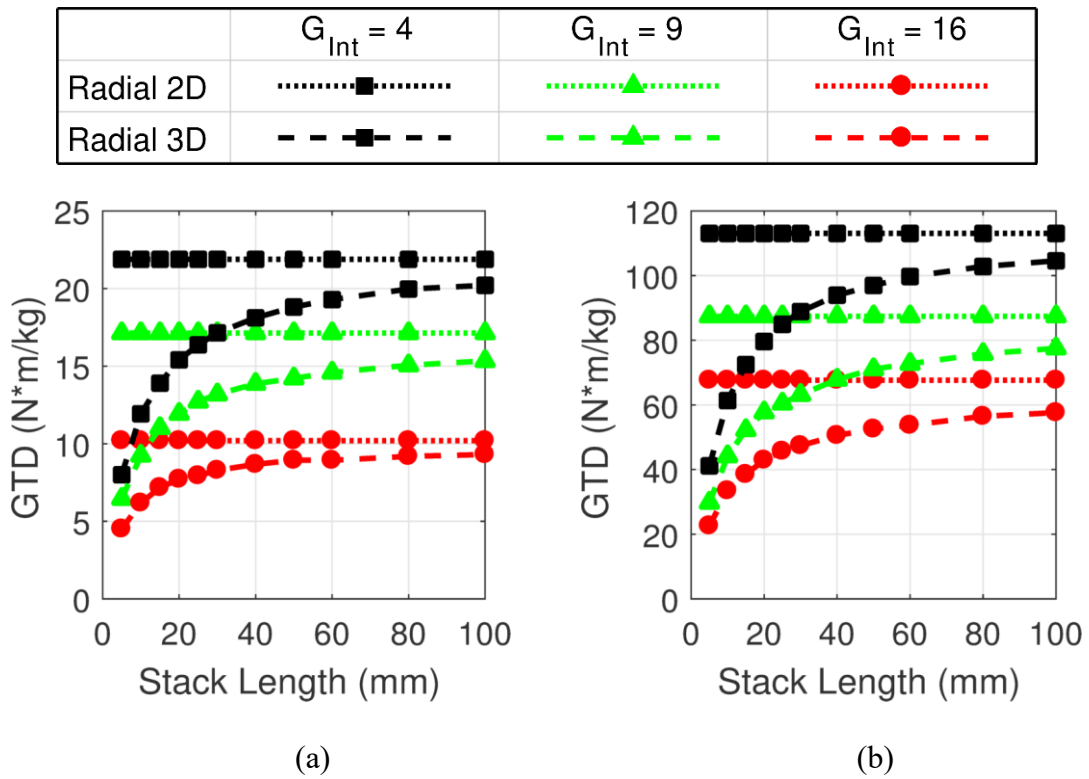
**Figure 3.14** Variation of maximum PM GTD with outer radius for both axial flux gears and 50 mm stack length radial flux gears at different  $G_{Int}$  values.

Figure 3.12, Figure 3.13, and Figure 3.14 also show that the 3D FEA predicts a lower torque for the radial flux designs than the 2D FEA, which is due to the magnetic gears' end-effects [35]. Figure 3.15, Figure 3.16, and Figure 3.17 compare the difference between the 2D FEA results and the 3D FEA results at different stack lengths, outer radii, and gear ratios, which leads to a few conclusions. First, the relative impact of the end-effects decreases as the stack length increases, with the 2D FEA VTD, GTD, and PM GTD representing the ideal limits for the 3D FEA results as the stack length is increased indefinitely. This means that, for a given outer radius, designs with higher torque ratings (and, thus, longer stack lengths) will tend to have higher VTDs, GTDs,

and PM GTDs than designs with lower torque ratings. Second, the end-effects tend to have a more significant impact on the maximum VTD designs than on the maximum PM GTD designs. This is likely due to the aforementioned facts that the maximum VTD designs have much thicker magnets, which increases both the effective air gap and the impact of the escaping flux, and lower pole pair counts, which leads to longer flux paths and more axially escaping leakage flux [35]. Finally, the stack length has a much stronger influence on the impact of end-effects than the outer radius (assuming that the other parameters, such as pole counts are optimized independently for each radius).



**Figure 3.15** Variation of maximum VTD (a) at a 50 mm outer radius and (b) at a 200 mm outer radius with stack length for radial flux gears at different  $G_{Int}$  values (based on 2D and 3D FEA).



**Figure 3.16** Variation of maximum GTD (a) at a 50 mm outer radius and (b) at a 200 mm outer radius with stack length for radial flux gears at different  $G_{Int}$  values (based on 2D and 3D FEA).

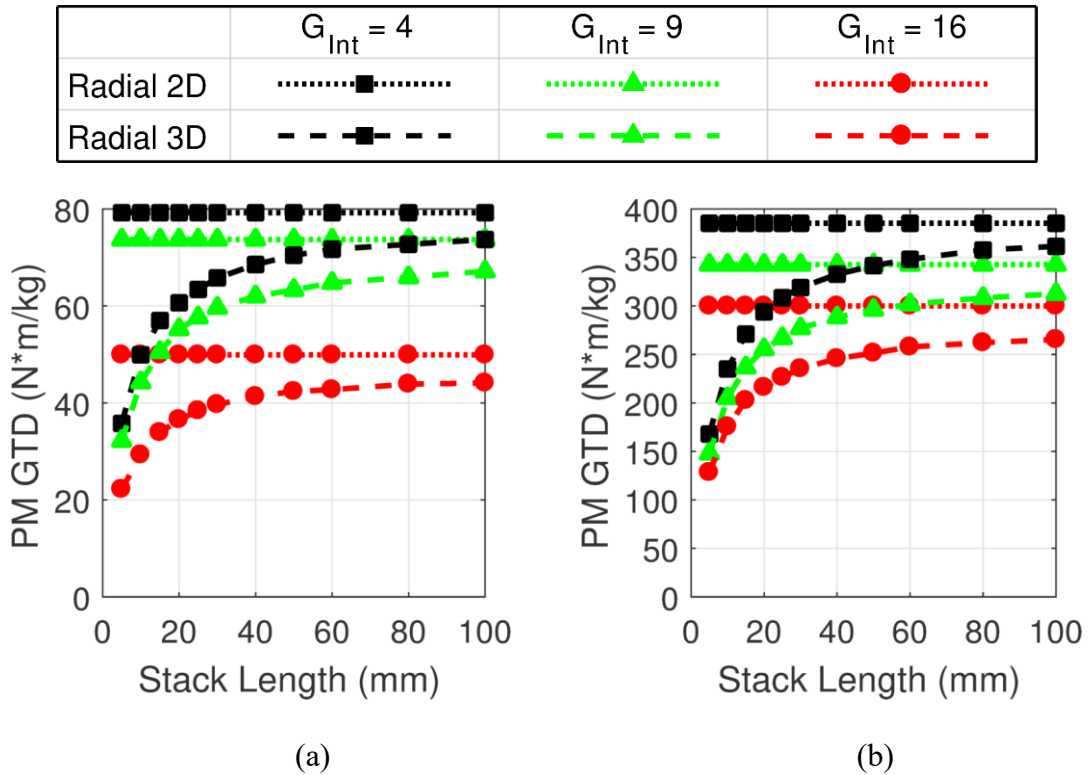


**Figure 3.17** Variation of maximum PM GTD (a) at a 50 mm outer radius and (b) at a 200 mm outer radius with stack length for radial flux gears at different  $G_{Int}$  values (based on 2D and 3D FEA).

The impact of the radii ratio on an axial flux gear's performance, which is depicted in Figure 3.18, Figure 3.19, and Figure 3.20, is more complex than the impact of the stack length on a radial flux gear's performance. Figure 3.18, Figure 3.19, and Figure 3.20 illustrate that relatively low radii ratios produce higher VTDs, whereas relatively high radii ratios produce higher GTDs and PM GTDs, especially at larger outer radii.

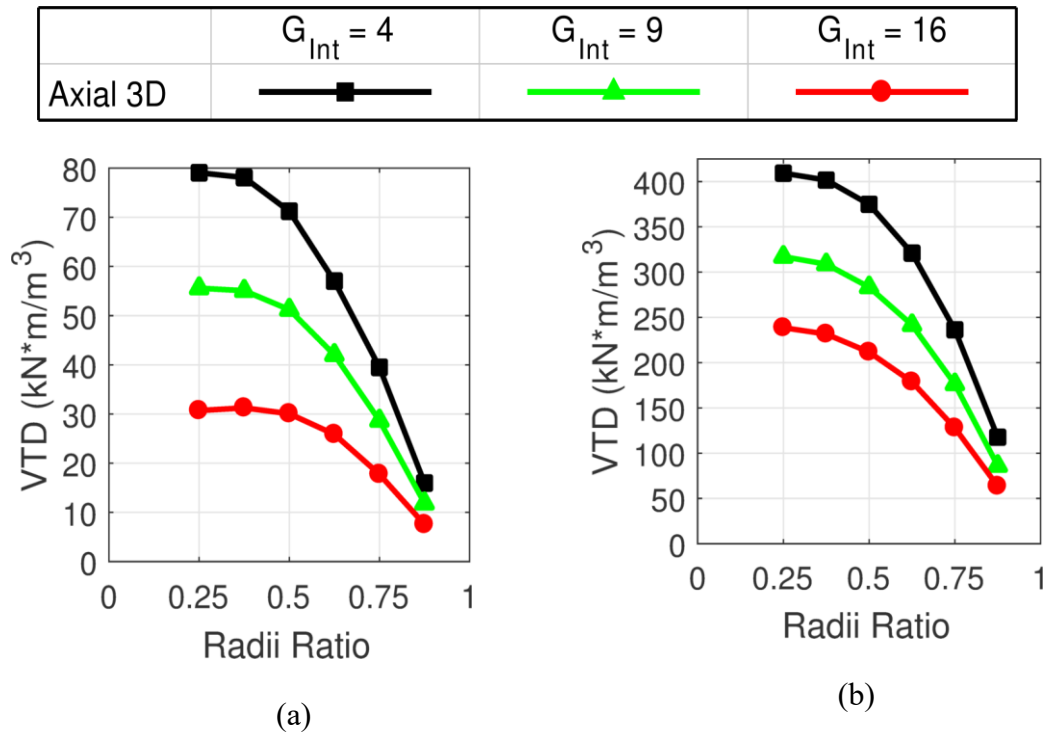


**Figure 3.18** Variation of maximum VTD (a) at a 50 mm outer radius and (b) at a 200 mm outer radius with radii ratio for axial flux gears at different  $G_{Int}$  values.

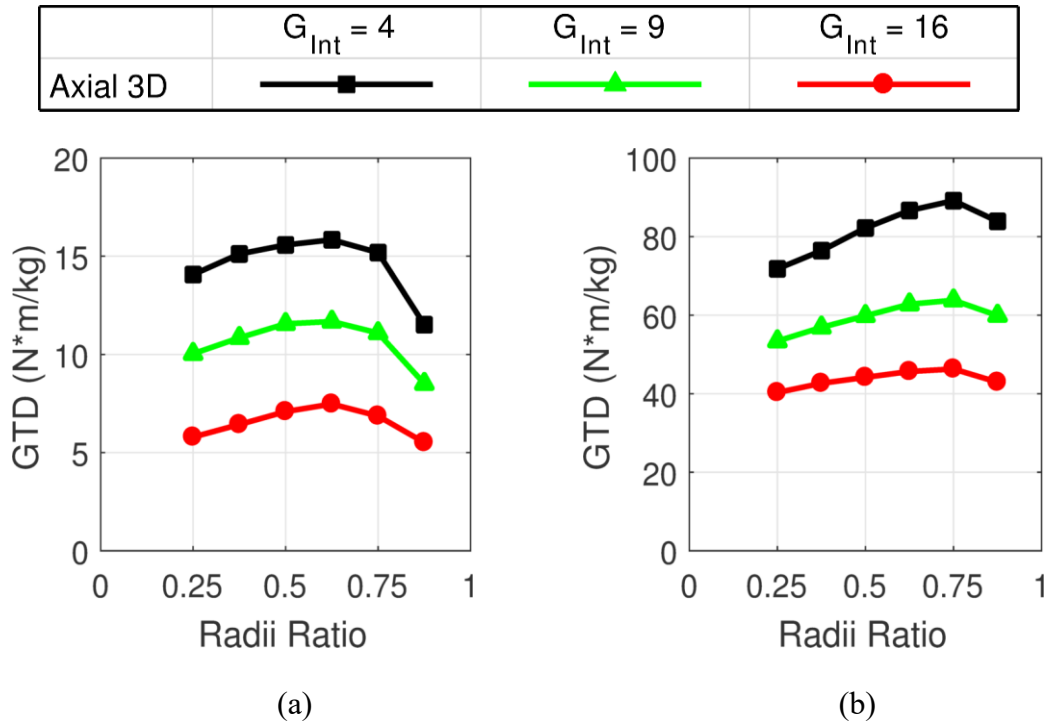


**Figure 3.19** Variation of maximum GTD (a) at a 50 mm outer radius and (b) at a 200 mm outer radius with radii ratio for axial flux gears at different  $G_{Int}$  values.



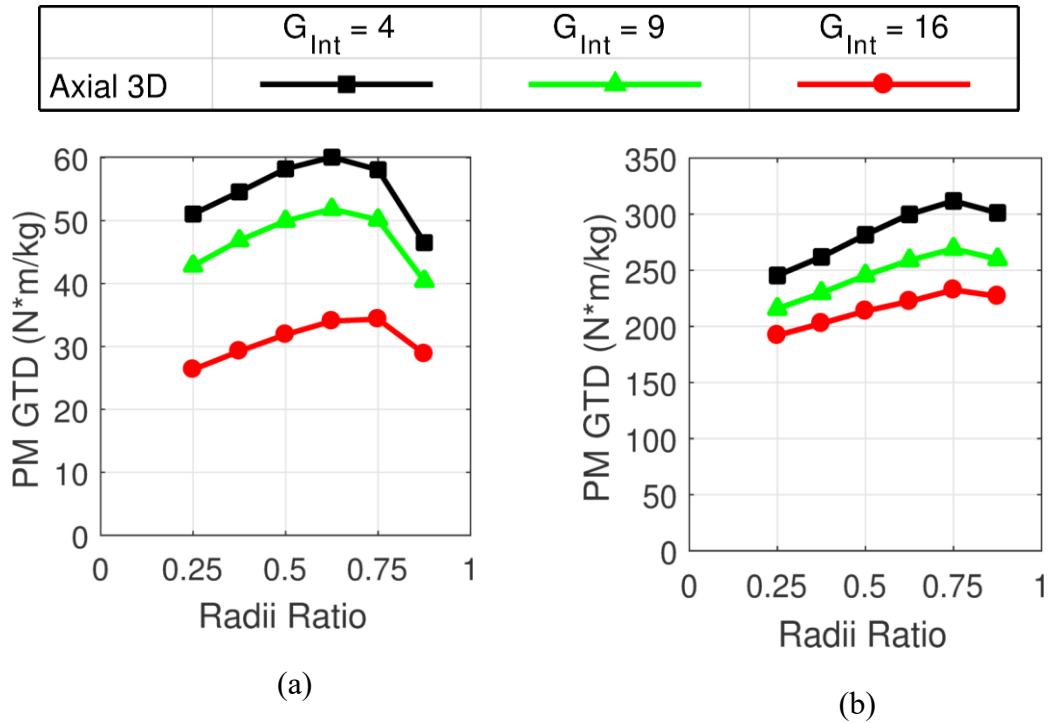
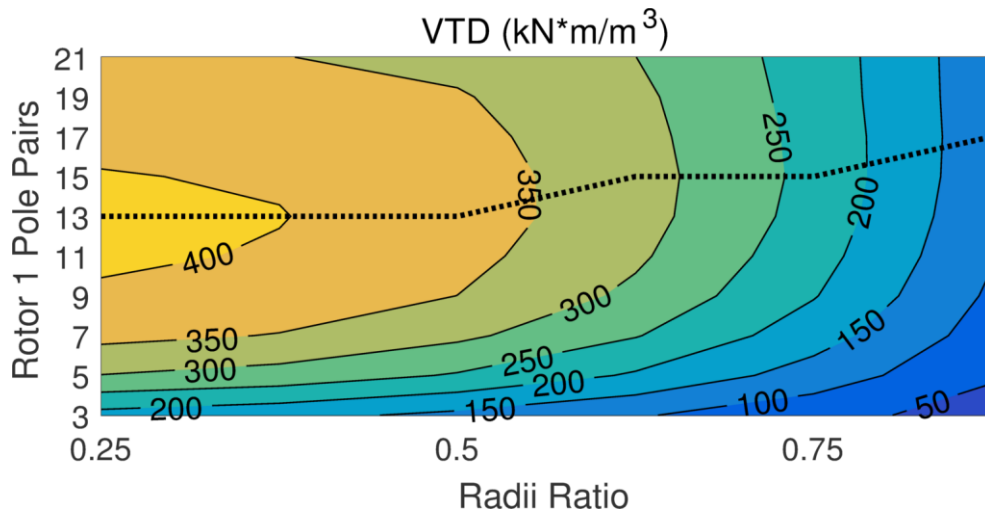


**Figure 3.20** Variation of maximum PM GTD (a) at a 50 mm outer radius and (b) at a 200 mm outer radius with radii ratio for axial flux gears at different  $G_{Int}$  values.

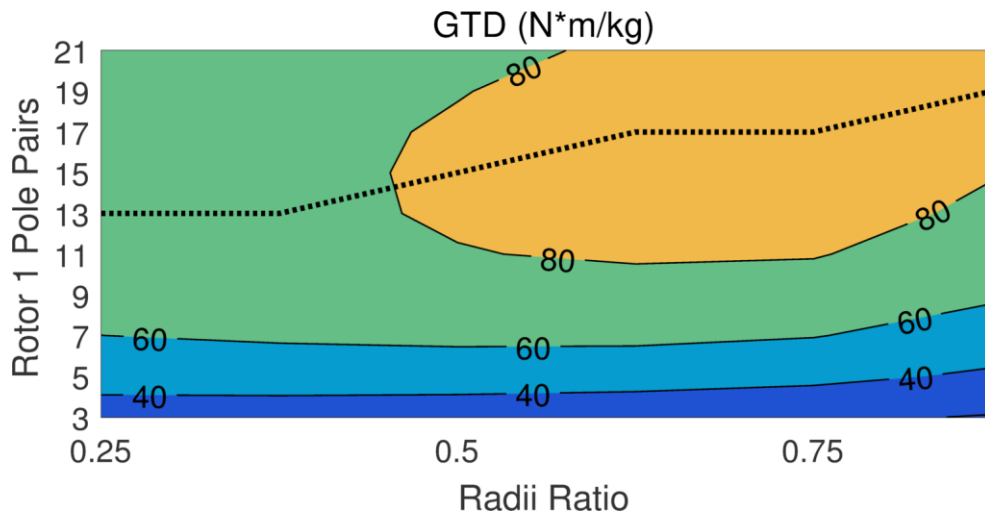
Reducing the radii ratio increases the portion of the total volume of the gear that is being used to produce torque. However, Figure 3.18 shows that the VTD returns diminish as the radii ratio is reduced. There are a few reasons for this. First, as the radii ratio is reduced, the increase in the active air gap area diminishes, because the new active material is added at a diminishingly smaller radius (assuming a fixed outer radius). Additionally, because the added material is placed at a lower radius, it has a smaller lever arm. Finally, a single  $P_1$  value is only optimal for a small range of radii. Thus, a single  $P_1$  value cannot be simultaneously optimal at the gear's outer and inner radii. As the radii ratio decreases, the degree of this sub-optimality increases. For these

reasons, the maximum GTD and PM GTD designs tend to have higher radii ratios to optimize the use of the active material. Nonetheless, the GTD and PM GTD are not simply maximized by raising the radii ratio to unity because the impact of end-effects (radial leakage flux) increases as the radii ratio increases and the active material becomes radially thinner. However, as illustrated by Figure 3.19 and Figure 3.20, the radii ratio that maximizes GTD and PM GTD increases slightly as the outer radius increases.

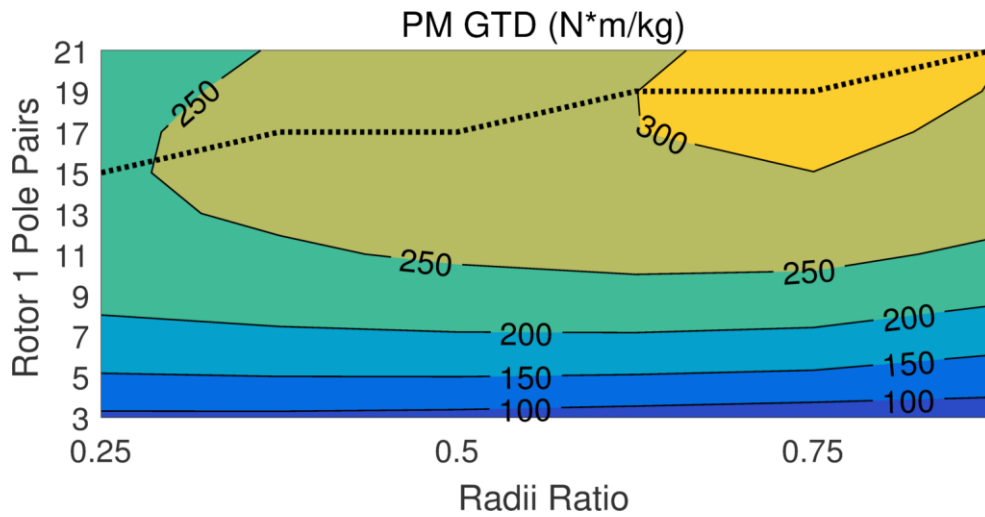
Changing the radial flux gear stack length scales the 2-D  $r$ - $\theta$  cross-section along the axial dimension. This has minimal impact on the optimal parameter values, except for a minor change in the optimal magnet thicknesses when optimizing for some metrics [51]. However, changing the axial flux gear radii ratio scales the 2-D  $\theta$ - $z$  cross-section along the radial dimension, which has a more significant impact on the optimal parameter values because it fundamentally impacts the flux path lengths. Figure 3.21, Figure 3.22, and Figure 3.23 illustrate the impact of the radii ratio on the optimal Rotor 1 pole pair counts (indicated by the dashed line) for axial flux designs with an outer radius of 200 mm and  $G_{\text{Int}} = 4$ . As indicated by Figure 3.21, Figure 3.22, and Figure 3.23, the optimal pole counts tend to decrease as the radii ratio decreases (for a fixed outer radius) because the effective average radius of the air gap decreases, which makes lower pole counts more optimal (as previously shown in Figure 3.4, Figure 3.5, and Figure 3.6). Similar trends are present for other outer radius and gear ratio combinations, but they are less pronounced because lower outer radii or higher gear ratios tend to already favor lower Rotor 1 pole pair counts.



**Figure 3.21** Variation of maximum VTD with radii ratio and Rotor 1 pole pair count for axial flux gears (with a 200 mm outer radius and  $G_{Int} = 4$ ). The dashed line indicates the optimal Rotor 1 pole pair count for each radii ratio.



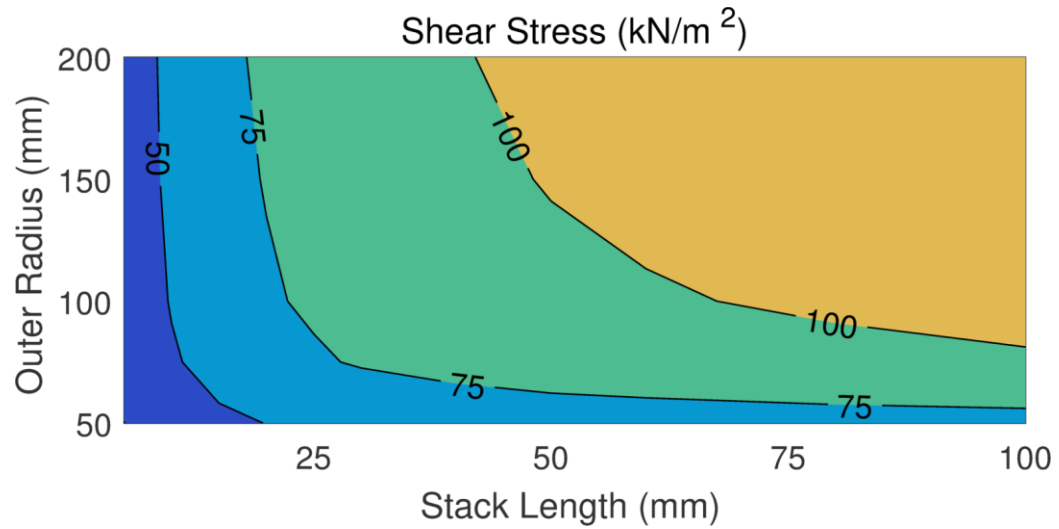
**Figure 3.22** Variation of maximum GTD with radii ratio and Rotor 1 pole pair count for axial flux gears (with a 200 mm outer radius and  $G_{Int} = 4$ ). The dashed line indicates the optimal Rotor 1 pole pair count for each radii ratio.



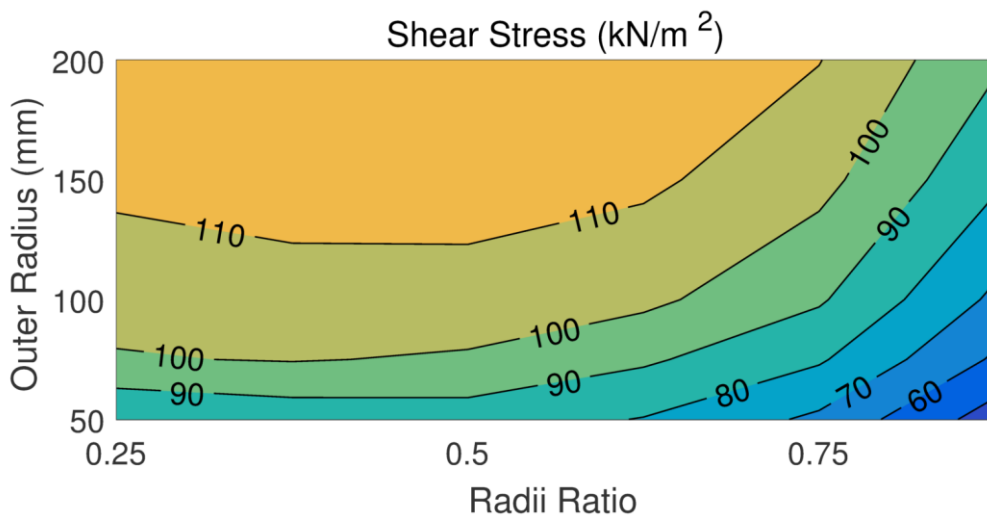
**Figure 3.23** Variation of maximum PM GTD with radii ratio and Rotor 1 pole pair count for axial flux gears (with a 200 mm outer radius and  $G_{\text{Int}} = 4$ ). The dashed line indicates the optimal Rotor 1 pole pair count for each radii ratio.

Figure 3.24 and Figure 3.25 illustrate the maximum average shear stress in the low speed air gaps for both radial and axial flux designs with  $G_{\text{Int}} = 4$ . Figure 3.24 shows that, for radial flux designs, shear stress increases with both stack length and outer radius. As the stack length increases, the impact of end-effects becomes less significant, resulting in higher average shear stress. The increase in shear stress with outer radius contributes to the sublinear increase in VTD with outer radius previously shown for radial flux gears in Figure 3.12. For axial flux gears, Figure 3.25 shows that shear stress increases with outer radius but is maximized at an intermediate radii ratio slightly below 0.5. If the radii ratio is too low, the best  $P_1$  value will be suboptimal for a significant portion of the air gap area, but, if the radii ratio is too high, the impact of end effects on the slip torque will be very significant. For both topologies, the shear stress tends to increase with the outer radius because, as previously noted, the designs can use more

optimal pole counts at higher outer radii. Figure 3.24 and Figure 3.25 also show that both topologies are able to achieve approximately the same shear stresses.



**Figure 3.24** Variation of maximum average low speed air gap shear stress for radial flux gears with  $G_{Int} = 4$ .



**Figure 3.25** Variation of maximum average low speed air gap shear stress for axial flux gears with  $G_{Int} = 4$ .

Figure 3.26 and Figure 3.27 show the Rotor 2 slip torques for the design points used to create Figure 3.24 and Figure 3.25, respectively. For both topologies, shear stress tends to increase with outer radius, but the Rotor 2 slip torque tends to increase even faster with outer radius. Thus, the achievable shear stress tends to increase as the torque rating increases, but with diminishing returns. For the radial flux gears, a similar trend is present as stack length increases. Thus, based on these figures, applications requiring larger torques will generally be able to achieve higher shear stresses, VTDs, GTDs, and PM GTDs than applications where the rated torque is much smaller.

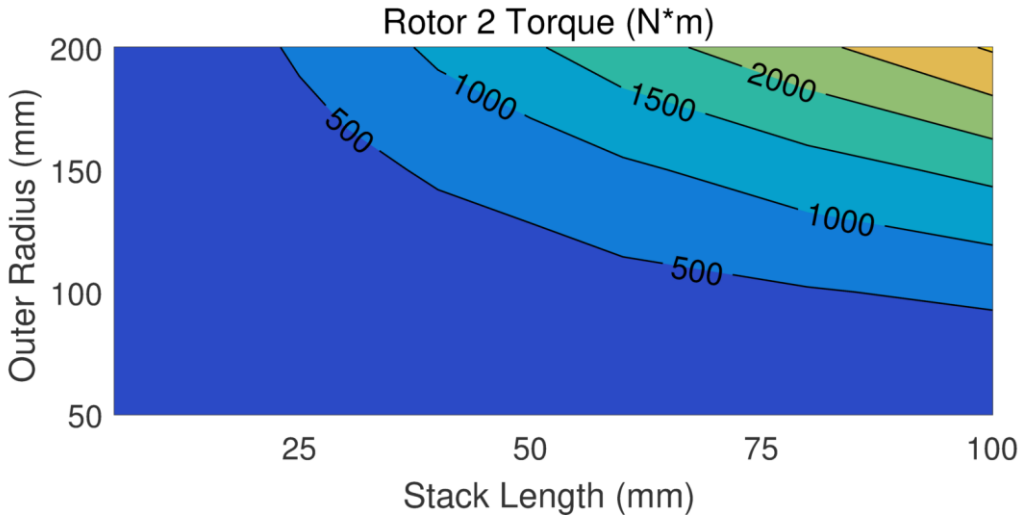


**Figure 3.26 Rotor 2 slip torques corresponding to the radial flux gear design points in Figure 3.24.**

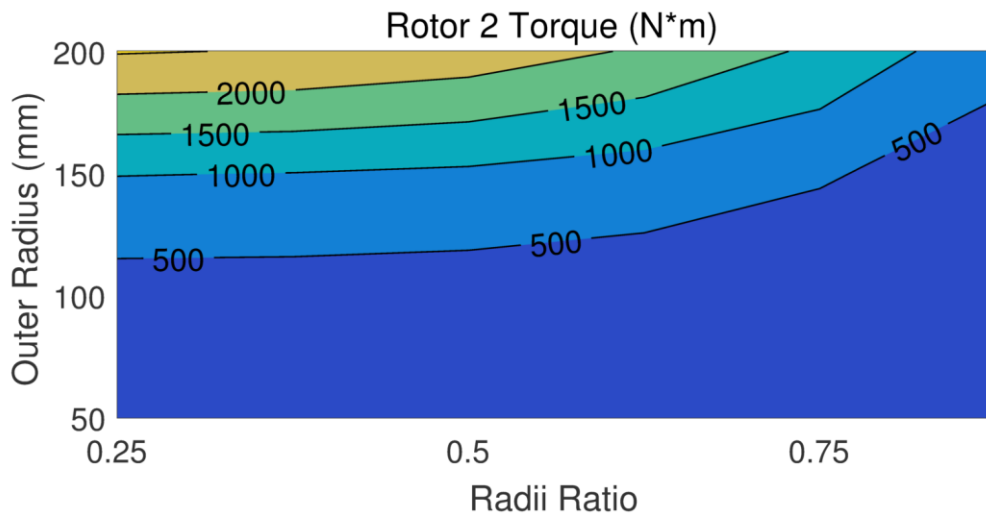


**Figure 3.27 Rotor 2 slip torques corresponding to the axial flux gear design points in Figure 3.25.**

Another major difference between radial flux and axial flux gears is the magnetic forces upon the rotors. While symmetry can ideally be used to cancel out the net radial magnetic forces on a radial flux gear rotor, each rotor in an axial flux gear will still experience unbalanced net axial magnetic forces. Figure 3.28 and Figure 3.29 illustrate the corresponding axial magnetic forces on Rotor 1 and Rotor 3 for each of the axial flux gear design points used to create Figure 3.25. The axial magnetic forces shown in Figure 3.28 and Figure 3.29 are those at the slip torque points (orientations). While the slip torque points are not necessarily the maximum axial force points, they do give an indication of the axial forces experienced by the rotors in the different designs [28]. A comparison of Figure 3.27, Figure 3.28, and Figure 3.29 indicates that the designs with higher torques generally experience larger axial forces. However, the axial forces grow faster than the slip torque as the radii ratio decreases because, unlike the slip torque, the

axial force created by a differential area of the air gap is independent of the lever arm of that differential area. Thus, the same slip torque can often be achieved with smaller axial forces by increasing both the outer radius and the radii ratio. While not shown in Figure 3.28 and Figure 3.29, the net axial force on Rotor 2 in a given design is simply the difference between the axial forces on Rotor 1 and Rotor 3 (in accordance with Newton’s third law). This means that the net axial force on Rotor 2 is generally much smaller than the net axial forces on Rotor 1 and Rotor 3.

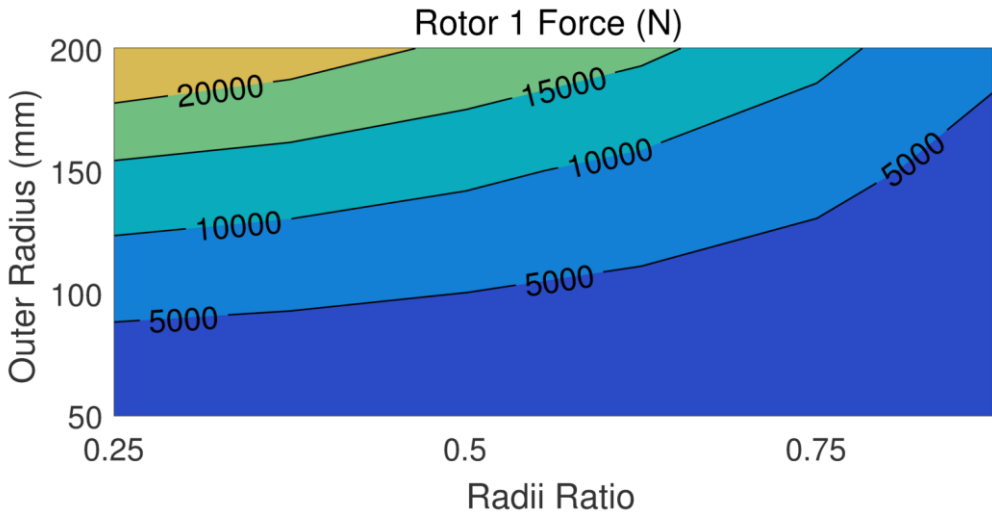


**Figure 3.28 Rotor 1 axial magnetic forces corresponding to the slip torque alignments of the axial flux gear design points in Figure 3.25.**



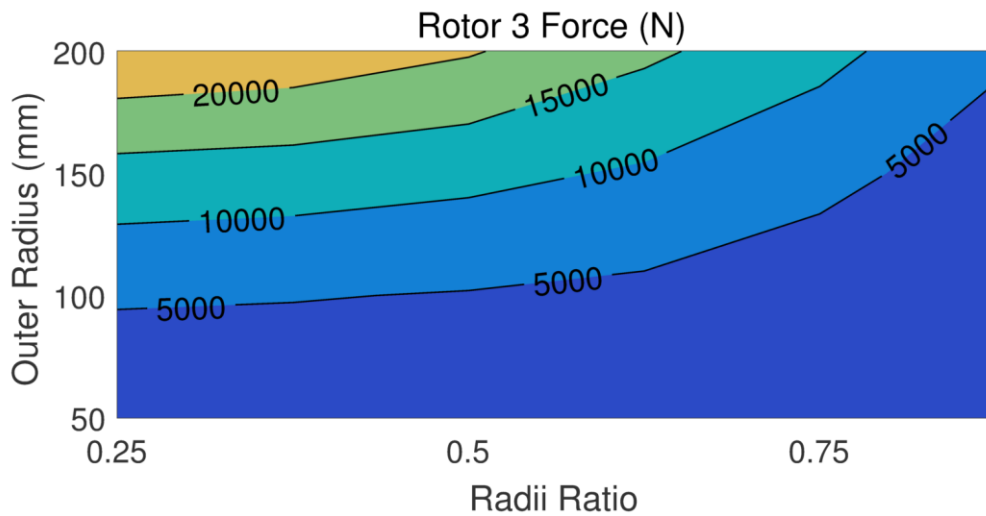


**Figure 3.29 Rotor 3 axial magnetic forces corresponding to the slip torque alignments of the axial flux gear design points in Figure 3.25.**

### 3.3. Conclusion

Radial flux and axial flux coaxial magnetic gears both provide gearing action without mechanical contact between rotors. Additionally, there are some significant similarities between their performances. Both topologies achieve higher VTDs, GTDs, and PM GTDs at higher torques and lower gear ratios (within the range of gear ratios evaluated). Also, the two topologies can achieve similar air gap shear stresses. However, there are some key performance differences.

First, while the achievable VTDs of both topologies tend to increase with outer radius, the achievable VTDs of axial flux gears grow faster than those of radial flux gears. Thus, the axial flux gear favors large outer radii with small axial lengths. However, the GTDs and PM GTDs of the two topologies tend to increase at similar rates as the outer radius increases.

Furthermore, the impact of end-effects on the two topologies is different. For radial flux gears, the axial end-effects become less significant as the stack length increases, which raises VTD, GTD, and PM GTD, as well as torque. For axial flux gears, shear stress is maximized with an intermediate radii ratio, but VTD is maximized with a lower radii ratio. On the other hand, GTD and PM GTD are maximized at a higher radii ratio.

Finally, whereas the net radial magnetic forces on each rotor of a radial flux gear can ideally be eliminated, the net axial forces on the rotors of an axial flux gear cannot be eliminated. This presents a significant challenge for the construction of axial flux gears.

While the conclusions presented above will generally hold true, it is important to recognize that the exact numbers and the extent of the trends presented in this study depend on the assumptions made in setting up these simulations, as is the case for all design studies. First, all of the results presented in this study are based on the assumption of consistent 1 mm air gaps for both the axial flux and radial flux gears. In practice, the unbalanced axial forces on the rotors in axial flux gears may necessitate the use of larger air gaps in this topology, which would shift the results in favor of radial flux gears. On the other hand, radial flux gears may require a larger effective inner air gap to accommodate a retention sleeve for the Rotor 1 PMs, especially if the gear is designed for high Rotor 1 speeds. However, to retain the Rotor 1 PMs in axial flux gears, a ring or lip can be placed radially beyond these PMs, which does not contribute to the effective air gap. Furthermore, this study maintained a constant air gap size (1

mm) regardless of other design settings. In practice, the air gap will likely need to increase as the outer radius increases, which would reduce (but not eliminate) the VTD and PM GTD gains achieved by going to a larger outer radius. The exact scaling of this air gap increase will depend on design specific mechanical and manufacturing considerations. Additionally, the simulation models employed in this study used a soft magnetic composite for the modulators in both topologies, and switching to traditional laminated steel modulators could slightly raise the torque ratings of the best designs due to its higher saturation flux density. However, while laminated steel modulators are perfectly feasible for radial flux gears, they are less practical for axial flux gears. Thus, if axial flux gears are constructed using soft magnetic composite modulators and radial flux gears are constructed using laminated steel modulators, this would also shift the findings a little further in favor of radial flux gears. Even if these factors are not considered, based on the results of this study, radial flux gears will likely be superior to axial flux gears in most applications due to their simpler construction and higher performance at most physical form factors. However, axial flux gears have a significant potential advantage in applications where a large outer radius and a small axial length are permissible or where mechanical power needs to be transmitted across a flat barrier.

#### 4. COMPARISON OF SURFACE PERMANENT MAGNET COAXIAL AND CYCLOIDAL RADIAL FLUX MAGNETIC GEARS\*

The previous section compared axial flux and radial flux coaxial magnetic gears. However, another promising magnetic gear topology is the cycloidal magnetic gear, the radial flux version of which is illustrated in Figure 1.5(a). Cycloidal magnetic gears have been the subject of a few studies, which tout their ability to achieve high torque densities and high gear ratios [19], [20], [21], [54].

For this section, the modulators are used as the low speed rotor of the coaxial magnetic gear and Rotor 3 is fixed, which yields the gear ratio in (6). For the cycloidal magnetic gear, the rotation of the inner rotor about its own axis is connected to the low speed shaft, and the outer rotor is fixed, which yields the gear ratio in (8). A comparison of these gear ratios suggests that it is generally more practical to achieve a higher gear ratio with the cycloidal gear than with the coaxial gear because there are practical limitations to the maximum number of modulators or poles that can be used on a rotor. While relatively high gear ratios can be achieved by using coaxial magnetic gears with  $P_{in} = 1$ , this generally results in relatively high torque ripple [3]. Additionally, a few papers state that cycloidal magnetic gears can achieve higher torque densities than coaxial magnetic gears [19], [20], [21]. Furthermore, one paper also claims that

---

© 2018 IEEE. Part of this section is reprinted with permission from M. C. Gardner, M. Johnson, and H. A. Toliyat, "Comparison of Surface Permanent Magnet Coaxial and Cycloidal Radial Flux Magnetic Gears," in *Proc. IEEE Energy Convers. Congr. and Expo*, 2018, pp. 5005-5012.

cycloidal magnetic gears can achieve better magnet utilization than coaxial magnetic gears [19].

While these foundational cycloidal magnetic gear studies do an excellent job of introducing the cycloidal magnetic gear topology, explaining its operating principle, demonstrating its potential for high torque densities at high gear ratios, and even describing working prototypes, their comparisons of coaxial and cycloidal magnetic gears' torque density capabilities are based on theoretical observations and anecdotal comparisons of individual designs or extremely limited optimizations, rather than thorough numerical comparisons of the topologies [19], [20], [21], [54]. As an example, [19] describes an un-optimized radial flux cycloidal magnetic gear prototype design constructed using the same number of outer rotor pole pairs and approximately the same air gap radius as the un-optimized coaxial magnetic gear described in [33]. While the cycloidal magnetic gear design in [19] achieves approximately double the torque density of the coaxial gear design in [33], this comparison is of limited value without some measure of the relative optimality of the two designs, especially since they use the same outer rotor pole pair count, which is unlikely to be equally optimal for both of the different topologies. If one design is very sub-optimal while the other is nearly optimal, this can bias the comparison heavily in favor of the more optimal design. Furthermore, [19] also describes a very limited cycloidal magnetic gear optimization study using an analytical model which achieves a volumetric torque density of  $183 \text{ kN}\cdot\text{m}/\text{m}^3$  and states that this is almost twice the commonly cited typical radial flux coaxial magnetic gear volumetric torque density of  $100 \text{ kN}\cdot\text{m}/\text{m}^3$  provided in [17]. However, [19] only

considers a single pole pair combination for the cycloidal gear (pole pair counts are an extremely important design parameter, as demonstrated in this section), and multiple more recent studies have demonstrated that the radial flux coaxial magnetic can achieve significantly higher torque densities than the  $100 \text{ kN}\cdot\text{m}/\text{m}^3$  figure, depending on the design constraints [5], [30], [32], [51]. This section builds upon these studies, which clearly demonstrate the radial flux cycloidal magnetic gear's tremendous potential for high torque densities at high gear ratios, by providing the first extensive parametric 2D and 3D finite element analysis (FEA) design study comparing the optimum magnetic performance potentials of the radial flux versions of the two topologies to produce thorough quantitative assessments of their relative capabilities and characterizations of their respective design trends.

#### **4.1. Design Study Methodology**

The two primary metrics considered in this study are volumetric torque density (VTD) and PM gravimetric torque density (PM GTD), which normalize the low speed rotor torque in terms of the active volume and the permanent magnet mass, respectively. Thus, PM GTD provides a practical quantitative measure of each design's magnet utilization.

Both topologies were simulated using FEA. For both topologies, the back irons are made from M47 steel, and the PMs are made from NdFeB N42 with a remanence of 1.3 T. The modulators in the coaxial magnetic gear are also made from M47 steel. Table 4.1 shows the design parameter values considered for each of the two topologies, excluding the inner pole pair counts, and Table 4.2 and Table 4.3 show the inner pole

pair counts evaluated for the two topologies. The inner pole pair counts specified in Table 4.2 and Table 4.3 for the coaxial gear were selected to ensure that the optimal values for both VTD and PM GTD were always inside the range considered, since the outer radius, air gap size, and gear ratio can significantly affect these values. The same set of inner pole pair counts was always considered for the cycloidal designs, since the inner pole pair count directly determines a cycloidal design's gear ratio according to (8). This range also includes the optimal inner pole pair count with respect to both VTD and PM GTD for all evaluated cycloidal gear designs.

**Table 4.1 Coaxial and Cycloidal Gear Parameter Sweep Values.**

| <b>Parameter</b>  | <b>Coaxial</b>                   | <b>Cycloidal</b>           |
|---|----------------------------------|----------------------------|
| Integer part of gear ratio ( $G_{Int}$ )  | 4, 9, 16                         | N/A                        |
| Outer radius ( $R_{Out}$ )  | 50, 75, 100, 150 mm              |                            |
| Inner back iron thickness ( $T_{BI1}$ )   | 5, 10, 20 mm                     |                            |
| Outer back iron thickness ( $T_{BI3}$ )<br>For $T_{BI1} = 5$ mm<br>For $T_{BI1} = 10$ mm<br>For $T_{BI1} = 20$ mm | 5 mm<br>5, 10 mm<br>5, 10, 20 mm |                            |
| Inner PM thickness ( $T_{PM1}$ )  | 3, 6, 9, 12, 15 mm               |                            |
| PM thickness ratio ( $k_{PM}$ )   | 0.5, 0.625, 0.75                 | 0.5, 0.625, 0.75, 0.875, 1 |
| Minimum air gap thicknesses ( $T_{AG}$ )  | 1 mm, $R_{Out}/50$               |                            |
| Axis Offset ( $T_{Off}$ )   | N/A                              | 1, 2, 3, 4, 5, 7, 10 mm    |
| Modulator thickness ( $T_{Mods}$ )  | 10 mm                            | N/A                        |
| Stack Length ( $L_{Stack}$ )  | 5, 10, 20, 30, 50 mm             |                            |

**Table 4.2 Inner Pole Pair Count ( $P_1$ ) Values with  $T_{AG} = 1$  mm.**

| <b>R<sub>Out</sub><br/>(mm)</b> | <b>Coaxial<br/><math>G_{Int} = 4</math></b> | <b>Coaxial<br/><math>G_{Int} = 9</math></b> | <b>Coaxial<br/><math>G_{Int} = 16</math></b> | <b>Cycloidal</b> |
|---------------------------------|---|---|--|------------------|
| 50                              | 3, 5, 7                                     | 3, 5, 7                                     | 3, 5   | 5, 9, 13, ... 89 |
| 75                              | 3, 5, 7, 9                                  | 3, 5, 7                                     | 3, 5   | 5, 9, 13, ... 89 |
| 100                             | 3, 5, 7, ... 17                             | 3, 5, 7, 9, 11                              | 3, 5, 7                                      | 5, 9, 13, ... 89 |
| 150                             | 3, 5, 7, ... 21                             | 3, 5, 7, ... 13                             | 3, 5, 7, 9                                   | 5, 9, 13, ... 89 |

**Table 4.3 Inner Pole Pair Count ( $P_1$ ) Values with  $T_{AG} = R_{Out}/50$ .**

| <b>R<sub>Out</sub><br/>(mm)</b> | <b>Coaxial<br/><math>G_{Int} = 4</math></b> | <b>Coaxial<br/><math>G_{Int} = 9</math></b> | <b>Coaxial<br/><math>G_{Int} = 16</math></b> | <b>Cycloidal</b> |
|---------------------------------|---|---|--|------------------|
| 50                              | 3, 5, 7                                     | 3, 5, 7                                     | 3, 5   | 5, 9, 13, ... 89 |
| 75                              | 3, 5, 7, 9                                  | 3, 5, 7                                     | 3, 5   | 5, 9, 13, ... 89 |
| 100                             | 3, 5, 7, 9                                  | 3, 5, 7                                     | 3, 5   | 5, 9, 13, ... 89 |
| 150                             | 3, 5, 7, 9, 11                              | 3, 5, 7                                     | 3, 5   | 5, 9, 13, ... 89 |

A derived parameter,  $k_{PM}$ , is used to control the ratio between the PM thicknesses on the two rotors, as given by (17), where  $T_{PM3}$  is the outer magnet thickness for the cycloidal magnetic gears. The  $k_{PM}$  range given for the coaxial topology in Table 4.1 is based on the optimal values indicated by the studies in [32], [51]. For the coaxial gear,  $G_{Int}$  is a derived parameter which represents the integer part of the desired gear ratio and is used to maintain an approximately constant target gear ratio while varying the inner rotor pole count, as shown in (16). For the cycloidal gear, the outer pole pair count is determined according to (7). For each coaxial design, the inner and outer air gap each have the same thickness,  $T_{AG}$ . All possible combinations of the parameter values listed in Table 4.1, Table 4.2, and Table 4.3 were evaluated using 2D FEA, except for cases which would result in a negative inner radius. Based on the 2D FEA simulation results,

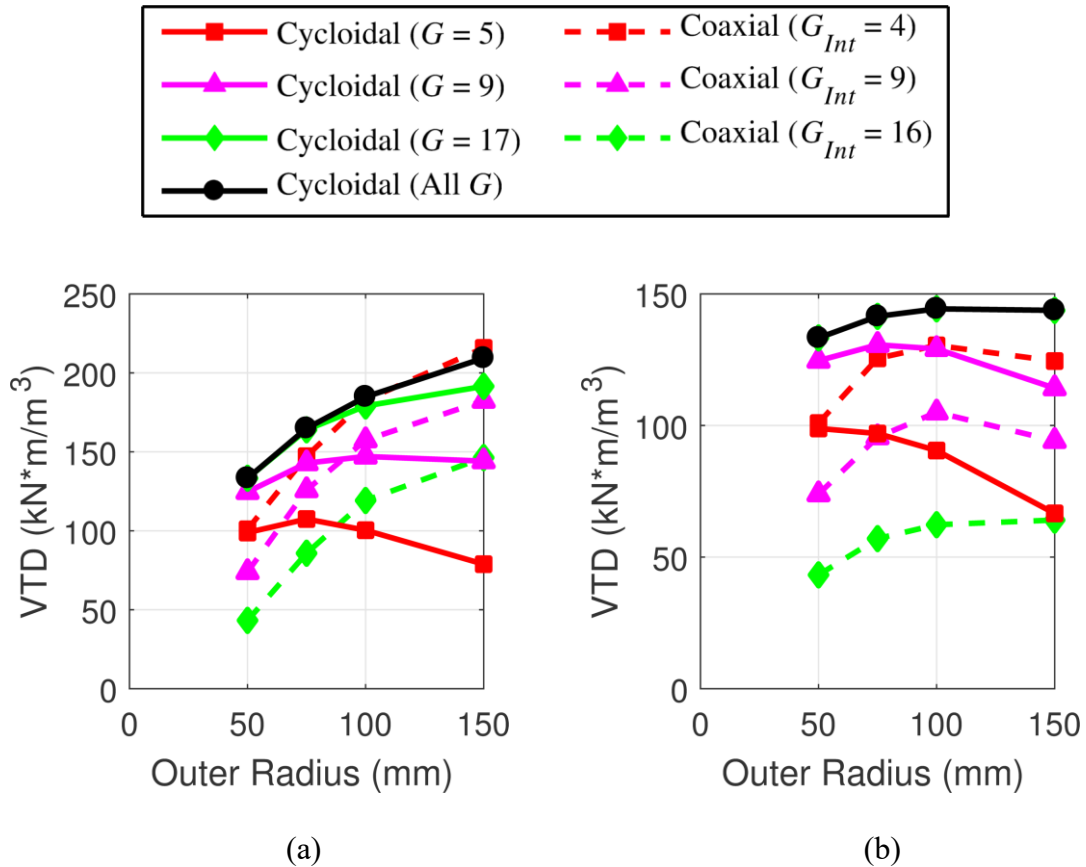


the best 906 coaxial designs and 6678 cycloidal designs were evaluated at each of the stack lengths specified in Table 4.1 using 3D FEA. The results presented in the rest of this section are based on 3D FEA for designs with stack lengths of 50 mm, except where specified otherwise.

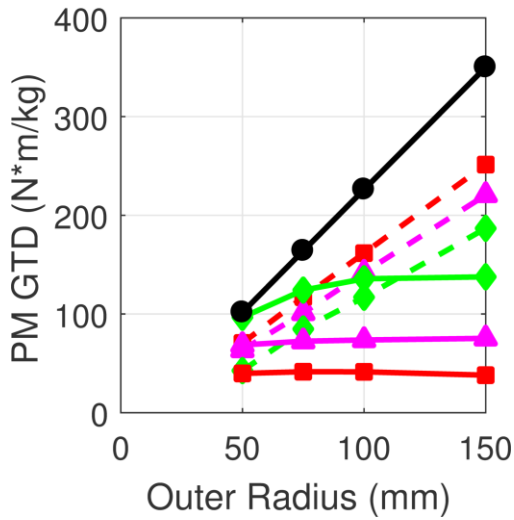
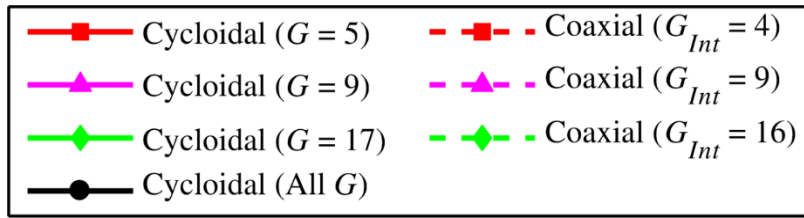
## 4.2. Results

Figure 4.1, Figure 4.2, and Figure 4.3 illustrate several design trends for the coaxial and cycloidal magnetic gears. Figure 4.1 and Figure 4.2 compare the maximum VTDs and PM GTDs that both topologies achieve at different outer radii, and Figure 4.3 shows the impacts of PM thickness. With a fixed air gap, the VTD and PM GTD both increase with the outer radius for both topologies (assuming that the cycloidal gear ratio is allowed to vary, as in the black curves in Figure 4.1, Figure 4.2, and Figure 4.3). However, when the air gap increases proportionally with the outer radius, both VTD and PM GTD vary much less with the outer radius for both topologies, but there is more variation for the cycloidal topology than for the coaxial topology, due in part to the fact that cycloidal gears only have a single air gap. Figure 4.1 and Figure 4.2 also illustrate that at lower gear ratios, optimal coaxial gears tend to achieve higher VTDs and PM GTDs than optimal cycloidal gears, and this advantage increases as the permissible outer radius increases. This is because a range of inner rotor pole pair counts can be used to achieve similar gear ratios for the coaxial gear, thus, providing the freedom to optimize this important design parameter, but a given inner rotor pole pair value directly determines a cycloidal design's gear ratio. However, the coaxial topology's achievable VTD and PM GTD tend to decrease significantly as the gear ratio is increased (due to

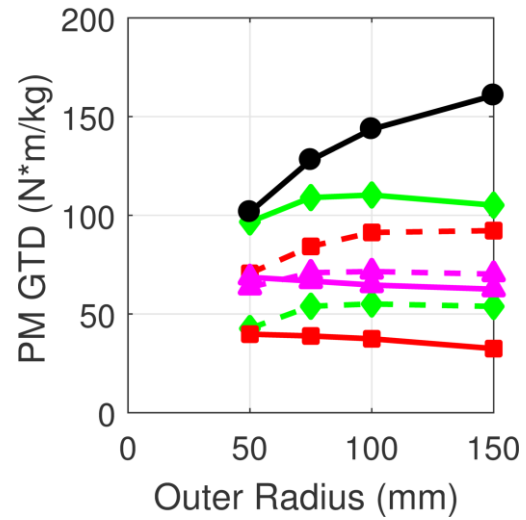
the increased discrepancy between the inner and outer rotor magnet pole counts and pole arcs). Accordingly, at medium to high gear ratios, unless the magnets are very thick and the air gaps relatively small, optimal coaxial designs tend to achieve lower VTDs and PM GTDs than optimal cycloidal designs. Furthermore, if any cycloidal gear ratio is permissible (corresponding to the black curves in Figure 4.1, Figure 4.2, and Figure 4.3), then the cycloidal topology can generally achieve higher torque densities than the coaxial topology at most design points in this study.



**Figure 4.1** Variation of the maximum VTD with outer radius for designs with (a)  $T_{AG} = 1$  mm and (b)  $T_{AG} = R_{Out}/50$ .

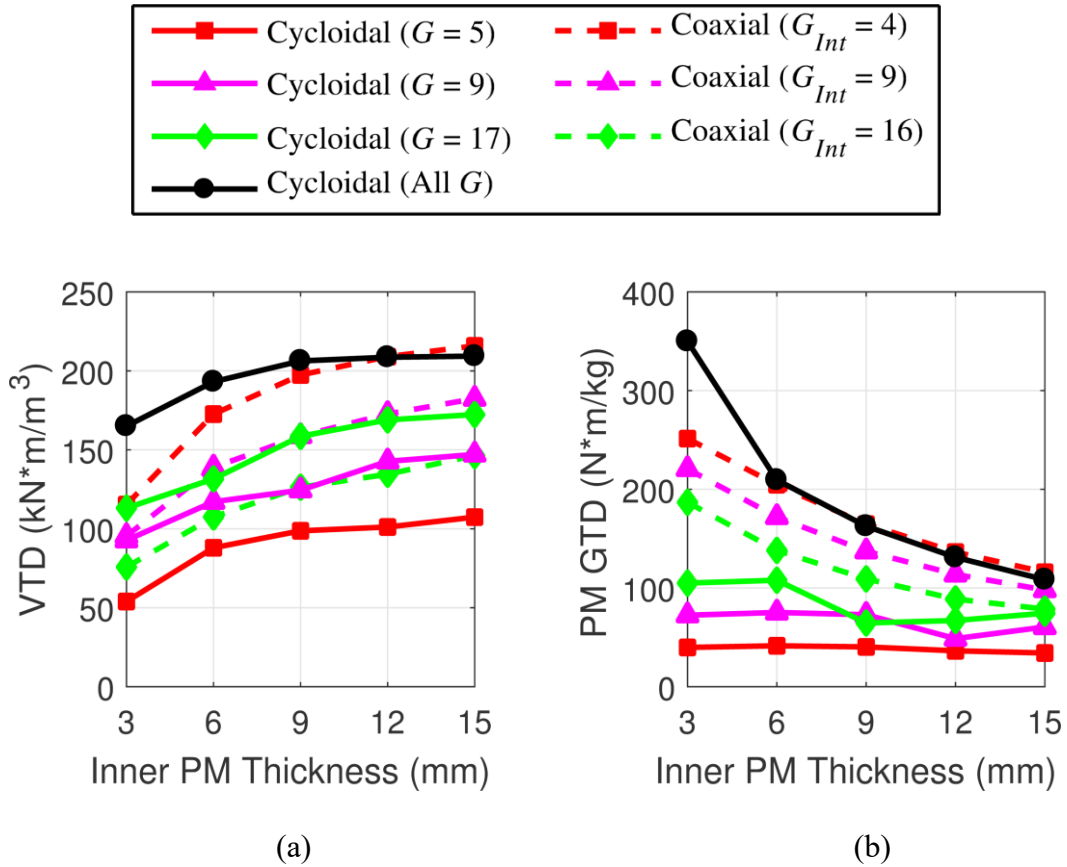


(a)



(b)

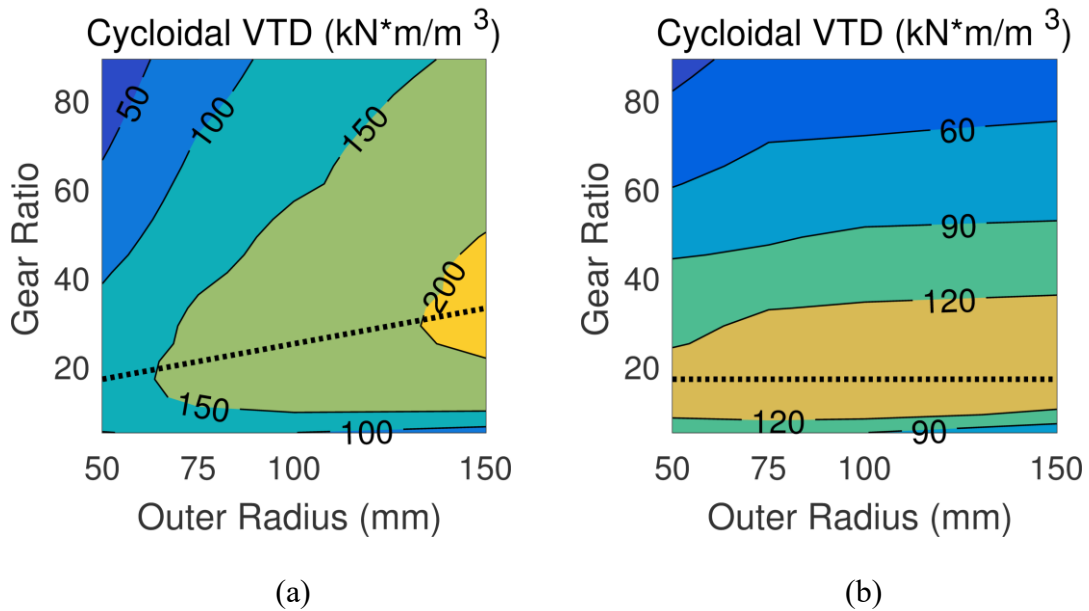
**Figure 4.2** Variation of the maximum PM GTD with outer radius for designs with (a)  $T_{AG} = 1$  mm and (b)  $T_{AG} = R_{Out}/50$ .



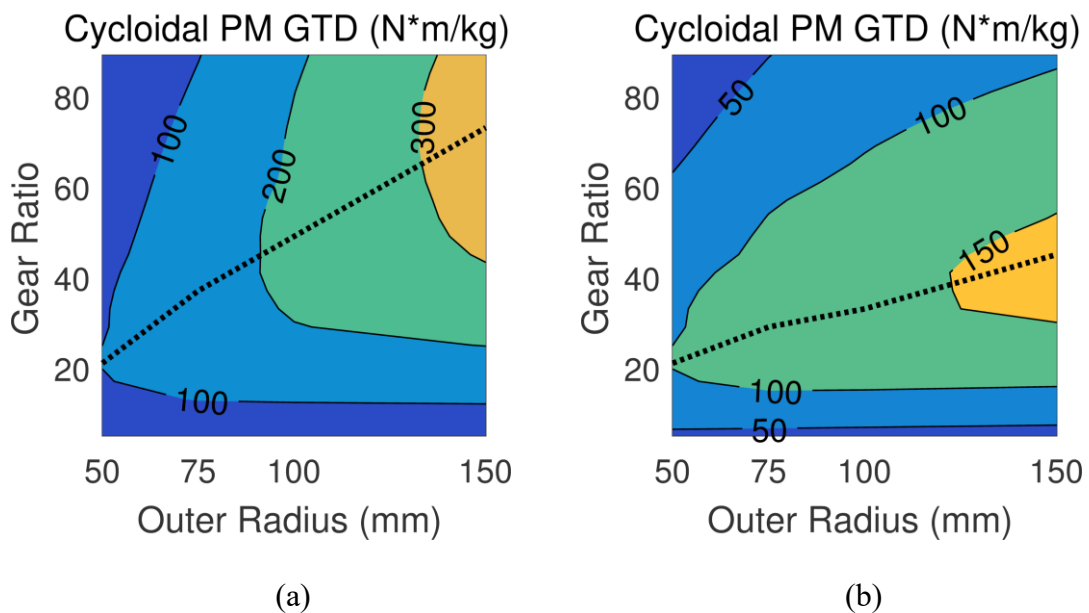
**Figure 4.3 Variation of the maximum (a) VTD and (b) PM GTD with the inner rotor PM thickness for designs with  $R_{Out} = 150$  mm and  $T_{AG} = 1$  mm.**

Figure 4.3 illustrates the impact of the inner rotor magnet thickness on VTD and PM GTD. For both topologies, within the evaluated range of thicknesses, VTD increases as the inner PM thickness is increased, whereas PM GTD decreases as the inner PM thickness is increased. However, as the PM thickness increases, the coaxial topology tends to benefit more in terms of VTD and suffer less in terms of PM GTD than the cycloidal topology.

For the coaxial topology, the optimal gear performance is generally achieved with a relatively low gear ratio [5]. However, for the cycloidal topology, the optimal gear ratio varies significantly based on the other design criterion. Figure 4.4 and Figure 4.5 illustrate how the optimal gear ratio changes with outer radius. The gear ratio for maximizing PM GTD is generally higher than the gear ratio for maximizing VTD. This is because maximum PM GTD designs favor thinner magnets (and, thus, smaller effective air gaps), which can tolerate higher pole counts and shorter pole arcs without suffering from reduced torque densities due to increased tangential leakage flux [5], [32], [51]. Additionally, the optimal gear ratio tends to increase with the outer radius but decrease as the air gap increases. This is because the increased air gap leads to increased leakage flux per pole, which can be counteracted by lower pole counts and longer pole arcs. Another important parameter that affects both the achievable performance and the optimal gear ratio of the cycloidal magnetic gear is the offset between the axes of the inner and outer rotors. As shown in Figure 4.6, the optimal gear ratio tends to decrease significantly as the axis offset increases. Again, this is partially because a larger axis offset leads to a larger average effective air gap, which leads to more leakage flux per pole if the pole arc lengths are not increased.



**Figure 4.4** Variation of the maximum VTD with outer radius and gear ratio for cycloidal designs with (a)  $T_{AG} = 1$  mm and (b)  $T_{AG} = R_{Out}/50$ . The dotted line indicates the gear ratio that maximizes VTD for each outer radius.



**Figure 4.5** Variation of the maximum PM GTD with outer radius and gear ratio for cycloidal designs with (a)  $T_{AG} = 1$  mm and (b)  $T_{AG} = R_{Out}/50$ . The dotted line indicates the gear ratio that maximizes PM GTD for each outer radius.

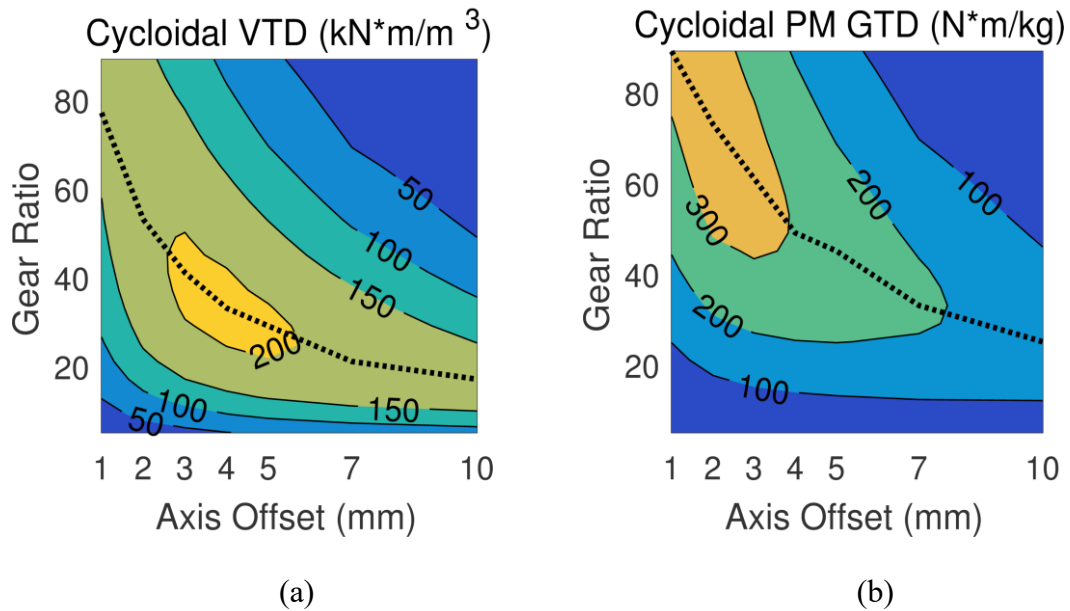


**Figure 4.6 Variation of the maximum (a) VTD and (b) PM GTD with axis offset and gear ratio for cycloidal designs with  $R_{Out}$  150 mm and  $T_{AG} = 1$  mm. The dotted line indicates the gear ratio that maximizes VTD or PM GTD for each axis offset.**

Another important factor that impacts magnetic gear performance is end-effects. Figure 4.7, Figure 4.8, Figure 4.9, and Figure 4.10 compare the maximum achievable VTDs and PM GTDs for designs with different stack lengths based on both 2D and 3D FEA. These figures show a greater discrepancy between 2D and 3D FEA for the coaxial designs than for the cycloidal designs, which means that the coaxial designs suffer more from end-effects, likely due to the phenomenon of escaping flux in coaxial magnetic gears, which is facilitated by the modulators [35], [51]. Additionally, the higher pole counts favored by cycloidal designs inherently lead to shorter flux paths and reduced end-effects, as demonstrated by the graphs in Figure 4.11 and Figure 4.12 which indicate that cycloidal designs suffer smaller torque reductions due to end-effects at higher gear

ratios (and, thus, higher pole counts). This difference in end-effects also means that the VTD and PM GTD advantages of the cycloidal topology over the coaxial topology will become more significant in applications requiring a smaller stack length, but these advantages will be reduced for applications requiring a larger stack length.

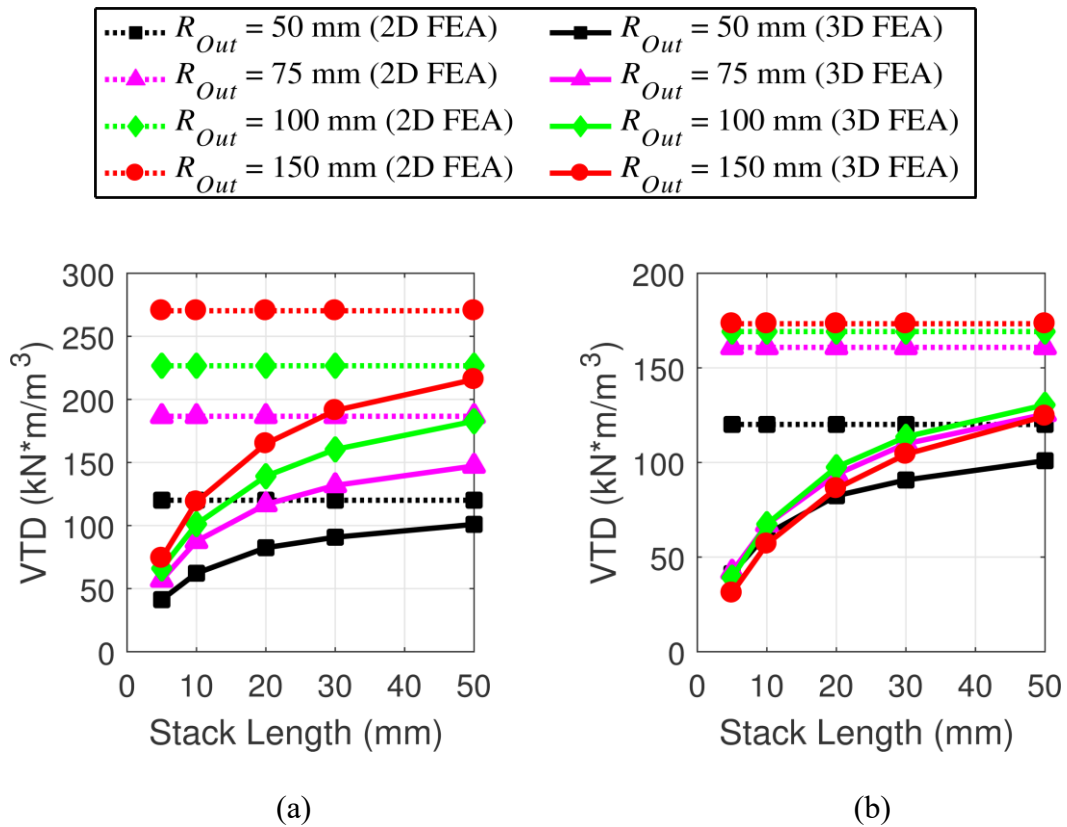


**Figure 4.7** Variation of the maximum VTD with the stack length for (a) coaxial designs with  $T_{AG} = 1$  mm and (b) coaxial designs with  $T_{AG} = R_{Out} / 50$  based on both 2D and 3D FEA.



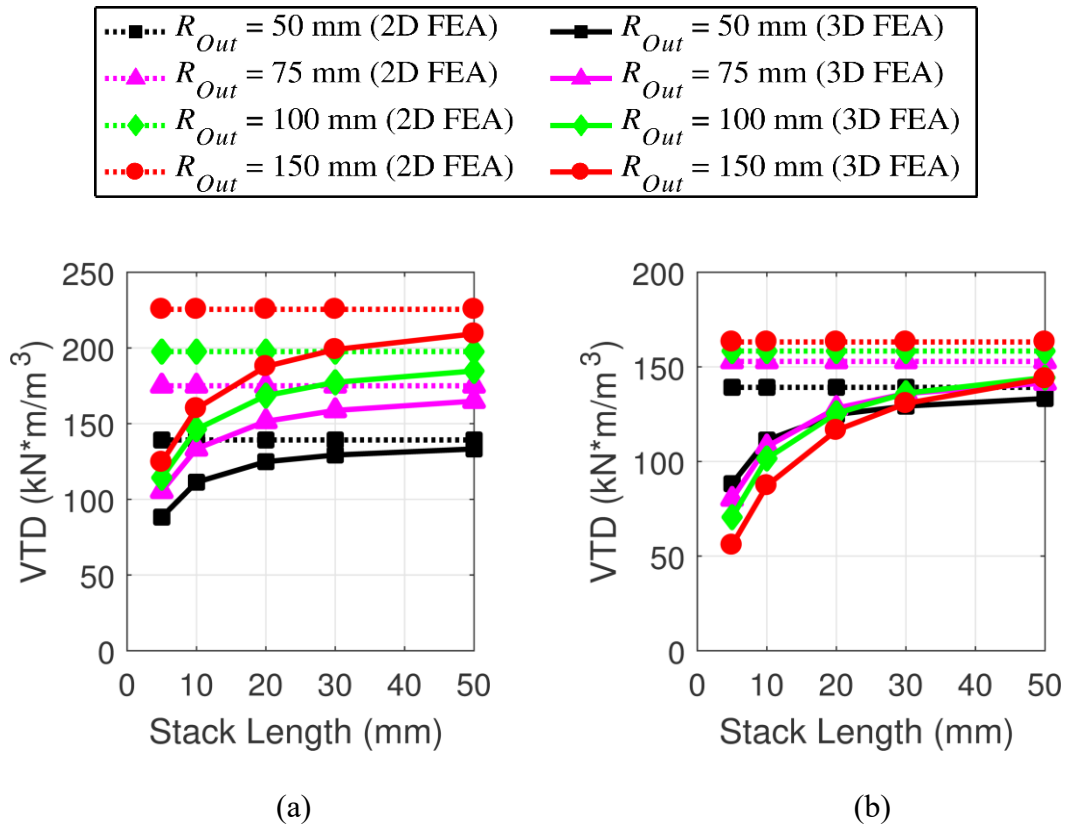
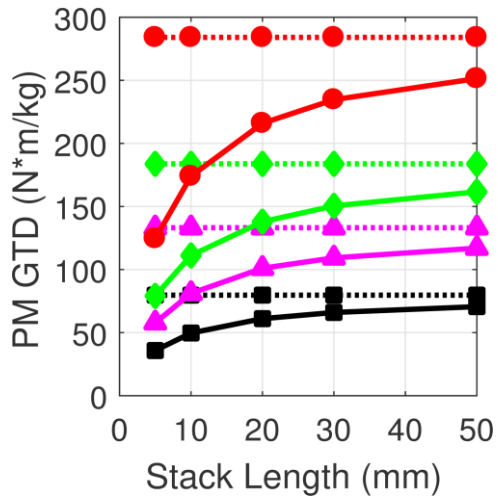
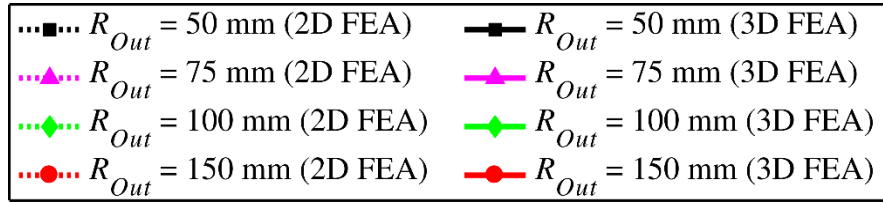
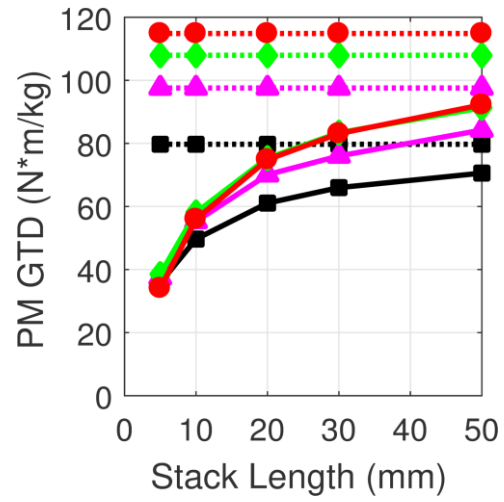


**Figure 4.8** Variation of the maximum VTD with the stack length for (a) cycloidal designs with  $T_{AG} = 1$  mm and (b) cycloidal designs with  $T_{AG} = R_{Out} / 50$  based on both 2D and 3D FEA.



(a)



(b)

**Figure 4.9** Variation of the maximum PM GTD with the stack length for (a) coaxial designs with  $T_{AG} = 1$  mm and (b) coaxial designs with  $T_{AG} = R_{Out} / 50$  based on both 2D and 3D FEA.

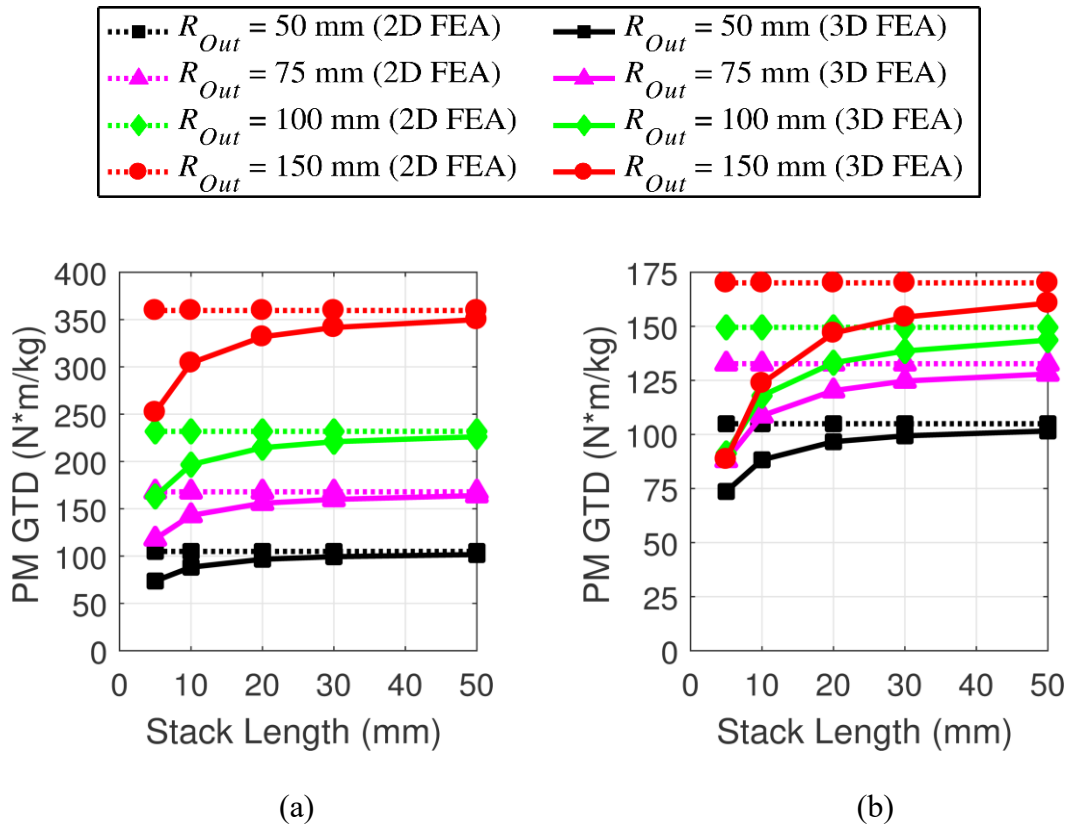
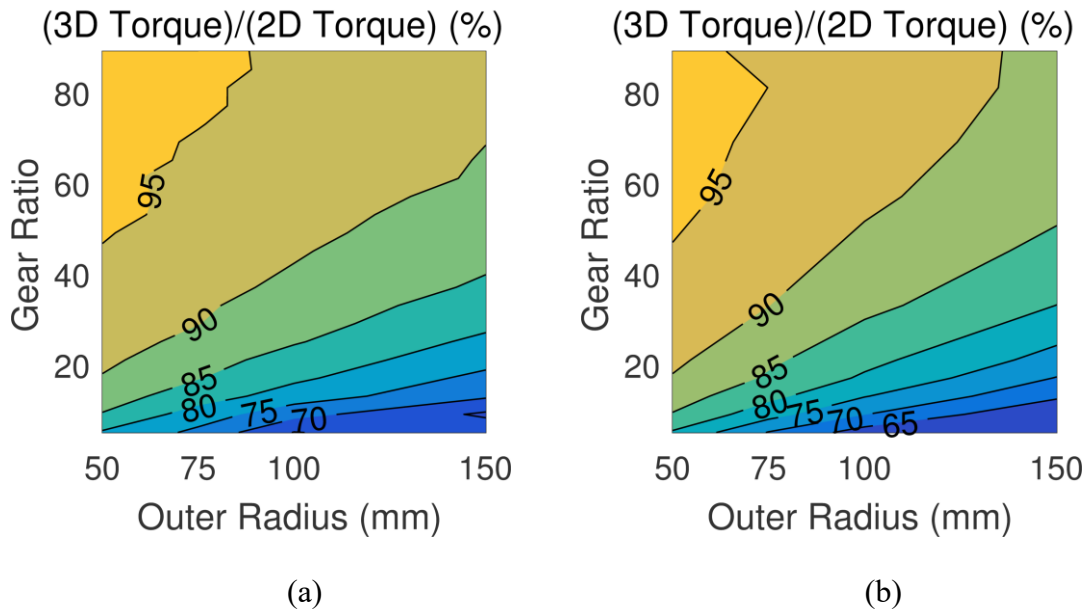
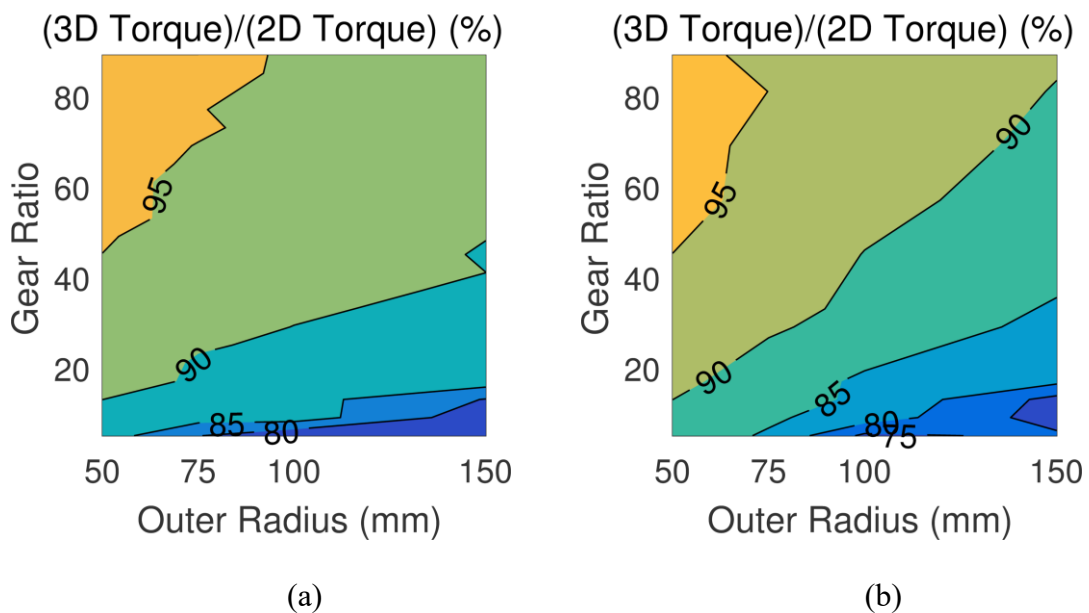


Figure 4.10 Variation of the maximum PM GTD with the stack length for (a) cycloidal designs with  $T_{AG} = 1$  mm and (b) cycloidal designs with  $T_{AG} = R_{Out} / 50$  based on both 2D and 3D FEA.



**Figure 4.11** Variation of 3D end-effects on the maximum VTD designs of Figure 4.4, but at a stack length of 20 mm, with outer radius and gear ratio for cycloidal designs with (a)  $T_{AG} = 1$  mm and (b)  $T_{AG} = R_{Out} / 50$ .



**Figure 4.12** Variation of 3D end-effects on the maximum PM GTD designs of Figure 4.5, but at a stack length of 20 mm, with outer radius and gear ratio for cycloidal designs with (a)  $T_{AG} = 1$  mm and (b)  $T_{AG} = R_{Out} / 50$ .

### 4.3. The Spatial Distribution of Torque Production

The previous section numerically illustrates differences in design trends between the two topologies. Some of these differences can be explained by considering an approximate analysis of the spatial distribution of torque production in the cycloidal topology. This analysis is based on a couple of simplifying assumptions, which make its implications more intuitive but prevent it from being used for exact analysis. First, only the fundamental harmonics from the PMs on the inner and outer rotors are considered, and other spatial magnetomotive force (mmf) harmonics are neglected. Second, the torque distribution at any angle,  $\theta$ , from the axis of the outer rotor is assumed to be proportional to the sine of the difference between the electromagnetic angles of the two rotors,  $k_\tau$ , as given by (23), where  $\theta_{EM1}$  and  $\theta_{EM2}$  are the electromagnetic angles of the inner and outer rotors at  $\theta = 0$ . Note that  $\theta'$  represents the angle from the axis of the inner rotor, which will be slightly different than  $\theta$  due to the cycloidal gear's axis offset. Figure 4.13 plots both  $k_\tau$  and the inverse effective air gap function,  $g^{-1}$ , as functions of  $\theta$  for an example cycloidal magnetic gear, and Figure 4.14 illustrates  $k_\tau$  as the color in the air gap of the example cycloidal magnetic gear. (Note that the thicknesses of the PMs on the two rotors are included in the effective air gap.)

$$k_\tau = \sin(P_{In} \cdot \theta' - P_{Out} \cdot \theta + \theta_{EM1} - \theta_{EM2}) \quad (23)$$

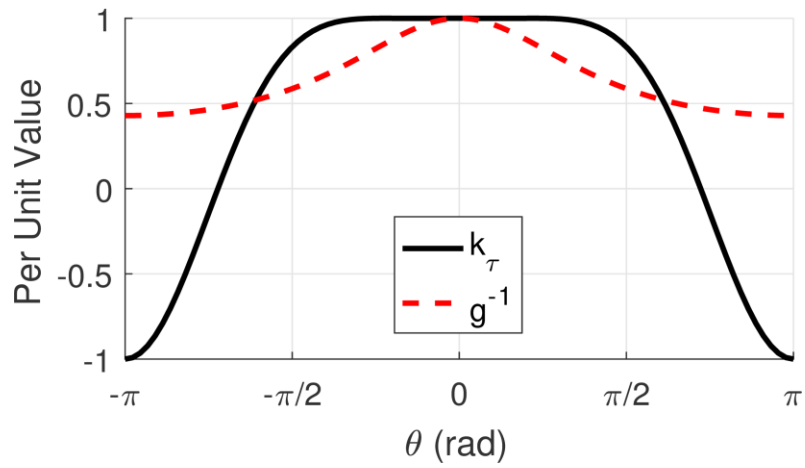


**Figure 4.13** Variation of  $k_\tau$  and the inverse effective air gap function (both in per unit values) with spatial position in an example cycloidal magnetic gear.

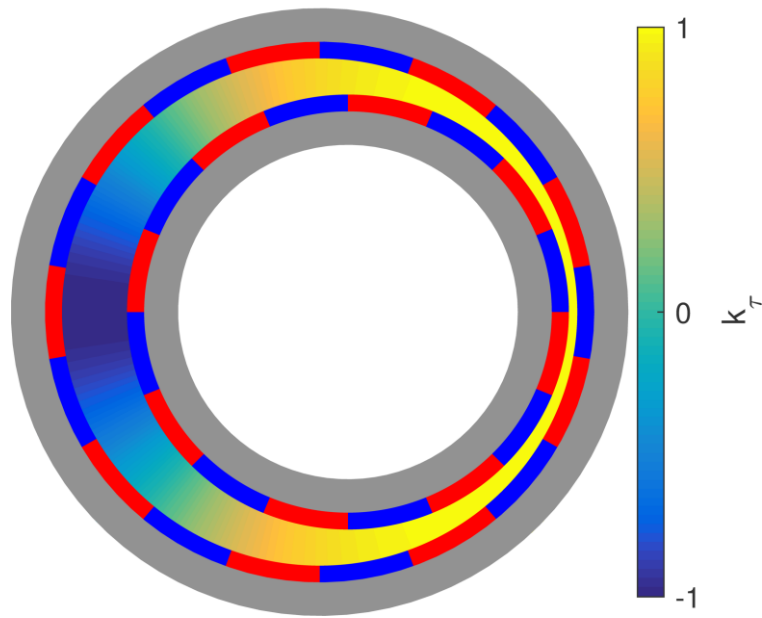


**Figure 4.14**  $k_\tau$  plotted as the color in the air gap of the same cycloidal magnetic gear from Figure 4.13.

When a cycloidal magnetic gear is at its maximum torque orientation, as shown in Figure 4.13 and Figure 4.14, positive torque is being produced in the area with the smallest air gap, and negative torque is being produced in the area with the largest air gap. Additionally, as illustrated by Figure 4.13 and Figure 4.14, the axis offset and the difference in pole counts result in positive torque being produced over a wider range of angles than the range of angles where negative torque is produced. Thus, significantly more positive torque is produced than negative torque. However, as the PM thicknesses increase, the effective air gap increases. To maintain the same ratio between the maximum and minimum values of the effective air gap, the axis offset must increase, as demonstrated in Figure 4.15. While increasing the axis offset reduces the negative torque produced in the region where  $k_\tau$  is negative, it also increases the air gap in much of the region where  $k_\tau$  is positive, which reduces the positive torque produced. On the other hand, in the coaxial magnetic gear, the modulators allow discrete steps in the effective air gap function. This contrast explains why increasing the PM thickness is more beneficial to the coaxial topology in terms of VTD and less detrimental to the coaxial topology in terms of PM GTD.

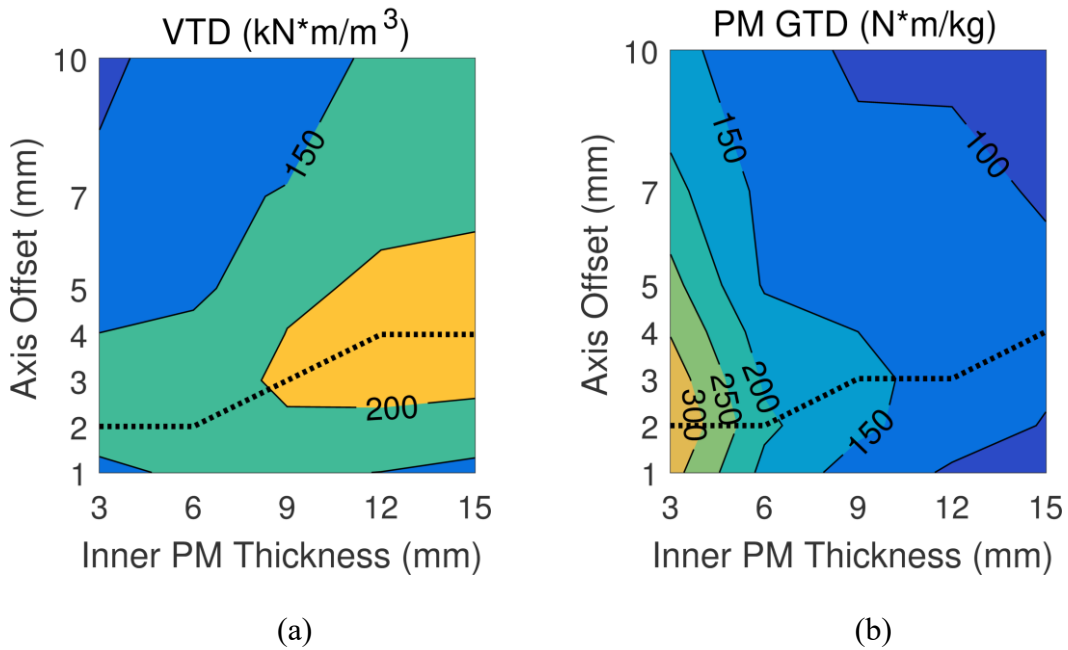


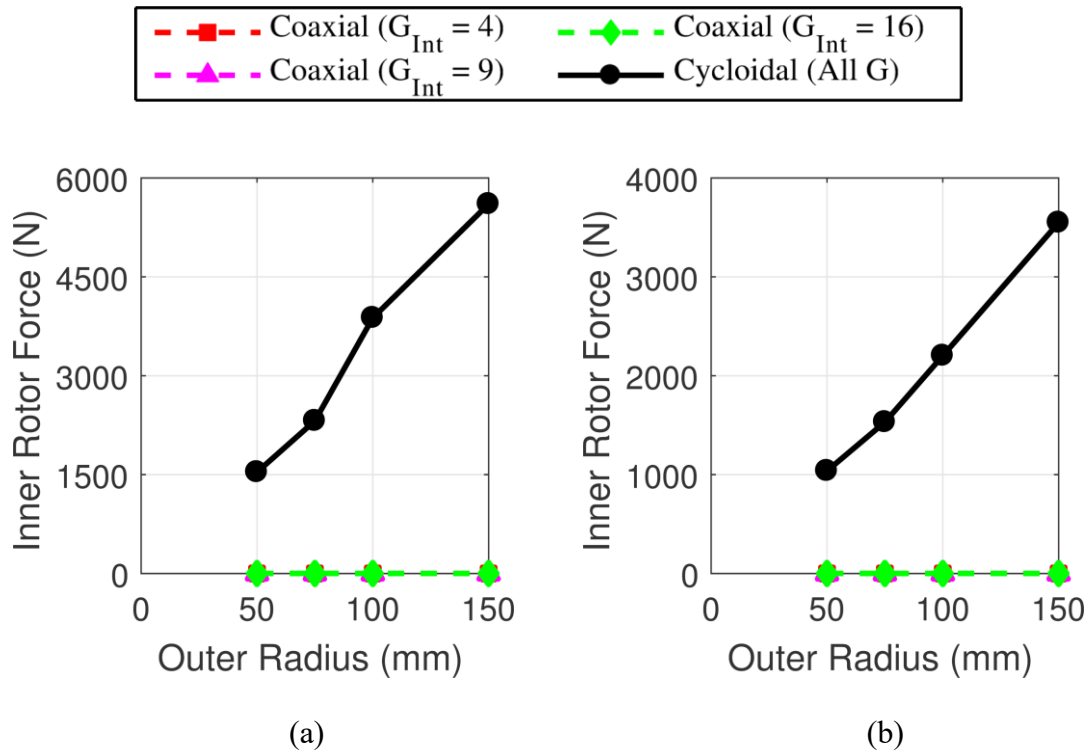
**Figure 4.15** Variation of the maximum (a) VTD and (b) PM GTD with the inner PM thickness and axis offset for cycloidal designs with  $R_{Out} = 150$  mm and  $T_{AG} = 1$  mm. The dotted line indicates the axis offset that maximizes VTD or PM GTD for each inner PM thickness.

This analysis also provides a partial explanation for why higher pole counts favor smaller axis offsets for the cycloidal gear. As the pole count increases, the flux paths become shorter. These shorter flux paths reduce the amount of flux crossing the air gap. Thus, the axis offset must be reduced to maintain the same torque production in the regions where  $k_\tau$  is positive; furthermore, because of these shorter flux paths, this reduction of the axis offset will not result in a large increase in the negative torque produced in regions where  $k_\tau$  is negative. Another factor driving the optimal axis offset is that the axis offset affects the geometric transformation between  $\theta$  and  $\theta'$ , which determines how much of the gear is producing positive torque.



#### 4.4. Rotor Forces and Torque Ripples

Another significant difference between the two topologies is the presence of net magnetic forces on the rotors of the cycloidal topology. Figure 4.16 shows the net magnetic forces on the inner rotors of the designs with the highest VTDs and PM GTDs for each outer radius, which correspond to points in Figure 4.1(a) and Figure 4.2(a). While the cycloidal magnetic gear designs experience significant net magnetic forces, the coaxial designs experience negligible (ideally zero if there are no manufacturing tolerances) net magnetic forces on the rotors due to the symmetry imposed by (16). Figure 4.16 also illustrates that the net magnetic forces tend to increase as the outer radius increases, which is largely due to the increase in air gap area. Furthermore, Figure 4.16 indicates that the maximum VTD designs have larger net magnetic forces than the maximum PM GTD designs, which is largely due to the thicker PMs of the maximum VTD designs.



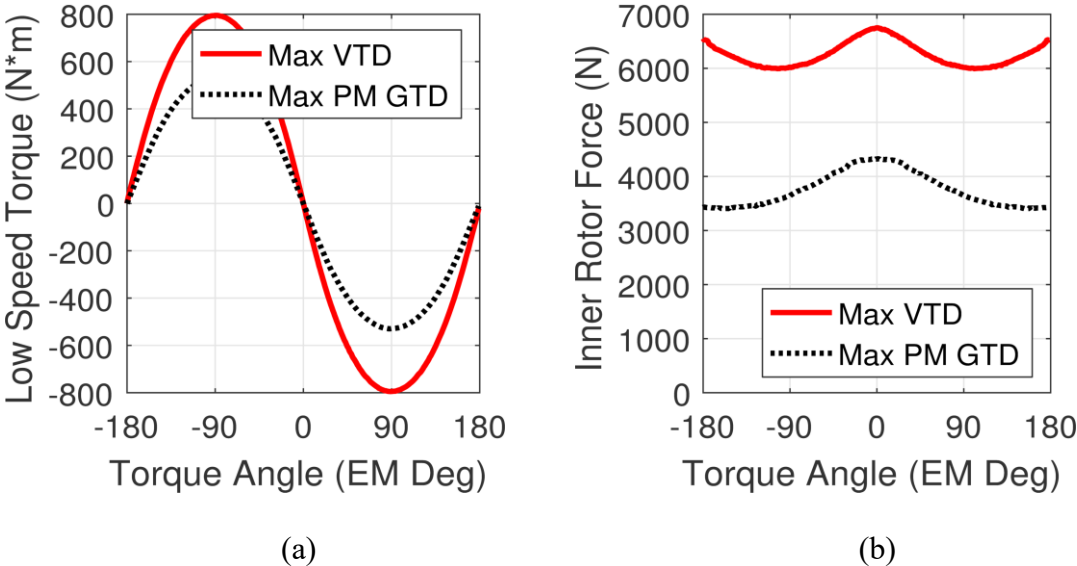
**Figure 4.16** The net forces on the inner rotor at the maximum torque points of (a) the maximum VTD designs corresponding to the points in Figure 4.1(a) and of (b) the maximum PM GTD designs corresponding to the points in Figure 4.2(a) based on 3D FEA for designs with 50 mm stack lengths.

Figure 4.16 illustrates the net magnetic forces at the maximum torque points for the designs, but the magnetic forces do vary significantly with the operating point.

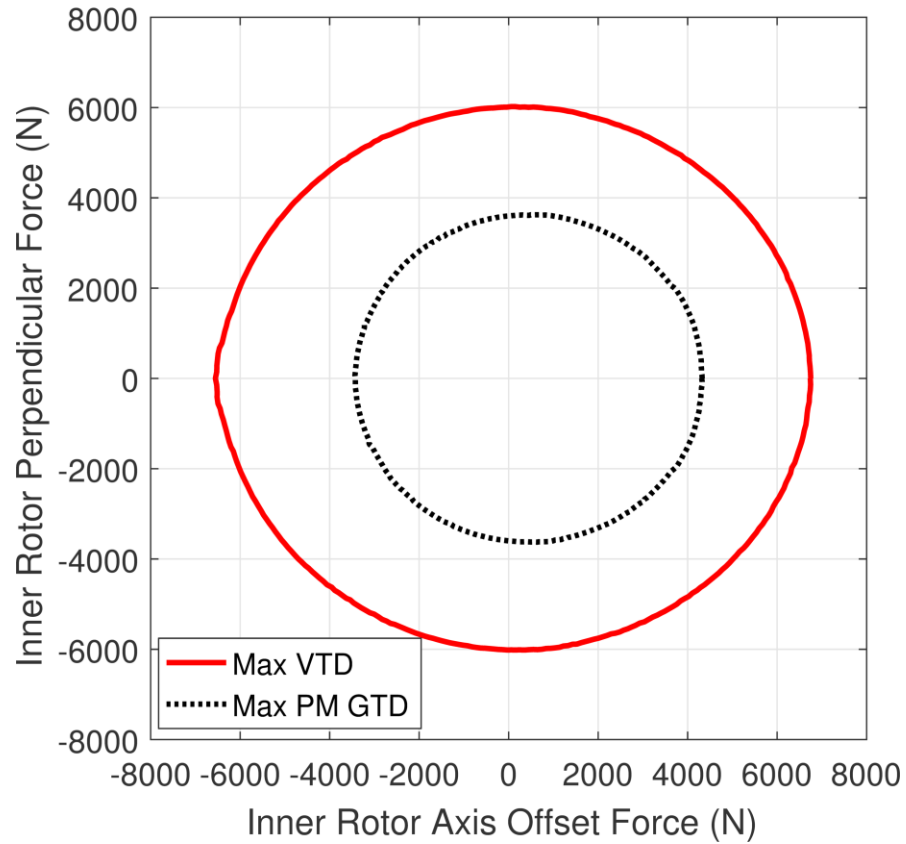
Figure 4.17 and Figure 4.18 illustrate the variation of torques and forces based on 2D FEA as the torque angle changes for the cycloidal designs with the absolute maximum VTD and PM GTD. The torque angle is defined as the difference between the electromagnetic angles of the two rotors at the point where the air gap is minimal.

Figure 4.17 shows that the maximum force occurs at the operating point where the torque angle is 0 and there is no torque. Figure 4.18 illustrates that the angle of the net

magnetic force varies with the torque angle. If too much torque was applied to either shaft and the gear began to slip, the forces on the inner rotor would trace the paths shown in Figure 4.18. The bearings on the inner rotor must be able to withstand these magnetic forces, which are significantly larger than the active weight of the inner rotor. For reference, the total combined masses of the back irons and PMs on the inner rotor are about 7.1 kg and 4.2 kg for the maximum VTD and maximum PM GTD designs, respectively.



**Figure 4.17 The 2D FEA variation of (a) low speed shaft torque and (b) net magnetic forces on the inner rotor as the torque angle is varied for the maximum VTD and PM GTD cycloidal designs from the entire simulation study.**



**Figure 4.18** The variation of the forces in the direction of the axis offset and in the direction perpendicular to the axis offset based on 2D FEA as the torque angle is varied for the maximum VTD and PM GTD cycloidal designs from the entire simulation study.

Figure 4.19 illustrates the torque and force ripple characteristics for the same optimal designs used in Figure 4.17 and Figure 4.18 during steady-state operation at the maximum torque angle based on 2D FEA. The rotation angle is defined as the electromagnetic angle which the inner rotor has both simultaneously rotated and orbited in opposite directions. Figure 4.19 shows that both designs exhibited negligible torque and force ripples. Additionally, when either gear is operating in steady-state at a

constant torque, the angle of net magnetic force is fixed with respect to the axis offset. Alternatively, for a coaxial magnetic gear, the net magnetic forces on the rotors and the rotor torque ripples are heavily dependent on the pole pair count selections. Coaxial gears designed with proper symmetry ideally experience zero net magnetic forces on their rotors. Furthermore, coaxial gear designs with relatively high lowest common multiples between  $P_1$ ,  $P_3$ , and  $Q_2$  and non-integer gear ratios can also achieve very low torque ripples. Both of these conditions can generally be simultaneously achieved by using (16). For example, the coaxial magnetic gear described in [5] uses a  $P_1 = 6$ ,  $P_3 = 68$  and  $Q_2 = 74$  design, resulting in simulated peak-to-peak high speed rotor and low speed rotor torque ripples of 2.2% and 0.02% relative to the slip torques of the high speed rotor and low speed rotor, respectively. However, a nearly identical variation of the design which only changes the pole pair count combinations to  $P_1 = 6$ ,  $P_3 = 66$  and  $Q_2 = 72$ , resulting in an integer gear ratio, exhibits significantly larger high speed rotor and low speed rotor torque ripples of 134.5% and 1.88% relative to the slip torques of the high speed rotor and low speed rotor, respectively. However, for smaller coaxial designs, it may be impractical to choose pole counts with a large lowest common multiple in order to minimize torque ripple.

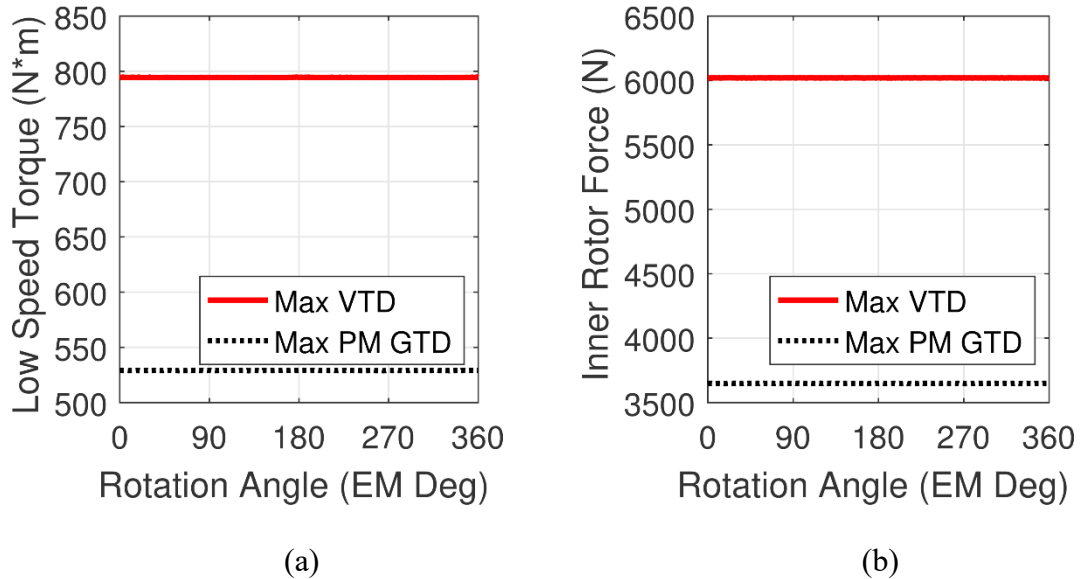


**Figure 4.19** The variation of the (a) low speed shaft torque and (b) net magnetic forces on the inner rotor based on 2D FEA during steady-state operation at the maximum torque angle for the maximum VTD and PM GTD cycloidal designs from the entire simulation study.

#### 4.5. Conclusion

This study employs an extensive parametric evaluation to quantitatively compare the optimal achievable performances of coaxial magnetic gears and cycloidal magnetic gears in terms of volumetric torque density (VTD) and magnet utilization (PM GTD). Each topology has its own benefits and drawbacks with respect to gear ratio, torque, and mechanical design.

Regarding gear ratio, the cycloidal magnetic gear can realistically achieve significantly higher gear ratios than the coaxial magnetic gear. The coaxial gear generally favors relatively low gear ratios with the performance (torque density) getting significantly worse as the gear ratio increases. However, the optimal gear ratio for a

cycloidal magnetic gear varies significantly with other design parameters, especially the outer radius, because the magnitude of the gear ratio is equivalent to the pole pair count on the inner rotor. Additionally, the cycloidal gear actually performs relatively poorly at low gear ratios, especially at larger outer radii. On the other hand, the coaxial gear consistently performs best at low gear ratios, regardless of outer radius, because both sets of pole counts can be varied with the outer radius without significantly changing the gear ratio.

Regarding torque, the cycloidal magnetic gear can generally outperform the coaxial magnetic gear in terms of both VTD and PM GTD, assuming that the optimal gear ratio is used for the cycloidal magnetic gear. However, if the gear ratio is restricted to a relatively low value, the coaxial topology can generally achieve higher VTD and PM GTD values. Furthermore, the coaxial magnetic gear benefits more in terms of VTD and suffers less in terms of PM GTD when the magnet thicknesses are increased. Thus, a coaxial magnetic gear may be more compact if relatively thick PMs can be used, which may be advantageous when size and mass are more important than material cost, but, when the PM thickness is constrained to limit the material cost, the cycloidal magnetic gear will generally be able to achieve higher VTDs and PM GTDs than the coaxial magnetic gear. For the coaxial magnetic gear, torque ripple can be kept small simply by choosing pole count combinations with a large lowest common multiple. The cycloidal topology itself ensures that the torque ripple in a cycloidal magnetic gear will be minimal, regardless of the pole counts.

Finally, there are significant differences regarding construction. The modulators present a challenge to the fabrication of coaxial magnetic gears because they must be held between the two sets of PMs and withstand strong magnetic forces, which can make it mechanically challenging to maintain small air gaps. The cycloidal magnetic gear also presents a couple of fabrication challenges. First, the axis of the inner rotor revolves around the axis of the outer rotor. This requires that the movement of the inner rotor be separated into two components, its orbital revolution about the axis of the outer rotor and its rotation about its own axis. (The dual-stage solution proposed in [20] does partially simplify this challenge at the expense of reduced VTD and PM GTD.) Additionally, the revolution of the inner rotor moves the gear's center of mass, which must be counterbalanced to avoid creating vibrations. Second, the rotors in a cycloidal magnetic gear experience strong magnetic forces, which must be supported by the bearings, whereas the net magnetic forces on the rotors of a coaxial magnetic gear can be canceled out using symmetry. The additional stress placed on the bearings of a cycloidal magnetic gear by these magnetic forces and the challenges of the inner rotor's revolution may reduce the reliability, maintenance, and acoustic noise benefits inherent in the noncontact power transmission of magnetic gears and mitigate some of the topology's advantages relative to coaxial gears with respect to achieving high torque densities at high gear ratios.



## 5. ANALYSIS OF HIGH GEAR RATIO CAPABILITIES FOR SINGLE-STAGE, SERIES MULTISTAGE, AND COMPOUND DIFFERENTIAL COAXIAL MAGNETIC GEARS\*

One of the conclusions in the previous section is that cycloidal magnetic gears are better able to achieve practical designs with high gear ratios than coaxial magnetic gears. However, the high gear ratio capability of cycloidal magnetic gears comes with an undesirable increase in the mechanical complexity of the gear relative to coaxial magnetic gears. Therefore, this section investigates and compares different means of achieving a high gear ratio with coaxial magnetic gears.

One of the primary advantages of using gears in high-torque, low-speed energy conversion applications is that it allows the electric machine to be much smaller than a direct-drive machine for the same application. The larger the gear ratio, the more the size of the electric machine can be reduced. However, most of the literature on coaxial magnetic gears focuses on designs with gear ratios less than 15:1, including several of the designs with the highest reported torque densities [3], [4], [5], [8], [9], [17], [30], [33], [55], [56]. This section uses 2D and 3D finite element analysis (FEA) to investigate three different means to achieve higher gear ratios using radial flux coaxial magnetic gears with surface mounted permanent magnets, such as the example shown in Figure 1.3. First, single-stage magnetic gears with higher gear ratios are evaluated.

---

© 2018 IEEE. Part of this section is reprinted with permission from M. C. Gardner, M. Johnson, and H. A. Toliyat, "Analysis of High Gear Ratio Capabilities for Single-Stage, Series Multistage, and Compound Differential Coaxial Magnetic Gears," *IEEE Trans. Energy Convers.*, vol. 34, no. 2, pp. 665-672, Jun. 2019.

Second, single-stage magnetic gears are connected in series to form multistage magnetic gears. Finally, two single-stage magnetic gears are interconnected to form the Compound Differential Coaxial Magnetic Gear (CDCMG). Although this study is limited to radial flux coaxial magnetic gears, many of the general trends analyzed in this work also apply to other coaxial flux magnetic gear variations (such as radial flux gears with flux focusing or Halbach array magnet configurations and axial and transverse flux coaxial magnetic gears of similar magnet configurations).

### **5.1. Single-Stage Coaxial Magnetic Gears**

A multi-objective genetic algorithm was used to determine the Pareto optimal front maximizing both gear ratio and gravimetric torque density (GTD) in single-stage radial flux magnetic gears based on 2D FEA. Table 5.1 shows the range of values over which each design parameter was swept by the genetic algorithm, and the same materials are used for the gears as those described in Table 2.1. The optimization was performed separately at each of the outer radii listed in Table 5.2. As described in the previous sections,  $G_{int}$  represents the integer part of the gear ratio and relates the pole pair counts according to (16), which eliminates unbalanced magnetic forces on the rotors and keeps the torque ripple relatively low. Also,  $k_{PM}$  determines the ratio of the magnet thicknesses on Rotor 1 and on Rotor 3 according to (17). In general, a gear's slip torque is theoretically magnetically maximized by using the smallest possible air gap, but mechanical concerns, such as machining tolerances, limit the minimum air gap that can be achieved. Thus, as indicated in Table 5.1, the air gaps are each fixed at 1 mm in this study as a compromise between these considerations. For other parameters, the ranges

used in Table 5.1 are informed by the results presented in [51]. For example, the PM and modulator fill factors are not swept all the way from 0 to 1 but across smaller regions around the optimal values presented in [51].

**Table 5.1 Magnetic Gear Single-State Design Parameter Ranges.**

| <b>Name</b>     | <b>Description</b>                              | <b>Range</b> | <b>Units</b> |
|-----------------|---|--------------|--------------|
| $G_{Int}$       | Integer portion of the gear ratio               | 3 – 31       |              |
| $P_1$           | Rotor 1 pole pair count                         | 3 – 25       |              |
| $T_{BI1}$       | Rotor 1 back iron thickness                     | 5 – 20       | mm           |
| $T_{PM1}$       | Rotor 1 permanent magnet thickness              | 3 – 12       | mm           |
| $T_{AG}$        | Air gap thicknesses                             | 1            | mm           |
| $T_{Mods}$      | Modulator thickness                             | 5 – 15       | mm           |
| $k_{PM}$        | Magnet thickness ratio                          | 0.5 – 1      |              |
| $T_{BI3}$       | Rotor 3 back iron thickness                     | 5 – 20       | mm           |
| $\alpha_{PM1}$  | Rotor 1 permanent magnet tangential fill factor | 0.75 – 1     |              |
| $\alpha_{Mods}$ | Modulators tangential fill factor               | 0.35 – 0.65  |              |
| $\alpha_{PM3}$  | Rotor 3 permanent magnet tangential fill factor | 0.75 – 1     |              |

**Table 5.2 Magnetic Gear Single-Stage Design Discrete Parameter Values.**

| <b>Name</b> | <b>Description</b>         | <b>Values</b>                              | <b>Units</b> |
|-------------|----------------------------|--|--------------|
| $R_{Out}$   | Magnetic gear outer radius | 50, 75, 100, 150                           | mm           |
| $L_{Stack}$ | Stack length               | 5, 10, 15, 20, 25, 30, 40, 50, 60, 80, 100 | mm           |

Because end-effects can have a significant impact on the torque of coaxial magnetic gears [35], each of the optimal cross-sectional designs selected based on the 2D FEA simulation results was simulated at each of the stack lengths in Table 5.2 using 3D FEA. Then, for each of these optimal cross-sectional designs, the correct stack length necessary to achieve a low speed rotor slip torque of 1000 N·m was interpolated

from the 3D FEA simulation results. For some of the smaller radii cases, the necessary stack length was beyond 100 mm and had to be extrapolated based on the torques at stack lengths of 80 mm and 100 mm. However, these stack lengths will still be fairly accurate since the torque becomes approximately linear with stack length at such high aspect ratios [35].

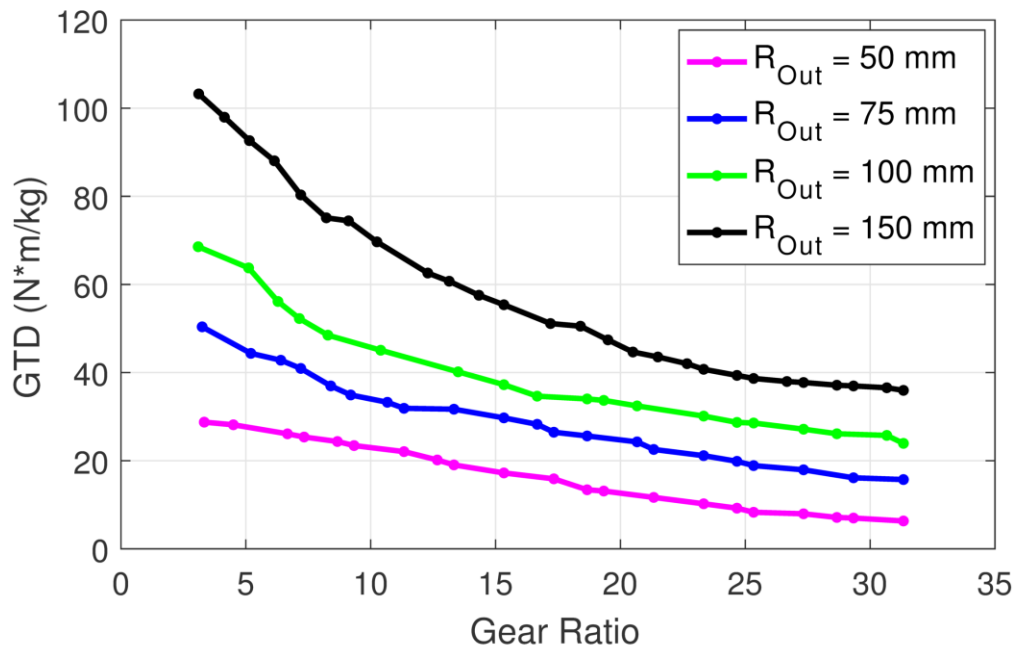
The GTD is calculated by dividing the low speed rotor slip torque by the total active mass, which is the sum of the masses of the back irons (made of M47 steel), the modulators (made of M47 steel), and the permanent magnets (made of NdFeB N42), as given by (14). GTD is chosen for this study because, in addition to minimizing a design's active mass, optimizing for GTD tends to achieve a reasonable compromise between minimizing volume and minimizing active material cost [51]. As in [51], [57], this study uses the GOSET genetic algorithm [39].

Figure 5.1 shows the Pareto optimal fronts maximizing both gear ratio and GTD based on the design parameter value ranges provided in Table 5.1 at each of the outer radii in Table 5.2. These Pareto optimal fronts indicate that, as the gear ratio increases, the maximum achievable gear GTD decreases. This presents the system designer with a fundamental tradeoff; as the gear ratio increases, the size of the electric machine decreases, but the size of the magnetic gear increases [5], [28]. The GTD of a system composed of a magnetic gear and an electric machine,  $GTD_{Sys}$ , is the magnetic gear's low speed rotor slip torque,  $T_{Gear}$ , divided by the total active mass of the system, as given by (24), where  $M_{Gear}$  and  $M_{Machine}$  are the active masses of the magnetic gear and the electric machine, respectively. If the rated torque of the electric machine matches the

slip torque of the gear's high speed rotor, which is  $T_{\text{Gear}}/G$  (where  $G$  is the gear ratio),  $GTD_{\text{Sys}}$  can be rewritten by expressing the masses of the magnetic gear and electric machine in terms of their respective GTDs,  $GTD_{\text{Gear}}$  and  $GTD_{\text{Machine}}$ , and factoring out  $T_{\text{Gear}}$  from both the numerator and denominator, which yields (25).

$$GTD_{\text{Sys}} = \frac{T_{\text{Gear}}}{M_{\text{Gear}} + M_{\text{Machine}}} \quad (24)$$

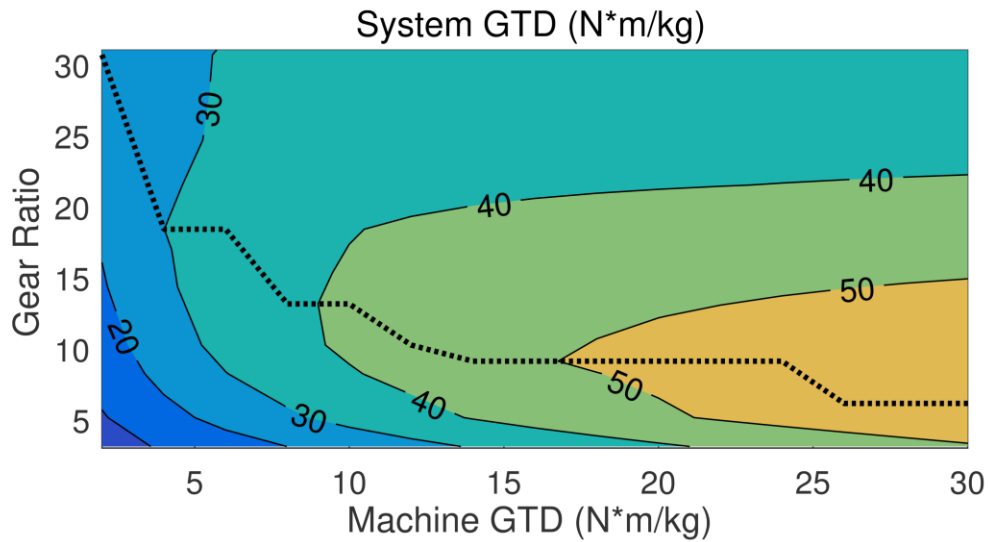
$$GTD_{\text{Sys}} = \left( \frac{1}{GTD_{\text{Gear}}} + \frac{1}{G \cdot GTD_{\text{Gear}}} \right)^{-1} \quad (25)$$



**Figure 5.1 Pareto optimal fronts maximizing the gear's GTD over a range of gear ratios and outer radii for a single-stage magnetic gear with a low speed rotor slip torque of 1000 N·m.**

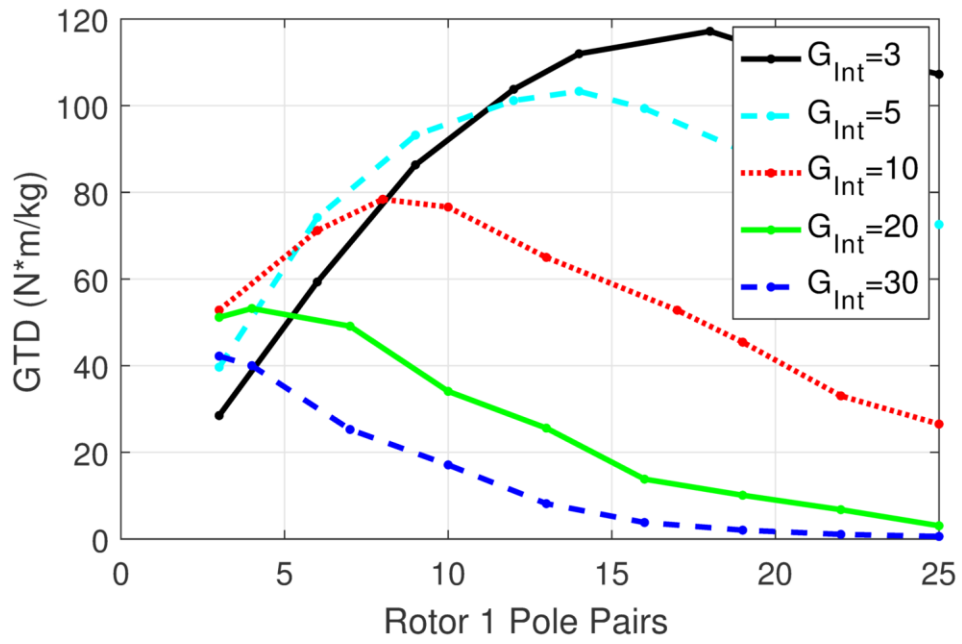
Figure 5.1 displays a significantly different trend than Figure 1.12 regarding how the torque density of coaxial magnetic gears varies with gear ratio. In Figure 5.1, increasing the gear ratio more significantly harms the torque density than in Figure 1.12. This is likely because the analysis presented in [29] only considers a single pole pair count for Rotor 1. Thus, it fails to optimize the torque density for low gear ratio designs.

Figure 5.2 illustrates the maximum system GTDs that can be achieved using the optimal 150 mm outer radius points in Figure 5.1 and electric machines with different GTDs. The dashed line in Figure 5.2 indicates the gear ratio that maximizes the system GTD for each machine GTD. Thus, a design with a relatively low gear ratio and a high torque density, such as those described in most of the literature on coaxial magnetic gears may be less desirable from a system optimization standpoint than a gear with lower torque density, but a higher gear ratio. This is especially true for systems where the electric machine has a relatively low torque density. However, as the gear ratio increases, the number of modulators and Rotor 3 pole pairs increases; this increases manufacturing complexity and cost and may eventually result in components that are impractically thin in the tangential direction. Accordingly, the designer must evaluate several considerations in conjunction with the relevant electric machine scaling characteristics to select the appropriate design point which results in the optimal system configuration.



**Figure 5.2 Variation of the maximum achievable system GTD with gear ratio and machine GTD for systems with a low speed slip torque of 1000 N·m. The dashed line traces the maximum achievable system GTD and the corresponding gear ratio for each machine GTD.**

As the gear ratio changes, the optimal design parameters also change. The most significant change occurs in the number of Rotor 1 pole pairs, as shown in Figure 5.3. Specifically, as the gear ratio increases, the optimal number of Rotor 1 pole pairs decreases to limit the increase in the number of Rotor 3 pole pairs and modulators because large numbers of Rotor 3 pole pairs or modulators result in excessive leakage flux. This reduction in the Rotor 1 pole count also reduces the flux leakage between adjacent magnets on Rotor 1, which leads to an increase in the optimal Rotor 1 magnet thickness, as illustrated in Figure 5.4.



**Figure 5.3** Variation of the maximum achievable gear GTD at various  $G_{Int}$  values with the Rotor 1 pole pair count for designs with an outer radius of 150 mm based on 2D FEA.



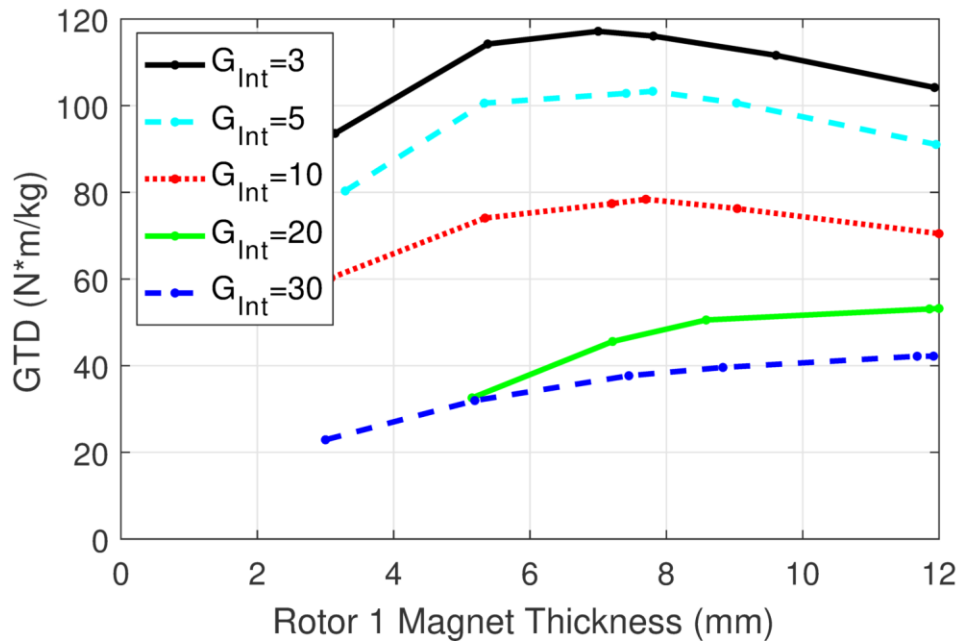


**Figure 5.4 Variation of the maximum achievable gear GTD at various  $G_{Int}$  values with the Rotor 1 magnet thickness for designs with an outer radius of 150 mm based on 2D FEA.**

Additionally, the gear ratio affects the gear's efficiency. Figure 5.5 illustrates the variation of the full load electromagnetic efficiency with gear ratio and the low speed shaft speed for the 150 mm outer radius design points included in Figure 5.1. Note that the electromagnetic efficiency calculations only account for the core losses (hysteresis and eddy current losses) in the back iron and modulator laminations and the eddy current losses in the magnets. These losses are calculated using 2D FEA and then scaled to the appropriate stack lengths based on the 3D FEA results. Efficiency decreases as speed increases because the eddy current losses increase with the square of the magnetic frequency, but the power rating only increases linearly with the speed. Additionally, efficiency decreases as the gear ratio increases, despite the fact that the optimal Rotor 1

pole count gradually decreases, which tends to lower the frequencies of the magnetic field harmonics. This efficiency reduction is partially due to the fact that for the same low speed shaft speed, a higher gear ratio yields a proportional increase in the high speed rotor speed, which results in a net increase in the magnetic frequencies. Furthermore, as illustrated by Figure 5.1, higher gear ratio designs require more active material (both magnets and steel) to transmit the same torque, which results in higher losses.

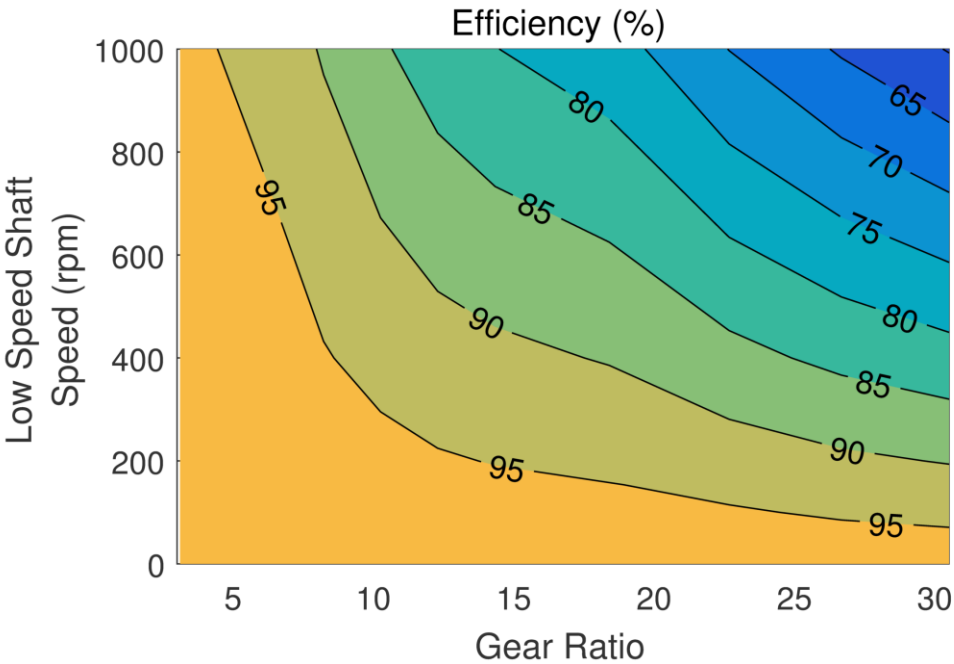


**Figure 5.5 Full load electromagnetic efficiencies of the optimal 150 mm outer radius points shown in Figure 5.1 over a wide range of speeds.**

## 5.2. Series Multistage Coaxial Magnetic Gears

Multiple single-stage coaxial magnetic gears can be connected in series to achieve a higher gear ratio than that which is practical with a single-stage coaxial magnetic gear [58], [59], [60]. If the high speed rotor of each stage is connected to the low speed rotor of the next stage, the net gear ratio is the product of the gear ratios of all the stages. Because each stage interacts with less torque than the previous stages (moving from the lowest speed rotor to the highest speed rotor), each subsequent stage can potentially be significantly smaller than the previous stages. (This study uses the convention that the low speed rotor of the first stage is connected to the low speed shaft of the multistage gearbox and the high speed rotor of the last stage is connected to the high speed shaft of the multistage gearbox.) Thus, as suggested in [58], successive stages could potentially be nested in the bore(s) of the preceding stage(s), which would result in a compact design. Although [58] only considers radial flux topologies, this idea could potentially be applied to other topologies, such as axial flux or transverse flux gears, or even with multiple different topologies used for different stages in the same gearbox.

The ratio between the torques needed for successive stages is ideally (assuming negligible losses) given by the gear ratio of the first (lowest speed) of the two stages; thus, the overall GTD of a multistage gear with  $n$  stages,  $GTD_{NET}$ , is given by (26), where  $GTD_i$  is the GTD of the  $i^{th}$  stage and  $G_j$  is the gear ratio of the  $j^{th}$  stage, based on the convention that the first stage is the stage rated for the lowest speed and the highest torque, while the  $n^{th}$  stage is rated for the lowest torque and the highest speed. Based on

(26), the cross-sectional designs along the Pareto optimal fronts in Figure 5.1 can be connected in series to form the Pareto optimal fronts illustrated in Figure 5.6 and Figure 5.7 for multistage gearboxes with 2, 3, or 4 series-connected stages, which are shown in addition to the single-stage designs. As with the single-stage designs, the slip torque of the low speed shaft of each magnetic gearbox is 1000 N·m. The optimal design for each individual stage in each of these multistage gear designs was selected by interpolating between the 3D FEA results at the stack lengths in Table 5.2 to determine the correct stack length required for each of the optimal 2D cross-sectional designs to achieve the necessary torque for a given individual stage. For the later stages, which have lower torques and, therefore, shorter stack lengths, end-effects become more significant, especially at the larger outer radii. Thus, even though the largest outer radius designs are optimal for the first stage, as in Figure 5.1, designs with smaller outer radii become optimal for the later stages with smaller torques, as shown in Figure 5.6. This choice between smaller outer radii or more significant end-effects means that the later stages tend to have lower GTDs than the first stage; however, since these later stages are rated for lower torques, they contribute less to the overall mass of the gearbox and have a less significant effect on the overall gearbox GTD.

$$\text{GTD}_{\text{Net}} = \left( \frac{1}{\text{GTD}_1} + \sum_{i=2}^n \frac{1}{\text{GTD}_i \cdot \prod_{j=1}^{i-1} G_j} \right)^{-1} \quad (26)$$

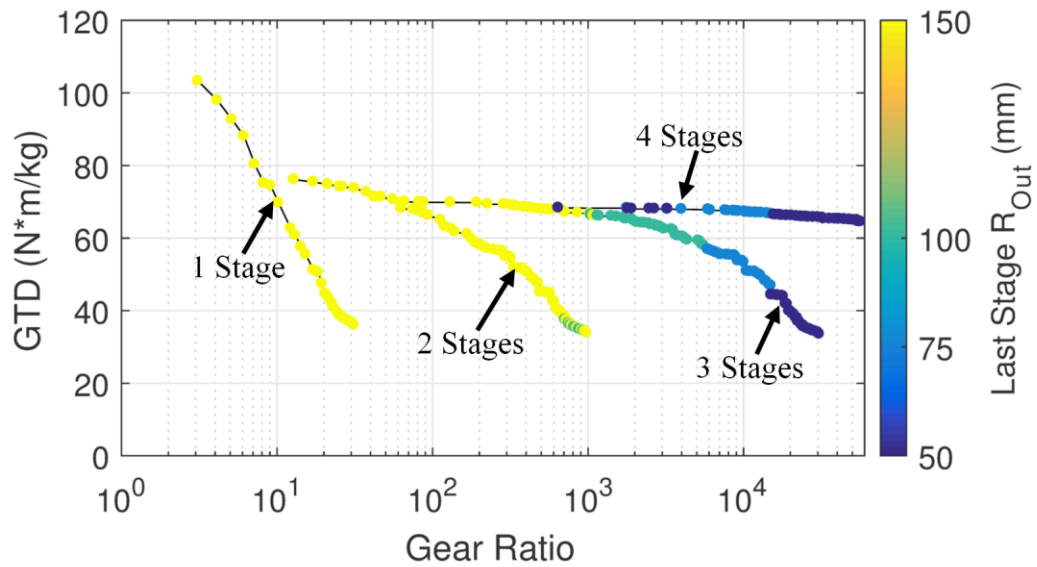


**Figure 5.6 Pareto optimal fronts maximizing gearbox GTD over a range of gear ratios for single-stage magnetic gearboxes and multistage magnetic gearboxes with 2, 3, or 4 series-connected stages and their last stage outer radii.**

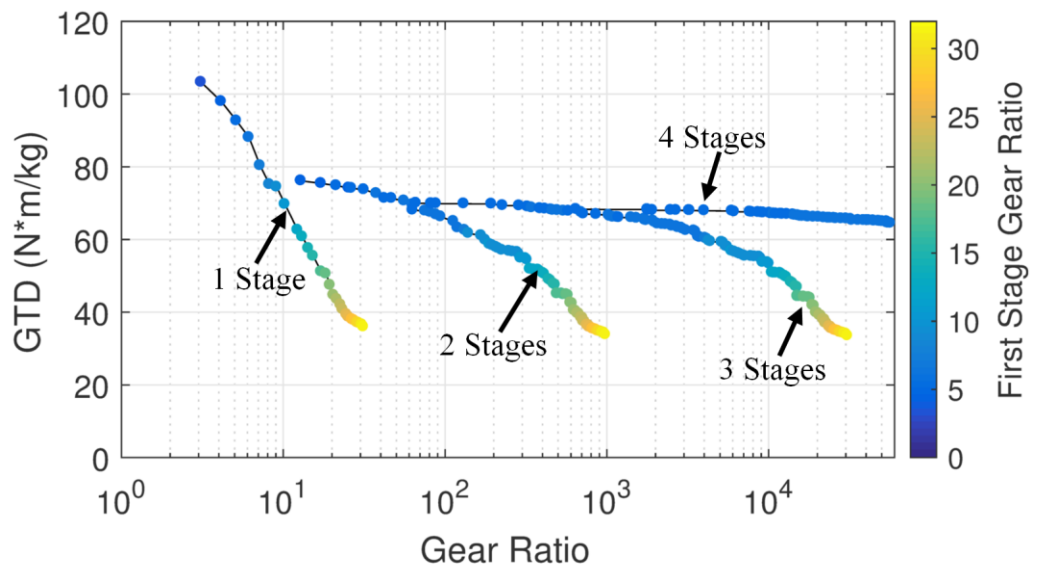
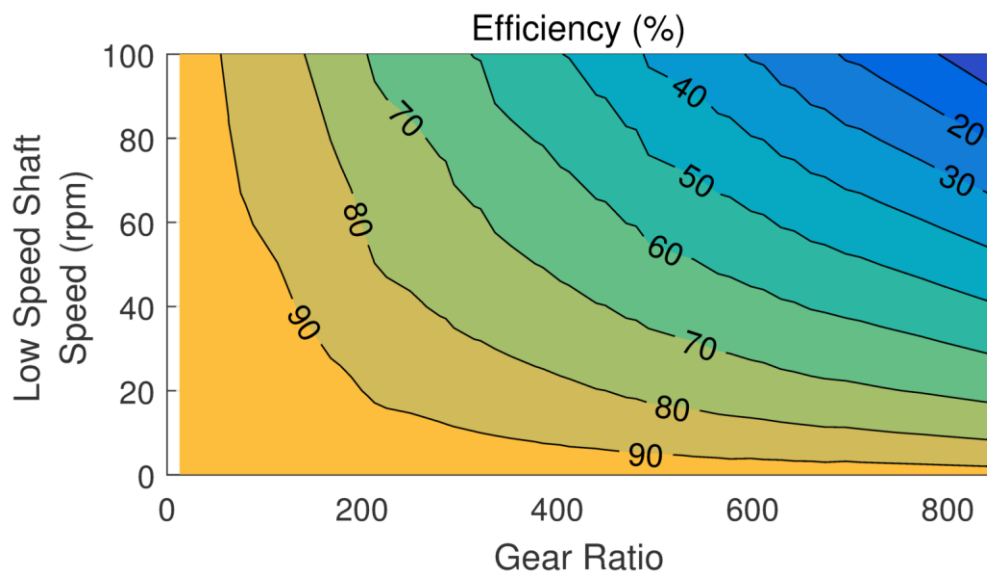


**Figure 5.7 Pareto optimal fronts maximizing gearbox GTD over a range of gear ratios for single-stage magnetic gearboxes and multistage magnetic gearboxes with 2, 3, or 4 series-connected stages and their first stage gear ratios.**

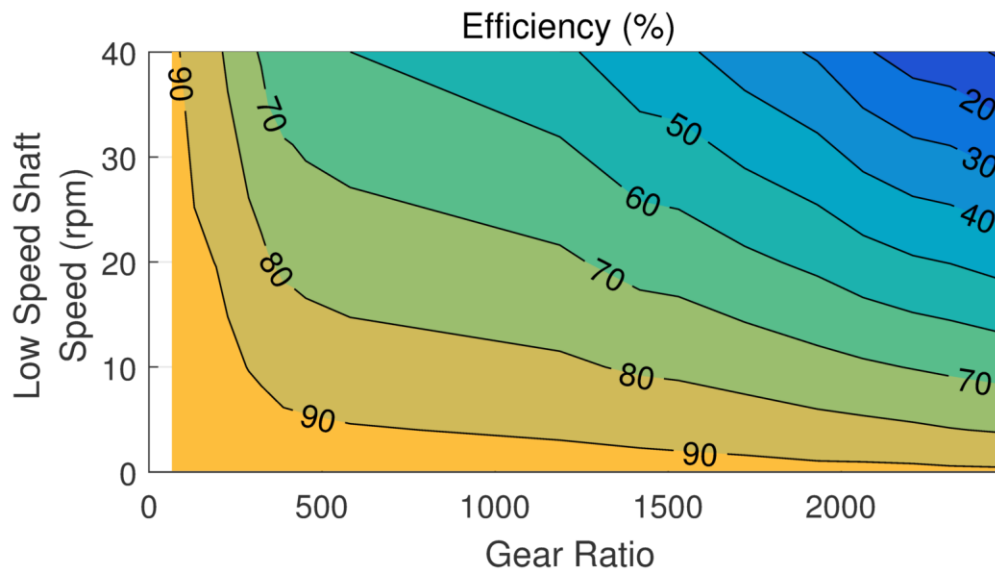
Figure 5.6 and Figure 5.7 show that designs with more series-connected stages can achieve significantly higher net gear ratios and higher GTDs for a given net gear ratio, as compared to single-stage designs and multistage design with fewer stages. The colors of the points along the curves in Figure 5.7 indicate the gear ratios used in the first (highest torque, lowest speed) stages of these optimal multistage gear designs. Because subsequent stages are rated for much smaller torques than the first stage, the mass of the first stage has the largest impact on the net GTD. Thus, it is advantageous to use a magnetic gear with a very high GTD for the first stage in order to minimize the total gearbox mass, even though that means that the first stage has a relatively low gear ratio. Based on (26) and Figure 5.6 and Figure 5.7, it is apparent that the net gear ratio can theoretically be raised to a very large value with a minimal impact on net GTD by connecting a large number of high GTD, low gear ratio stages in series. However, this analysis neglects structural material and bearings. As the number of stages increases, more structural material and bearings are required, which increases the overall size, mass, and cost. Additionally, increasing the number of stages increases the gearbox complexity.

Figure 5.8 and Figure 5.9 illustrate the electromagnetic efficiencies of some of the maximum GTD 2-stage and 3-stage designs included in Figure 5.6 and Figure 5.7. Since the efficiency of each single-stage design has already been determined for a range of speeds, as shown in Figure 5.5, the efficiency of each stage in the multistage design can be interpolated for its operating speed. The net efficiency of a series multistage design is simply the product of the efficiencies of each of its stages. Thus, as with the

single-stage designs, the efficiencies of the multistage designs tend to decrease as the gear ratio or low speed shaft speed increases. Magnetically, the number of stages only has a small impact on the efficiency because the compounding effect of using more stages approximately cancels out the benefits of using lower gear ratio, higher efficiency designs for each stage.



**Figure 5.8 Full load electromagnetic efficiencies of the optimal 2-stage coaxial magnetic gearboxes shown in Figure 5.6 and Figure 5.7.**



**Figure 5.9 Full load electromagnetic efficiencies of the optimal 3-stage coaxial magnetic gearboxes shown in Figure 5.6 and Figure 5.7.**

### 5.3. Compound Differential Coaxial Magnetic Gears

The single-stage coaxial magnetic gearbox can provide a high GTD at very low gear ratios, but the GTD decreases significantly as the gear ratio increases.

Alternatively, a multistage magnetic gearbox can achieve much higher net gear ratios without as significant a reduction in GTD, especially with numerous stages; however, the multistage gearbox's complexity increases with the number of stages. The CDCMG provides an alternative that can combine two single-stage coaxial magnetic gears to achieve a net gear ratio much greater than the product of the individual stage gear ratios. Similarly to the connection of two cycloidal magnetic gears proposed in [20], the CDCMG is formed by connecting two single-stage coaxial magnetic gears, as illustrated in the  $\theta$ - $z$  transverse-sections of a radial flux CDCMG in Figure 5.10.



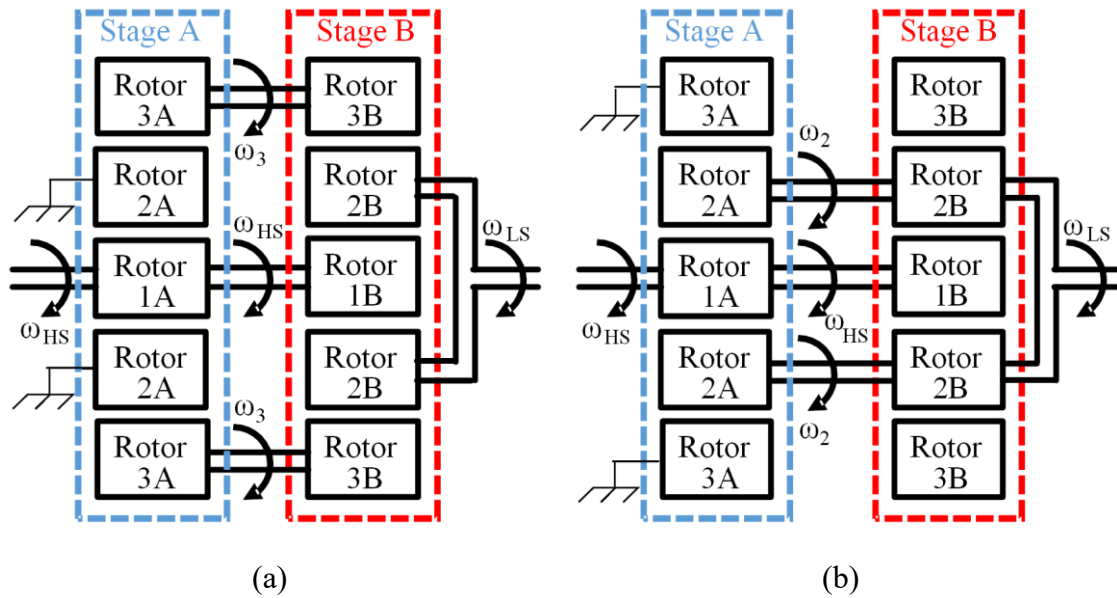


**Figure 5.10  $\theta$ -z transverse-sections of a radial flux CDCMG connected in the (a) Free Spinning Rotor 3 (FSR3) and (b) Free Spinning Rotor 2 (FSR2) configurations.**

Although Figure 5.10 only illustrates CDCMGs formed from radial flux coaxial gears, the CDCMG can be implemented with other coaxial topologies, such as axial or transverse flux gears, or even with a combination of two stages of different topologies. Additionally, there are multiple different ways to connect the two stages in a CDCMG, but the Free Spinning Rotor 3 (FSR3) configuration shown in Figure 5.10(a) and the Free Spinning Rotor 2 (FSR2) configuration shown in Figure 5.10(b) will generally provide the highest gear ratio. In the FSR3 configuration, the high speed shaft is connected to Rotor 1 in both stages, the Rotor 3s of the two stages are connected together and allowed to rotate freely, the Rotor 2 of Stage A is fixed in place, and the Rotor 2 of Stage B is connected to the low speed shaft. Similarly, in the FSR2 configuration, the high speed shaft is connected to Rotor 1 in both stages, the Rotor 2s of

the two stages are connected together and allowed to rotate freely, the Rotor 3 of Stage A is fixed in place, and the Rotor 3 of Stage B is connected to the low speed shaft. For the FSR3 configuration, applying (4) to Stage A results in (27), which relates the angular velocity of both Rotor 3s ( $\omega_3$ ) to the angular velocity of the high speed shaft ( $\omega_{HS}$ ).

Applying (4) and (27) to Stage B yields (28), which relates the the angular velocity of the low speed shaft ( $\omega_{LS}$ ) to that of the high speed shaft. Thus, the net gear ratio of the FSR3 configuration is given by (29). Alternatively, the net gear ratio can be expressed as (30), where  $G_A$  and  $G_B$  are the gear ratios of Stage A and Stage B, as defined by (6).

Thus, the net gear ratio of the CDCMG is essentially related to the product of the two single-stage gear ratios ( $G_A - 1$  is the single-stage gear ratio of Stage A if the modulators are held stationary and Rotor 3 is allowed to rotated), divided by the difference between the two single-stage gear ratios.

$$\omega_3 = \frac{-P_{1A}}{P_{3A}} \cdot \omega_{HS} \quad (27)$$

$$\omega_{LS} = \left( \frac{P_{1B}}{Q_{2B}} - \frac{P_{3B} \cdot P_{1A}}{Q_{2B} \cdot P_{3A}} \right) \cdot \omega_{HS} \quad (28)$$

$$\text{FSR3 Gear Ratio} = \frac{\omega_{HS}}{\omega_{LS}} = \left( \frac{P_{1B}}{Q_{2B}} - \frac{P_{3B} \cdot P_{1A}}{Q_{2B} \cdot P_{3A}} \right)^{-1} \quad (29)$$

$$\text{FSR3 Gear Ratio} = \frac{\omega_{HS}}{\omega_{LS}} = \frac{(G_A - 1) \cdot G_B}{G_A - G_B} \quad (30)$$

A similar analysis for the FSR2 configuration yields (31). The FSR2 configuration's gear ratio can also be expressed as (32).

$$\text{FSR2 Gear Ratio} = \frac{\omega_{\text{HS}}}{\omega_{\text{LS}}} = \left( \frac{Q_{2\text{B}} \cdot P_{1\text{A}}}{Q_{2\text{A}} \cdot P_{3\text{B}}} - \frac{P_{1\text{B}}}{P_{3\text{B}}} \right)^{-1} \quad (31)$$

$$\text{FSR2 Gear Ratio} = \frac{\omega_{\text{HS}}}{\omega_{\text{LS}}} = \frac{(G_{\text{B}} - 1) \cdot G_{\text{A}}}{G_{\text{B}} - G_{\text{A}}} \quad (32)$$

From (30) and (32), it is evident that the CDCMG's net gear ratio can be increased by increasing the gear ratios of the two stages and by decreasing the difference between the gear ratios of the two stages. However, increasing the gear ratio of each stage reduces the GTD of each stage. On the other hand, as shown in Figure 5.3, lower gear ratios favor higher Rotor 1 pole counts, and, as indicated by (6), higher Rotor 1 pole counts allow for smaller increments of change in the gear ratio, which makes it possible to achieve smaller differences between the gear ratios of the two stages. Additionally, from (30) and (32), it is evident that the gear ratio of the FSR2 configuration is the same as that of the FSR3 configuration with Stages A and B interchanged; this means that both configurations can achieve the same gear ratios. However, the FSR3 configuration has an advantage with respect to GTD because the low speed shaft is connected to Rotor 2B, which has a higher slip torque than Rotor 3B. The ratio of the slip torques for these two configurations is  $R_{\text{B}}/(R_{\text{B}}-1)$ , which is especially significant if  $R_{\text{B}}$  is relatively small. Finally, (30) and (32) both indicate that if the gear ratios of the two stages are the same, then the CDCMG will ideally have an infinite gear ratio. In this case, the low speed shaft will have non-zero steady-state velocity only when slipping, and the high speed shaft will rotate freely, decoupled from the low speed shaft.

To illustrate the ability of the CDCMG to simultaneously achieve a high gear ratio and a relatively high GTD, an example radial flux CDCMG with a very aggressive

gear ratio is presented, with the two stages connected in the FSR3 configuration. The parameters of Stages A and B are given as Design 1 in Table 5.3. Additionally, Design 2 is given as a design example with a less aggressive gear ratio. Both design examples are rated for a low speed slip torque of 1000 N·m. As in the previous sections, each design was optimized for the specified pole counts in Table 5.3 using 2D FEA; then, each stage was evaluated at the stack lengths in Table 5.2 using 3D FEA, and the correct stack lengths were interpolated from the torques at the simulated stack lengths.

**Table 5.3 CDCMG Design Examples.**

| Name               | Design 1 |         | Design 2 |         | Units  |
|--------------------|----------|---------|----------|---------|--------|
|                    | Stage A  | Stage B | Stage A  | Stage B |        |
| P <sub>1</sub>     | 17       | 19      | 8        | 9       |        |
| Q <sub>2</sub>     | 52       | 58      | 58       | 64      |        |
| P <sub>3</sub>     | 35       | 39      | 50       | 55      |        |
| G                  | 3.059    | 3.053   | 7.25     | 7.11    |        |
| R <sub>Out</sub>   | 150      | 150     | 150      | 150     | mm     |
| T <sub>B11</sub>   | 5.0      | 5.0     | 6.9      | 6.0     | mm     |
| T <sub>PM1</sub>   | 6.7      | 5.4     | 9.4      | 8.4     | mm     |
| T <sub>AG</sub>    | 1        | 1       | 1        | 1       | mm     |
| T <sub>Mods</sub>  | 5.0      | 5.0     | 5.2      | 5.0     | mm     |
| k <sub>PM</sub>    | 0.80     | 0.78    | 0.51     | 0.52    |        |
| T <sub>B13</sub>   | 5.0      | 5.0     | 5.0      | 5.0     | mm     |
| α <sub>PM1</sub>   | 0.86     | 0.94    | 0.79     | 0.75    |        |
| α <sub>Mods</sub>  | 0.55     | 0.54    | 0.50     | 0.46    |        |
| α <sub>PM3</sub>   | 0.92     | 0.95    | 0.93     | 0.84    |        |
| L <sub>Stack</sub> | 63.1     | 66.8    | 78.4     | 84.4    | mm     |
| GTD                | 103.4    | 104.3   | 75.6     | 78.5    | N·m/kg |
| Net Gear Ratio     | 1015     |         | 320      |         |        |
| Net GTD            | 52.0     |         | 38.6     |         | N·m/kg |

Design 1 combines two single-stage coaxial magnetic gears with gear ratios of 3.059 and 3.053 to achieve a net gear ratio of 1015 with a net GTD of 52.0 N·m/kg. For comparison, as indicated by the information in Figure 5.1 and Figure 5.6, a single-stage gear and a two stage series connected gear are generally incapable of practically achieving this high of a gear ratio with realistic magnet and modulator pole piece sizes and acceptable torque ripple characteristics. The largest gear ratio achieved by a two stage series connected gear considered in this study is 981.8 and that design only exhibits a GTD of 33.8 N·m/kg (with extremely high and relatively impractical single-stage gear ratios of 31.333 for both stages). Three and four stage series connected gears can achieve comparably high gear ratios over 1000, while maintaining high GTDs of 66.7 N·m/kg and 68.2 N·m/kg, respectively, but they require the added complexity associated with the additional gearing stages. Thus, the CDCMG is capable of achieving a very large net gear ratio with just two stages of relatively low gear ratios, while simultaneously maintaining a reasonable GTD. Alternatively, Design 2 combines two stages with gear ratios of 7.25 and 7.11 to achieve a much lower net gear ratio of 320 with a net GTD of 38.6 N·m/kg. This performance is quite achievable with a two stage series connected gear, but the CDCMG does have a slight advantage in the fact that each of its stages uses a lower gear ratio than what would be required in the stages of a series multistage solution.

However, the CDCMG suffers from poor efficiency. As shown in Figure 5.11, at speeds above 1 rpm, Design 1 is less than 10% efficient and Design 2 is less than 50% efficient. This poor efficiency occurs because power circulates between the two stages,

which means that each stage handles significantly more power than the amount transferred from the input shaft to the output shaft. Thus, even though the individual stages may have high efficiencies at their operating points, the net efficiency may be much lower than the product of the efficiencies of the two stages.

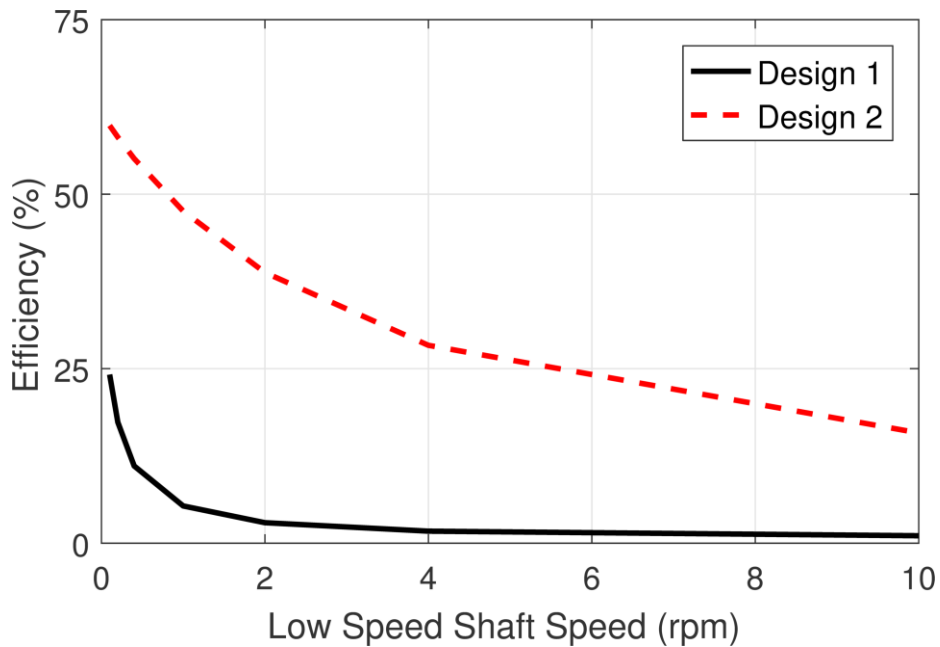


**Figure 5.11 Full load electromagnetic efficiencies for CDCMG Designs 1 and 2 in Table 5.3.**

The circulating power travels through the magnetic fields of Stage A, through the mechanical connection of the free spinning rotor between the two stages, through the magnetic fields of Stage B, and then through the mechanical connection of the high speed shaft between the stages. The power transferred between the stages through the free spinning rotor,  $P_{FSR}$ , is given by (33), where  $\tau_{1A}$  is the torque on the high speed shaft from Stage A (assuming negligible electromagnetic losses in Stage A). In the FSR3

configuration, for there to be no steady-state net torque on the free spinning rotor, the torque on the high speed shaft from Stage B,  $\tau_{1B}$ , must be given by (34), assuming that the ratio of the torques between two rotors is given by the gear ratio between them. (This assumption is correct in the case of lossless transmission in each stage.) Thus, the net power on the high speed shaft,  $P_{HS}$ , is given by (35). If  $G_A < G_B$ , the circulating power,  $P_{circ}$ , is the difference between  $P_{FSR}$  and  $P_{HS}$  and is given by (36). However, if  $G_A > G_B$ , the circulating power is simply  $P_{FSR}$ , which is given by (37).

$$P_{FSR} = \omega_{HS} \cdot \tau_{1A} \quad (33)$$

$$\tau_{1B} = \frac{G_A - 1}{G_B - 1} \cdot \tau_{1A} \quad (34)$$

$$P_{HS} = \omega_{HS} \cdot (\tau_{1A} + \tau_{1B}) = \left(1 - \frac{G_A - 1}{G_B - 1}\right) \cdot P_{FSR} \quad (35)$$

$$P_{circ} = P_{FSR} - P_{HS} = \left(\frac{G_A - 1}{G_B - G_A}\right) \cdot P_{HS} \quad (36)$$

$$P_{circ} = P_{FSR} = \left(\frac{G_B - 1}{G_B - G_A}\right) \cdot P_{HS} \quad (37)$$

A similar analysis can be performed for the FSR2 configuration where  $G_A - 1$  and  $G_B - 1$  would be replaced with  $G_A$  and  $G_B$ , respectively. This analysis reveals a tradeoff involved in the selection of the gear ratios; as the difference between  $G_A$  and  $G_B$  decreases, the net gear ratio increases, but the efficiency also tends to decrease. As an example, Design 1 uses a smaller difference between  $G_A$  and  $G_B$  than Design 2 to achieve a higher net gear ratio, despite employing stages with smaller individual gear ratios, but Design 1 suffers from much higher losses. Additionally, if the difference between  $G_A$  and  $G_B$  is small, torque ripple may become a significant concern because the

average net torque on the high speed shaft will be much smaller than the torques from each of the two stages.

The low efficiency caused by this circulating power makes the CDCMG impractical for most applications. However, at very low speeds, the efficiency is not as abysmal, so the CDCMG might be a reasonable solution for applications with very low speeds where efficiency is not one of the most important performance metrics, such as a solar tracking system or a system to raise a drawbridge. Additionally, the CDCMG's use of lower single-stage gear ratios eliminates the need for an excessive number of modulators or Rotor 3 pole pairs. This provides more flexibility to pursue strategies to improve efficiency or reduce torque ripple, such as using a Halbach array on Rotor 3.

#### **5.4. Conclusion**

This study evaluates three different options for achieving a high gear ratio using coaxial radial flux magnetic gears with surface permanent magnets. First, the gear ratio of a single-stage magnetic gear can be increased by increasing the ratio of the number of modulators to the number of pole pairs on the high speed rotor. However, as the gear ratio increases, both gravimetric torque density (GTD) and efficiency tend to decrease. Additionally, practical constraints limit the number of modulators and pole pairs that can be used, which limits the maximum gear ratio that can realistically be achieved. Second, multistage magnetic gearboxes can be formed by connecting single-stage designs in series. Connecting more gear stages in series allows a design to achieve very high gear ratios with a smaller reduction in GTD at the expense of increased complexity. To achieve a high GTD in a multistage gearbox, it is optimal to use a design with a



relatively low gear ratio and a high GTD for the first stage connected directly to the low speed shaft. Because the other stages operate at much lower torques, they are much smaller and have less impact on the net GTD of the design. Third, the CDCMG can be formed by interconnecting two single-stage coaxial magnetic gears as shown in Figure 5.10. This allows the CDCMG to achieve a much higher net gear ratio than the product of the gear ratios of the two stages. However, a significant amount of power circulates between these two stages, which results in a very low efficiency except at extremely low operating speeds.

This study provides an initial analysis of these three different means of achieving a high gear ratio. There are significant opportunities for further analysis in this area. This study only considers coaxial radial flux magnetic gears with surface permanent magnets. Although the trends presented in this section will generally apply to other types of coaxial magnetic gears, future work could evaluate these trends more precisely for other types of coaxial magnetic gears. Furthermore, the fabrication and testing of prototype multistage magnetic gearboxes or CDCMGs would be a significant contribution. Finally, a CDCMG could be designed to achieve a higher efficiency using techniques to reduce losses, such as using Halbach arrays.

## 6. NONLINEAR ANALYSIS OF MAGNETIC GEAR DYNAMICS USING SUPERPOSITION AND CONSERVATION OF ENERGY\*

The previous sections have considered magnetic gears in terms of their slip torques and gear ratios. However, the dynamic behavior of a magnetic gear is also important in many applications, and this behavior is influenced by various design parameters.

The noncontact nature of magnetic gearing is responsible for many of magnetic gears' potential benefits, such as reduced maintenance requirements, improved reliability, reduced acoustic noise, and inherent overload protection, but it also introduces some challenges. First, if torque is applied too suddenly or if too much torque is applied, the magnetic gear can slip, decoupling the rotation of the two shafts. While slipping is often better than the permanent damage that can occur if too much torque is applied to a mechanical gear, it is still desirable to avoid slipping when possible. Second, the magnetic coupling between the two rotors is not as stiff as the coupling in a mechanical gear. This can result in a quite underdamped system, especially if the magnetic gear is very efficient [61], [62], [63]. Third, the torque on both rotors is a nonlinear function of their positions [61], [62], [63], [64]. Many papers on the dynamics or control of magnetic gears linearize the system around an operating point [61], [63]. However, this becomes inaccurate when there is a significant change in

---

© 2019 IEEE. Part of this section is reprinted with permission from M. C. Gardner and H. A. Toliyat, "Nonlinear Analysis of Magnetic Gear Dynamics Using Superposition and Conservation of Energy," in *Proc. IEEE Int. Elect. Mach. and Drives Conf.*, 2019, pp 210-217.

torques [64]. Other papers employ numerical time-stepping models to accurately model the nonlinearity [62], but this provides less intuition and insight into the dynamic behavior of magnetic gears. This section provides a nonlinear analytical model for the dynamic behavior of magnetically geared systems and presents relevant insights into parameters affecting this behavior.

### 6.1. Magnetic Gear Dynamic Model

As in [61], [63], [64], a magnetic gear can be dynamically modeled as two inertias separated by two ideal gearboxes and a nonlinear torsional spring, as shown in Figure 6.1 and described by (38) and (39), where  $J_h$ ,  $\omega_h$ ,  $B_h$ ,  $p_h$ , and  $\theta_h$  are the moment of inertia, angular velocity, viscous friction coefficient, pole pair count, and angular position of the high speed side,  $J_l$ ,  $\omega_l$ ,  $B_l$ ,  $p_l$ , and  $\theta_l$  are the same quantities for the low speed side,  $T_M$  is the torque provided by the machine connected to the high speed rotor (HSR),  $T_L$  is the torque of the load connected to the low speed rotor (LSR), and  $T_C$  is the gear's characteristic torque, which is defined as the slip torque on either rotor divided by the number of pole pairs on that rotor. The torque angle,  $\theta_T$ , is defined by (40) and determines the magnetic torque produced by the gear. These equations can describe several different types of magnetic gears, including coaxial, spur, and cycloidal topologies, with the appropriate choices of  $p_h$  and  $p_l$ , which should result in a gear ratio,  $G = p_l/p_h$ . One of the pole pair counts may be the number of modulators for a coaxial gear [3], [56] or simply 1 in the case of a cycloidal gear [19]. Additionally, in cases where the rotors rotate in opposite directions,  $p_h$  or  $p_l$  should be negative [3], [17].

$$J_h \frac{d\omega_h}{dt} = T_M - B_h \omega_h - p_h T_C \sin(p_h \theta_h - p_l \theta_l) \quad (38)$$

$$J_l \frac{d\omega_l}{dt} = T_L - B_l \omega_l + p_l T_C \sin(p_h \theta_h - p_l \theta_l) \quad (39)$$

$$\theta_T = p_h \theta_h - p_l \theta_l \quad (40)$$

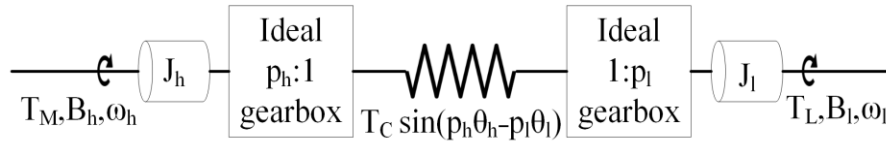


**Figure 6.1 Magnetic gear dynamic model.**

As in [65], the system can be transformed by referring the HSR and LSR quantities through the ideal gearboxes. This produces the model described by (41) and (42), where the HSR and LSR side quantities have been referred through the ideal gearboxes, according to (43), (44), (45), (46), (47), (48), (49), (50), (51), and (52). This model is effectively analogous to a magnetic coupling or a magnetic gear with a 1:1 gear ratio, and is illustrated in Figure 6.2.

$$J'_h \frac{d\omega'_h}{dt} = T'_M - B'_h \omega'_h - T_C \sin(\theta'_h - \theta'_l) \quad (41)$$

$$J'_l \frac{d\omega'_l}{dt} = T'_L - B'_l \omega'_l + T_C \sin(\theta'_h - \theta'_l) \quad (42)$$

$$J'_h = \frac{J_h}{p_h^2} \quad (43)$$

$$T'_M = \frac{T_M}{p_h} \quad (44)$$

$$B'_h = \frac{B_h}{p_h^2} \quad (45)$$

$$\omega'_h = \omega_h p_h \quad (46)$$

$$\theta'_h = \theta_h p_h \quad (47)$$

$$J'_1 = \frac{J_1}{p_1^2} \quad (48)$$

$$T'_L = \frac{T_L}{p_1} \quad (49)$$

$$B'_1 = \frac{B_1}{p_1^2} \quad (50)$$

$$\omega'_1 = \omega_1 p_1 \quad (51)$$

$$\theta'_1 = \theta_1 p_1 \quad (52)$$

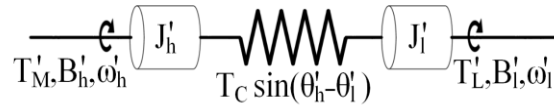


**Figure 6.2 Magnetic gear dynamic model transformed to 1:1 gear ratio.**

### 6.1.1. Superposition of Rigid Body and Fixed Center Motion

It is assumed that the viscous friction on each rotor is proportional to its inertia, as described by (53), (or that the design is relatively efficient and the friction on each rotor can be neglected). Then, using superposition, the motion of the gear can be decomposed into the sum of the motions of the two systems shown in Figure 6.3 and Figure 6.4, with the torques given by (54), (55), and (56).

$$\frac{B'_h}{J'_h} = \frac{B'_l}{J'_l} \quad (53)$$

$$T'_h{}^{RB} = \frac{(T'_M + T'_L)J'_h}{J'_h + J'_l} \quad (54)$$

$$T'_l{}^{RB} = \frac{(T'_M + T'_L)J'_l}{J'_h + J'_l} \quad (55)$$

$$T'^{FC} = \frac{T'_M J'_l - T'_L J'_h}{J'_h + J'_l} \quad (56)$$

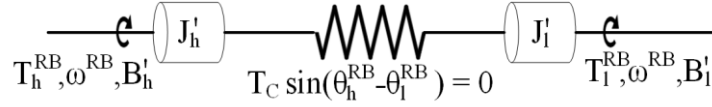


**Figure 6.3 Rigid body motion component of the magnetic gear dynamic model.**

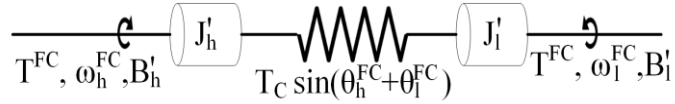


**Figure 6.4 Fixed center motion component of the magnetic gear dynamic model.**

This superposition satisfies the conditions given in (57), (58), (59), (60), (61), and (62).

$$T'_M = T'_h{}^{RB} + T'^{FC} \quad (57)$$

$$T'_L = T'_l{}^{RB} - T'^{FC} \quad (58)$$

$$\omega'_h = \omega'^{RB} + \omega'^{FC} \quad (59)$$

$$\omega_1' = \omega^{RB} - \omega_1^{FC} \quad (60)$$

$$\theta_h' = \theta_h^{RB} + \theta_h^{FC} \quad (61)$$

$$\theta_l' = \theta_l^{RB} - \theta_l^{FC} \quad (62)$$

Since both rotors in Figure 6.3 have the same acceleration, which is given by (63), and the initial conditions presume that both rotors in Figure 6.3 have the same initial speeds and angles, both inertias in Figure 6.3 have the same speeds and angles as each other at all times. Thus, the rigid body torque angle,  $\theta_h^{RB} - \theta_l^{RB}$ , is always zero, and the nonlinear spring torque in Figure 6.3 is always zero. Since this rigid body motion does not affect the system's torque angle, superposition can isolate the rigid body motion of Figure 6.3 from the torque angle changes occurring in Figure 6.4 without violating the system's nonlinearity.

$$\alpha^{RB} = \frac{T_h^{RB} - B_h' \omega^{RB}}{J_h'} = \frac{T_l^{RB} - B_l' \omega^{RB}}{J_l'} \quad (63)$$

Since equal and opposite torques are applied to the two shafts in Figure 6.4, the net torque is always zero. Thus, the system can be represented as the motion of each rotor relative to a fixed point, as shown in Figure 6.5. This is analogous to the fixed center of mass in a system with zero net force. As the same torque is applied to  $J_h'$  and  $J_l'$ , their accelerations,  $\alpha_h^{FC}$  and  $\alpha_l^{FC}$ , are inversely proportional to their respective inertias, as described by (64). Thus, the condition given by (65) will hold true at all times if it is valid at the initial time. Therefore, each side of Figure 6.5 can be transformed to the torque angle reference frame in Figure 6.6 with the new quantities in the torque angle reference frame defined by (66), (67), (68), and (69). Thus, the behavior of the torque

angle, which is critical to the analysis of both slipping and the gear's oscillations, can be evaluated in terms of the dynamics of a single inertia connected to a fixed point by a nonlinear spring.

$$\frac{\alpha_h^{FC}}{\alpha_l^{FC}} = \frac{J_l'}{J_h'} \quad (64)$$

$$\frac{\omega_h^{FC}}{\omega_l^{FC}} = \frac{\theta_h^{FC}}{\theta_l^{FC}} = \frac{J_l'}{J_h'} \quad (65)$$

$$\theta_T = \theta_h^{FC} \cdot \left(1 + \frac{J_h'}{J_l'}\right) = \frac{\theta_h^{FC} \cdot (J_h' + J_l')}{J_l'} = \theta_l^{FC} \cdot \left(1 + \frac{J_l'}{J_h'}\right) = \frac{\theta_l^{FC} \cdot (J_h' + J_l')}{J_h'} \quad (66)$$

$$\omega_T = \omega_h^{FC} \cdot \left(1 + \frac{J_h'}{J_l'}\right) = \frac{\omega_h^{FC} \cdot (J_h' + J_l')}{J_l'} = \omega_l^{FC} \cdot \left(1 + \frac{J_l'}{J_h'}\right) = \frac{\omega_l^{FC} \cdot (J_h' + J_l')}{J_h'} \quad (67)$$

$$J_T = \frac{J_h' J_l'}{J_h' + J_l'} \quad (68)$$

$$B_T = \frac{B_h' B_l'}{B_h' + B_l'} \quad (69)$$

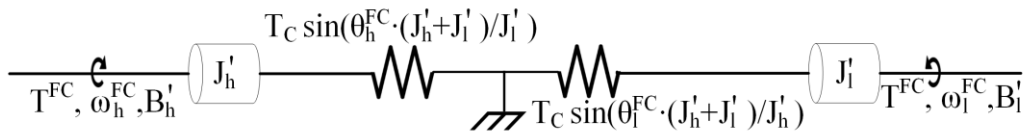


**Figure 6.5 Both the HSR and the LSR represented as moving relative to a fixed center of inertia.**



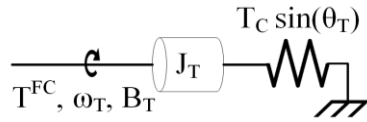


**Figure 6.6 Both the HSR and the LSR transformed to the torque angle reference frame.**

### 6.1.2. Conservation of Energy

This system could be evaluated by linearizing the spring about an operating point and solving in the frequency domain, but, if the losses are assumed to be negligible, the conservation of energy principle yields an approach that preserves the nonlinearity. For the torque angle reference frame of Figure 6.6, energy enters or leaves the system as  $T^{FC}$  is applied and the inertia rotates. Energy is also converted between the rotational kinetic energy of the inertia and the potential energy of the spring. If  $T^{FC}$  is known as a function of the torque angle, the kinetic energy can be determined as a function of the torque angle. Figure 6.7 illustrates this for the case where the gear is initially in steady-state at a torque angle of  $\theta_T^i$ , and  $T^{FC}$  suddenly increases. In Figure 6.7, the rotational kinetic energy at a torque angle of  $\theta$  can be found by subtracting the area under the nonlinear torque curve (the spring's potential energy) from the area under the step torque curve (the input energy). This can be used to calculate the angular velocity of the rotating inertia in Figure 6.6 at any torque angle. The system will oscillate as energy from the external torque enters or leaves the system and is transformed between potential energy and kinetic energy. Any losses in the system will dissipate the energy, and, if it does not

slip, it will eventually reach steady-state at the torque angle where the nonlinear spring's torque equals  $T^{FC}$ .

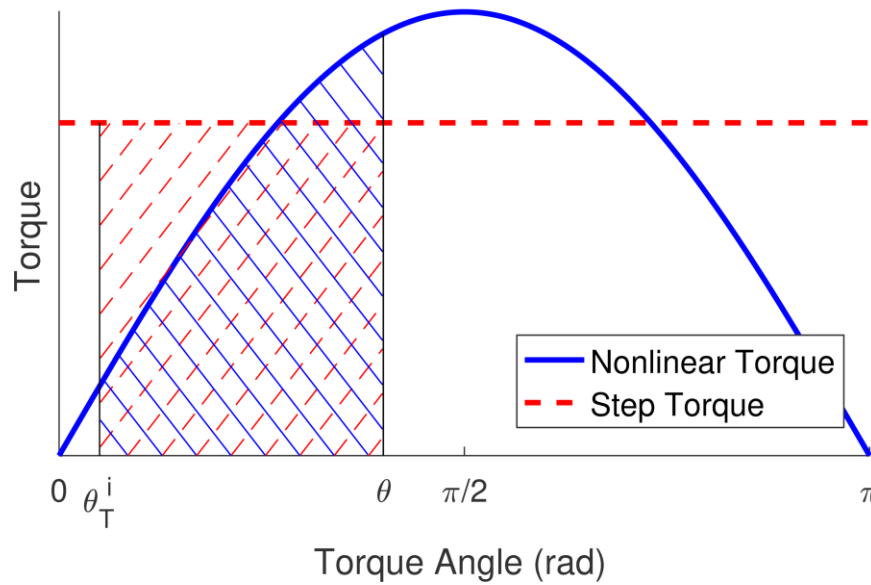


**Figure 6.7** The energy input into the Figure 6.6 system is the area under the step torque curve, and the energy stored in the nonlinear spring is the area under the nonlinear torque curve. The kinetic energy of the inertia is the difference between these two energies (assuming negligible losses).

## 6.2. Design Implications

### 6.2.1. Effective Inertia Ratio

Figure 6.4 and (56) indicate that the ratio between  $J'_h$  and  $J'_l$  directly determines the extent to which the torques on the two sides of the gear impact the torque angle. To quantify these trends, the effective inertia ratio,  $k_I$ , is defined by (70). If the machine and the physical load are stiffly connected to the HSR and LSR, respectively, then,  $J_h$  and  $J_l$  should include their respective inertias, in addition to the inertias of the gear's

rotors. Figure 6.8 shows what portions of the per unit external torques contribute to the changes in the torque angle for a given effective inertia ratio. (The per unit torque on each rotor is defined relative to the slip torque of that rotor.) Thus,  $k_J$  significantly affects the system's dynamic performance. A large  $k_J$  means that disturbances in the load torque will have less effect on the torque angle, which is advantageous if the load torque may change suddenly, but disturbances in the machine torque will cause larger torque angle oscillations. Additionally, with a large  $k_J$ , a transient load torque much larger than the LSR slip torque may not necessarily cause the gear to slip, if it is not opposed by a corresponding torque from the machine. Alternatively, a small  $k_J$  will make the gear's oscillatory and slipping behavior more susceptible to the load torque and less susceptible to the machine torque, which could be advantageous if the machine has a high torque ripple and the load changes relatively slowly. Furthermore,  $k_J$  determines how much of the oscillations appear in  $\theta_h^{FC}$  and  $\theta_l^{FC}$ . Increasing  $k_J$  will increase the extent of oscillations on the HSR while reducing the extent of oscillations on the LSR. Thus, when selecting the gear ratio, the designer must consider both the gear ratio's impact on the overall size of the system [5], [66] and its impact on the system's dynamic behavior.

$$k_J = \frac{J_l}{J_h G^2} = \frac{J_l'}{J_h'} \quad (70)$$

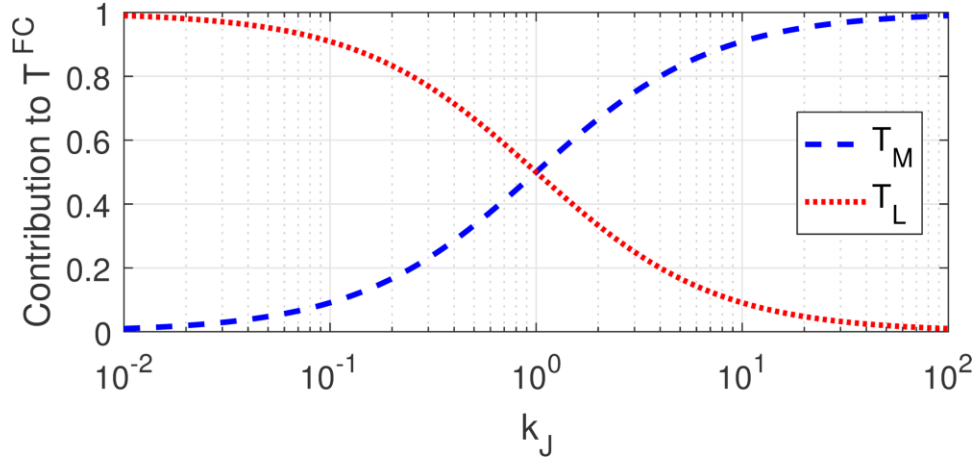


**Figure 6.8** The impact of  $k_J$  on how much the per unit (relative to the slip torques of their respective rotors) machine torque and load torque contribute to  $T^{FC}$ .

### 6.2.2. Responses to Step Changes in Torque

The conservation of energy approach has two significant limitations. First, the torques must be known as a function of position, rather than time, and, second, it assumes that the losses are negligible. However, this approach can still address one significant issue: whether a given step change in torque on either side of the gear will cause it to slip. With a step change in torque, the torque is known with respect to position. Also, magnetic gears are often quite underdamped, so very little energy is lost by the time the gear reaches the maximum extent of its torque angle oscillation for the first time after the step change [61], [62]. The maximum torque angle reached,  $\theta_T^m$ , is the angle at which the kinetic energy of the rotating inertia reaches 0, which is where the energy input into the Figure 6.6 system equals the change in the energy stored in the nonlinear spring, as given by (71), where the torque angle was initially in steady-state at  $\theta_T^i$ . In the case of a step change in torque, (71) becomes (72), where  $T^{FC}$  is the torque in

Figure 6.6 after the step change. This is equivalent to finding the angle where the areas under the step torque and the nonlinear torque curves in Figure 6.7 are equal. The trivial solution,  $\theta_T^m = \theta_T^i$ , is the minimum boundary of the oscillation, which is the initial torque angle. The nontrivial solution of (72) gives the maximum boundary of the oscillation. If no nontrivial solution exists, the gear will slip. To check this, the kinetic energy can be evaluated at the torque angle between  $\pi/2$  and  $3\pi/2$  where  $T^{FC}$  is equal to the nonlinear spring torque, defined as  $\theta_T^{slip}$  in (73). For the gear not to slip,  $T^{FC}$  must be less than  $T_C$ , and the condition given in (74) must also be true.

$$\int_{\theta_T^i}^{\theta_T^m} T^{FC} d\theta_T = \int_{\theta_T^i}^{\theta_T^m} T_C \sin(\theta_T) d\theta_T \quad (71)$$

$$T^{FC} \cdot (\theta_T^m - \theta_T^i) = T_C \cdot (\cos(\theta_T^i) - \cos(\theta_T^m)) \quad (72)$$

$$\theta_T^{slip} = \pi - \sin^{-1} \left( \frac{T^{FC}}{T_C} \right) \quad (73)$$

$$(\theta_T^{slip} - \theta_T^i) < \frac{T_C}{T^{FC}} \cdot (\cos(\theta_T^i) - \cos(\theta_T^{slip})) \quad (74)$$

The angular velocity of the inertia in the torque angle reference frame can be determined as a function of the torque angle from the inertia's kinetic energy, according to (75), assuming that losses are negligible. The angular velocity in the torque angle reference frame can be transformed back to the Figure 6.1 model to determine the angular velocities of the oscillations on each rotor. If the step change in torque does not cause the gear to slip, the maximum angular velocity in the torque angle reference frame,  $\omega_T^{max}$ , occurs at the torque angle between  $-\pi/2$  and  $\pi/2$  where the torque from the

nonlinear spring is equal to  $T^{FC}$ . This angle is given as  $\theta_T^{eq}$  in (76). The maximum angular velocity in the torque angle reference frame is given by (77).

$$\omega_T(\theta_T) = \pm \sqrt{\frac{2}{J_T} \int_{\theta_T^i}^{\theta_T} (T^{FC} - T_C \sin(\theta)) d\theta} \quad (75)$$

$$\theta_T^{eq} = \sin^{-1} \left( \frac{T^{FC}}{T_C} \right) \quad (76)$$

$$\omega_T^{\max} = \sqrt{\frac{2 \cdot (T^{FC} \cdot (\theta_T^{eq} - \theta_T^i) - T_C \cdot (\cos(\theta_T^i) - \cos(\theta_T^{eq})))}{J_T}} \quad (77)$$

With the velocity known as a function of the torque angle, the frequency of oscillation can be calculated as  $f_o$  in (78), using the positive sign in (75). Similar equations can be derived for cases where changing  $T^{FC}$  decreases the torque angle.

$$f_o = \left( 2 \int_{\theta_T^i}^{\theta_T^m} \frac{1}{\omega_T(\theta_T)} d\theta_T \right)^{-1} \quad (78)$$

### 6.3. Model Validation

The proposed nonlinear model is used to evaluate a scenario where the external torque applied to the HSR is suddenly changed to various per unit values starting from different initial steady-state torque angles. The external torque on the LSR is kept at its initial value. The magnitude of the torque angle oscillation, the maximum angular velocity of the inertia in the torque angle reference frame, and the oscillation frequency are calculated using (72), (77), and (78), respectively. Three values of  $k_f$  are considered. In each case,  $J_T$  is set to 1 pu where, in the torque angle reference frame, the base torque, base time, and base angle are  $T_C$ , 1 s, and 1 rad, respectively. The base torque for each

rotor is the slip torque of that rotor. The results are compared against those produced by a Simulink model with the same parameters, which is shown in Figure 6.9. The proposed model and the Simulink model both assume that the torque is a sinusoidal function of the torque angle, but, in an actual magnetic gear, harmonics produce torque ripples on the rotors. Thus, transient finite element analysis (FEA) is used to evaluate three different coaxial magnetic gear designs, FEA 1, FEA 2, and FEA 3, with gear ratios of -2.053:1, -12.33:1, and -12:1, respectively, which have their cross-sections depicted in Figure 6.10. Figure 6.11, Figure 6.12, and Figure 6.13 show the torque angle curves of these designs. FEA 1's torque angle curves are very sinusoidal due to the high least common multiple of the pole counts [3]. However, due to its integer gear ratio, FEA 3's HSR torque angle curve is more distorted. FEA 2's torque angle curve is more distorted than that of FEA 1 but less distorted than that of FEA 3. For the FEA, eddy effects in the NdFeB N42 magnets and core losses in the M47 modulators and back irons also affect the torques on the two rotors. In each case, both rotors are assumed to be initially stationary. A model linearized about the initial torque angle is also used to evaluate the designs.

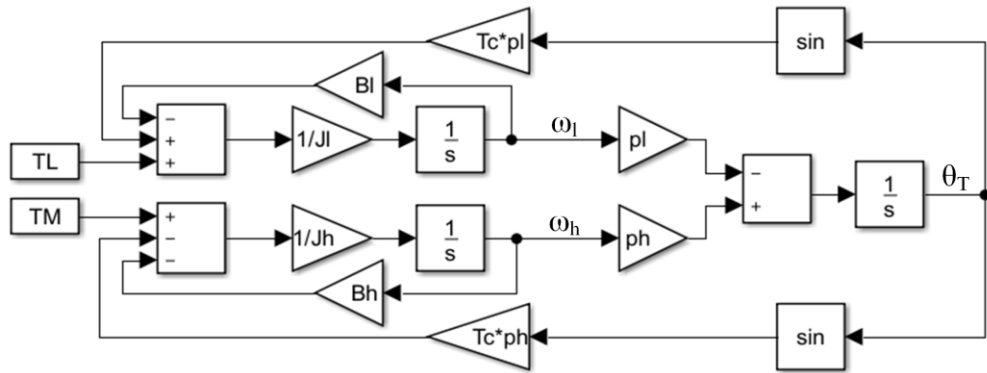


Figure 6.9 The Simulink model used for comparison in this study.

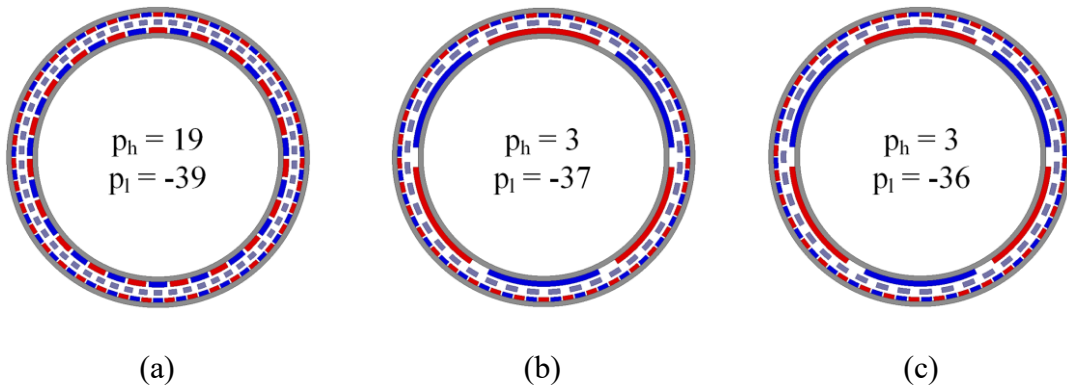
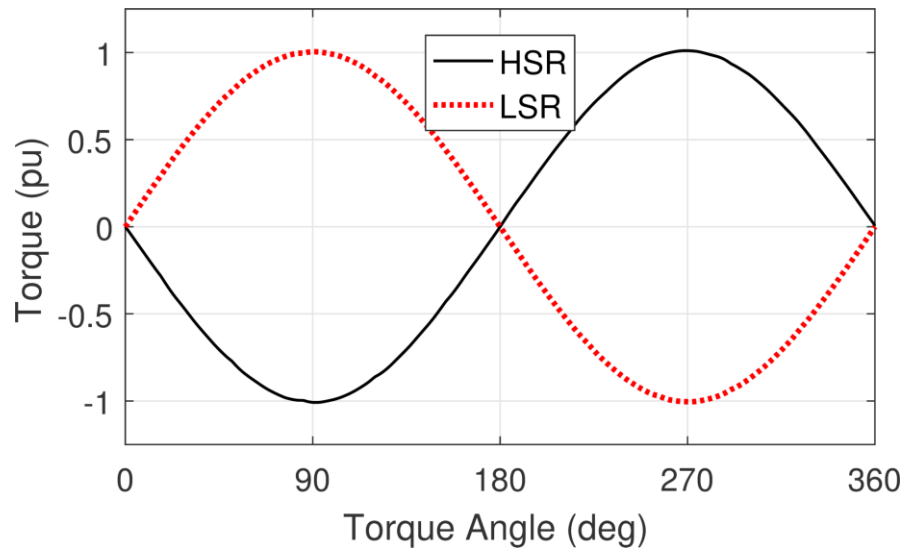
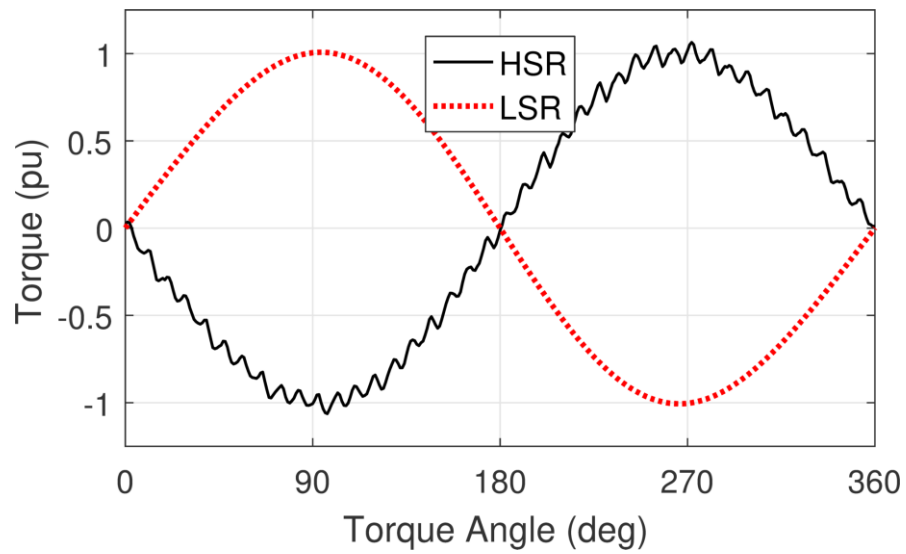


Figure 6.10 Cross-sections of the (a) FEA 1, (b) FEA 2, and (c) FEA 3 coaxial magnetic gear designs.





**Figure 6.11 Torque angle curves of the FEA 1 design.**



**Figure 6.12 Torque angle curves of the FEA 2 design.**

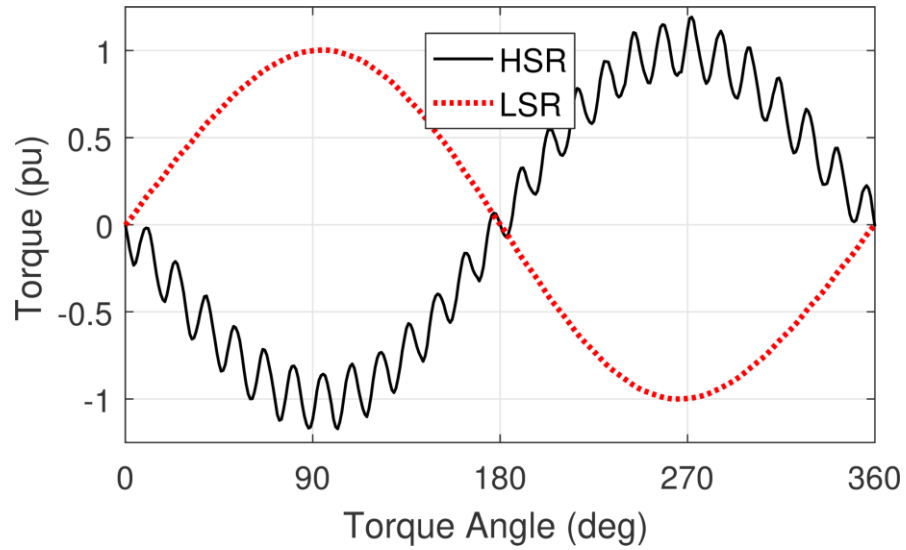


**Figure 6.13 Torque angle curves of the FEA 3 design.**

Table 6.1 and Table 6.2 compare the results for each of the different analysis methods with  $k_J = 0.25$ , Table 6.3 and Table 6.4 compare the results with  $k_J = 1$ , and Table 6.5 and Table 6.6 compare the results with  $k_J = 4$ . In these tables the red areas indicate cases that cause the gear to slip. These tables also show the percentages of the cases in which the proposed model agrees with each of the other models about whether the gear will slip. For the cases that both models agree will not slip, the tables provide the average value of the absolute difference between the quantities predicted by the two models. For the linearized model, the gear is assumed to slip if it reaches the same torque angle as would cause slipping in the nonlinear model ( $\pi - \sin^{-1}(T^{FC}/T_C)$ ).

**Table 6.1 Analysis Methods Oscillation Comparison with  $k_J = 0.25$  and  $B_T = 0$ .**

| Model      | Slip Prediction Agreement | Torque Angle Oscillation (deg)  |
|------------|---------------------------|---|
| Proposed   | N/A                       | <p>HSR Torque (pu) vs Initial Torque (pu)</p>                                       |
| Simulink   | 100.0%                    | <p>HSR Torque (pu) vs Initial Torque (pu)</p> <p>Average Discrepancy = 0.0 deg</p>  |
| FEA 1      | 99.7%                     | <p>HSR Torque (pu) vs Initial Torque (pu)</p> <p>Average Discrepancy = 0.5 deg</p>  |
| FEA 2      | 98.8%                     | <p>HSR Torque (pu) vs Initial Torque (pu)</p> <p>Average Discrepancy = 4.0 deg</p>  |
| FEA 3      | 98.7%                     | <p>HSR Torque (pu) vs Initial Torque (pu)</p> <p>Average Discrepancy = 4.4 deg</p>  |
| Linearized | 85.3%                     | <p>HSR Torque (pu) vs Initial Torque (pu)</p> <p>Average Discrepancy = 12.4 deg</p> |

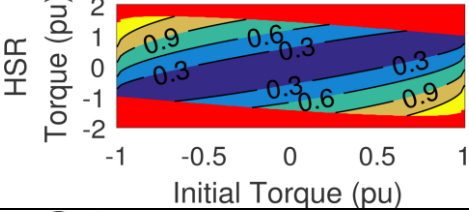
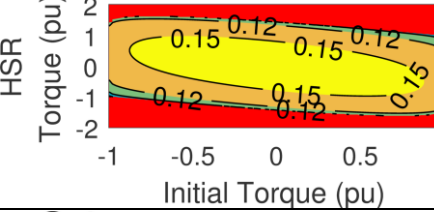
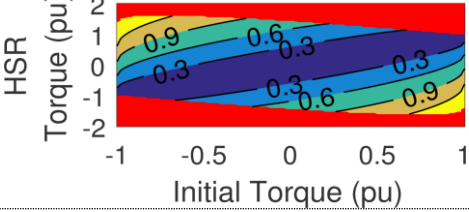
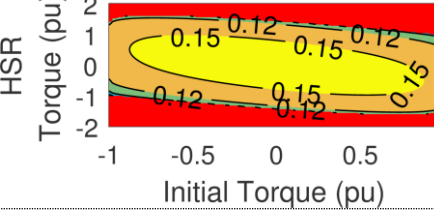
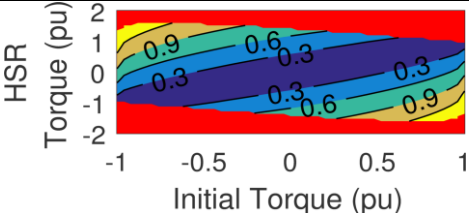
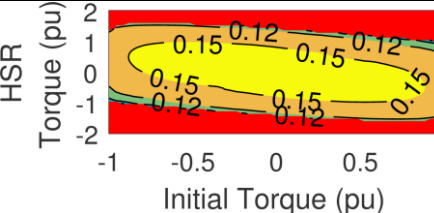
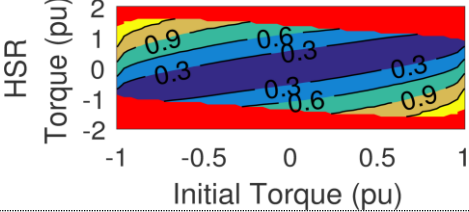
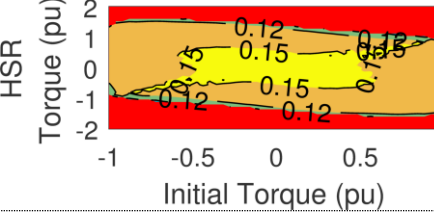
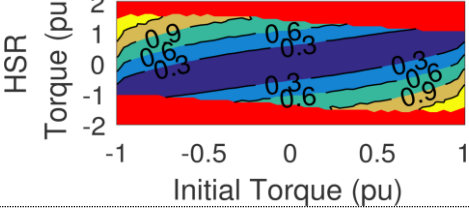
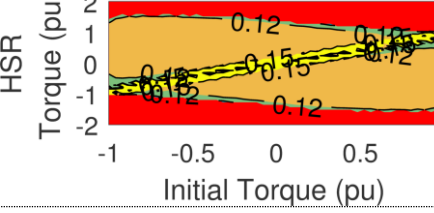
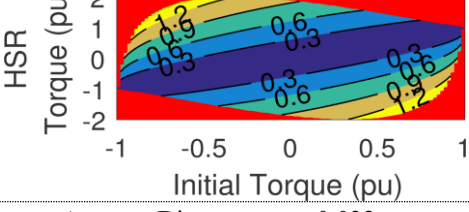
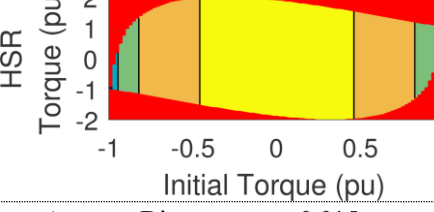
**Table 6.2 Analysis Methods Frequency and Velocity Comparison with  $k_J = 0.25$  and  $B_T = 0$ .**

| Model      | Maximum Angular Velocity (pu)  | Oscillation Frequency (pu)     |
|------------|--------------------------------|--------------------------------|
| Proposed   |                                |                                |
|            | Average Discrepancy = 0.000 pu | Average Discrepancy = 0.000 pu |
| Simulink   |                                |                                |
|            | Average Discrepancy = 0.000 pu | Average Discrepancy = 0.000 pu |
| FEA 1      |                                |                                |
|            | Average Discrepancy = 0.004 pu | Average Discrepancy = 0.000 pu |
| FEA 2      |                                |                                |
|            | Average Discrepancy = 0.024 pu | Average Discrepancy = 0.008 pu |
| FEA 3      |                                |                                |
|            | Average Discrepancy = 0.032 pu | Average Discrepancy = 0.010 pu |
| Linearized |                                |                                |
|            | Average Discrepancy = 0.032 pu | Average Discrepancy = 0.015 pu |

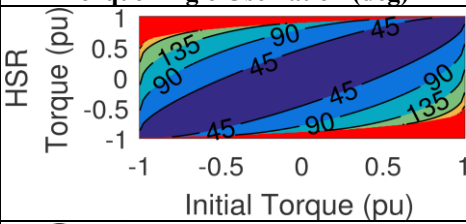
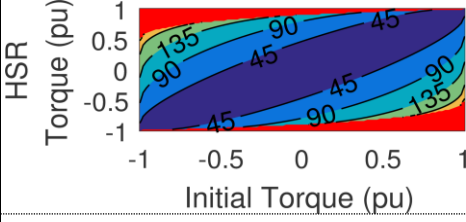
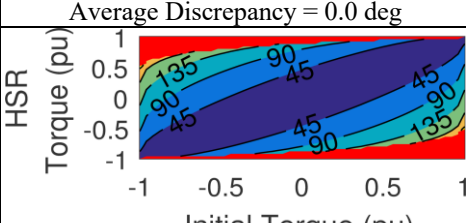
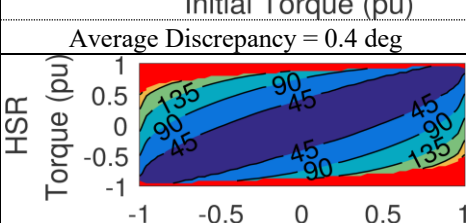
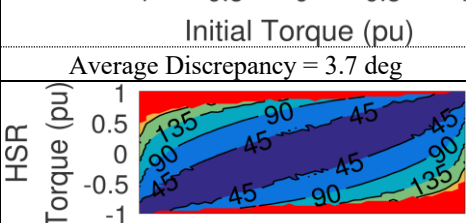
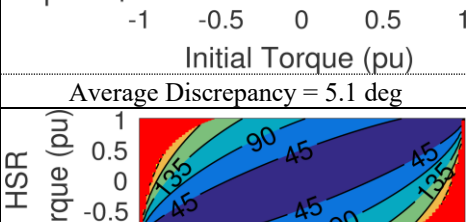
**Table 6.3 Analysis Methods Oscillation Comparison with  $k_J = 1$  and  $B_T = 0$ .**

| Model      | Slip Prediction Agreement | Torque Angle Oscillation (deg)  |
|------------|---------------------------|---|
| Proposed   | N/A                       | <p>HSR Torque (pu) vs Initial Torque (pu)</p>                                       |
| Simulink   | 100.0%                    | <p>HSR Torque (pu) vs Initial Torque (pu)</p> <p>Average Discrepancy = 0.0 deg</p>  |
| FEA 1      | 99.8%                     | <p>HSR Torque (pu) vs Initial Torque (pu)</p> <p>Average Discrepancy = 0.4 deg</p>  |
| FEA 2      | 99.2%                     | <p>HSR Torque (pu) vs Initial Torque (pu)</p> <p>Average Discrepancy = 4.0 deg</p>  |
| FEA 3      | 98.5%                     | <p>HSR Torque (pu) vs Initial Torque (pu)</p> <p>Average Discrepancy = 4.1 deg</p>  |
| Linearized | 82.4%                     | <p>HSR Torque (pu) vs Initial Torque (pu)</p> <p>Average Discrepancy = 12.4 deg</p> |

**Table 6.4 Analysis Methods Frequency and Velocity Comparison with  $k_J = 1$  and  $B_T = 0$ .**

| Model      | Maximum Angular Velocity (pu)   | Oscillation Frequency (pu)   |
|------------|---|--|
| Proposed   |    |    |
|            | Average Discrepancy = 0.000 pu  | Average Discrepancy = 0.000 pu   |
| Simulink   |    |    |
|            | Average Discrepancy = 0.000 pu  | Average Discrepancy = 0.000 pu   |
| FEA 1      |   |   |
|            | Average Discrepancy = 0.004 pu  | Average Discrepancy = 0.001 pu   |
| FEA 2      |  |  |
|            | Average Discrepancy = 0.028 pu  | Average Discrepancy = 0.005 pu   |
| FEA 3      |  |  |
|            | Average Discrepancy = 0.033 pu  | Average Discrepancy = 0.021 pu   |
| Linearized |  |  |
|            | Average Discrepancy = 0.032 pu  | Average Discrepancy = 0.015 pu   |

**Table 6.5 Analysis Methods Oscillation Comparison with  $k_J = 4$  and  $B_T = 0$ .**

| Model      | Slip Prediction Agreement | Torque Angle Oscillation (deg)   |
|------------|---------------------------|--|
| Proposed   | N/A                       |  <p>HSR Torque (pu)</p> <p>Initial Torque (pu)</p>   |
| Simulink   | 100.0%                    |  <p>HSR Torque (pu)</p> <p>Initial Torque (pu)</p> <p>Average Discrepancy = 0.0 deg</p>    |
| FEA 1      | 100.0%                    |  <p>HSR Torque (pu)</p> <p>Initial Torque (pu)</p> <p>Average Discrepancy = 0.4 deg</p>    |
| FEA 2      | 98.8%                     |  <p>HSR Torque (pu)</p> <p>Initial Torque (pu)</p> <p>Average Discrepancy = 3.7 deg</p>   |
| FEA 3      | 98.6%                     |  <p>HSR Torque (pu)</p> <p>Initial Torque (pu)</p> <p>Average Discrepancy = 5.1 deg</p>  |
| Linearized | 86.6%                     |  <p>HSR Torque (pu)</p> <p>Initial Torque (pu)</p> <p>Average Discrepancy = 12.4 deg</p> |

**Table 6.6 Analysis Methods Frequency and Velocity Comparison with  $k_J = 4$  and  $B_T = 0$ .**

| Model      | Maximum Angular Velocity (pu)  | Oscillation Frequency (pu)     |
|------------|--------------------------------|--------------------------------|
| Proposed   |                                |                                |
|            | Average Discrepancy = 0.000 pu | Average Discrepancy = 0.000 pu |
| Simulink   |                                |                                |
|            | Average Discrepancy = 0.000 pu | Average Discrepancy = 0.000 pu |
| FEA 1      |                                |                                |
|            | Average Discrepancy = 0.006 pu | Average Discrepancy = 0.001 pu |
| FEA 2      |                                |                                |
|            | Average Discrepancy = 0.036 pu | Average Discrepancy = 0.004 pu |
| FEA 3      |                                |                                |
|            | Average Discrepancy = 0.054 pu | Average Discrepancy = 0.037 pu |
| Linearized |                                |                                |
|            | Average Discrepancy = 0.032 pu | Average Discrepancy = 0.015 pu |



Table 6.1, Table 6.2, Table 6.3, Table 6.4, Table 6.5, and Table 6.6 show that the proposed model agrees very well with the Simulink model and with the FEA 1 model. However, for the FEA 2 and FEA 3 models, the torque ripple in the torque angle curves produces some discrepancies in the oscillation frequency and maximum angular velocity in the torque angle reference frame, especially when the applied torque does not change very much and the behavior of the system is dominated by the torque ripple, rather than the change in applied torque. Both the proposed model and the Simulink model fail to accurately capture the behavior for these cases because the discrepancies result from the assumption that the torques are a perfectly sinusoidal function of the torque angle. Therefore, the only way to accurately account for this behavior is to incorporate the torque ripples into the model. Nonetheless, the proposed model still achieves very good agreement with FEA 2 and FEA 3 about which cases will cause the gear to slip. The linearized model correlates fairly well with the Simulink model and FEA 1 when the change in applied torque is small. However, the linearized model becomes quite inaccurate for large changes in applied torque and incorrectly predicts whether the gear will slip for over 13% of the cases.

Table 6.1, Table 6.2, Table 6.3, Table 6.4, Table 6.5, and Table 6.6 also illustrate that with small  $k_J$  values, much larger torques can be applied to the HSR without slipping the gear. If the gear is driven by a motor on the HSR, this would allow the motor to rapidly accelerate the gear by applying torques larger than the HSR slip torque while the gear is accelerating. The tables also illustrate that the oscillation frequency depends on both the starting torque angle and the change in applied torque. Because the

nonlinear spring is stiffest at a torque angle of 0, the oscillation frequency is highest when the torque angle oscillates near 0, but the oscillation frequency becomes lower when the gear is close to slipping. However, for designs with large torque ripples, such as FEA 2 and FEA 3, the torque ripple significantly affects the oscillation frequency if the change in applied torque is small. This torque ripple is the reason that there is a diagonal band of higher frequencies around the line where the HSR torque equals the initial torque on the oscillation frequency plots for the FEA 3 model

In Table 6.1, Table 6.2, Table 6.3, Table 6.4, Table 6.5, and Table 6.6, the FEA models incorporate the effects of eddy currents and core losses, but viscous friction is assumed to be negligible in all cases. To illustrate the impact of viscous friction on the proposed model's accuracy, Table 6.7, Table 6.8, Table 6.9, Table 6.10, Table 6.11, and Table 6.12 compare the proposed model, which assumes the losses are negligible, against the Simulink and FEA models with  $B_T = 0.1$  pu. Eddy current losses and core losses are again included in the FEA models.

**Table 6.7 Analysis Methods Oscillation Comparison with  $k_J = 0.25$  and  $B_T = 0.1$  pu.**

| Model    | Slip Prediction Agreement | Torque Angle Oscillation (deg)       |
|----------|---------------------------|--------------------------------------|
| Proposed | N/A                       |                                      |
| Simulink | 95.9%                     | <p>Average Discrepancy = 6.3 deg</p> |
| FEA 1    | 95.6%                     | <p>Average Discrepancy = 6.3 deg</p> |
| FEA 2    | 96.5%                     | <p>Average Discrepancy = 6.1 deg</p> |
| FEA 3    | 96.5%                     | <p>Average Discrepancy = 6.4 deg</p> |

**Table 6.8 Analysis Methods Frequency and Velocity Comparison with  $k_J = 0.25$  and  $B_T = 0.1$  pu.**

| Model    | Maximum Angular Velocity (pu)  | Oscillation Frequency (pu)     |
|----------|--------------------------------|--------------------------------|
| Proposed |                                |                                |
|          | Average Discrepancy = 0.039 pu | Average Discrepancy = 0.003 pu |
| Simulink |                                |                                |
|          | Average Discrepancy = 0.039 pu | Average Discrepancy = 0.003 pu |
| FEA 1    |                                |                                |
|          | Average Discrepancy = 0.039 pu | Average Discrepancy = 0.003 pu |
| FEA 2    |                                |                                |
|          | Average Discrepancy = 0.052 pu | Average Discrepancy = 0.007 pu |
| FEA 3    |                                |                                |
|          | Average Discrepancy = 0.055 pu | Average Discrepancy = 0.010 pu |

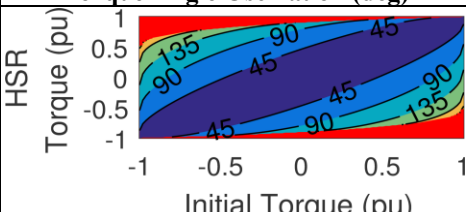
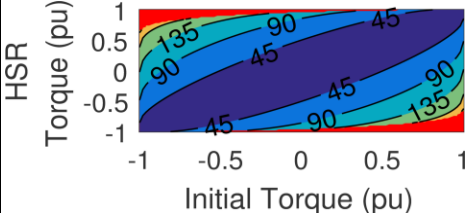
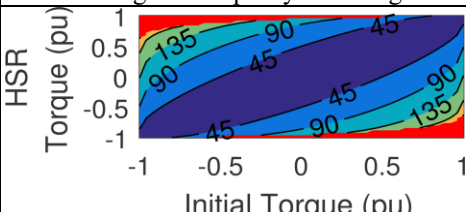
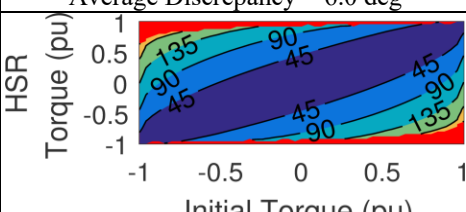
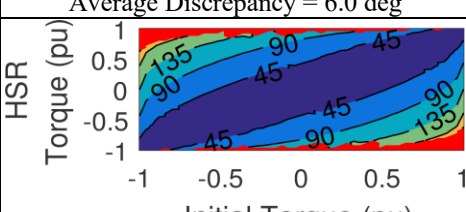
**Table 6.9 Analysis Methods Oscillation Comparison with  $k_J = 1$  and  $B_T = 0.1$  pu.**

| Model    | Slip Prediction Agreement | Torque Angle Oscillation (deg)   |
|----------|---------------------------|--|
| Proposed | N/A                       | <p>HSR Torque (pu) vs Initial Torque (pu) contour plot. The plot shows torque angle oscillation contours for 45, 90, and 135 degrees. The x-axis (Initial Torque) ranges from -1 to 1, and the y-axis (HSR Torque) ranges from -2 to 2.</p>                                      |
| Simulink | 94.8%                     | <p>HSR Torque (pu) vs Initial Torque (pu) contour plot. The plot shows torque angle oscillation contours for 45, 90, and 135 degrees. The x-axis (Initial Torque) ranges from -1 to 1, and the y-axis (HSR Torque) ranges from -2 to 2.</p> <p>Average Discrepancy = 6.2 deg</p> |
| FEA 1    | 94.9%                     | <p>HSR Torque (pu) vs Initial Torque (pu) contour plot. The plot shows torque angle oscillation contours for 45, 90, and 135 degrees. The x-axis (Initial Torque) ranges from -1 to 1, and the y-axis (HSR Torque) ranges from -2 to 2.</p> <p>Average Discrepancy = 6.2 deg</p> |
| FEA 2    | 95.5%                     | <p>HSR Torque (pu) vs Initial Torque (pu) contour plot. The plot shows torque angle oscillation contours for 45, 90, and 135 degrees. The x-axis (Initial Torque) ranges from -1 to 1, and the y-axis (HSR Torque) ranges from -2 to 2.</p> <p>Average Discrepancy = 6.1 deg</p> |
| FEA 3    | 95.2%                     | <p>HSR Torque (pu) vs Initial Torque (pu) contour plot. The plot shows torque angle oscillation contours for 45, 90, and 135 degrees. The x-axis (Initial Torque) ranges from -1 to 1, and the y-axis (HSR Torque) ranges from -2 to 2.</p> <p>Average Discrepancy = 6.5 deg</p> |

**Table 6.10 Analysis Methods Frequency and Velocity Comparison with  $k_J = 1$  and  $B_T = 0.1$  pu.**

| Model    | Maximum Angular Velocity (pu)  | Oscillation Frequency (pu)     |
|----------|--------------------------------|--------------------------------|
| Proposed |                                |                                |
|          | Average Discrepancy = 0.038 pu | Average Discrepancy = 0.003 pu |
| Simulink |                                |                                |
|          | Average Discrepancy = 0.037 pu | Average Discrepancy = 0.003 pu |
| FEA 1    |                                |                                |
|          | Average Discrepancy = 0.053 pu | Average Discrepancy = 0.006 pu |
| FEA 2    |                                |                                |
|          | Average Discrepancy = 0.057 pu | Average Discrepancy = 0.021 pu |
| FEA 3    |                                |                                |
|          | Average Discrepancy = 0.053 pu | Average Discrepancy = 0.006 pu |

**Table 6.11 Analysis Methods Oscillation Comparison with  $k_J = 4$  and  $B_T = 0.1$  pu.**

| Model    | Slip Prediction Agreement | Torque Angle Oscillation (deg)  |
|----------|---------------------------|---|
| Proposed | N/A                       |   |
| Simulink | 93.6%                     |  <p>Average Discrepancy = 6.2 deg</p>   |
| FEA 1    | 93.5%                     |  <p>Average Discrepancy = 6.0 deg</p>   |
| FEA 2    | 94.5%                     |  <p>Average Discrepancy = 6.0 deg</p> |
| FEA 3    | 93.7%                     |  <p>Average Discrepancy = 6.9 deg</p> |

**Table 6.12 Analysis Methods Frequency and Velocity Comparison with  $k_J = 4$  and  $B_T = 0.1$  pu.**

| Model    | Maximum Angular Velocity (pu)  | Oscillation Frequency (pu)     |
|----------|--------------------------------|--------------------------------|
| Proposed |                                |                                |
|          | Average Discrepancy = 0.039 pu | Average Discrepancy = 0.003 pu |
| Simulink |                                |                                |
|          | Average Discrepancy = 0.036 pu | Average Discrepancy = 0.003 pu |
| FEA 1    |                                |                                |
|          | Average Discrepancy = 0.054 pu | Average Discrepancy = 0.005 pu |
| FEA 2    |                                |                                |
|          | Average Discrepancy = 0.063 pu | Average Discrepancy = 0.037 pu |
| FEA 3    |                                |                                |
|          | Average Discrepancy = 0.063 pu | Average Discrepancy = 0.037 pu |



Table 6.7, Table 6.8, Table 6.9, Table 6.10, Table 6.11, and Table 6.12 show that the viscous friction does prevent a few cases from slipping. Thus, the proposed model predicts that some cases would slip where the other models predict that those cases would not slip. Nonetheless, the proposed model still agrees with each of the other models for at least 93.5% of the cases. Thus, even with  $B_T$  as high as 0.1 pu, the viscous friction has a limited impact on the transient performance of the system immediately after the change in applied torque. Even though the proposed model neglects the viscous friction, it can still predict the dynamic response of the system for the first torque angle oscillation after a step change in applied torque with reasonable accuracy. After this first oscillation, the losses in the system will gradually damp out the energy in the later oscillations. Therefore, if this first oscillation does not cause the gear to slip, the later oscillations will not cause it to slip, unless there is another change in the applied torque.

#### **6.4. Conclusion**

This section presents a nonlinear approach for evaluating the dynamics of magnetic gears. First, superposition is applied to separate the rigid body motion of the two rotors from the motion about a fixed center. Second, this motion about a fixed center is transformed into the torque angle reference frame, which contains a single inertia and a single nonlinear torsional spring. Third, the extent of the torque angle oscillations, the maximum angular velocity, and the oscillation frequency are evaluated in the torque angle reference frame using the conservation of energy principle for the system (assuming losses are negligible). This approach is verified through comparison with Simulink and FEA results. The proposed model agrees extremely well with the

Simulink model and a FEA model with very little torque ripple. However, for the FEA models with larger torque ripples, there are discrepancies between the velocities and oscillation frequencies predicted by the proposed approach and those predicted by the FEA when the system experiences only a small change in torque. These discrepancies result from the deviation from the assumed perfectly sinusoidal torque angle curves, so the only way to eliminate these discrepancies is to include the torque ripple in the model. Nonetheless, the proposed model agrees with each FEA model about whether the gear will slip for over 98.5% of the cases, and the proposed model is able to analyze cases significantly faster than FEA. On the other hand, a linearized model is shown to be inaccurate when there is a significant change in the torque applied to the gear. Thus, the linearized model incorrectly predicts whether the gear will slip for over 13% of the cases. A case with a viscous friction coefficient of 0.1 pu is also evaluated using Simulink and FEA, but the viscous friction in this case makes a limited impact on the dynamic behavior of the system immediately following a change in the applied torque. Even though the proposed model does not consider losses, it still agrees with each FEA model for at least 93.5% of the cases when the FEA model considers viscous friction.

This analysis also reveals that the effective inertia ratio, which depends on the gear ratio and the inertias of the two rotors, has a significant impact on the dynamic performance of the system. It determines the extent to which torques applied to each rotor affect the torque angle of the gear and the extent to which oscillations of the torque angle cause oscillations on each rotor. A small effective inertia ratio means that the torques applied to the LSR will affect the torque angle much more than torques applied

to the HSR and that torque angle oscillations will cause more oscillations on the LSR than on the HSR, whereas a large effective inertia ratio will have the opposite effects.

## 7. ANALYSIS OF RADIAL FLUX COAXIAL MAGNETIC GEARS WITH HALBACH ARRAYS

The previous sections focused on magnetic gears with surface mounted magnets magnetized radially for radial flux gears or axially for axial flux gears. However, other strategies have been proposed for magnetic gears, including interior permanent magnets [55], flux focusing magnet arrangements [4], [30], [33], [42], [54], [60], and reluctance poles [67]. This section focuses on evaluating magnetic gears with Halbach arrays.

Halbach arrays involve magnets with a tangential magnetization component, in addition to the radially or axially magnetized magnets, as illustrated in Figure 7.1, Figure 7.2, and Figure 7.3 for Halbach arrays with different number of discrete magnetizations. A Halbach array can be used to increase the magnetic field strength on one side of the array while decreasing the magnetic field strength on the other side of the array [68]. For a discrete Halbach array, the effectiveness of the magnetic flux strengthening on one side and the flux shielding on the other side increases with the number of segments per pole. Thus, the conventional magnetization pattern in Figure 7.1 will tend to produce the same flux pattern on both sides of the array, but the discrete Halbach array with two segments per pole depicted in Figure 7.2 will have more flux above the array and less flux below it. This effect will be even more significant for the discrete Halbach array with four segments per pole depicted in Figure 7.3. Additionally, Halbach arrays may result in a more sinusoidal flux distribution than conventional surface mounted magnet arrangements with purely axial, radial, or parallel magnetizations [68].



**Figure 7.1 Conventional surface permanent magnet magnetization arrangement, which is equivalent to a discrete Halbach array with one segment per pole.**



**Figure 7.2 Discrete Halbach array with two segments per pole.**



**Figure 7.3 Discrete Halbach array with four segments per pole.**

Therefore, Halbach arrays have been proposed for use in electric machines [68], [69], [70], [71], [72]. The stronger field on one side of the Halbach array can be used to increase the air gap flux density to provide more torque [72]. Additionally, the flux shielding effect on the other side of the array can be used to reduce the need for a rotor back iron, which can reduce the weight and the rotor inertia [73], [74], [75], [76]. Halbach arrays have also been shown to have the potential to improve the efficiency of electric machines [69], [72]. Furthermore, the more sinusoidal flux density distribution created by the Halbach array can reduce the cogging torque and torque ripple of the design [68], [71].

Similarly, Halbach arrays have been shown to increase torque density, improve efficiency, and reduce torque ripple in magnetic gears [31], [49], [77], [78]. Based on the flux shielding effect, it has been proposed that Halbach arrays can reduce the amount

of flux in the back irons of radial flux coaxial magnetic gears, allowing smaller back irons to be used, which reduces the weight and rotor inertias [78]. Additionally, the flux shielding effect of Halbach arrays has been shown to reduce the need for back irons in axial flux coaxial magnetic gears [31]. If the back irons are removed completely from an electric machine, the design is called “coreless” or described as having an “air core,” even though the magnets must be mounted on something, often a lightweight, nonmetallic material, such as plastic. Figure 7.4 compares the cross-section of a conventional radial flux coaxial magnetic gear with magnets mounted on the surfaces of conventional back irons with the cross-section of an air core radial flux coaxial magnetic gear with Halbach arrays on Rotor 1 and Rotor 3. The design presented in Figure 7.4(b) has three segments per pole on Rotor 1 and two segments per pole on Rotor 3. This study uses a parametric simulation study to evaluate radial flux coaxial magnetic gears with Halbach arrays either with or without back irons for applications where minimizing weight is critical.

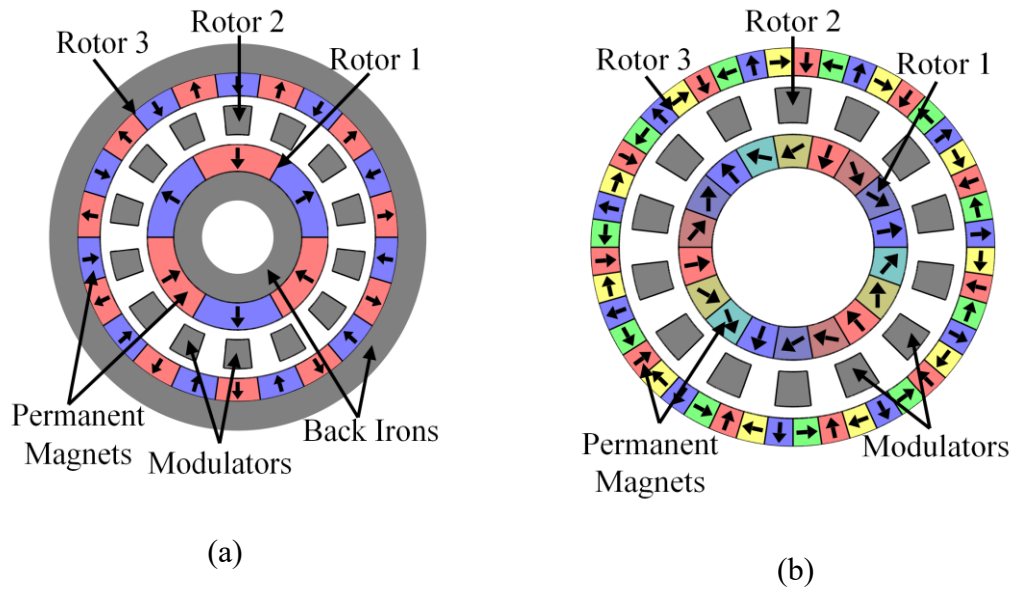


**Figure 7.4 Magnetically active cross-sections of radial flux coaxial magnetic gears with (a) permanent magnets mounted on back irons and (b) Halbach arrays mounted on air cores.**

### 7.1. Design Study Methodology

Since the most significant advantage of Halbach air core designs is their low mass, the primary metric considered in this study is gravimetric torque density (GTD), as defined in (14), which normalizes the design's slip torque in terms of its active mass. Both 2D and 3D finite element analysis (FEA) were used to evaluate the designs. The modulators are made from M47 steel, and the permanent magnets (PMs) are made from NdFeB N42, which has a remanence of 1.3 T. For designs with back irons, the back irons are made from M47 steel.

The design parameters for this study are specified in Table 7.1. The Rotor 1 pole pair counts are specified in Table 7.2. These pole counts are selected to ensure that the optimal values for maximizing GTD are not higher than the largest pole count

considered for each outer radius and nearest integer gear ratio combination. All of the cases specified in Table 7.1 and Table 7.2 were evaluated using 2D FEA, except for those cases which would have a negative inner radius. Based on the results of the 2D simulations, 2600 of the best cross-sectional designs were evaluated using 3D FEA at each of the stack lengths specified in Table 7.1. The PM tangential fill factors were set at 100% for each case and modulator fill factors of 50% were used. For the discrete Halbach arrays, all the segments on each rotor were assumed to have the same tangential widths.

**Table 7.1 Parameter Sweep Values.**

| <b>Parameter</b>                          | <b>Values</b>        |
|---|----------------------|
| Integer part of gear ratio ( $G_{Int}$ )  | 4, 9, 16             |
| Outer radius ( $R_{Out}$ )                | 50, 75, 100, 150 mm  |
| Rotor 1 segments per pole ( $N_1$ )       | 1, 2, 3, 4           |
| Rotor 3 segments per pole ( $N_3$ )       | 1, 2, 3, 4           |
| Rotor 1 back iron thickness ( $T_{BI1}$ ) | 0, 5, 10, 20 mm      |
| Rotor 3 back iron thickness ( $T_{BI3}$ ) |                      |
| For $T_{BI1} = 0$ mm                      | 0, 5, 10, 20 mm      |
| For $T_{BI1} = 5$ mm                      | 0, 5 mm              |
| For $T_{BI1} = 10$ mm                     | 0, 5, 10 mm          |
| For $T_{BI1} = 20$ mm                     | 0, 5, 10, 20 mm      |
| Rotor 1 PM thickness ( $T_{PM1}$ )        | 3, 6, 9, 12, 15 mm   |
| PM thickness ratio ( $k_{PM}$ )           | 0.5, 0.625, 0.75     |
| Air gap thicknesses ( $T_{AG}$ )          | 1 mm                 |
| Modulator thickness ( $T_{Mods}$ )        | 10 mm                |
| Stack Length ( $L_{Stack}$ )              | 5, 10, 20, 30, 50 mm |



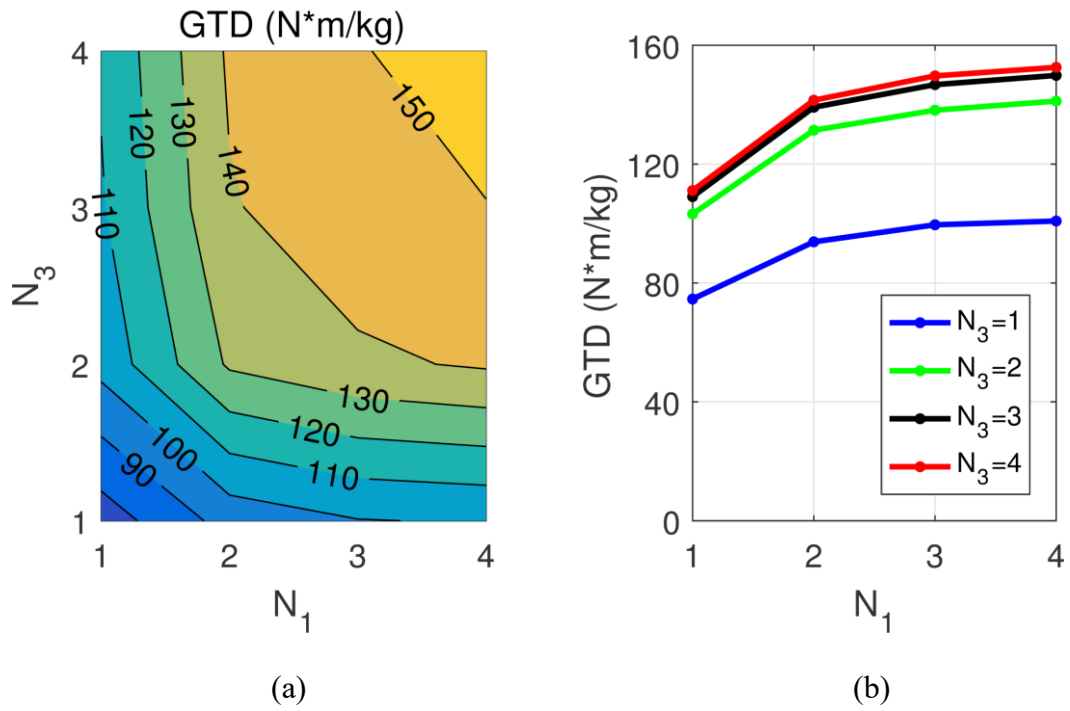
**Table 7.2 Rotor 1 Pole Pair Counts for Each Outer Radius and Nearest Integer Gear Ratio Combination.**

| <b>R<sub>Out</sub></b> | <b>G<sub>Int</sub> = 4</b> | <b>G<sub>Int</sub> = 9</b> | <b>G<sub>Int</sub> = 16</b> |
|------------------------|----------------------------|----------------------------|-----------------------------|
| 50 mm                  | 3, 5, 7                    | 3, 5, 7                    | 3, 5                        |
| 75 mm                  | 3, 5, 7, 9                 | 3, 5, 7                    | 3, 5                        |
| 100 mm                 | 3, 5, 7, ... 17            | 3, 5, 7, 9, 11             | 3, 5, 7                     |
| 150 mm                 | 3, 5, 7, ... 21            | 3, 5, 7, ... 13            | 3, 5, 7, 9                  |

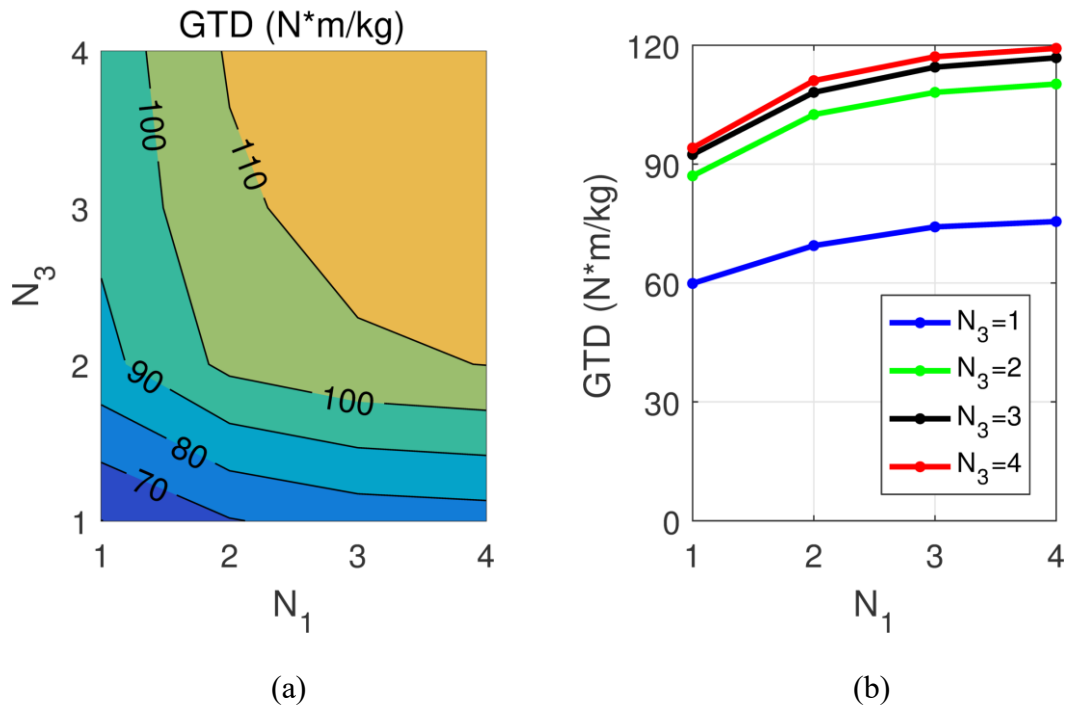
As in the previous sections,  $k_{PM}$  and  $G_{Int}$  are used to determine the ratios of PM thicknesses and pole pair counts on the two rotors according to (17) and (16), respectively. For the rest of this section, the results shown are based on 3D FEA for designs with 50 mm stack lengths, except where specified otherwise.

## 7.2. Results

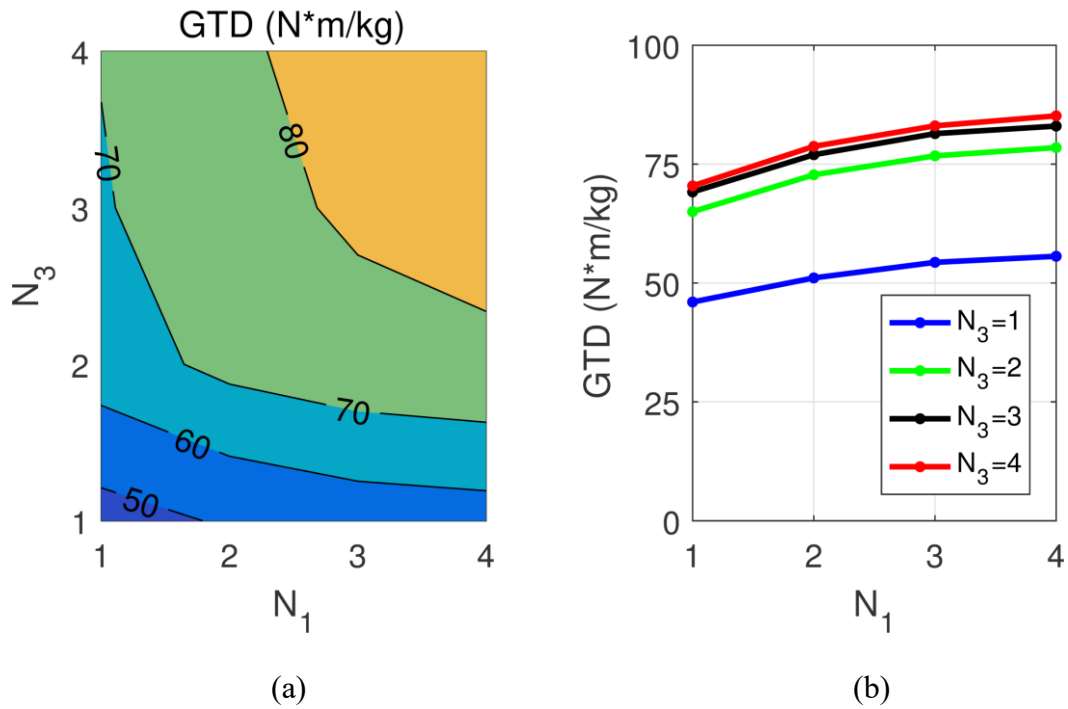
Figure 7.5, Figure 7.6, and Figure 7.7 illustrate the impact of the number of segments per pole on Rotor 1 and Rotor 3 on the maximum achievable GTD for each of the different nearest integer gear ratios. These figures show that using a Halbach array can significantly increase the achievable GTD. These figures also show that the number increasing the number of segments per pole on Rotor 3 can yield larger gains in GTD than increasing the number of segments per pole on Rotor 1, especially for designs with higher gear ratios, such as those in Figure 7.7. However, in practice, it is generally easier to implement a high number of segments per pole on Rotor 1 than on Rotor 3 because Rotor 3 has more poles.



**Figure 7.5** Variation of the maximum achievable GTD with the numbers of segments per pole on Rotor 1 and Rotor 3 for designs with  $G_{Int} = 4$  and 50 mm stack lengths, based on 3D FEA, depicted as a (a) contour plot and (b) line plot.



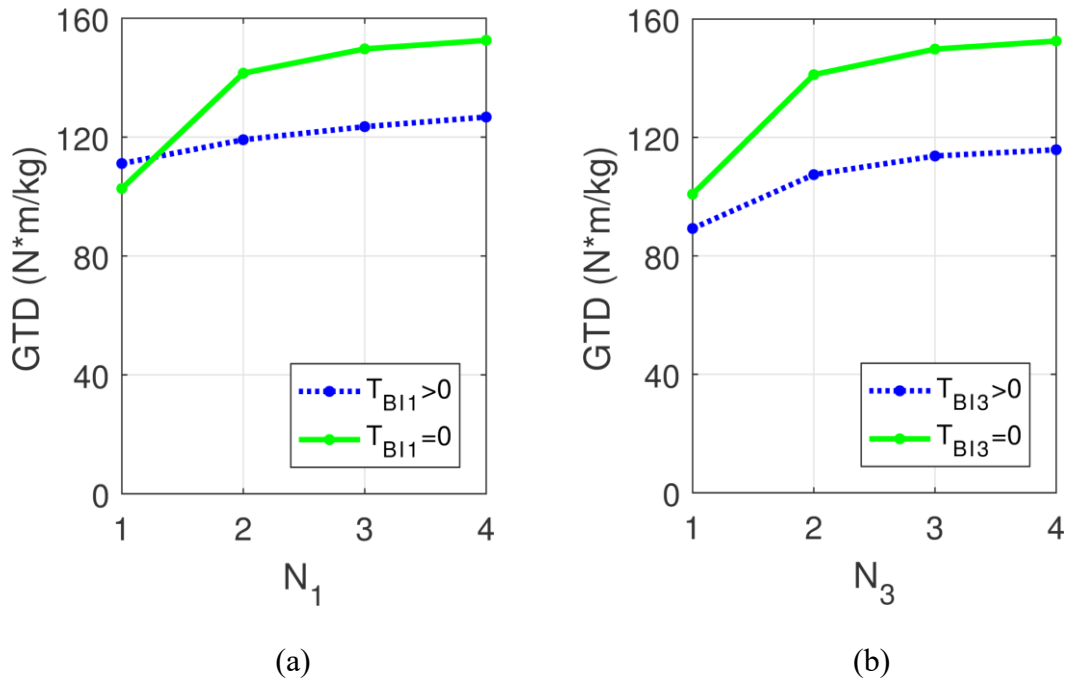
**Figure 7.6** Variation of the maximum achievable GTD with the numbers of segments per pole on Rotor 1 and Rotor 3 for designs with  $G_{Int} = 9$  and 50 mm stack lengths, based on 3D FEA, depicted as a (a) contour plot and (b) line plot.



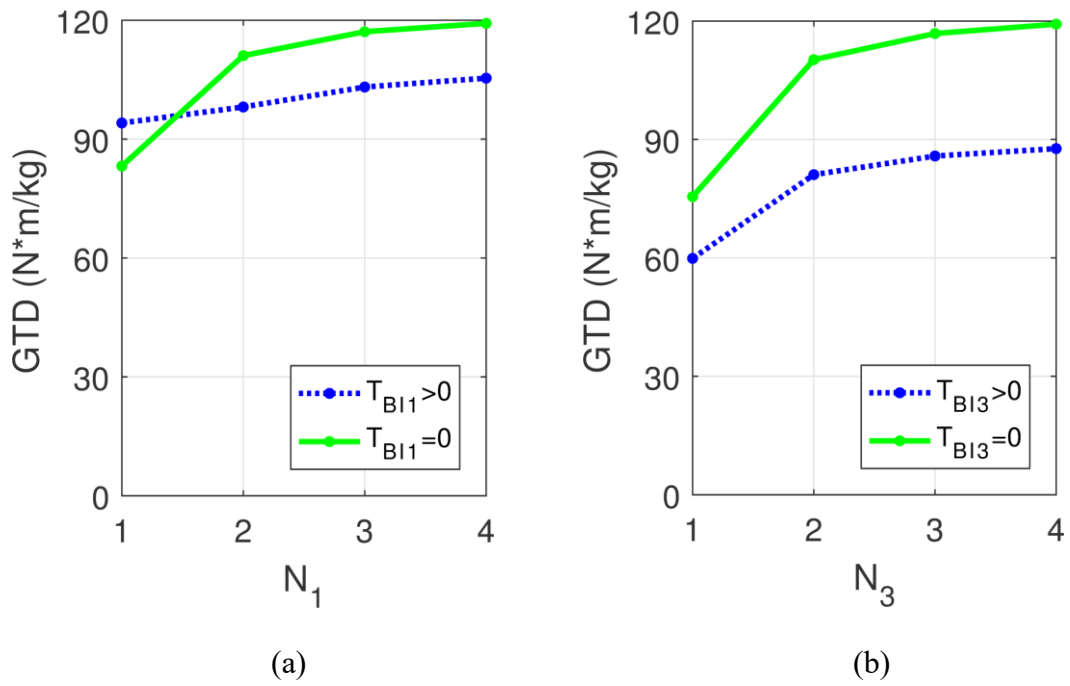
**Figure 7.7 Variation of the maximum achievable GTD with the numbers of segments per pole on Rotor 1 and Rotor 3 for designs with  $G_{Int} = 16$  and 50 mm stack lengths, based on 3D FEA, depicted as a (a) contour plot and (b) line plot.**

Figure 7.5, Figure 7.6, and Figure 7.7 depict designs with and without back irons. To clarify the interrelationships between the Halbach arrays and the back irons, Figure 7.8, Figure 7.9, and Figure 7.10 depict the impact of the number of segments per pole on each rotor for designs with or without a back iron on that rotor. These figures show that using a Halbach array helps the designs without a back iron much more than the designs with a back iron. These figures show that without a Halbach array on Rotor 1, it is generally desirable to have a back iron on Rotor 1, especially for the higher gear ratios. However, it is still desirable to eliminate the Rotor 3 back iron, even if there is no Halbach array on Rotor 3. There are two major reasons for this pattern. First, Rotor 1

has much lower pole counts than Rotor 3, so the flux from the Rotor 1 PMs has to travel much farther radially inside the Rotor 1 PMs than the flux from the Rotor 3 PMs has to travel outside the Rotor 3 PMs. Thus, with this larger flux path inside Rotor 1, the effect of a Rotor 1 back iron on the overall reluctance of the Rotor 1 PM flux paths are more significant than the effect of a Rotor 3 back iron on the overall reluctance of the much shorter Rotor 3 flux paths. Since the larger gear ratios result in a larger difference between the pole pair counts on the two rotors, the difference in the impact of the back irons on Rotor 1 and Rotor 3 becomes more pronounced for the designs with larger gear ratios. Second, using a thick Rotor 3 back iron reduces the air gap radii, which reduces the torque. However, using a back iron on Rotor 1 simply takes up space that would otherwise be empty. These figures also show that going from one segment per pole to two segments per pole provides a much more significant boost in GTD than subsequent increases in the number of segments per pole. This is important because using a large number of segments per pole may result in magnets that are impractically thin in the tangential direction; however, these results show that much of the GTD gains from using Halbach arrays can be achieved with just two segments per pole.



**Figure 7.8** Variation of the maximum achievable GTD with (a) the number of segments per pole on Rotor 1 with and without Rotor 1 back irons and (b) the number of segments per pole on Rotor 3 with and without Rotor 3 back irons for designs with  $G_{Int} = 4$  and 50 mm stack lengths, based on 3D FEA.



**Figure 7.9** Variation of the maximum achievable GTD with (a) the number of segments per pole on Rotor 1 with and without Rotor 1 back irons and (b) the number of segments per pole on Rotor 3 with and without Rotor 3 back irons for designs with  $G_{Int} = 9$  and 50 mm stack lengths, based on 3D FEA.

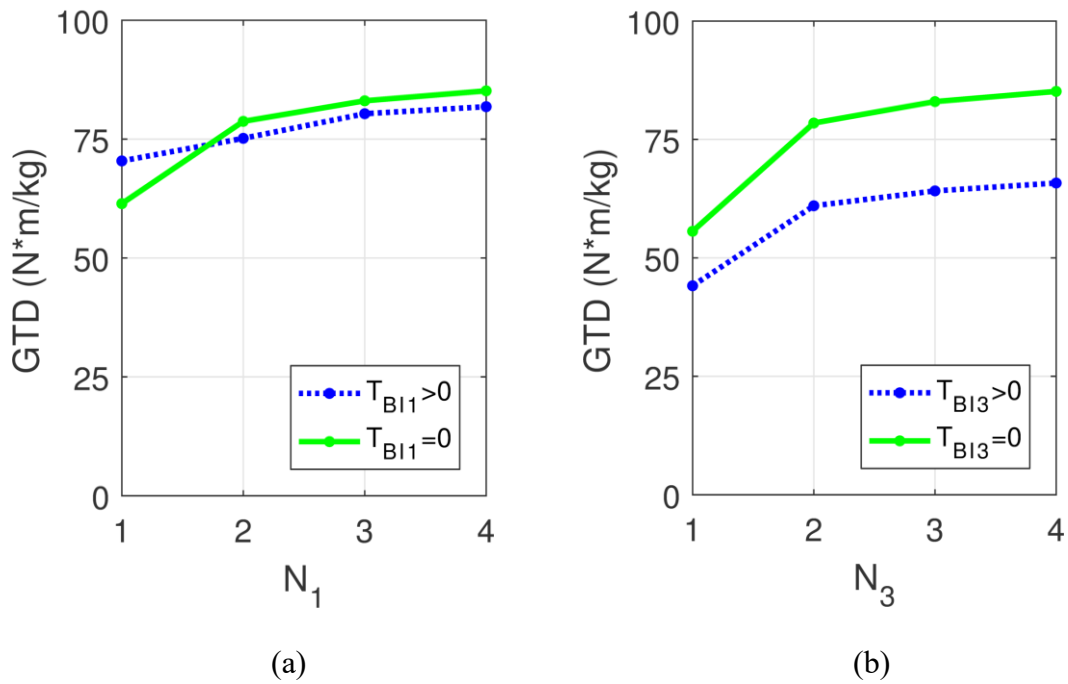


**Figure 7.10** Variation of the maximum achievable GTD with (a) the number of segments per pole on Rotor 1 with and without Rotor 1 back irons and (b) the number of segments per pole on Rotor 3 with and without Rotor 3 back irons for designs with  $G_{Int} = 16$  and 50 mm stack lengths, based on 3D FEA.

The flux shielding effect of Halbach arrays is the result of the flux being able to travel tangentially through the magnets instead of the back irons. This reduces the need for back irons, which can significantly improve a design's GTD. However, since the flux is traveling tangentially through the magnets instead of through a back iron, thicker magnets are often required to accommodate this flux path. Using thicker magnets will tend to lower the PM GTD, meaning that more PM material is required to produce the same torque. Figure 7.11, Figure 7.12, Figure 7.13, Figure 7.14, Figure 7.15, and Figure 7.16 depict the Pareto optimal fronts showing the tradeoffs between maximizing GTD and maximizing PM GTD.



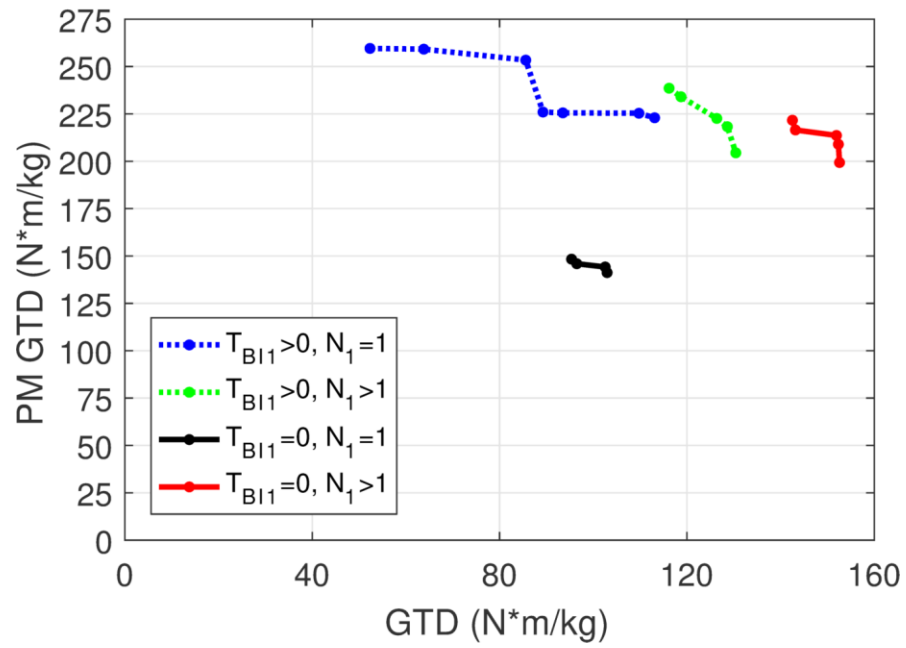


**Figure 7.11 Pareto optimal front indicating the tradeoff between maximizing GTD and maximizing PM GTD with and without Halbach arrays on Rotor 1 and with and without Rotor 1 back irons for designs with  $G_{int} = 4$ , based on 3D FEA.**

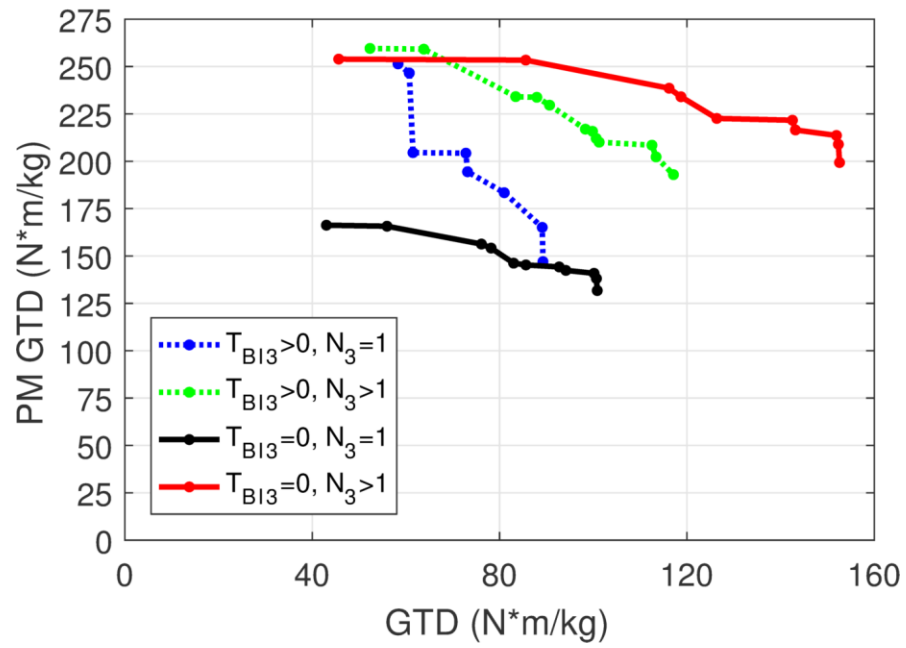


**Figure 7.12 Pareto optimal front indicating the tradeoff between maximizing GTD and maximizing PM GTD with and without Halbach arrays on Rotor 3 and with and without Rotor 3 back irons for designs with  $G_{int} = 4$ , based on 3D FEA.**

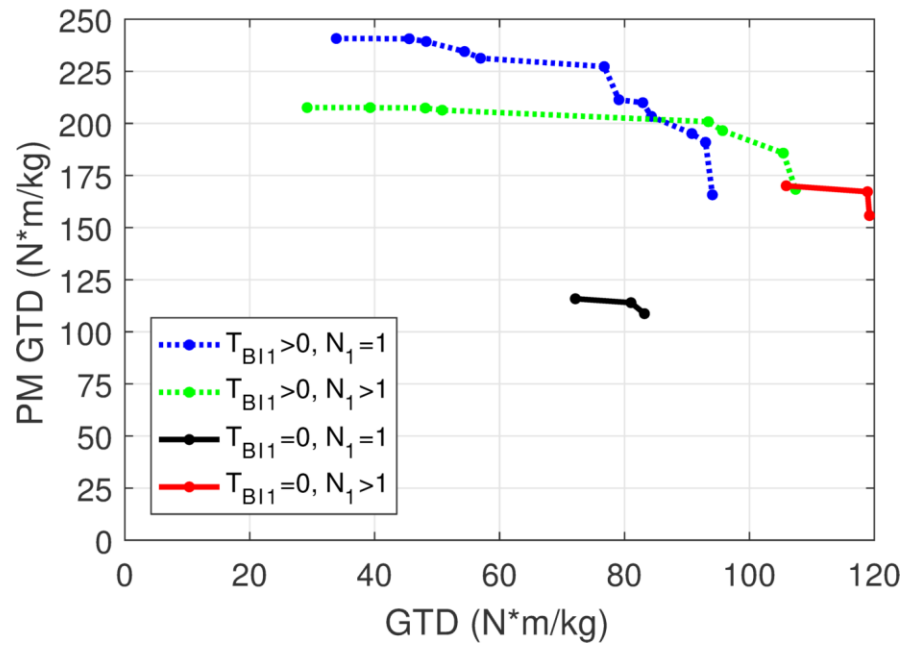


**Figure 7.13** Pareto optimal front indicating the tradeoff between maximizing GTD and maximizing PM GTD with and without Halbach arrays on Rotor 1 and with and without Rotor 1 back irons for designs with  $G_{int} = 9$ , based on 3D FEA.

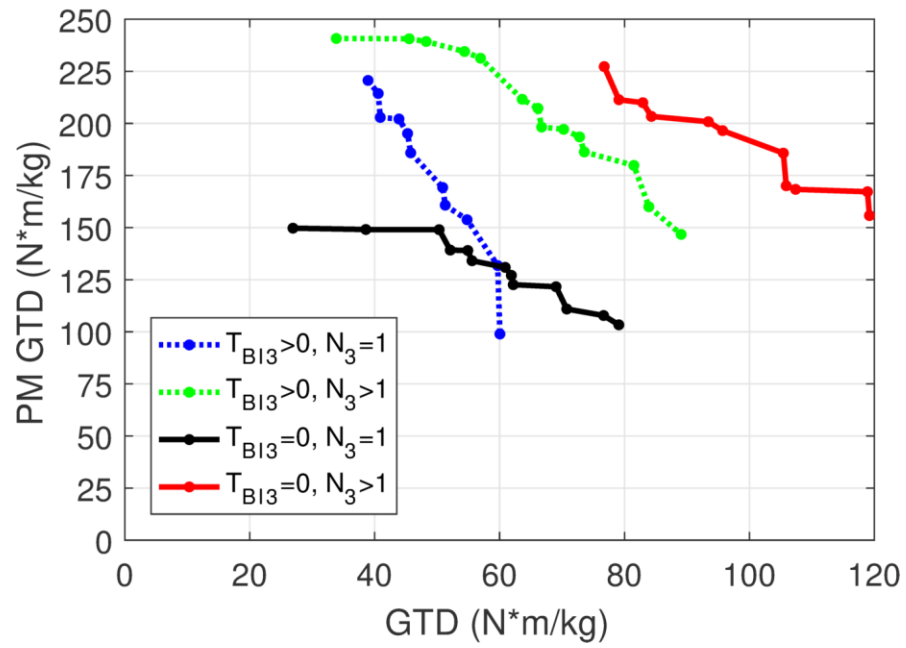


**Figure 7.14 Pareto optimal front indicating the tradeoff between maximizing GTD and maximizing PM GTD with and without Halbach arrays on Rotor 3 and with and without Rotor 3 back irons for designs with  $G_{int} = 9$ , based on 3D FEA.**

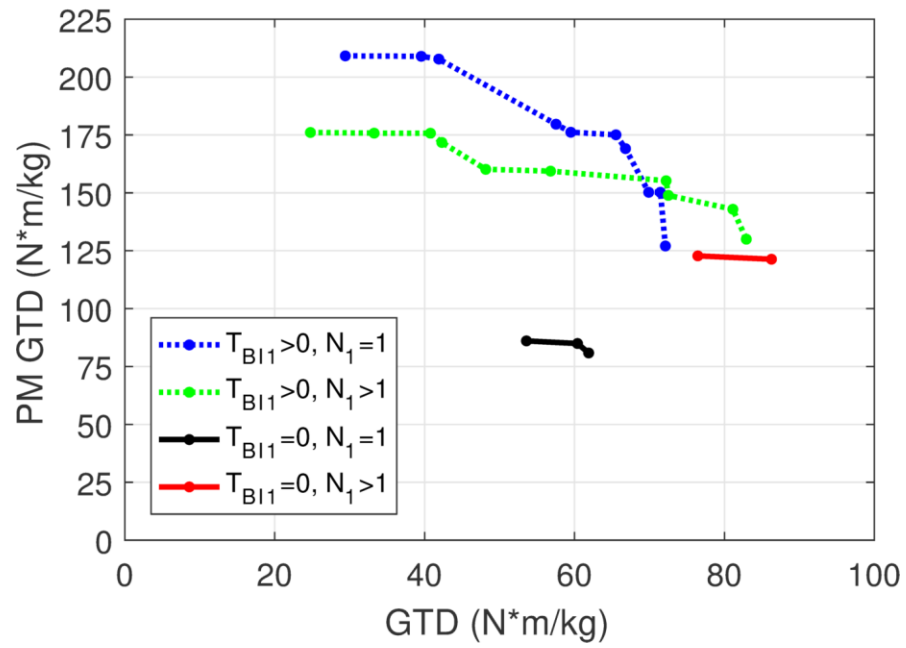


**Figure 7.15 Pareto optimal front indicating the tradeoff between maximizing GTD and maximizing PM GTD with and without Halbach arrays on Rotor 1 and with and without Rotor 1 back irons for designs with  $G_{int} = 16$ , based on 3D FEA.**

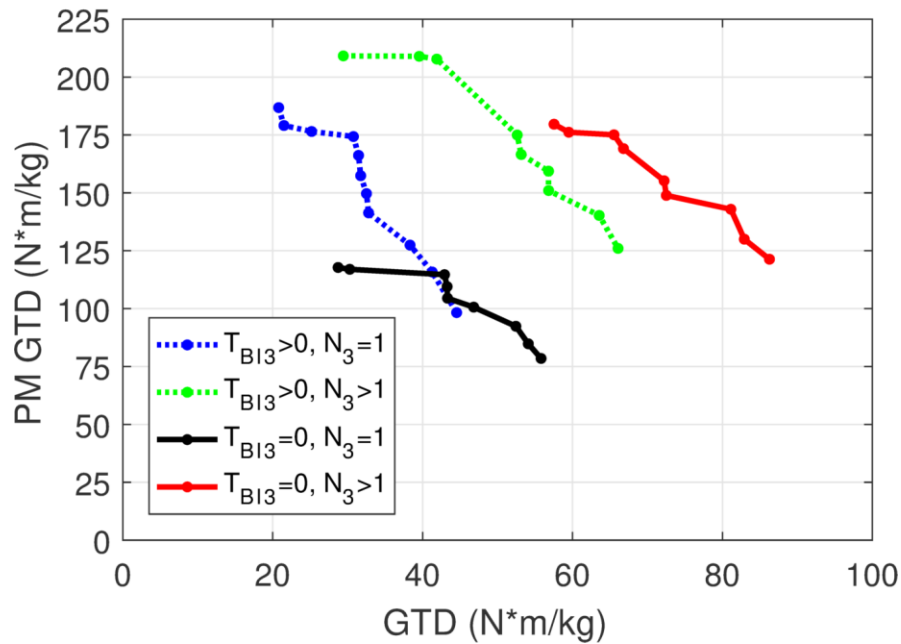


**Figure 7.16 Pareto optimal front indicating the tradeoff between maximizing GTD and maximizing PM GTD with and without Halbach arrays on Rotor 3 and with and without Rotor 3 back irons for designs with  $G_{int} = 16$ , based on 3D FEA.**

For the Rotor 1 PM arrangement, Figure 7.11, Figure 7.13, and Figure 7.15 show that the maximum PM GTD is obtained with a back iron and conventionally magnetized magnets, but the maximum GTD is obtained with a Halbach array mounted on an air core. A Halbach array mounted on a back iron can result in intermediate performance between having a Halbach array on an air core and having conventionally magnetized magnets on a back iron. However, having conventionally magnetized magnets on an air core provides no benefits. For the Rotor 3 PM arrangement, Figure 7.12, Figure 7.14, and Figure 7.16 show that the maximum PM GTD is obtained with a Halbach array on a back iron, but the maximum GTD is obtained with a Halbach array on an air core. The difference in behaviors between Rotor 1 and Rotor 3 is the result of the difference in

their respective pole counts. The low pole counts of Rotor 1 result in long flux paths, which requires Halbach arrays to have thick magnets to provide any benefit. However, with the higher pole counts of Rotor 3, the shorter flux paths do not require the magnets to be very thick. The relationship between PM thickness and the benefits of Halbach arrays is further illustrated by Figure 7.17, Figure 7.18, and Figure 7.19. These figures show that going from one segment per pole to two segments per pole actually decreases the GTD for designs with a back iron and thin PMs. For these designs, most of the flux passes through the back irons, instead of through the tangentially magnetized PMs. Thus, the tangentially magnetized PMs do not significantly contribute to the air gap flux density, but using two segments per pole decreases the tangential widths of the radially magnetized PMs, which does reduce the air gap flux density. However, in designs without back irons or with thicker PMs, enough flux travels through the tangentially magnetized PMs that the Halbach array does increase the GTD.

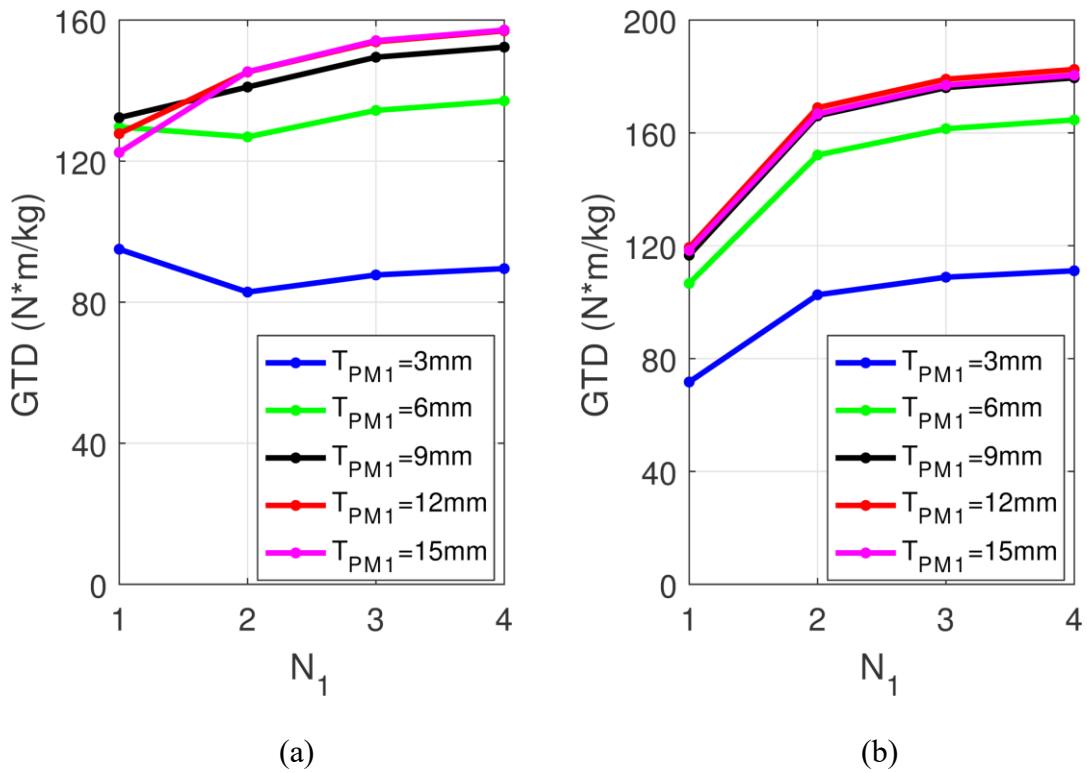


**Figure 7.17** Variation of the maximum achievable GTD with the number of segments per pole on Rotor 1 and the Rotor 1 PM thickness for designs (a) with Rotor 1 back irons and (b) without Rotor 1 back irons for designs with  $G_{Int} = 4$ , based on 2D FEA.



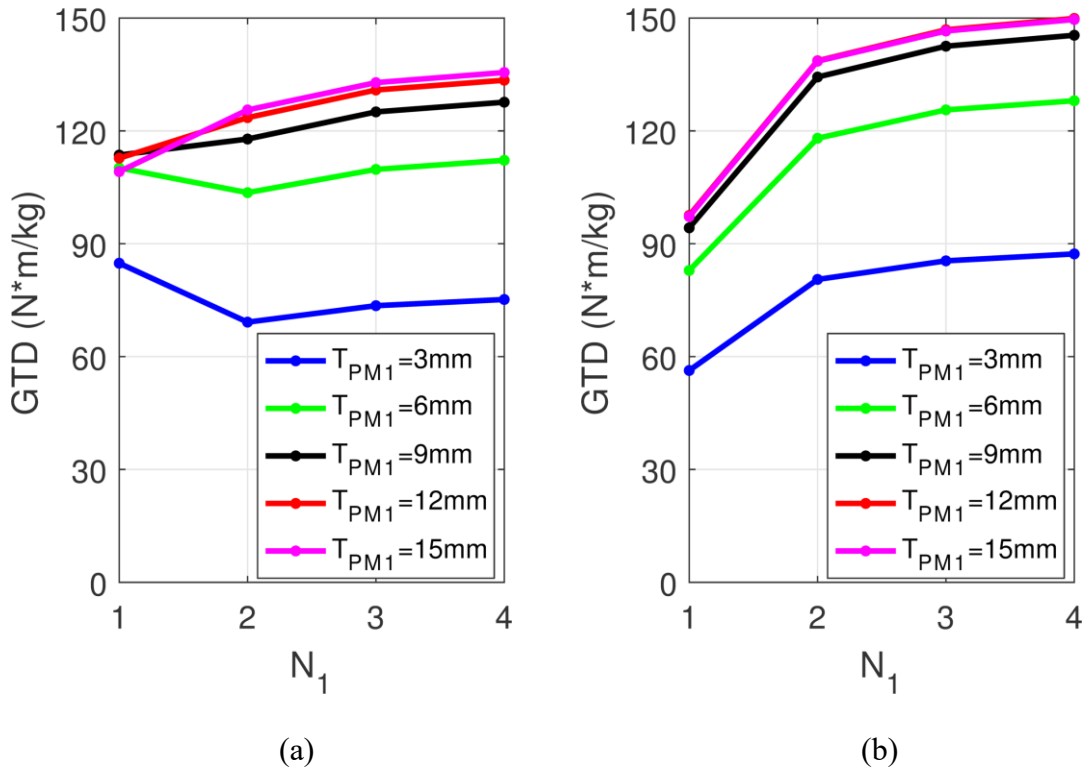


**Figure 7.18 Variation of the maximum achievable GTD with the number of segments per pole on Rotor 1 and the Rotor 1 PM thickness for designs (a) with Rotor 1 back irons and (b) without Rotor 1 back irons for designs with  $G_{Int} = 9$ , based on 2D FEA.**

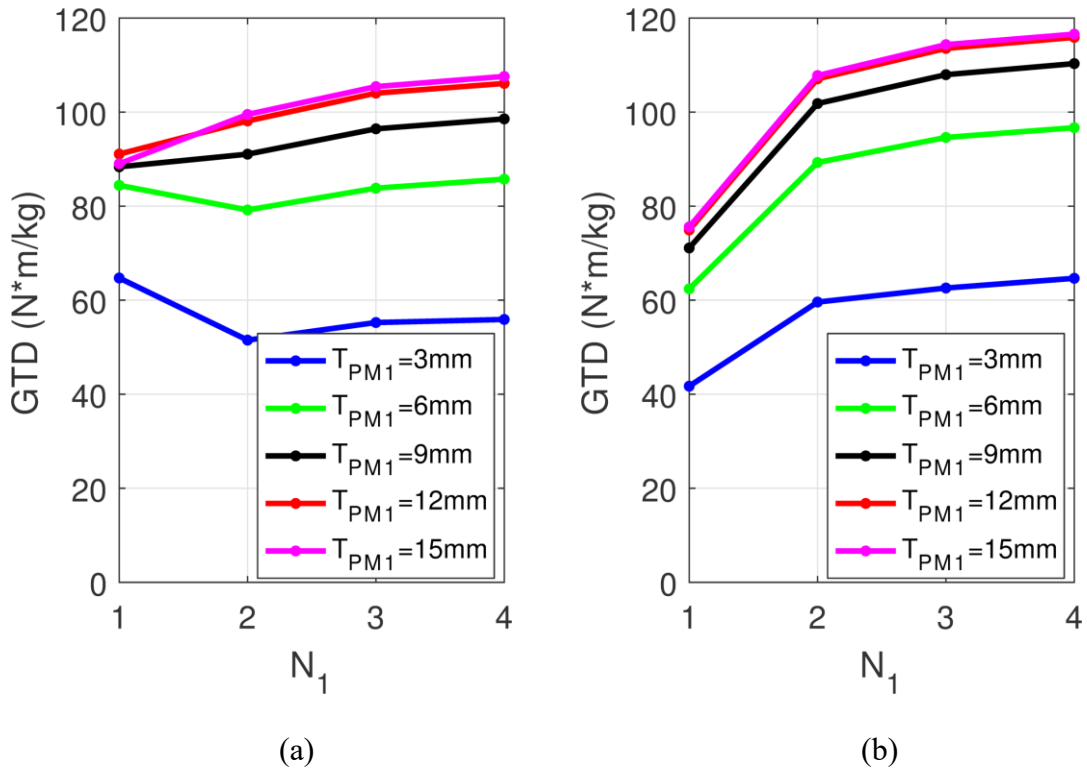


**Figure 7.19 Variation of the maximum achievable GTD with the number of segments per pole on Rotor 1 and the Rotor 1 PM thickness for designs (a) with Rotor 1 back irons and (b) without Rotor 1 back irons for designs with  $G_{Int} = 16$ , based on 2D FEA.**

Another significant concern for magnetic gears is the impact of end effects, which can have a significant impact on the torque of a design [35]. Figure 7.20, Figure 7.21, Figure 7.22, Figure 7.23, Figure 7.24, and Figure 7.25 show how the GTD varies with stack length. As in the previous sections, the 2D FEA provides a limit for the GTD attainable as the stack length approaches infinity, based on 3D FEA. These figures do not show a significant difference between the impacts of end effects on designs with

Halbach arrays and designs without Halbach arrays or between the impacts of end effects on designs with air cores and designs with back irons.

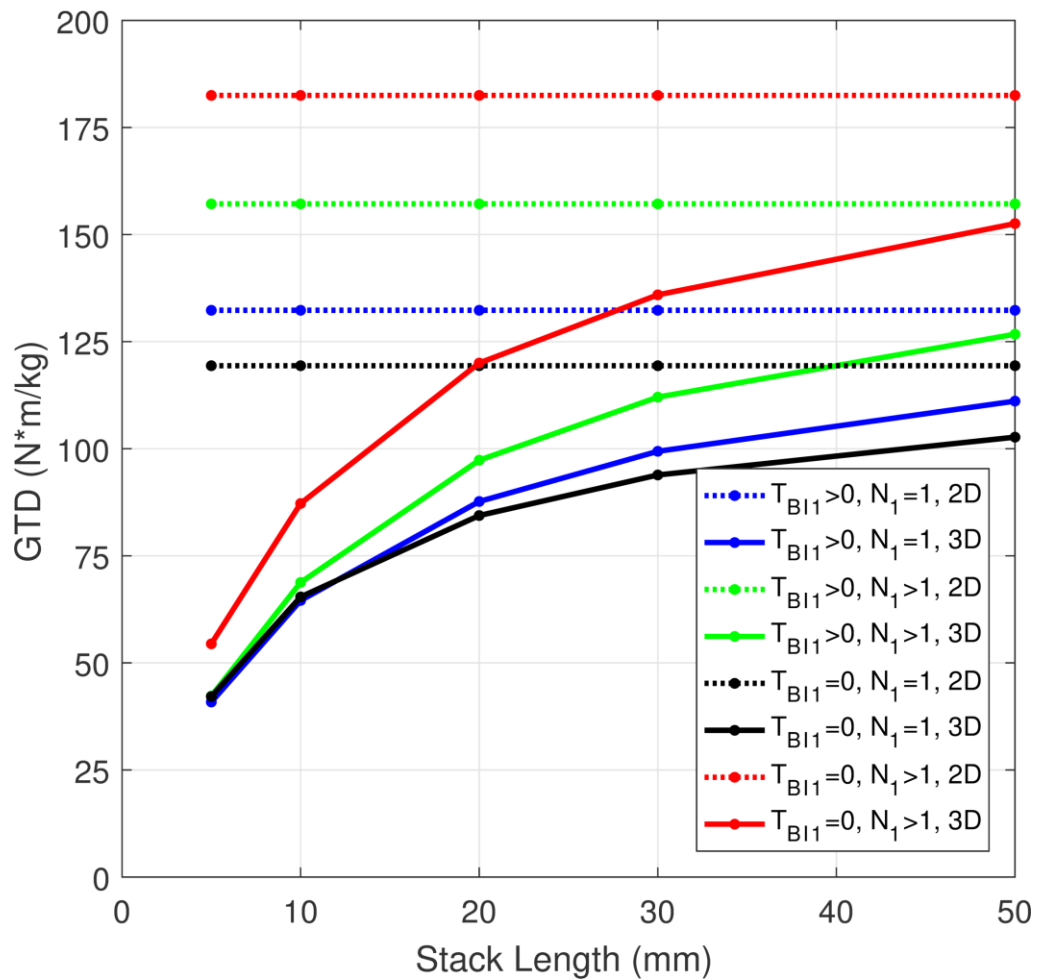


**Figure 7.20 Impact of stack length on the maximum achievable GTD for designs with and without Halbach arrays on Rotor 1 and with and without Rotor 1 back irons for designs with  $G_{Int} = 4$ , based on 2D and 3D FEA.**

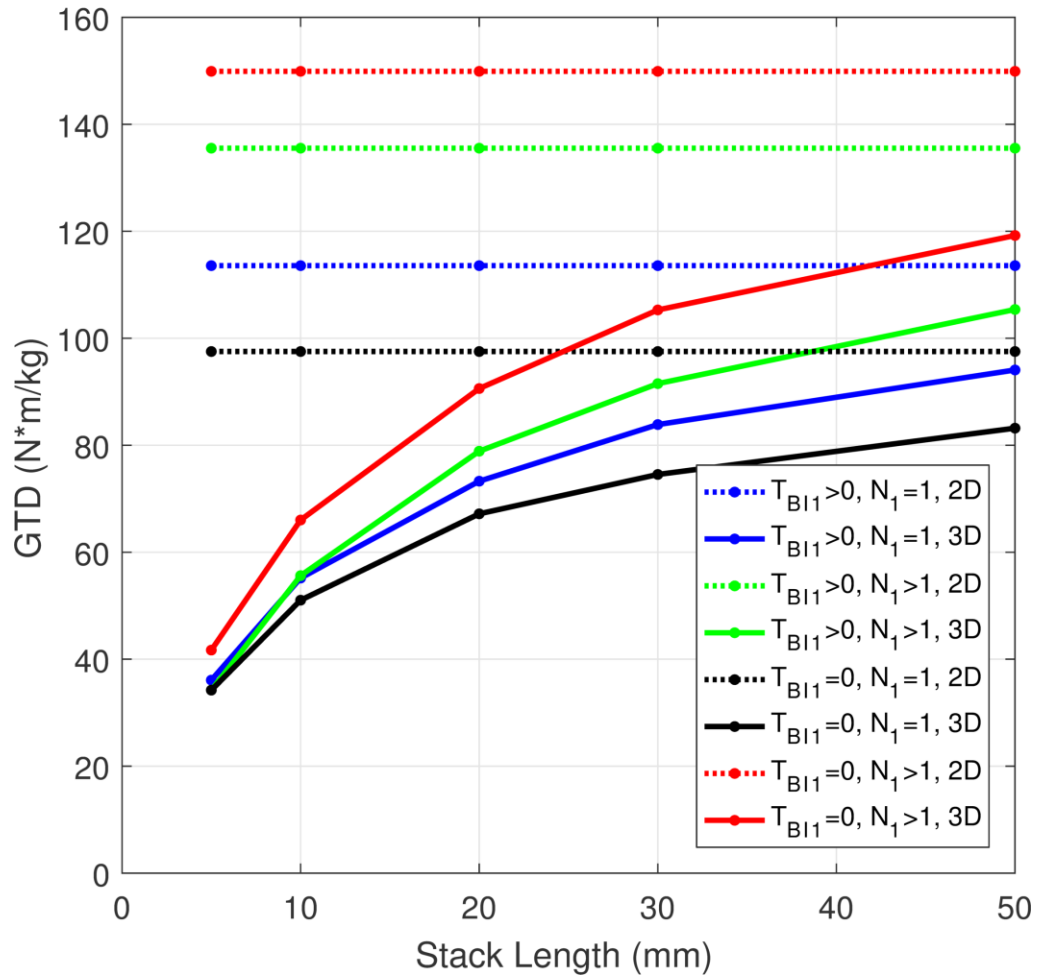


**Figure 7.21 Impact of stack length on the maximum achievable GTD for designs with and without Halbach arrays on Rotor 1 and with and without Rotor 1 back irons for designs with  $G_{Int} = 9$ , based on 2D and 3D FEA.**

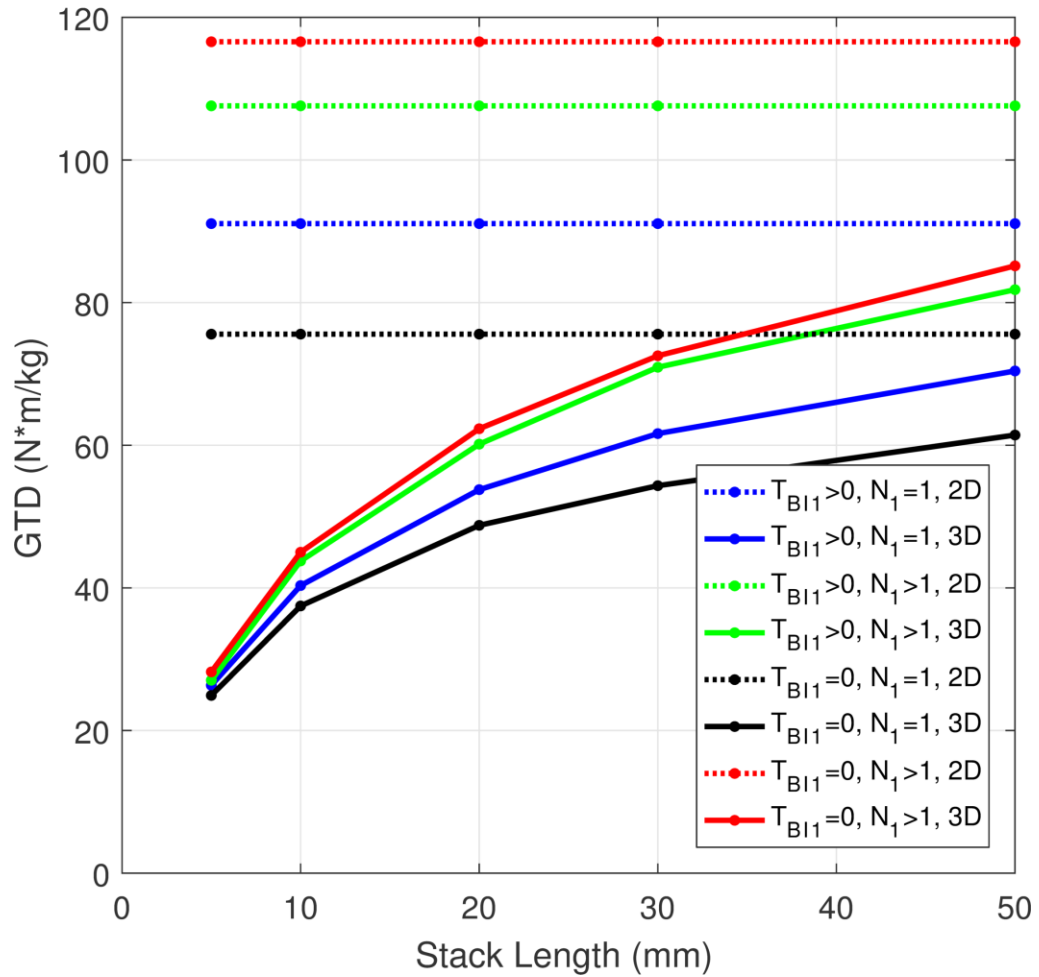


**Figure 7.22 Impact of stack length on the maximum achievable GTD for designs with and without Halbach arrays on Rotor 1 and with and without Rotor 1 back irons for designs with  $G_{Int} = 16$ , based on 2D and 3D FEA.**

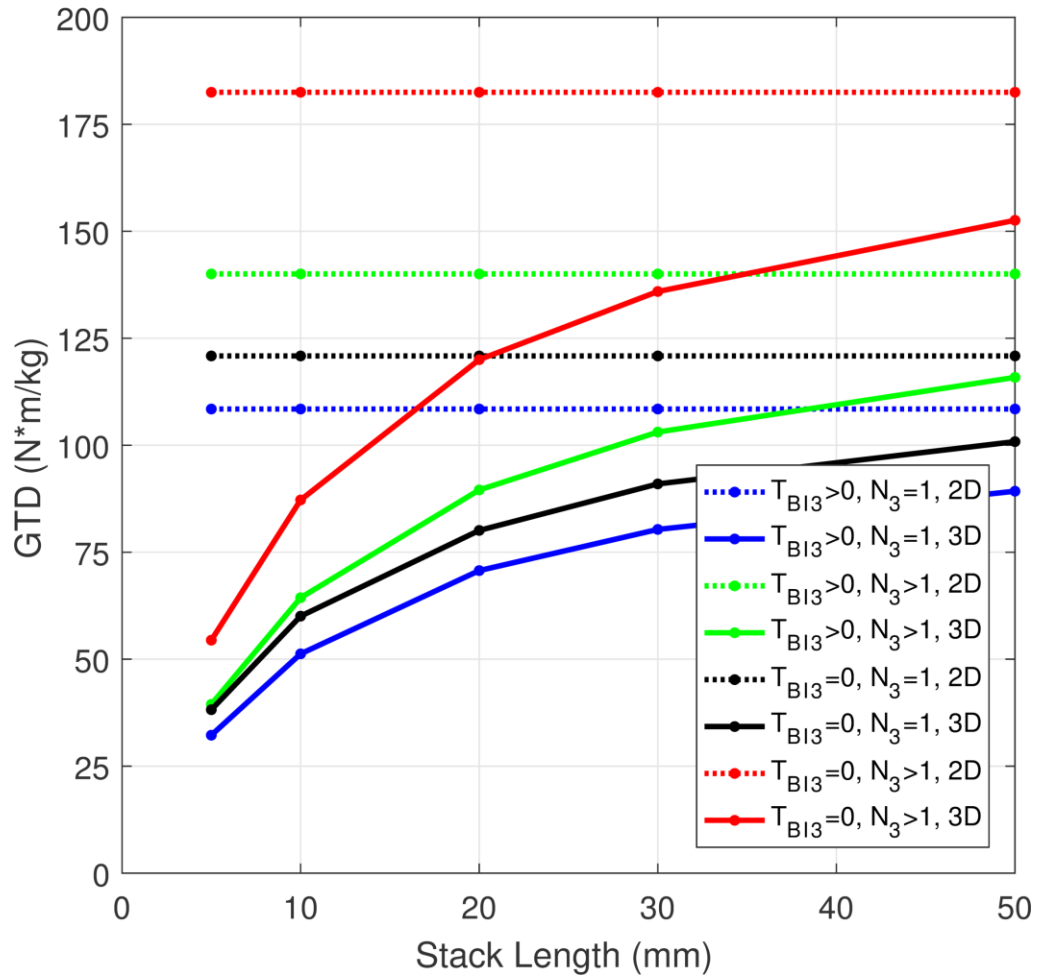


**Figure 7.23 Impact of stack length on the maximum achievable GTD for designs with and without Halbach arrays on Rotor 3 and with and without Rotor 3 back irons for designs with  $G_{Int} = 4$ , based on 2D and 3D FEA.**

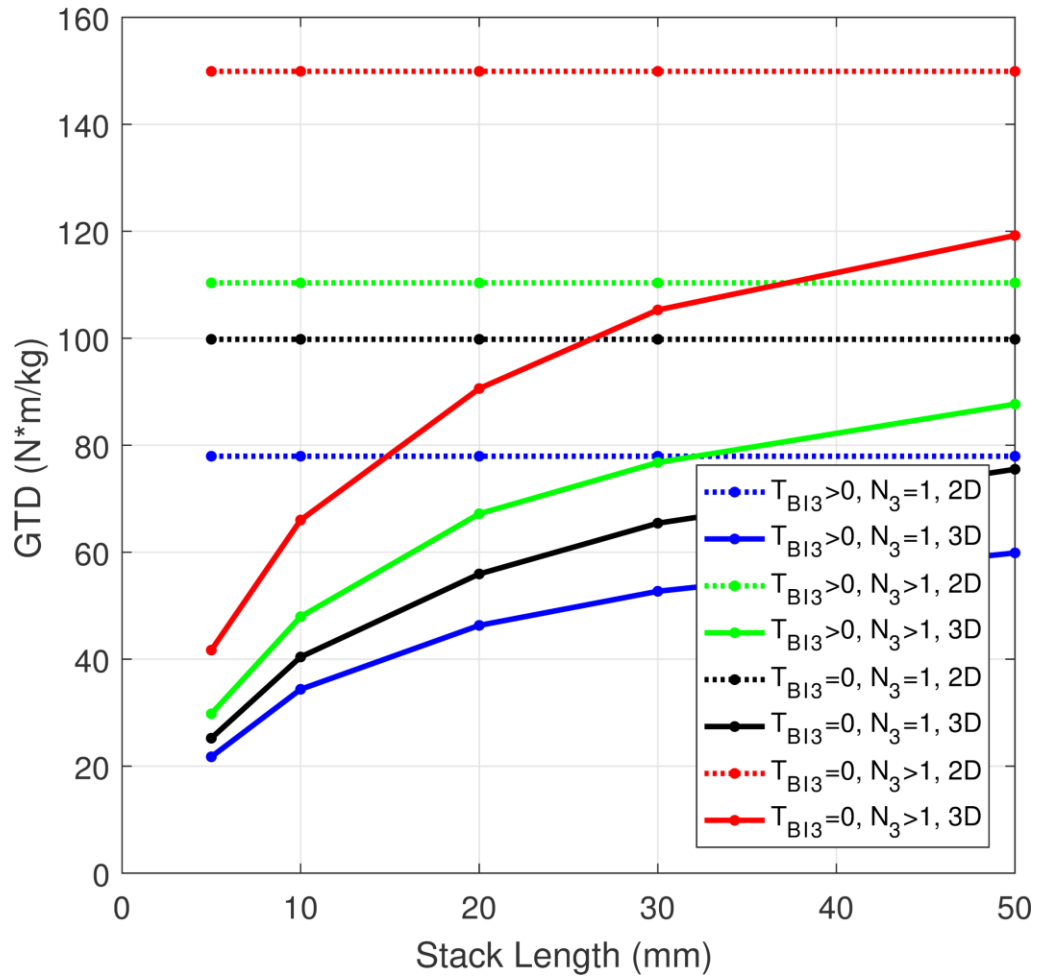


**Figure 7.24 Impact of stack length on the maximum achievable GTD for designs with and without Halbach arrays on Rotor 3 and with and without Rotor 3 back irons for designs with  $G_{Int} = 9$ , based on 2D and 3D FEA.**

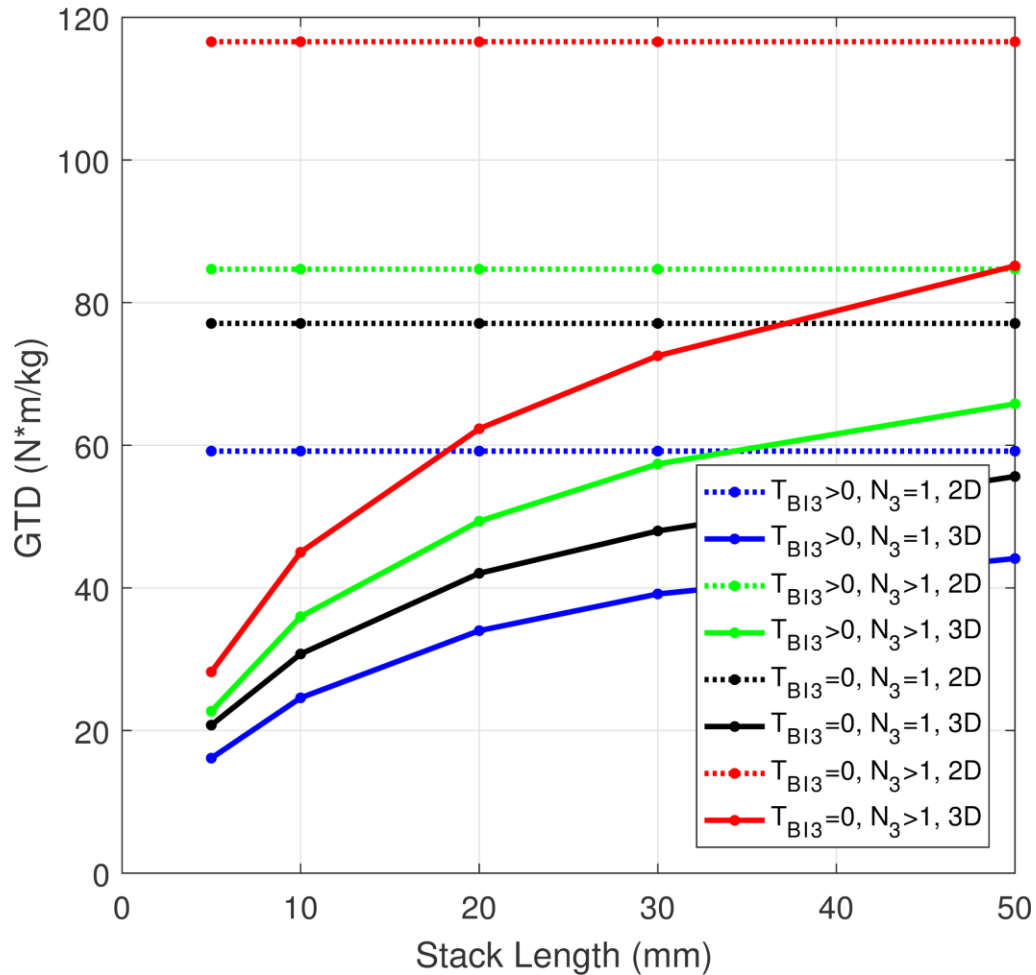


**Figure 7.25 Impact of stack length on the maximum achievable GTD for designs with and without Halbach arrays on Rotor 3 and with and without Rotor 3 back irons for designs with  $G_{Int} = 16$ , based on 2D and 3D FEA.**

### 7.3. Conclusion

A parametric analysis was performed using 2D FEA and 3D FEA to evaluate the benefits of using Halbach arrays and air cores in radial flux coaxial magnetic gears.

Using Halbach arrays with air cores can significantly increase the GTD achievable by radial flux coaxial magnetic gears. However, using air cores without Halbach arrays



provides significantly less benefit and may even reduce the GTD relative to designs with radially magnetized magnets mounted on back irons. Additionally, using a Halbach array for designs with back irons and relatively thin magnets may also reduce GTD relative to using only radially magnetized magnets. Therefore, the GTD improvement from using Halbach arrays and air cores often comes at the expense of reduced PM GTD, which can entail a larger material cost. Using Halbach arrays and air cores did not significantly impact the extent of end effects.

## 8. PROTOTYPE RADIAL FLUX COAXIAL MAGNETIC GEAR WITH HALBACH ARRAYS AND AIR CORES

The previous section provides a numerical analysis illustrating the potential performance benefits achieved by using Halbach arrays and air cores in magnetic gears. In this section, a prototype is designed, fabricated, and tested to explore the challenges associated with using Halbach arrays and air cores in a magnetic gear and to validate the numerical models used in the previous section. While many magnetic gear prototypes have been fabricated and tested, the use of Halbach arrays and air cores increases the complexity of fabricating a magnetic gear. First, there are strong magnetic forces on each of the pieces in a discrete Halbach array, which makes assembly and PM retention more challenging. This is exacerbated by the fact that the PMs do not experience any magnetic attraction to the air cores (as they would to back irons). Additionally, due to the lack of magnetic containment provided by the back irons, the flux from Rotor 1 may extend beyond Rotor 3 [79]. This may cause losses in nearby conductive objects and attract nearby magnetic objects.

### 8.1. Magnetic and Mechanical Tradeoff Analysis

A cross-sectional view of the magnetically active portions of the prototype design is shown in Figure 8.1. The basic design parameters of the prototype are given in Table 8.1. The modulators are made from 26 gauge M19 laminations, and the PMs are made from NdFeB N52. For this prototype, Rotor 2 serves as the low speed rotor and Rotor 3 is fixed, which yields a gear ratio of 4.67:1. The design parameters in Table 8.1

were selected to achieve a design that would be feasible to assemble with the limited tools available in the lab and to have a slip torque that would be compatible with the lab's existing equipment. Additionally, the selection of several parameters involved tradeoffs between mechanical and magnetic objectives. The simulation results illustrating these tradeoffs were produced by sweeping only one or two of the design parameters from their base values, which are provided in Table 8.1, at a time.

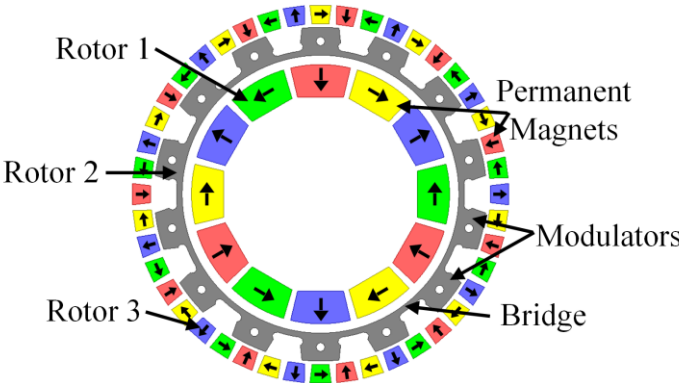


**Figure 8.1** Cross-section of the magnetically active portions of the prototype.

**Table 8.1 Prototype Design Parameter Values.**

| <b>Symbol</b>       | <b>Description</b>   | <b>Values</b> |
|---------------------|--|---------------|
| $P_1$               | Number of Rotor 1 pole pairs                               | 3             |
| $Q_2$               | Number of modulators                                       | 14            |
| $P_3$               | Number of Rotor 3 pole pairs                               | 11            |
| $N_1$               | Number of pieces per Rotor 1 pole                          | 2             |
| $N_3$               | Number of pieces per Rotor 3 pole                          | 2             |
| $R_{Out}$           | Outer radius of Rotor 3 PMs                                | 50.8 mm       |
| $T_{PM3}$           | Radial thickness of Rotor 3 PMs                            | 5 mm          |
| $T_{OAG}$           | Outer air gap thickness                                    | 1 mm          |
| $T_{Mods}$          | Radial thickness of Rotor 2                                | 7.5 mm        |
| $T_{Bridge}$        | Radial thickness of bridge                                 | 1.5 mm        |
| $T_{IAG}$           | Inner magnetic air gap thickness                           | 2.5 mm        |
| $T_{PM1}$           | Radial thickness of Rotor 1 PMs                            | 8 mm          |
| $w_{R3,Out}$        | Tangential width between Rotor 3 PMs at their outer radius | 1.5 mm        |
| $w_{R3,In}$         | Tangential width between Rotor 3 PMs at their inner radius | 2 mm          |
| $w_{R1}$            | Tangential width between Rotor 1 PMs                       | 1.5 mm        |
| $\alpha_{Mods,Out}$ | Modulators fill factor at the Rotor 2 outer radius         | 0.5           |
| $\alpha_{Mods,In}$  | Modulators fill factor at the Rotor 2 inner radius         | 0.7           |
| $R_{Hole}$          | Radius of modulator holes                                  | 1.2 mm        |
| $L_{PM3}$           | Axial length of Rotor 3 PMs                                | 51.8 mm       |
| $L_{Mods}$          | Axial length of modulators                                 | 37.8 mm       |
| $L_{PM1}$           | Axial length of Rotor 1 PMs                                | 47.8 mm       |

### 8.1.1. Modulators Support

To simplify handling and fabrication, the modulator stack is bonded. However, additional modulator support is required. One means of support is to place rods through their axial length, as in [5], [80]. For this design, these rods are made of glass-filled epoxy to provide high strength with high electrical resistivity. Additionally, the slots

between adjacent modulators are filled with glass filled nylon spacers. Circular arc shaped holes are cut out of the modulators' inner corners to allow the spacers to interlock well with the modulators. Both the circular holes for the rods and the arc shaped holes remove magnetically permeable material from the flux paths in the modulators, as depicted in Figure 8.1. Figure 8.2 illustrates how the radii of these holes impact the design's slip torque and electromagnetic efficiency at the rated Rotor 2 speed of 400 rpm, based on 2D finite element analysis (FEA). Generally, these holes do not have much effect on the performance unless they become large enough that the area between them is thoroughly saturated, worsening gear performance. For this design, the holes have radii of 1.2 mm. Figure 8.2(b) also indicates that this design has a very high electromagnetic efficiency (neglecting mechanical losses), which mitigates thermal concerns. A Halbach array produces more sinusoidal fields than a conventional SPM configuration, which reduces both torque ripple and losses due to unwanted harmonics. Additionally, the PMs are segmented into multiple pieces per pole to form the discrete Halbach arrays, which reduces eddy current losses.

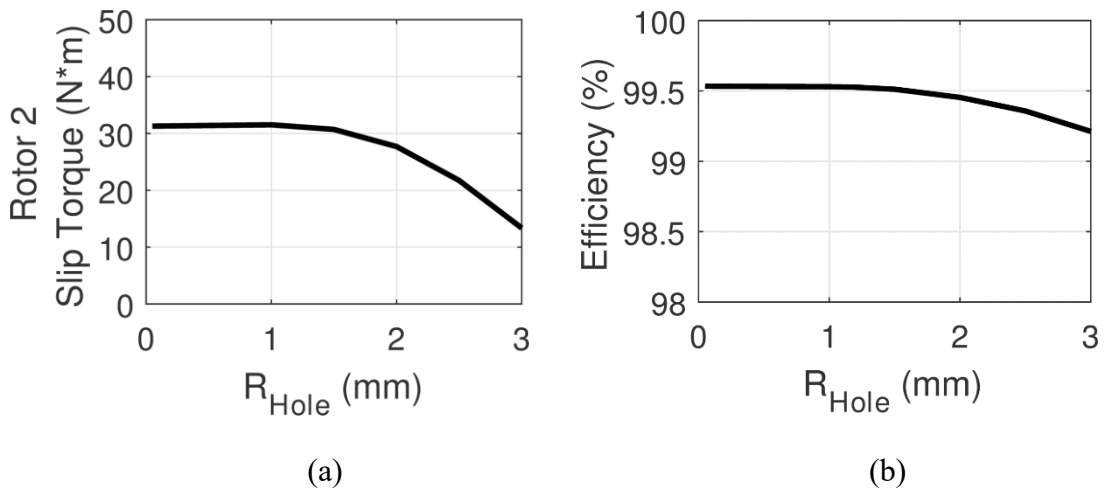


**Figure 8.2 Impact of the modulator holes radii (varied together) on (a) Rotor 2 slip torque, based on 3D FEA simulations, and (b) electromagnetic efficiency at rated speed and maximum torque, based on 2D FEA simulations.**

Another way to support the modulators is to connect adjacent modulators with one or more thin bridges [5]. This also allows all of the modulators to be formed from a single lamination stack. Figure 8.3 illustrates the impacts of the bridge thickness and position based on 2D FEA. The bridge position (BP) indicates the radial location of the bridge, with 0 and 1 being on the inner and outer edges of Rotor 2, respectively. The bridge provides a flux leakage path, so increasing its thickness reduces the slip torque. This is exacerbated if the bridge is placed near the outer air gap because Rotor 3's higher pole count produces shorter leakage paths and more leakage flux. Nonetheless, the impact of the bridge position is less significant for this design than it is in [5] because this design has a lower gear ratio, so there is less difference between the pole counts on Rotors 1 and 3. The reduction in slip torque as the bridge gets thicker reduces the efficiency when operating at maximum torque. The loss distribution is also affected. As

the bridge thickness increases, the losses in both sets of PMs decrease for two reasons. The bridge reduces the spatial harmonics in the modulators' permeance function and short-circuits some of the flux, especially higher spatial harmonics, preventing it from crossing both air gaps. However, a thicker bridge increases core losses in Rotor 2 due to the losses in the heavily saturated bridge. This design has a 1.5 mm thick bridge on the inside edge (BP = 0).

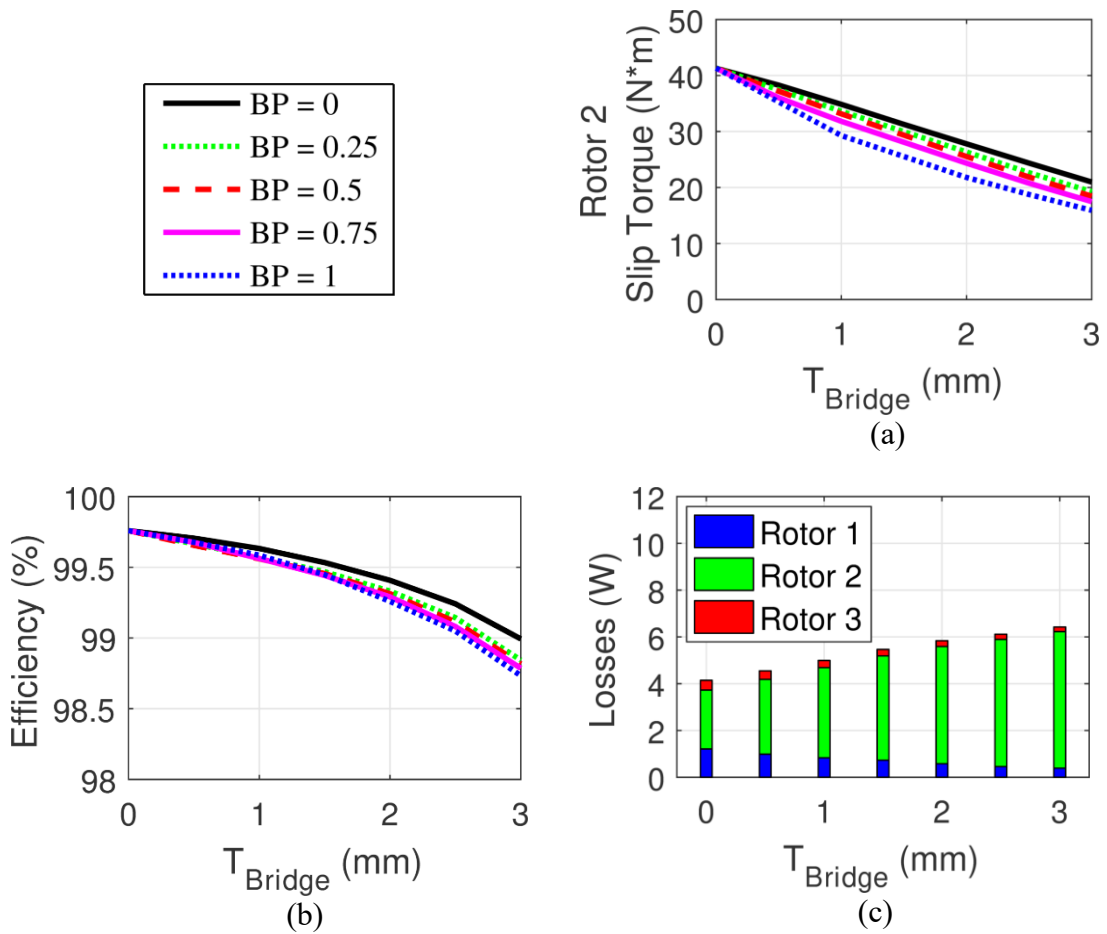


**Figure 8.3 Impact of the bridge position (BP) and thickness on (a) Rotor 2 slip torque, based on 3D FEA simulations, and (b) electromagnetic efficiency at rated speed and maximum torque and (c) impact of bridge thickness with BP = 0 on the loss distribution at rated speed, as in (b), both based on 2D FEA simulations.**

### 8.1.2. Magnet Retention

Retaining the PMs is another critical mechanical challenge. One conventional solution for electric machines is to fit a sleeve over the PMs, but this increases the effective air gaps. Figure 8.4 and Figure 8.5 illustrate the impacts of the effective air gaps on the performance of the design. As the air gaps increase, the slip torque decreases. The outer air gap has a larger impact on slip torque than the inner air gap because Rotor 3 has a higher pole count than Rotor 1, which leads to more leakage flux in the outer air gap. Increasing either air gap within the considered range tends to reduce the losses, with the inner air gap having a larger impact on the Rotor 1 PM losses and the outer air gap having a larger impact on the Rotor 3 PM losses. This occurs because the larger air gap attenuates the spatial flux harmonics. This effect is most pronounced for the inner air gap and the Rotor 1 PM losses because the permeance harmonics and Rotor 3 PM flux harmonics, which cause losses in the Rotor 1 PMs, have higher spatial frequencies than the Rotor 1 PM flux harmonics, and a larger air gap has more effect on higher frequency spatial harmonics. While increasing the inner air gap within this range does slightly increase the electromagnetic efficiency, increasing the outer air gap does not increase the electromagnetic efficiency because this also significantly reduces the slip torque and, thus, the transmitted power. Similarly, the reduction of these spatial harmonics with an increasing air gap decreases the torque ripple as the inner air gap increases. The non-integer gear ratio [3] and Halbach arrays [31], [78] also keep the torque ripple relatively small. This design has an outer air gap of 1 mm and an effective inner air gap of 2.5 mm, including a 1.5 mm thick plastic sleeve.



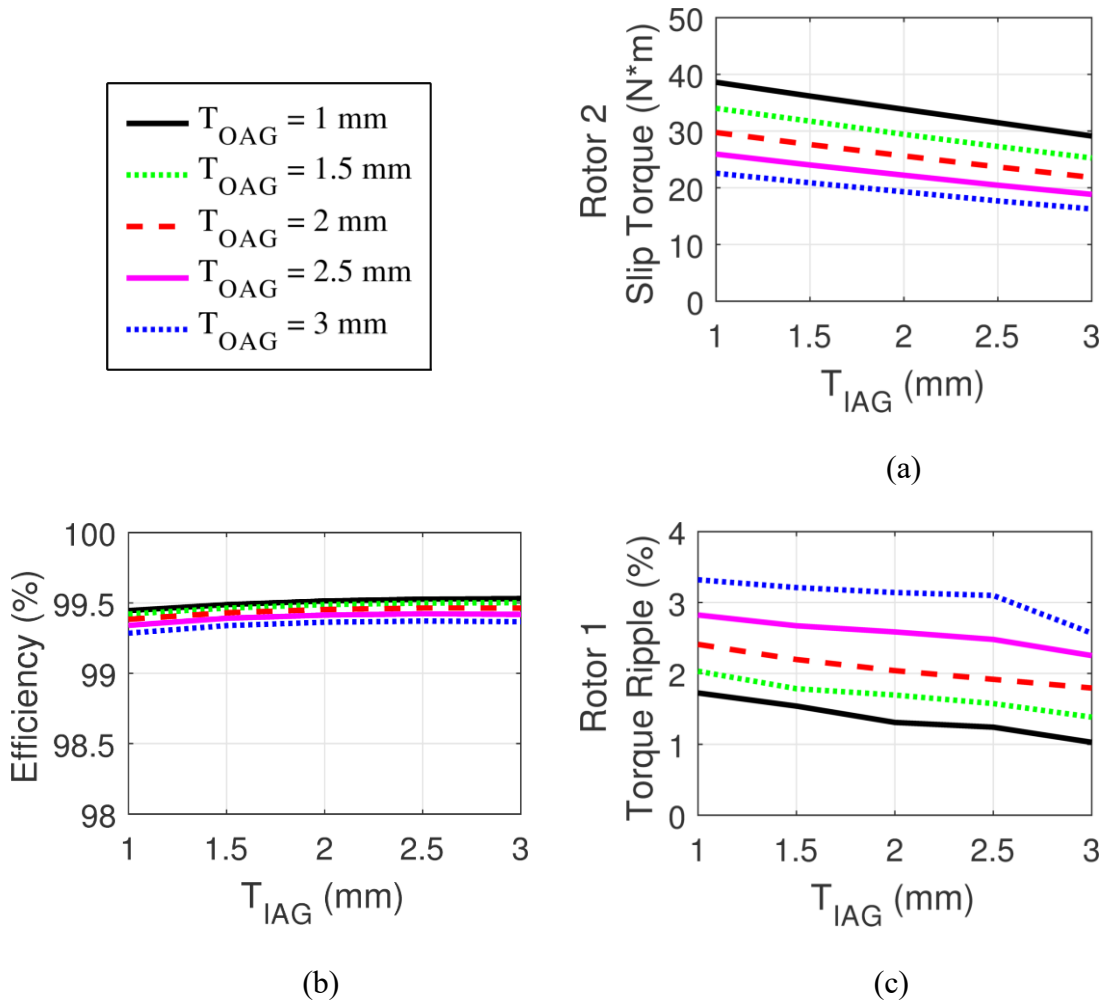


**Figure 8.4 Impact of the effective air gap thicknesses on (a) Rotor 2 slip torque, based on 3D FEA simulations, (b) electromagnetic efficiency at rated speed and maximum torque, based on 2D FEA simulations, and (c) Rotor 1 peak-to-peak torque ripple as a percentage of Rotor 1 slip torque, based on 2D FEA simulations.**

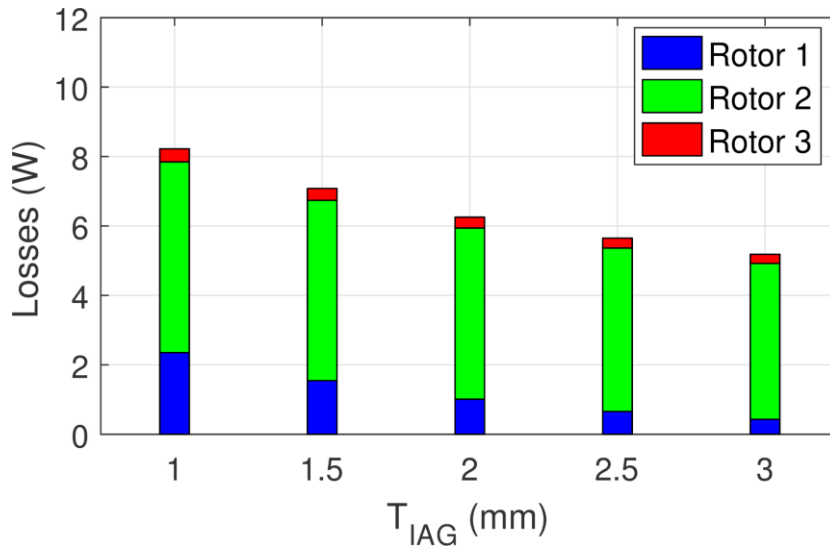


**Figure 8.5 Impact of the effective air gap thicknesses on loss distribution at rated speed and maximum torque as the inner air gap is varied with the outer air gap fixed at 1 mm, based on 2D FEA simulations.**

In a conventional magnetic gear without Halbach arrays and with back irons, the Rotor 3 PMs are attracted to the Rotor 3 back iron. However, the Halbach array results in forces pushing the radially magnetized PMs inward towards Rotor 2. Thus, it is necessary to retain the Rotor 3 PMs, but it is highly undesirable to do this in a way that increases the effective magnetic air gap. One alternative is to reduce the PM fill factor and use nonmagnetic walls between the PMs to hold them in place, particularly if the walls are thicker at the inside than they are at the outside, as in Figure 8.1. Figure 8.6 illustrates the impact of changing the thickness of the walls between adjacent Rotor 3 PMs. Comparing Figure 8.4(a) and Figure 8.6 reveals that reducing the Rotor 3 PM fill factors to accommodate this retention strategy lowers the slip torque less than increasing the effective outer air gap to insert a PM retention sleeve. Furthermore, this has a

negligible impact on the electromagnetic efficiency. This design uses Rotor 3 PM nonmagnetic walls that are 1.5 mm and 2 mm thick at their outer and inner radii, respectively. Additionally, 1.5 mm thick nonmagnetic walls between the Rotor 1 PMs connect the Rotor 1 plastic core with the Rotor 1 PM retention sleeve, so that it can be formed as a single piece. Figure 8.7 illustrates the impact of the thicknesses of these walls between the Rotor 1 PMs on the Rotor 2 slip torque. Because the Rotor 1 PMs are tangentially wider than the Rotor 3 PMs, the walls between the Rotor 1 PMs have a smaller impact on the Rotor 2 slip torque than the walls between the Rotor 3 PMs. The thicknesses chosen for this design are limited by minimum wall thicknesses that the additive manufacturing processes can achieve.

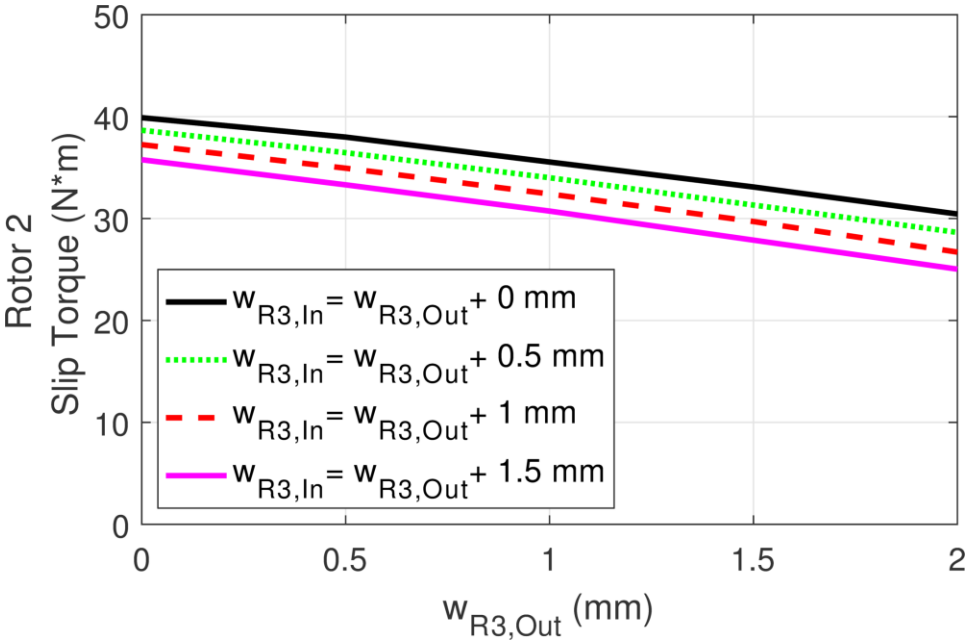


**Figure 8.6 Impact of the thickness of the nonmagnetic walls between adjacent Rotor 3 PMs on the Rotor 2 slip torque, based on 3D FEA simulations.**

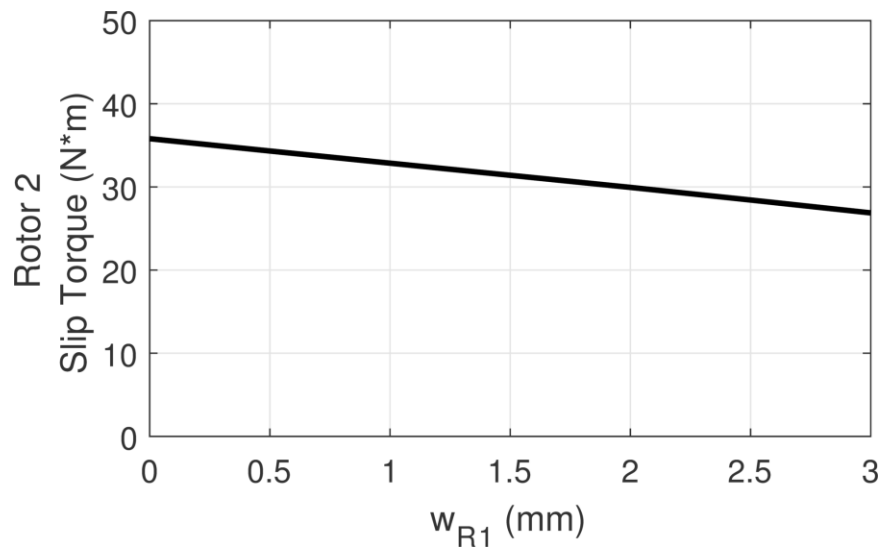


**Figure 8.7 Impact of the thickness of the nonmagnetic walls between adjacent Rotor 1 PMs on the Rotor 2 slip torque, based on 2D FEA simulations.**

In addition to the walls retaining the Rotor 3 PMs, the Rotor 3 PMs can be extended axially beyond the modulators, which allows the Rotor 3 PMs to be retained by material axially beyond the modulators. Beyond providing space for additional support, extending the PMs axially beyond the modulators can increase the slip torque, as suggested in [35]. Figure 8.8 illustrates how extending each set of PMs axially beyond the modulators affects the Rotor 2 slip torque, with the modulators' stack length fixed at 37.8 mm. For the prototype design, the Rotor 1 PMs are extended 5 mm axially past the modulators on both sides and the Rotor 3 PMs are extended 7 mm axially past the modulators on both sides. This raises the Rotor 2 slip torque from 22.0 N·m (with the PMs having the same axial length as the modulators) to 31.1 N·m. Extending the Rotor 1 PMs axially beyond the modulators does increase the volume of the design when structural material is included because the end caps for Rotor 2 and Rotor 3 must extend

past the Rotor 1 PMs. However, the Rotor 3 PMs can be extended several millimeters axially beyond the Rotor 1 PMs without impacting the overall volume of the design when structural material is included because the Rotor 3 end caps must extend farther than the Rotor 1 PMs by at least the axial length of a bearing.

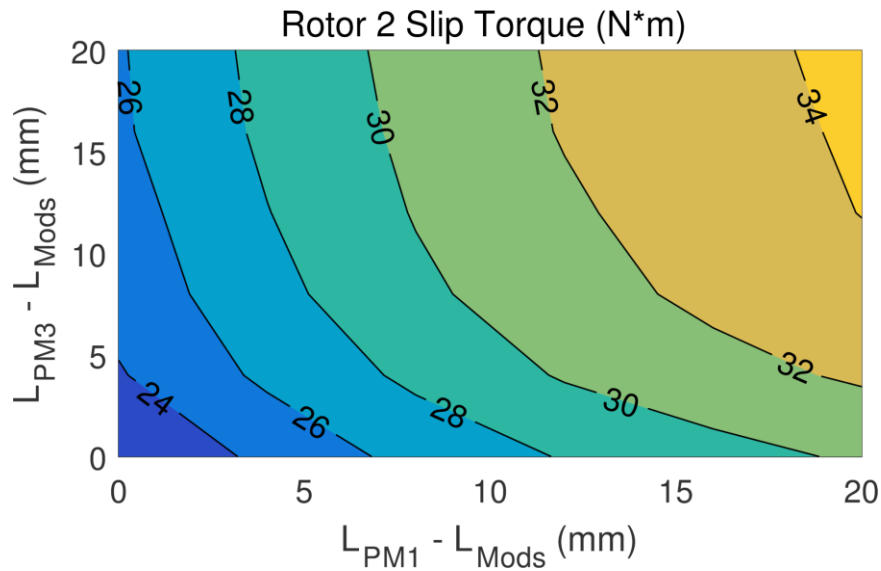


**Figure 8.8 Impact of the difference between the PM axial lengths and the modulators axial length with the modulator’s stack length fixed at 37.8 mm, based on 3D FEA simulations.**

### 8.1.3. Impact of Back Irons

The prototype base design was also simulated with 5 mm thick back irons on both Rotors 1 and 3. Replacing the plastic with steel increases the design’s magnetically active mass from 1.2 kg to 2.2 kg, but, based on 3D FEA, it only increases the Rotor 2 slip torque by 9%, resulting in a net 40% decrease in active gravimetric torque density. However, based on 3D FEA, the addition of back irons reduces the radial forces pulling

the radially magnetized PMs into the adjacent air gaps from 330 N on the Rotor 1 PMs and from 170 N on the Rotor 3 PMs to the point where the forces on both sets of PMs pull them away from the air gaps and towards the back irons. Additionally, while the use of back irons does not appreciably affect the design's electromagnetic efficiency, it does improve its flux containment, as shown in Figure 8.9. Although Halbach arrays focus most of the flux on one side, in this case, there are only two pieces per pole, which limits the impact of this flux shielding effect. For larger designs, where it is more practical to use more pieces per pole, there will be more flux shielding. Nonetheless, most of the flux on the outside of the gear is from the Rotor 1 PMs, which will not be significantly affected by using more pieces per pole on Rotor 3 [79].

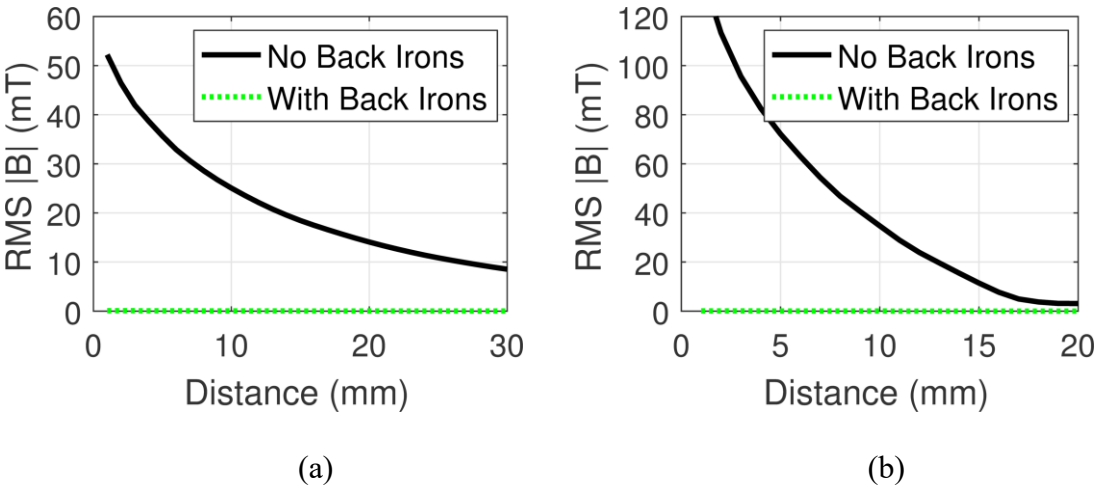


**Figure 8.9 Flux density at different radial distances (a) beyond the 5 mm back iron or Rotor 3 plastic core and (b) inside the 5 mm back iron or Rotor 1 plastic core.**

## 8.2. Prototype Fabrication

### 8.2.1. Structural Material Selection

To achieve a rapid fabrication time for the structural portions of the prototype, many components of the prototype were created using additive manufacturing. To evaluate the effectiveness of each manufacturing method and material, the Rotor 1 plastic core was fabricated, its dimensions measured and the Rotor 1 PMs inserted. Table 8.2 provides a summary of the materials evaluated.

**Table 8.2 Additive Manufacturing Material Properties Comparison.**

| Material                           | Ultem 9085   | Glass-filled Nylon | Accura Bluestone | Accura 48HTR | Accura 60 |
|------------------------------------|--------------|--------------------|------------------|--------------|-----------|
| Process                            | FDM          | SLS                | SLA              | SLA          | SLA       |
| Tensile Strength (MPA)             | 71.6         | 38.1               | 66-68            | 64-67        | 58-68     |
| Tensile Modulus (MPA)              | 2200         | 5910               | 7600-11700       | 2800-3980    | 2690-3100 |
| Elongation at Break (%)            | 6            | 2                  | 1.4-2.4          | 4-7          | 5-13      |
| Flexural Strength (MPA)            | 115.1        | Not Provided       | 124-154          | 105-118      | 87-101    |
| Flexural Modulus (MPA)             | 2500         | 3300               | 8300-9800        | 2760-3400    | 2700-3000 |
| Impact Strength (J/m)              | 106          | 96                 | 13-17            | 22-29        | 15-25     |
| Heat Deflection Temp @ 66 PSI (C)  | Not Provided | 175                | 65-66            | 130          | 53-55     |
| Heat Deflection Temp @ 264 PSI (C) | 153          | 110                | 65               | 110          | 48-50     |
| Density (g/cm <sup>3</sup> )       | 1.34         | 1.4                | 1.78             | 1.23         | 1.21      |

First, Ultem 9085, a high-strength thermoplastic, was selected due to its high tensile and flexural strengths and its high heat deflection temperature. The Rotor 1 plastic core was fabricated using fused deposition modeling (FDM). The Rotor 1 PMs could be inserted into the holes when some force was exerted. However, the outer diameter of the part was too small by about 0.5%. This tolerance was deemed to be too significant, especially for parts where such an error would significantly reduce the air gap.

Second, a glass-filled nylon part was fabricated using selective laser sintering (SLS). Again, the Rotor 1 PMs could be inserted into the holes with the exertion of some force. However, the outer diameter for the part was about 1% too small, which was again deemed unacceptable. Additionally, spacers for the slots between the modulators were fabricated from glass filled nylon using SLS. These spacers could be inserted between the modulators with significant effort. As a very tight fit for these spacers is desirable, these spacers were used in the prototype.

Third, the Rotor 1 plastic core was fabricated from Accura Bluestone, a composite material similar to a ceramic, using stereolithography (SLA). This part achieved acceptable dimensional tolerances. However, when force was applied to insert the Rotor 1 PMs into the appropriate holes, the part broke, instead of expanding slightly to accommodate the PMs.

Fourth, the Rotor 1 plastic core was produced from Accura 48HTR, a stiff, polycarbonate-like, high temperature plastic, using SLA. This part achieved acceptable



dimensional tolerances. However, when tapping threads into holes in the part, the part cracked, and pieces fell off.

Finally, the Rotor 1 plastic core was produced from Accura 60, a translucent, polycarbonate-like plastic, using SLA. This part achieved acceptable dimensional tolerances, could have threads tapped into its holes, and accommodated the insertion of the Rotor 1 PMs without significant force being applied.

Thus, the SLA process was the only process evaluated that achieved acceptable dimensional tolerances for this prototype, and Accura 60 was selected for the material to be used in most of the prototype structural parts. One major concern with the use of Accura 60 is its relatively low heat deflection temperature. As previously illustrated, the simulated losses in the prototype are very low, so it should not generate much heat, and, in a controlled laboratory environment, the prototype will not be exposed to high external temperatures. Nonetheless, outside of a laboratory setting, a magnetic gear would probably be exposed to temperatures that might cause the Accura 60 parts to deform. Therefore, it may be reasonable to use Accura 60 for rapid and inexpensive prototyping. However, it would probably be beneficial to use another process, such as injection molding or subtractive manufacturing using a computer numerically controlled (CNC) machine, for fabricating production parts.

Additionally, a few tool parts were manufactured for purposes such as positioning and inserting the PMs and pressing bearings into place on the shafts. For the tool parts that did not need to achieve strict dimensional tolerances, the SLS process was

used to make nylon parts. The tool parts that required very accurate dimensions were fabricated from Accura 60 using SLA.

### **8.2.2. Assembly**

The Rotor 1 PMs were inserted into the Rotor 1 plastic core, as shown in Figure 8.10. However, the Halbach array results in strong outward forces on the radially magnetized magnets. These forces caused Rotor 1 to bulge into the air gap in a few places by as much as 0.5 mm. To counteract this bulging, the radially magnetized Rotor 1 PMs were moved inward by 0.5 mm. Additionally, the height of the core was reduced by 5 mm, and the Rotor 1 end cap was designed to interlock with the PMs. This provided additional support for the PMs near their axial end. This revised Rotor 1 is shown in Figure 8.11 with the PMs inserted into the air core and the end cap attached. Simulations using 3D FEA predicted that moving the radially magnetized Rotor 1 PMs inward by 0.5 mm would reduce the Rotor 2 slip torque from 31.1 N·m to 30.4 N·m, which was deemed acceptable.



**Figure 8.10 Rotor 1 PMs placed in the original Rotor 1 plastic core, which was attached to the high speed shaft.**

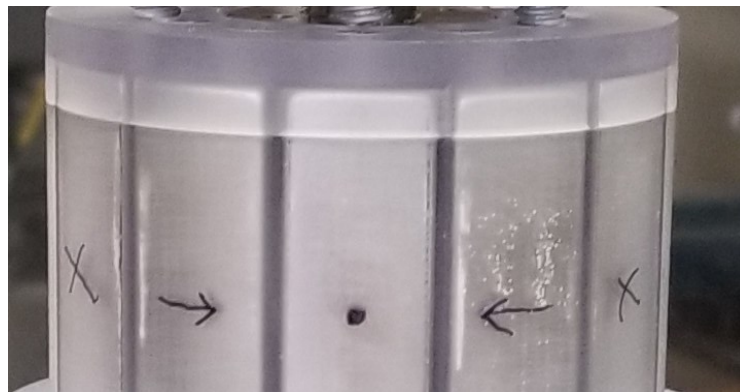


**Figure 8.11 Rotor 1 PMs placed in the revised Rotor 1 plastic core with the revised Rotor 1 end cap attached.**

The modulator stack was fabricated from 26 gauge M19 steel and was bonded together to form a single piece. Glass-filled nylon spacers were used to provide support for the modulators. These spacers were intentionally designed to be slightly shorter than

the modulator stack length so that they would not prevent axial compression of the modulator stack. These spacers were forced into the slots between the modulators using a mallet. Additionally, garolite G10 rods were inserted through the circular holes in the modulators. The modulator end caps were connected to the modulators with screws going into the spacers and by fitting the G10 rods into holes in the end caps. Figure 8.12 shows the modulator stack with all of the spacers and rods inserted and with one of the modulator end caps attached.

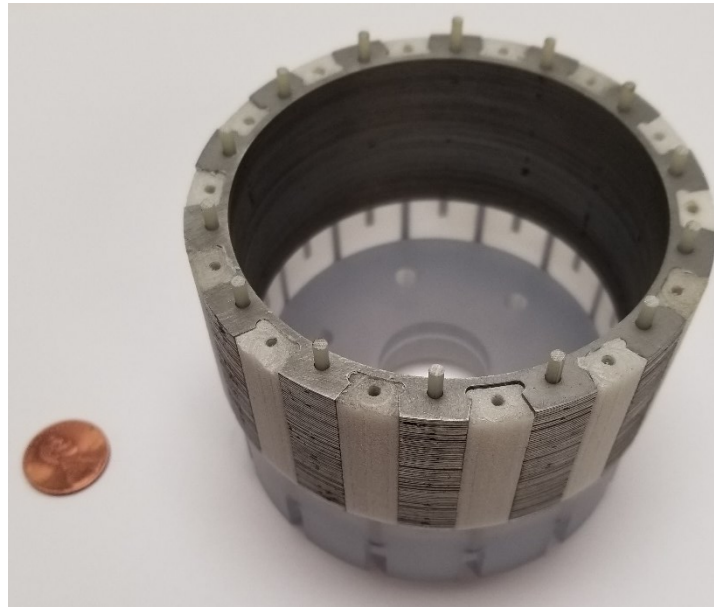


**Figure 8.12 Modulator stack with all of the spacers and rods inserted and with one of the end caps attached with a penny shown to provide a reference for size.**

The modulators end cap that was not attached to the modulators was affixed to the low speed shaft, which was then inserted into a bearing seated in the Rotor 1 plastic core. Then, a bearing was seated in the modulators end cap that was attached to the

modulators. This end cap and the modulators were then lowered along the high speed shaft into position, and the modulators were attached to the other modulators end cap. The resulting assembly is shown in Figure 8.13.



**Figure 8.13 Rotor 2 placed around Rotor 1 with a penny provided for a size reference.**

Next, the Rotor 3 magnets were inserted into the Rotor 3 plastic core. Figure 8.14 shows the Rotor 3 plastic core, and Figure 8.15 shows one of the Rotor 3 PMs. However, without the Rotor 3 end cap supporting one of the axial ends of the PMs, the radially magnetized PMs tended to lean into the air gap slightly at the top. Fortunately, this leaning was not large enough to prevent the modulators from fitting inside of Rotor 3.

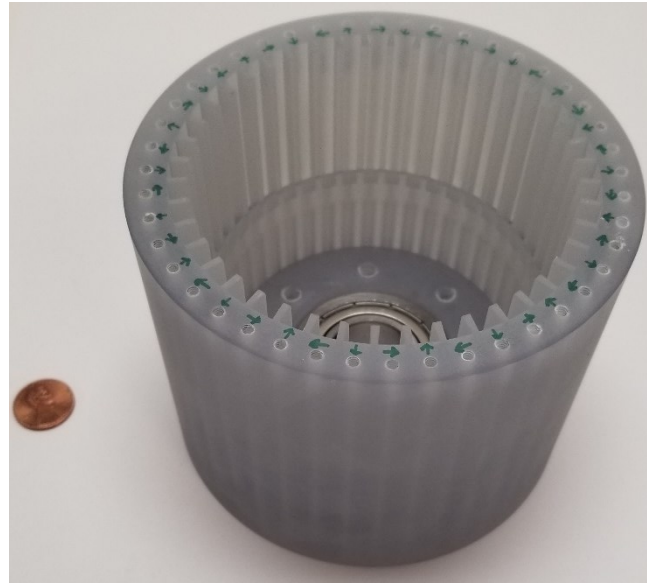


**Figure 8.14 Rotor 3 plastic core with a bearing inserted with a penny provided for a size reference.**



**Figure 8.15 Rotor 3 PM with a penny provided for a size reference.**

Then, a bearing was inserted into the Rotor 3 end cap, and the Rotor 3 end cap was moved into position on the high speed shaft. Next, the Rotor 3 plastic core with its PMs and bearing was slid along the low speed shaft into position. This process is shown in Figure 8.16. Because some of the Rotor 3 PMs were leaning inward, significant force was required to press them into their holes in the Rotor 3 end cap. Figure 8.17 shows the prototype with all three rotors assembled.

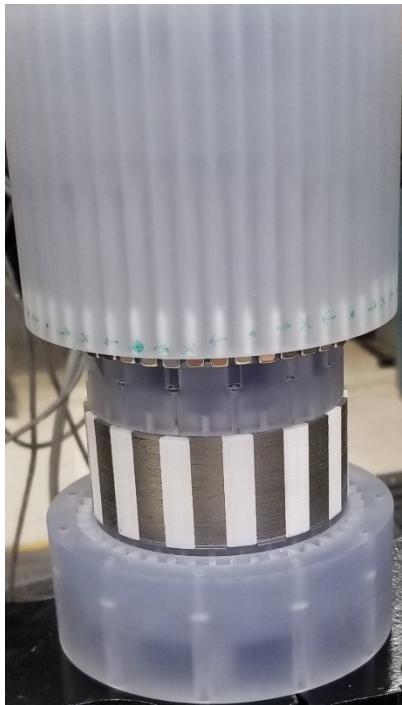


**Figure 8.16 The Rotor 3 plastic core with its PMs and bearings being slid along the low speed shaft into position.**



**Figure 8.17 Prototype with all three rotors assembled.**

Finally, supports were added to the axial ends of the prototype to mount it on the testbed. The prototype is shown with these axial end supports in Figure 8.18. With the end supports, the prototype's mass was 4.4 kg. Without the end supports the mass was 3.6 kg. Table 8.3 provides a breakdown of the masses of the various types of components in the prototype. Out of the total 4.4 kg (or 3.6 kg without the end supports), the total mass of the PMs and modulators was less than 1.3 kg.





**Figure 8.18 Fully assembled prototype with end supports.**

**Table 8.3 Prototype Mass Breakdown.**

|                              | Mass (g) |
|------------------------------|----------|
| Magnets                      | 920      |
| Modulators                   | 318      |
| Additive Manufacturing Parts | 2093     |
| Shafts                       | 612      |
| Bearings                     | 182      |
| Fasteners                    | 240      |
| Miscellaneous                | 14       |

### **8.3. Experimental Results**

The slip torque on Rotor 2 was measured to be 31.2 N·m, which is about 2.6% higher than the simulated slip torque of 30.4 N·m with the revised Rotor 1 design where the radially magnetized PMs were moved radially inward by 0.5 mm. The slip torque on

Rotor 1 was 6.4 N·m, which is about 3% lower than the simulated slip torque of 6.6 N·m. Thus, both the Rotor 1 and Rotor 2 slip torques show good agreement with simulation. This yields a GTD of 25.2 N·m/kg considering only the active materials (PMs and modulators), a GTD of 8.7 N·m/kg considering the mass of the prototype without the end supports, and a GTD of 7.1 N·m/kg considering the total mass of the prototype with the end supports included.

To measure the no load losses, the high speed shaft was connected to an induction motor, which was run at different speeds. The speeds of the high speed shaft and low speed shaft were measured. Additionally, the torque was measured on the high speed shaft to determine how much torque is required to overcome the no load losses. Figure 8.19 compares the measured speeds with the ideal gear ratio, and shows that the gear does produce a 4.67:1 gear ratio. Figure 8.20 compares the simulated electromagnetic losses with the measured no load losses. Because the losses are so small, it is difficult to measure them precisely with the torque meter, which is rated for the torques seen in normal operation of the gear, so there is some noise in the experimental loss measurements. Nonetheless, the experimental losses are significantly higher than the simulated electromagnetic losses, likely due to mechanical losses in the bearings. As shown in Figure 8.20(a) and [5], [48], the losses in a magnetic gear vary very little with torque. Based on the assumption that losses do not change with torque, the efficiency of the magnetic gear is projected in Figure 8.21 based on the measured no load losses in Figure 8.20(b).

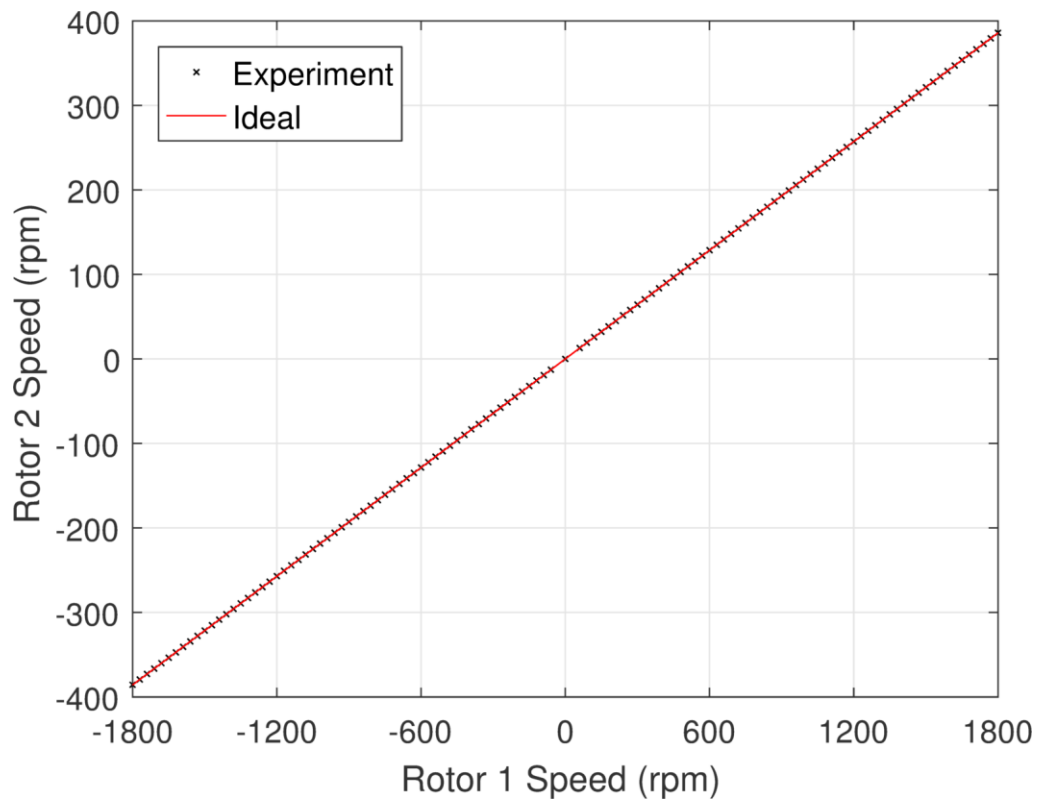


**Figure 8.19 Measured speeds on both rotors compared with the ideal gear ratio.**

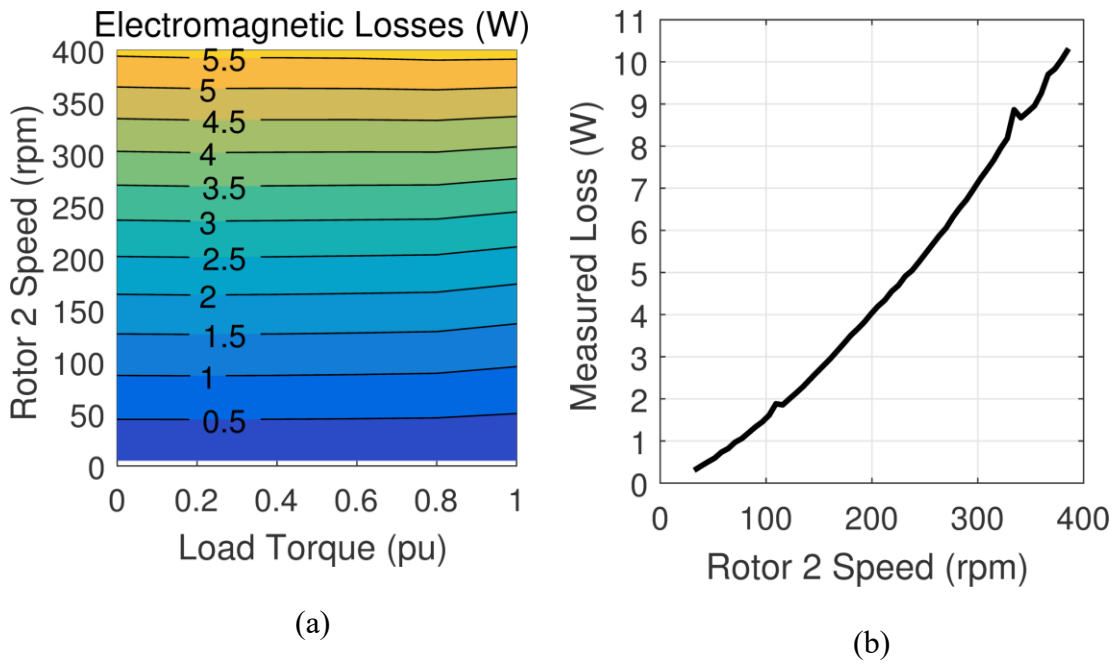


**Figure 8.20 (a) Simulated electromagnetic losses for the prototype and (b) measured no load losses in the prototype.**

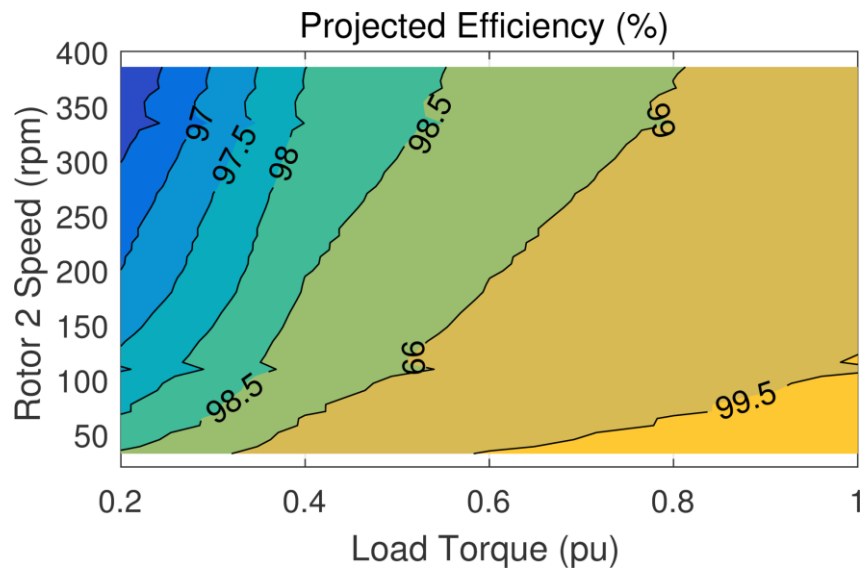


**Figure 8.21 Projected prototype efficiency.**

#### 8.4. Comparison with Mechanical Gears

Table 8.4 provides a list of the specifications of a few commercially available mechanical gears rated for roughly similar values to the prototype described in this section. Table 8.4 shows a significant variation in the masses and efficiencies achieved by these different mechanical gears. The magnetic gear prototype's projected efficiency compares very favorably with the nominal efficiencies listed for these mechanical gears, and the prototype's mass is comparable to some of these commercially available mechanical gears.

**Table 8.4 Mechanical Gear Comparison.**

|                           |             |             |              |              |         |              |
|---------------------------|-------------|-------------|--------------|--------------|---------|--------------|
| Model Number              | B518-7-L-12 | EL-B813-5-L | EPL-SA-064-5 | HERA45AS8.02 | RS-RT40 | CHC 20PB 4,6 |
| Manufacturer              | Grove Gear  | Grove Gear  | Eisele       | Hub City     | Varvel  | Chiaravalli  |
| Gear Type                 | Worm        | Worm        | Planetary    | Hypoid       | Worm    | Helical      |
| Gear Ratio                | 7:1         | 5:1         | 5:1          | 8.02:1       | 5:1     | 4.6:1        |
| Rated Output Torque (N·m) | 31.4        | 23.6        | 26.0         | 41.1         | 32.0    | 33.0         |
| Rated Output Speed (rpm)  | 250         | 350         | 700          | 312          | 720     | 302          |
| Nominal Efficiency        | 80%         | 93%         | 94%          | 90%          | 89%     | 95%          |
| Mass (kg)                 | 2.7         | 5.0         | 1.0          | 13.6         | 2.5     | 4.7          |
| GTD (N·m/kg)              | 11.6        | 4.7         | 26.0         | 3.0          | 12.8    | 7.0          |
| Reference                 | [81]        | [82]        | [83]         | [84]         | [85]    | [86]         |

## 9. CONCLUSIONS

This work has provided the results of several extensive parametric simulation studies of different topologies of magnetic gears. Additionally, a novel approach to evaluating magnetic gear dynamics has been described. Finally, the design and fabrication of a prototype have been described and its experimental test results provided.

First, radial flux coaxial magnetic gear designs optimized to maximize volumetric torque density (VTD), gravimetric torque density (GTD), and torque per dollar (TPD) were compared. There were significant differences between the designs optimizing VTD and those optimizing TPD, especially when end effects were considered. The designs optimizing GTD tended to have performances intermediate between those of the designs optimizing VTD and the designs optimizing TPD. Most of these differences focused on stuffing as much permanent magnet (PM) material into a small volume for the designs optimizing VTD versus using the PM material as cost effectively as possible for the designs optimizing TPD. End effects were shown to significantly reduce the achievable performances in terms of VTD, GTD, and TPD. Additionally, the designs optimizing VTD were optimized to a smaller outer radius when end effects were considered. The optimal pole counts for each design depended on other parameters, especially the PM thicknesses and the outer radius.

Second, radial flux coaxial magnetic gears were compared against axial flux coaxial magnetic gears. Similar trends between the performances of the two topologies included achieving higher VTDs, GTDs, and PM GTDs at higher torques and lower gear

ratios. Additionally, both topologies achieved similar average air gap shear stresses. However, the axial flux designs tended to achieve better VTDs than the radial flux designs for form factors with large outer radii and short stack lengths. Additionally, end effects cause the VTD, GTD, and PM GTD to increase with stack length in radial flux magnetic gears, whereas the radii ratio maximizing VTD is much lower than the radii ratio maximizing GTD or PM GTD for an axial flux magnetic gear. Furthermore, the radial forces on the bearings of a radial flux coaxial magnetic gear can be significantly mitigated through the use of symmetry, but the axial forces on the bearings of an axial flux magnetic gear cannot be mitigated by simply using a design with an even number of modulators. Overall, radial flux magnetic gears seemed to have an advantage over magnetic gears in terms of performance and manufacturability, except in applications with a large outer radius and a small axial length.

Third, radial flux coaxial and cycloidal magnetic gears were compared. The cycloidal designs were shown to be able to achieve higher torque densities at high gear ratios. While the coaxial designs favor low gear ratios, regardless of the outer radius, the optimal gear ratio for the cycloidal designs increases with the outer radius. The coaxial gears benefit more from using thicker PMs than the cycloidal gears benefit. However, the coaxial gears suffer a larger reduction in torque from end effects than the cycloidal gears. Both topologies can achieve very low torque ripple, but the cycloidal topology suffers from large forces on the bearings. The cycloidal topology eliminates the complexity of having to support the modulators, but it requires the orbital motion of the

inner rotor's axis about the outer rotor's axis to be separated from the inner rotor's rotation about its own axis.

Fourth, alternative approaches to achieving high gear ratios with coaxial magnetic gears were evaluated. The torque density and efficiency achievable with a single-stage coaxial magnetic gear decrease as the gear ratio increases. Using a multistage magnetic gearbox allows much higher gear ratios to be achieved without as much of a reduction in torque density, but this increases the complexity of the gearbox. For multistage gearboxes, it is generally optimal for the gear ratio of the first stage to be relatively small so that the first stage, which interacts with the largest torque, has a high torque density. Furthermore, the compound differential coaxial magnetic gear was proposed. It is able to achieve very large gear ratios with just two coaxial magnetic gear stages, but this comes from having circulating power, which significantly harms the efficiency.

Next, a nonlinear analytical approach to evaluating magnetic gear dynamics was presented. First, the motion of the magnetic gear is described as the superposition of rigid body motion and fixed center motion, without violating the nonlinearity of the system. Then, the fixed center motion can be referred into the torque angle reference frame, where the conservation of energy principle can be used to evaluate the oscillation of the magnetic gear's torque angle in response to changes in the torques applied to the magnetic gear (assuming that losses are negligible). This analysis reveals that the effective inertia ratio is a critical design parameter, determining the magnetic gears' response to torques applied to each rotor. The proposed nonlinear model was shown to



agree very well with a Simulink model and with an FEA model for a coaxial magnetic gear with very little torque ripple. However, there were some small discrepancies compared to FEA models with larger torque ripples. Nonetheless, the proposed model was much more consistent with the Simulink and FEA models than a linearized model. Additionally, even a significant amount of viscous friction was shown to have only a limited impact on the dynamic behavior of the magnetic gear immediately following a step change in torque.

Then, Halbach arrays and air cores were evaluated for use in coaxial radial flux magnetic gears. Together, Halbach arrays and air cores can significantly increase the achievable GTDs of magnetic gears relative to more conventional designs with radially magnetized PMs mounted on back irons. However, without Halbach arrays, removing the back irons actually reduces the GTDs of many designs. On the other hand, if a back iron is present, using a Halbach array only benefits the design if the PMs are relatively thick. Thus, the GTD benefits of using Halbach arrays and air cores are often accompanied by a reduction in PM GTD.

Finally, to validate the models and explore the challenges associated with using Halbach arrays and air cores in magnetic gears, a prototype was designed, fabricated, and tested. Various tradeoffs between magnetic performance and mechanical design considerations were evaluated. The modulators were supported using a bridge and circular cutouts to accommodate rods and spacers. The Rotor 1 PMs were retained with a nonmagnetic sleeve, while the Rotor 3 PMs were retained with tapered walls between adjacent PMs and by material axially beyond the modulators. The assembly was

facilitated by making tools using additive manufacturing to simplify tasks such as inserting the PMs into place and pressing the bearings into place. The prototype showed good agreement with the simulation results regarding its slip torque, which was measured to be 31.2 N·m. This results in a GTD of 25.2 N·m/kg considering only the active materials (PMs and modulators), a GTD of 8.7 N·m/kg considering the total mass of the prototype without the end supports, and a GTD of 7.1 N·m/kg considering the total mass of the prototype with the end supports included. However, the prototype's losses were higher than those predicted by electromagnetic analysis, likely due to bearing losses. Nonetheless, the prototype's projected 99% efficiency based on the measured no load losses compares very favorably against a few commercially available mechanical gears with roughly similar ratings. The prototype's mass is within the range of the masses of similarly rated commercially available mechanical gears.

## REFERENCES

- [1] S. Sheng, "Report on Wind Turbine Subsystem Reliability – A Survey of Various Databases," Nat. Renewable Energy Lab., Golden, CO, Jun. 2013.
- [2] L. Jian, K. T. Chau, and J. Z. Jiang, "A Magnetic-Geared Outer-Rotor Permanent-Magnet Brushless Machine for Wind Power Generation," *IEEE Trans. Ind. Appl.*, vol. 45, no. 3, pp. 954-962, May-Jun. 2009.
- [3] N. W. Frank and H. A. Toliyat, "Gearing Ratios of a Magnetic Gear for Wind Turbines," in *Proc. IEEE Int. Elect. Mach. and Drives Conf.*, 2009, pp. 1224-1230.
- [4] K. K. Uppalapati, J. Z. Bird, D. Jia, J. Garner, and A. Zhou, "Performance of a Magnetic Gear Using Ferrite Magnets for Low Speed Ocean Power Generation," in *Proc. IEEE Energy Convers. Congr. and Expo.*, 2012, pp. 3348-3355.
- [5] M. Johnson, M. C. Gardner, H. A. Toliyat, S. Englebretson, W. Ouyang, and C. Tschida, "Design, Construction, and Analysis of a Large Scale Inner Stator Radial Flux Magnetically Geared Generator for Wave Energy Conversion," *IEEE Trans. Ind. Appl.*, vol. 54, no. 4, pp. 3305-3314, Jul.-Aug 2018.
- [6] N. W. Frank and H. A. Toliyat, "Gearing Ratios of a Magnetic Gear for Marine Applications," in *Proc. IEEE Electr. Ship Technol. Symp.*, 2009, pp. 477-481.
- [7] D. J. Powell, S. D. Calverley, F. de Wildt, and K. Daffey, "Design and Analysis of a Pseudo Direct-Drive Propulsion Motor," in *Proc. IET Int. Conf. Power Electron., Mach. and Drives*, 2010, pp. 1-2.
- [8] L. MacNeil, B. Claus, and R. Bachmayer, "Design and Evaluation of a Magnetically-Geared Underwater Propulsion System for Autonomous Underwater and Surface Craft," in *Proc. Int. Conf. IEEE Oceans*, 2014, pp. 1-8.
- [9] T. V. Frandsen, L. Mathe, N. I. Berg, R. K. Holm, T. N. Matzen, P. O. Rasmussen, and K. K. Jensen, "Motor Integrated Permanent Magnet Gear in a Battery Electrical Vehicle," *IEEE Trans. Ind. Appl.*, vol. 51, no. 2, pp. 1516-1525, Mar.-Apr. 2015.
- [10] W. J. McDonald, T. F. Price, and G. P. Hatch, "Wellbore Motor Having Magnetic Gear Drive," U.S. Patent 7 481 283 B2, Jan. 27, 2009.

- [11] J. J. Scheidler, V. M. Asnani and T. F. Tallerico, "NASA's Magnetic Gearing Research for Electrified Aircraft Propulsion," in *Proc. AIAA/IEEE Elect. Aircraft Technol. Symp.*, 2018, pp. 1-12.
- [12] C. G. Armstrong, "Power Transmitting Device," U.S. Patent 687 292, Nov. 26, 1901.
- [13] H. T. Faus, "Magnetic Gearing," U.S. Patent 2 243 555, May 27, 1941.
- [14] A. H. Neuland, "Apparatus for Transmitting Power," U.S. Patent 1 171 351, Feb. 8, 1916.
- [15] G. A. Reese, "Magnetic Gearing Arrangement," U.S. Patent 3 301 091, Jan. 31, 1967.
- [16] T. B. Martin Jr., "Magnetic Transmission," U.S. Patent 3 378 710, Apr. 16, 1968.
- [17] K. Atallah and D. Howe, "A Novel High-Performance Magnetic Gear," *IEEE Trans. Magn.*, vol. 37, no. 4, pp. 2844-2846, Jul. 2001.
- [18] S. Mezani, K. Atallah, and D. Howe, "A High-Performance Axial-Field Magnetic Gear," *J. Appl. Phys.*, vol. 99, no. 8, pp. 1-3, Apr. 2006.
- [19] F. T. Jorgensen, T. O. Andersen, and P. O. Rasmussen, "The Cycloid Permanent Magnetic Gear," *IEEE Trans. Ind. Appl.*, vol. 44, no. 6, pp. 1659-1665, Nov.-Dec. 2008.
- [20] J. Rens, K. Atallah, S. D. Calverley, and D. Howe, "A Novel Magnetic Harmonic Gear," *IEEE Trans. Ind. Appl.*, vol. 46, no. 1, pp. 206-212, Jan.-Feb. 2010.
- [21] K. Davey, T. Hutson, L. McDonald and G. Hutson, "The Design and Construction of Cycloidal Magnetic Gears," in *Proc. IEEE Int. Elect. Mach. And Drives Conf.*, 2017, pp. 1-6.
- [22] K. Davey, L. McDonald, and T. Hutson, "Axial Flux Cycloidal Magnetic Gears," *IEEE Trans. Magn.*, vol. 50, no. 4, pp. 1-7, Apr. 2014.
- [23] K. Atallah, J. Wang, and D. Howe, "A High-Performance Linear Magnetic Gear," *J. Appl. Phys.*, vol. 97, no. 10, pp. 1-3, 2004.
- [24] R. K. Holm, N. I. Berg, M. Walkusch, P. O. Rasmussen, and R. H. Hansen, "Design of a Magnetic Lead Screw for Wave Energy Conversion," *IEEE Trans. Ind. Appl.*, vol. 49, no. 6, pp. 2699-2708, Nov.-Dec. 2013.
- [25] M. B. Kouhshahi and J. Z. Bird, "Analysis of a Magnetically Geared Lead Screw," in *Proc. IEEE Energy Convers. Congr. and Expo.*, pp. 1-5, 2016.

- [26] K. Atallah, J. Rens, S. Mezani, and D. Howe, "A Novel 'Pseudo' Direct-Drive Brushless Permanent Magnet Machine," *IEEE Trans. Magn.*, vol. 44, no. 11, pp. 4349-4352, Nov. 2008.
- [27] L. Brönn, "Design and Performance Evaluation of a Magnetically Geared Axial-Flux Permanent Magnet Generator," M.S. thesis, Dept. Elect. Eng., Stellenbosch Univ., Stellenbosch, South Africa, 2012.
- [28] M. Johnson, M. C. Gardner, and H. A. Toliyat, "Design and Analysis of an Axial Flux Magnetically Geared Generator," *IEEE Trans. Ind. Appl.*, vol. 53, no. 1, pp. 97-105, Jan.-Feb. 2017.
- [29] E. Gouda, S. Mezani, L. Baghli, and A. Rezzoug, "Comparative Study between Mechanical and Magnetic Planetary Gears," *IEEE Trans. Magn.*, vol. 47, no. 2, pp. 439-450, Feb. 2011.
- [30] K. K. Uppalapati, J. Z. Bird, J. Wright, J. Pitchard, M. Calvin, and W. Williams, "A Magnetic Gearbox with an Active Region Torque Density of 239Nm/L," in *Proc. IEEE Energy Convers. Congr. and Expo.*, 2014, pp. 1422-1428.
- [31] M. Johnson, M. C. Gardner, and H. A. Toliyat, "Analysis of Axial Field Magnetic Gears with Halbach Arrays," in *Proc. IEEE Int. Elect. Mach. and Drives Conf.*, 2015, pp. 108-114.
- [32] M. Johnson, M. C. Gardner, and H. A. Toliyat, "Design Comparison of NdFeB and Ferrite Radial Flux Magnetic Gears," in *Proc. IEEE Energy Convers. Congr. and Expo.*, 2016, pp. 1-8.
- [33] P. O. Rasmussen, T. O. Andersen, F. T. Jorgensen, and O. Nielsen, "Development of a High-Performance Magnetic Gear," *IEEE Trans. Ind. Appl.*, vol. 41, no. 3, pp. 764-770, May-Jun. 2005.
- [34] S. Gerber and R. J. Wang, "Evaluation of a Prototype Magnetic Gear," in *Proc. IEEE Int. Conf. Ind. Technol.*, 2013, pp. 319-324.
- [35] S. Gerber and R. J. Wang, "Analysis of the End-Effects in Magnetic Gears and Magnetically Geared Machines," in *Proc. Int. Conf. Elect. Mach.*, 2014, pp. 396-402.
- [36] T. D. Nguyen, V. Lanfranchi, C. Doc and J. P. Vilain, "Comparison of Optimization Algorithms for the Design of a Brushless DC Machine with Travel-Time Minimization," in *Proc. Electromotion*, 2009, pp. 1-6.

- [37] S. Stipetic, W. Miebach and D. Zarko, "Optimization in Design of Electric Machines: Methodology and Workflow," in *Proc. Acemp – Optim – Electromotion*, 2015, pp. 441-448.
- [38] A. Krishnamoorthy and K. Dharmalingam, "Application of Genetic Algorithms in the Design Optimization of Three Phase Induction Motor," *J. Comput. Applicat.*, vol. 2, no. 4, pp. 1 – 5, Oct – Dec. 2009.
- [39] S. D. Sudhoff and Y. Lee, "Energy Systems Analysis Consortium (ESAC) Genetic Optimization System Engineering Tool (GOSET) Version Manual," School Electr. Comput. Eng., Purdue Univ., West Lafayette, IN, 2003.
- [40] D. J. Evans and Z. Q. Zhu, "Influence of Design Parameters on Magnetic Gear's Torque Capability," in *Proc. IEEE Int. Elect. Mach. and Drives Conf.*, 2011, pp. 1403-1408.
- [41] T. Lubin, S. Mezani, and A. Rezzoug, "Development of a 2-D Analytical Model for the Electromagnetic Computation of Axial-Field Magnetic Gears," *IEEE Trans. Magn.*, vol. 49, no. 11, pp. 5507-5521, Nov. 2013.
- [42] V. M. Acharya, J. Z. Bird, and M. Calvin, "A Flux Focusing Axial Magnetic Gear," *IEEE Trans. Magn.*, vol. 49, no. 7, pp. 4092-4095, Jul. 2013.
- [43] R.-J. Wang, L. Brönn, S. Gerber, and P. M. Tlali, "Design and Evaluation of a Disc-Type Magnetically Geared PM Wind Generator," in *Proc. Int. Conf. Power Eng., Energy and Electr. Drives*, 2013, pp. 1259-1264.
- [44] K. Atallah, S. D. Calverley, and D. Howe, "Design, Analysis and Realisation of a High-Performance Magnetic Gear," *IEE Proc. Elec. Power Appl.*, vol. 151, no. 2, pp. 135-143, Mar. 2004.
- [45] S. Gerber and R. J. Wang, "Design and Evaluation of a Magnetically Geared PM Machine," *IEEE Trans. Magn.*, vol. 51, no. 8, pp. 1-10, Aug. 2015.
- [46] T. V. Frandsen, P. O. Rasmussen and K. K. Jensen, "Improved Motor Intergrated Permanent Magnet Gear for Traction Applications" in *Proc. IEEE Energy Convers. Congr. and Expo.*, 2012, pp. 3332-3339.
- [47] M. Johnson, A. Shapoury, P. Boghrat, M. Post, and H. A. Toliyat, "Analysis and Development of an Axial Flux Magnetic Gear," in *Proc. IEEE Energy Convers. Congr. and Expo.*, 2014, pp. 5893-5900.
- [48] G. Jungmayr, J. Loeffler, B. Winter, F. Jeske, and W. Amrhein, "Magnetic Gear: Radial Force, Cogging Torque, Skewing, and Optimization," *IEEE Trans. Ind. Appl.*, vol. 52, no. 5, pp. 3822-3830, Sep.-Oct. 2016.

- [49] A. Rahideh, A. A. Vahaj, M. Mardaneh, and T. Lubin, "Two-Dimensional Analytical Investigation of the Parameters and the Effects of Magnetisation Patterns on the Performance of Coaxial Magnetic Gears," *IET Elec. Syst. Transp.*, vol. 7, no. 3, pp. 230-245, Aug. 2017.
- [50] Y. Chen, W. N. Fu, S. L. Ho, H. Liu, "A Quantitative Comparison Analysis of Radial-Flux, Transverse-Flux, and Axial-Flux Magnetic Gears," *IEEE Trans. Magn.*, vol. 50, no. 11, pp. 1-4, Nov. 2014.
- [51] M. C. Gardner, B. E. Jack, M. Johnson, and H. A. Toliyat, "Comparison of Coaxial Radial Flux Magnetic Gears Independently Optimized for Volume, Cost, and Mass," *IEEE Trans. Ind. Appl.*, vol. 54, no. 3, pp. 2237-2245, May-Jun. 2018.
- [52] D. J. Patterson, J. L. Colton, B. Mularcik, B. J. Kennedy, S. Camilleri, and R. Rohoza, "A Comparison of Radial and Axial Flux Structures in Electrical Machines," in *Proc. IEEE Int. Elect. Mach. and Drives Conf.*, 2009, pp. 1029-1035.
- [53] A. Penzkofer and K. Atallah, "Scaling of Pseudo Direct Drives for Wind Turbine Application," *IEEE Trans. Magn.*, vol. 52, no. 7, pp. 1-5, Jul. 2016.
- [54] K. Li, J. Bird, J. Kadel and W. Williams, "A Flux-Focusing Cycloidal Magnetic Gearbox," *IEEE Trans. Magn.*, vol. 51, no. 11, pp. 1-4, Nov. 2015.
- [55] N. W. Frank and H. A. Toliyat, "Analysis of the Concentric Planetary Magnetic Gear with Strengthened Stator and Interior Permanent Magnet Inner Rotor," *IEEE Trans. Ind. Appl.*, vol. 47, no. 4, pp. 1652-1660, Jul.-Aug. 2011.
- [56] P. M. Tlali, R.-J. Wang, and S. Gerber, "Magnetic Gear Technologies: A Review," in *Proc. Int. Conf. Elect. Mach.*, 2014, pp. 544-550.
- [57] J. M. Crider, and S. D. Sudhoff, "An Inner Rotor Flux-Modulated Permanent Magnet Synchronous Machine for Low-Speed High-Torque Applications," *IEEE Trans. Energy Convers.*, vol. 30, no. 3, pp. 1247-1254, Sep. 2015.
- [58] M. Filippini and P. Alotto, "Coaxial Magnetic Gears Design and Optimization," *IEEE Trans. Ind. Elect.*, vol. 64, no. 12, pp. 9934-9942, Dec. 2017.
- [59] M. Desvaux, B. Multon, H. B. Ahmed, S. Sire, A. Fasquelle, and D. Laloy, "Gear Ratio Optimization of a Full Magnetic Indirect Drive Chain for Wind Turbine Applications," in *Proc. Twelfth Int. Conf. Ecological Veh. Renewable Energies*, 2017, pp. 1-9.

- [60] K. Li, J. Wright, S. Modaresahmadi, D. Som, W. Williams and J. Z. Bird, "Designing the First Stage of a Series Connected Multistage Coaxial Magnetic Gearbox for a Wind Turbine Demonstrator," in *Proc. IEEE Energy Convers. Congr. and Expo.*, 2017, pp. 1247-1254.
- [61] S. Pakdelian, M. Moosavi, H. A. Hussain, and H. A. Toliyat, "Control of an Electric Machine Integrated With the Trans-Rotary Magnetic Gear in a Motor Drive Train," *IEEE Trans. Ind. Appl.*, vol. 53, no. 1, pp. 106–114, Jan.-Feb. 2017.
- [62] M. Desvaux, R. Le Goff Latimier, B. Multon, S. Sire, and H. Ben Ahmed, "Analysis of the Dynamic Behaviour of Magnetic Gear with Nonlinear Modelling for Large Wind Turbines," in *Proc. Int. Conf. Elect. Mach.*, 2016, pp. 1332–1138.
- [63] R. G. Montague, C. M. Bingham, and K. Atallah, "Magnetic Gear Dynamics for Servo Control," in *Proc. IEEE Mediterranean Electrotechnical Conf.*, 2010, pp. 1192–1197.
- [64] M. Bouheraoua, J. Wang, and K. Atallah, "A Complex Frequency Domain Analysis of a Closed Loop Controlled Pseudo Direct Drive," in *Proc. Int. Conf. Elect. Mach.*, 2012, pp. 2428–2434.
- [65] R. G. Montague, C. M. Bingham, and K. Atallah, "Dual-Observer-Based Position-Servo Control of a Magnetic Gear," *IET Elect. Power. Appl.*, vol. 5, no. 9, pp. 708–714, Nov. 2011.
- [66] M. C. Gardner, M. Johnson, and H. A. Toliyat, "Analysis of High Gear Ratio Capabilities for Single-Stage, Series Multistage, and Compound Differential Coaxial Magnetic Gears," *IEEE Trans. Energy Convers.*, vol. pp, no. 99, pp. 1-8, 2018.
- [67] K. Aiso, K. Akatsu, and Y. Aoyama, "A Novel Reluctance Magnetic Gear for High-Speed Motor," *IEEE Trans. Ind. Appl.*, vol. 55, no. 3, pp. 2690-2699, May-Jun. 2019.
- [68] Z. Q. Zhu and D. Howe, "Halbach Permanent Magnet Machines and Applications: A Review," *IEE Proc. Elect. Power. Appl.*, vol. 148, no. 4, pp. 299-308, Jul. 2001.
- [69] Z. Q. Zhu, "Recent Development of Halbach Permanent Magnet Machines and Applications," in *Proc. Power Convers. Conf.*, 2007, pp. 9-16.



- [70] S. Sadeghi and L. Parsa, "Multiobjective Design Optimization of Five-Phase Halbach Array Permanent-Magnet Machine," *IEEE Trans. Magn.*, vol. 47, no. 6, pp. 1658-1666, Jun. 2011.
- [71] L. Yang, S. L. Ho, W. N. Fu, and W. Li, "Design Optimization of a Permanent Magnet Motor Derived From a General Magnetization Pattern," *IEEE Trans. Magn.*, vol. 51, no. 11, pp. 1-4, Nov. 2015.
- [72] K. Bastiaens, J. W. Jansen, S. Jumayev, and E. A. Lomonova, "Design of an Axial-Flux Permanent Magnet Machine for an In-Wheel Direct Drive Application," in *Proc. IEEE Int. Elect. Mach. and Drives Conf.*, 2017, pp. 1-7.
- [73] Z. P. Xia, Z. Q. Zhu and D. Howe, "Analytical Magnetic Field Analysis of Halbach Magnetized Permanent-Magnet Machines," *IEEE Trans. Magn.*, vol. 40, no. 4, pp. 1864-1872, Jul. 2004.
- [74] M. Markovic and Y. Perriard, "Optimization Design of a Segmented Halbach Permanent-Magnet Motor Using an Analytical Model," *IEEE Trans. Magn.*, vol. 45, no. 7, pp. 2955-2960, Jul. 2009.
- [75] G. I. Oosthuizen and P. J. Randewijk, "Design of an Ironless Double-Rotor Radial Flux Permanent Magnet Machine," in *Proc. IEEE Int. Elect. Mach. and Drives Conf.*, 2015, pp. 683-688.
- [76] M. Munaro, N. Bianchi and G. Meneghetti, "High Torque Density PM Motor for Racing Applications," in *Proc. IEEE Energy Convers. Congr. and Expo.*, 2017, pp. 5826-5833.
- [77] L. Jian, K. T. Chau, Y. Gong, J. Z. Jiang, C. Yu and W. Li, "Comparison of Coaxial Magnetic Gears With Different Topologies," *IEEE Trans. Magn.*, vol. 45, no. 10, pp. 4526-4529, Oct. 2009.
- [78] L. Jian and K. T. Chau, "A Coaxial Magnetic Gear With Halbach Permanent-Magnet Arrays," *IEEE Trans. Energy Convers.*, vol. 25, no. 2, pp. 319-328, Jun. 2010.
- [79] M. C. Gardner, D. A. Janak and H. A. Toliyat, "A Parameterized Linear Magnetic Equivalent Circuit for Air Core Radial Flux Coaxial Magnetic Gears with Halbach Arrays," in *Proc. IEEE Energy Convers. Congr. and Expo.*, 2018, pp. 2351-2358.
- [80] H. Baninajar, J. Z. Bird, S. Modaresahmadi and W. Williams, "Electromagnetic and Mechanical Design of a Hermetically Sealed Magnetic Gear for a Marine Hydrokinetic Generator," in *Proc. IEEE Energy Convers. Congr. and Expo.*, 2018, pp. 4987-4993.

- [81] Grove Gear, "BRAVO Series eCatalog," Accessed: May 13, 2019,  
<http://grovegear.smartcats.com/ecatalog/BRAVO-Single-Solid/en/B518-7-L-12>.
- [82] Grove Gear, "Electra-Gear EL Series eCatalog," Accessed: May 13, 2019,  
<http://grovegear.smartcats.com/ecatalog/Electragear-EL-Single-Solid/en/EL-B813-5-L>.
- [83] Eisele Getriebe, "Eisele Katalog Planetengetriebe," Accessed: May 13, 2019,  
[http://eisele-getriebe.com/wordpress/wp-content/uploads/2017/03/Eisele-Katalog\\_Planetengetriebe\\_20170312.pdf](http://eisele-getriebe.com/wordpress/wp-content/uploads/2017/03/Eisele-Katalog_Planetengetriebe_20170312.pdf).
- [84] Hub City, "HERA Catalog Section," Accessed: May 19, 2019,  
<https://www.hubcityinc.com/documents/7H-HubCityHERAgearDrives.pdf>.
- [85] Varvel, "RS RT Catalog," Accessed: May 19, 2019,  
<http://www.varvel.com/varvel-download/3248>.
- [86] Chiaravalli, "Gear Boxes and Motors Catalog," Accessed: May 21, 2019,  
[https://feyc.eu/download/catalogos/transmission/chiaravalli/Gear%20Boxes%20and%20Motors%20%20\(1\).pdf](https://feyc.eu/download/catalogos/transmission/chiaravalli/Gear%20Boxes%20and%20Motors%20%20(1).pdf).